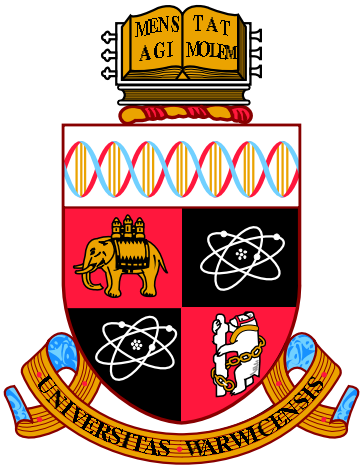

Exploring the final stages of stars in our Milky Way using large sky surveys

by

Sandra Magdy Kamel Greiss

Thesis

Submitted to the University of Warwick

for the degree of

Doctor of Philosophy

Department of Physics

July 2014

THE UNIVERSITY OF WARWICK

Contents

List of Tables **iv**

List of Figures **vi**

Acknowledgments **xiv**

Declarations **xvi**

Abstract **xvii**

Chapter 1 Motivation **1**

Chapter 2 Compact stars **5**
2.1 The Hertzsprung-Russell diagram 5
2.2 Stellar evolution in a nutshell 5
2.2.1 Nuclear processes 5
2.2.2 Shell-hydrogen burning and red-giant phase 7
2.2.3 Death of stars like the Sun 9
2.2.4 Death of massive stars 10
2.3 White Dwarfs 11
2.3.1 Spectral types 12
2.3.2 Mass distribution 12
2.3.3 Why are they useful? 12
2.3.4 Pulsating white dwarfs 16
2.3.4.1 Theoretical context 17
2.4 Neutron Stars 23
2.5 Black holes 25
2.6 Compact binary systems 25
2.6.1 Cataclysmic variables 26
2.6.2 Low-mass X-ray binaries 28

Chapter 3 Astronomical tools and methods **30**
3.1 Charge-coupled devices 30
3.2 Photometry 30
3.2.1 Colour-colour and colour-magnitude diagrams 34
3.2.2 Time-series photometry 34

3.3 Spectroscopy . . . 36
3.3.1 Bias removal . . . 36
3.3.2 Flat Fielding . . . 37
3.3.3 Spectrum extraction . . . 37
3.3.4 Wavelength calibration . . . 37
3.3.5 Flux calibration . . . 37
3.4 Summary . . . 38

Chapter 4 Large Sky Surveys **39**
4.1 X-ray survey . . . 39
4.1.1 Galactic Bulge Survey (GBS) . . . 39
4.2 The near-infrared surveys . . . 41
4.2.1 The Two Micron All Sky Survey (2MASS) . . . 41
4.2.2 UKIDSS Galactic Plane Survey (GPS) . . . 42
4.2.3 VISTA Variables in the Via Lactea (VVV) . . . 43
4.3 Optical survey: The *Kepler*-INT Survey . . . 45
4.3.1 *Kepler* mission . . . 45
4.3.2 Survey imaging with the Isaac Newton Telescope . . . 48
4.3.3 INT observations and data . . . 49
4.3.3.1 Observations . . . 49
4.3.3.2 Data . . . 49
4.3.3.3 Quality control flags . . . 50
4.3.3.4 Photometric calibration . . . 50
4.3.3.5 Catalogue description . . . 56
4.4 Summary . . . 60

Chapter 5 Near-infrared and optical study of the GBS sources **63**
5.1 Near-infrared coverage of the Bulge . . . 63
5.1.1 Coverage . . . 63
5.1.2 VVV vs 2MASS . . . 64
5.1.3 VVV vs UKIDSS GPS . . . 66
5.2 Extinction . . . 68
5.3 Results . . . 69
5.3.1 Quantifying the false alarm rate . . . 71
5.3.2 Random matching . . . 72
5.3.3 Positional uncertainties . . . 74
5.3.4 Total FAP . . . 74
5.3.5 Multiple matches . . . 74
5.3.6 Final table . . . 78
5.3.7 Influence of the hardness of the X-ray sources . . . 81
5.4 Near-infrared photometry discussion . . . 81
5.4.1 NIR colours of Hα emission line objects . . . 81
5.4.2 Towards the identification of key GBS source classes . . . 83
5.5 VVV Variability . . . 84
5.6 Mosaic optical data . . . 88

5.7 Optical Variability . . . 94
5.8 Summary . . . 96

Chapter 6 White dwarfs in the *Kepler* field **99**
6.1 Searching for white dwarfs in the *Kepler* field . . . 99
6.2 Spectroscopy . . . 99
6.3 Ground-based confirmation of pulsators . . . 107
6.4 *Kepler* data of four ZZ Ceti stars . . . 108
6.4.1 KIC 11911480 . . . 108
6.4.1.1 Significance threshold . . . 113
6.4.1.2 Pulsation modes of KIC 11911480 . . . 113
6.4.1.3 Rotation rate of KIC 11911480 . . . 116
6.4.2 KIC 10132702 . . . 118
6.4.2.1 Pulsation modes of KIC 10132702 . . . 118
6.4.2.2 Rotation rate of KIC 10132702 . . . 118
6.4.3 KIC 04357037 . . . 120
6.4.3.1 Pulsation modes of KIC 04357037 . . . 121
6.4.3.2 Rotation rate of KIC 04357037 . . . 121
6.4.4 KIC 07594781 . . . 123
6.4.4.1 Pulsation modes of KIC 07594781 . . . 123
6.4.4.2 Rotation rate of KIC 07594781 . . . 124
6.4.5 Summary . . . 125
6.5 Asteroseismic model of KIC 11911480 . . . 126
6.5.1 Method . . . 127
6.5.2 Optimal model . . . 128
6.5.3 Stellar rotation . . . 128
6.5.4 Nonadiabatic approach . . . 132
6.5.5 Asteroseismic properties of KIC 11911480 . . . 133

Chapter 7 Conclusion and future work **135**

Abbreviations **139**

List of Tables

2.1 *Stellar evolution end-states as a function of initial masse (Tauris & van den Heuvel, 2006)* . . . 11
2.2 *White dwarf spectral types (Koester, 2013).* . . . 13
2.3 *Observational properties of LMXBs (Tauris & van den Heuvel, 2006)* 29

4.1 *Exposure times and 5σ limiting magnitudes in all three NIR surveys used in this paper. The GPS integration times are longer than those applied in VVV, allowing for deeper observations of the Bulge than VVV. The magnitude limits given here are for fields that are moderately crowded similar to the GBS areas.* . . . 45
4.2 *Filter parameters of INT observations (González-Solares et al., 2008; Groot et al., 2009)* . . . 48
4.3 *Morphological flags* . . . 50
4.4 *$\Delta\{filter\}$ is the median offset between the KIC and KIS magnitudes (see Section 4.3.3.4). The standard deviations of the distributions in each filter are also given here ($\sigma_{\{filter\}}$). The distributions are shown in Figure 4.8.* . . . 54
4.5 *Description of columns in KIS catalogue* . . . 61
4.6 *Example of light version of the KIS catalogue* . . . 62

5.1 *Percentage of total number of GBS X-ray sources with possible counterparts found within a 5 arcseconds (upper section) radius and 2.8 arcseconds (lower section) of the X-ray positions, in 2MASS, UKIDSS GPS (DR8) and VVV* . . . 65
5.2 *Positions of the 4 closest matches of CX0013 found within R_{95} in VVV. The red cross indicates the X-ray position and the large dashed green circle indicates the R_{95} boundary of 2.84 arcseconds in this case. The table below provides information on their magnitudes and false alarm probabilities.* . . . 78
5.3 *Four closest VVV matches to CX0013.* . . . 78
5.4 *Table containing all NIR data and FAP of matches within R_{95}* . . . 80

6.1 *Summary of photometric data of our WD candidates selected for spectroscopic follow-up.* . . . 102

6.2 *Summary of spectroscopic observations and results from model atmosphere fits to the spectra.* 106
6.3 *Summary of ground-based time-series data of six ZZ Ceti stars confirmed from our survey. The dominant periods and frequencies found in the amplitude power spectra of each source are given here.* 108
6.4 *Pulsation frequencies of KIC 11911480 from the Q12 and Q16 data. The uncertainties are given in parentheses.* Δf *corresponds to the frequency spacing between two consecutive frequencies in the table* . . 112
6.5 *Pulsation frequencies of KIC 10132702 from the Q15 data.* Δf *corresponds to the frequency spacing between two consecutive frequencies in the table* 119
6.6 *Pulsation frequencies of KIC 04357037 from one month of Q16 observations.* Δf *corresponds to the frequency spacing between two consecutive frequencies in the table* 122
6.7 *Pulsation frequencies of KIC 07594781 from one month of Q16 observations.* Δf *corresponds to the frequency spacing between two consecutive frequencies in the table* 123
6.8 *Identified modes and their periods of optimal model of KIC 11911480.* 129
6.9 *Pulsation frequencies of KIC 11911480 from the combined Q12 and Q16 data (see Table 6.4). The uncertainties are given in between brackets.* Δf *corresponds to the frequency spacing between two consecutive frequencies in the table.* 131
6.10 *Non adiabatic properties of the optimal model of KIC 11911480.* . . 133

List of Figures

2.1 *The Hertzsprung-Russell diagram, showing the locii of the main-sequence where most stars actually lie, as well as other phases. The positions of some specific stars are also included in this sketch.* 6
2.2 *The H-R diagram with evolutionary tracks of stars with different main-sequence masses.* 8
2.3 *Sketch of the stellar composition during different stages of its stellar evolution.* 9
2.4 *SDSS DA, DB, DAO and DZ spectra of white dwarf stars (top to bottom). The legend for the lines is the following: cyan ≡ H, pink dashed ≡ HeI, blue dotted ≡ HeII, yellow ≡ CaII.* 14
2.5 *Surface gravity and mass distribution of DA WD stars with $T_{\rm eff}$ >13 000 K from the Palomar Green survey (Liebert et al., 2005). The mean values and standard deviations of both distributions are given at the top of each panel.* 15
2.6 *A pulsation H-R diagram showing different classes of pulsating stars, taken from Aerts et al. (2010).* 16
2.7 *Chemical composition of ZZ Ceti model (taken from Fontaine & Brassard 2008). The x-axis corresponds to the logarithm of the fractional mass depth, a scale chosen to emphasize the outer layers of the star, where most of the 'action' takes place.* 18
2.8 *Profiles of the Lamb (dotted) and Brunt-Väisälä (solid) frequencies in a typical ZZ Ceti model (taken from Fontaine & Brassard 2008).* 20
2.9 *Typical ZZ Ceti model with excited mode l=1, k=1 (taken from Fontaine & Brassard 2008). For the explanation of curves, see Section 2.3.4.1.* 22
2.10 *Mass-radius diagram for neutron stars, taken from Lattimer & Prakash 2004. The black and green curves are for different equations of state of neutron stars. Regions excluded by general relativity (GR), causality, and rotation constraints are also indicated.* 24
2.11 *Equipotential lines in a binary system, also indicating the five Lagrangian points of potential equilibrium (Tauris & van den Heuvel, 2006).* 27

3.1 *Illustration of the concept of a CCD where the 'raindrops' are actually the photons.* 31

3.2 *Filter curves and the WFC's quantum efficiency transmission curve (black dashed line) of the five filters (purple: U, blue: g, red: r, green: i, red dotted:* Hα*) used for the Kepler-INT Survey observations (see Chapter 4).* 32
3.3 *Schematic colour-magnitude diagram for a globular cluster produced from selected stars of several galactic globular clusters (Harris, 2003). The different stages of stellar evolution are indicated. This diagram is equivalent to the 'observers' H-R diagram.* 33
3.4 *Light curve (top) and amplitude power spectrum (bottom) of a pulsating WD in the Kepler field.* 35
3.5 *Typical (raw) 2D spectrum of a source observed with ISIS on the WHT. The x axis corresponds to the spectral direction whereas the y-axis is the spatial direction. The latter is always aligned with the slit. The black horizontal lines indicate the spectra of observed stars whereas the dark vertical lines correspond to sky lines.* 36

4.1 *The GBS coverage in galactic coordinates. The grey scale image depicts the total absorption E(B-V), estimated from the extinction maps from the VVV (Gonzalez et al., 2011). The overplotted white circles indicate the positions of the 1658 Xray sources detected in the GBS. The size of the white circles is proportional to the number of Chandra counts detected for the given source. (see Section 5.2 for more details).* 40
4.2 *Planned final UKIDSS coverage (Lawrence et al., 2007). The colour-code is the following: dark grey for the Galactic Plane Survey, light grey for the Galactic Clusters Survey, cross-hatched for the Large Area Survey and white for the Deep Extragalactic Survey. The dashed curve corresponds to the Galactic Plane.* 42
4.3 *VISTA surveys coverage* 43
4.4 *We plot the magnitude against its uncertainty for different VVV fields. The typical 5σ limits of sources located in the Galactic Bulge are given in Table 4.1. It is clear that the different VVV fields do not have the same depth due to seeing variations from observations taken on different nights. This explains the large spread seen in the limiting magnitude values.* 46
4.5 *r-band seeing in arcseconds of all INT pointings. Fields observed under seeing conditions worse than 2 arcsec were not included in the data release catalogues.* 51
4.6 *INT coverage of Kepler fields. The open circles correspond to the centres of the INT pointings which passed our quality control tests and are part of the released catalogues. The boundaries of the sky footprints of the CCDs on the Kepler satellite are shown in red.* . . 52

4.7 *Difference between u from SDSS (AB system) and U from KIS (Vega system) against $(u - g)$ from SDSS (AB system), showing that the transformations from AB to Vega (and vice versa) are more colour-dependent when looking at non-main-sequence stars. The red points correspond to the medians of $(u - U)$ over 0.1 magnitude bins in $(u - g)$[AB]. The median of $(u - U)$ is 0.825, a value close to the fixed term found in Equations 4.4. The data points with no error bars simply mean that only one data point was used to determine the median.* 53

4.8 *Distribution of Δg, Δr and Δi, for all pointings, where $\Delta\{filter\}$ is the offset between the KIC and KIS magnitudes (see Section 4.3.3.4). Fields with offsets > 0.2 mag from the median are not included in the final catalogues.* 55

4.9 *Colour-colour diagrams of some of the published pulsators, WDs, CVs, ultra-cool dwarfs and AGNs in the Kepler field. The Pickles tracks are taken from Drew et al. (2005) in the lower panel, and from Groot et al. (2009) in the top panel. The magenta tracks in both panels correspond to Koester models of DA WDs with constant surface gravity, log g = 8, taken from Verbeek et al. (2012). The grey scale and black points are stellar objects taken from the KIS catalogue which have photometric errors smaller than 0.02 mag in all five filters, as well as r-band magnitudes between 12 and 20. The grey scale shows the densest region of the colour-colour diagrams using a logarithmic scale.* 57

4.10 *Limiting magnitudes in all five bands. Sources with magnitudes smaller than 12^{th} mag are detected but not shown because they are not considered reliable. The survey depth is $\sim 20^{th}$ mag in all filters. We use a linear scale in order to show the densest regions of the plots.* . 59

4.11 *Distribution of the number of sources as a function of KIS magnitudes. The objects taken into account are those classified as 'stellar' in all five filters independently.* 60

5.1 *Distribution of distances to the closest VVV matches within 5 arcseconds of the X-ray position (solid) and the 95% confidence positional X-ray uncertainty of each GBS source (dashed). It is clear that the positional uncertainity can become very large in some cases making it impossible to choose the correct NIR match from positional coincidence alone.* 65

5.2 *Difference between the VVV and UKIDSS GPS magnitudes against magnitudes in J, H and K_s. The solid horizontal lines correspond to the median of the difference in magnitudes between both surveys.* . . 67

5.3 *Distribution of the fraction of detected sources UKIDSS GPS (N_{GPS}) and VVV (N_{VVV}) as a function of K_s magnitude. Δ_N corresponds to (N_{GPS} - N_{VVV}). From the increase towards 1 in the ratio towards fainter magnitudes, we conclude that the UKIDSS GPS limiting magnitude is fainter than that of VVV (see text for more details). We further conclude that crowding is not a limiting factor over the whole GBS area given that the median seeing of the GPS is 1 arcseconds (Lucas et al., 2008) whereas that of the VVV is 0.8 arcseconds.* . . . 68

5.4 *Distribution of the number of matches found in UKIDSS GPS (left panel) and VVV (right panel) within 5 arcseconds of the X-ray position out of the total number of 1658 GBS X-ray sources. The solid line corresponds to the J-band, the dashed line to the H-band and the dotted line to the K-band. Note that the reason why the total number of sources (y-axis) in GPS is smaller than in VVV is due to the larger coverage in VVV.* 69

5.5 *Postage stamps of CX0377 (Wu et al. 2014, submitted), illustrating the high density of sources within 5 arcseconds of the X-ray position plotted in yellow. The red circles correspond to the VVV sources detected in each band separately. We also plot 3 colour-colour diagrams ($Z-Y$ vs $Y-J$, $Y-J$ vs $J-H$, $J-H$ vs $H-K_s$) with the VVV matches found in each case. We add reddened and un-reddened synthetic tracks of main-sequence stars, in red and grey respectively, as well as a reddening vector (with E(B-V) = 1.53 in this case). The high number of possible matches is due to the very large qualitative uncertainties in the X-ray position. Many sources suffer from blending and they only become clearer in the K_s-band (the seeing gets better at longer wavelengths, but not necessarily the PSF). We also notice the non-detection of some objects in the given filters, despite their clear presence in the images. This is probably due to issues with the crowding and sky subtraction in the pipeline.* 70

5.6 *Left: Density plot of the K_s-band magnitudes of the nearest VVV matches of $\sim$ 40 000 generated sources in the Bulge against their distances to the corresponding sources. The grey scale is a normalized logarithmic scale. The red dots correspond to the nearest VVV matches to the GBS sources. Sources brighter than 8^{th} magnitude are not included in this figure because they are the main focus of the study carried out by Hynes et al. (2012). Right: Same as left hand side but with all matches within 5 arcseconds of the random positions.* 71

5.7 *Cummulative distribution of the FAP of having the real VVV match. The contours indicate false alarm probabilities at 0.01, 0.05, 0.1, 0.15, 0.25, 0.5, 0.75 and 0.9. The grey dots correspond to the nearest VVV counterparts of the GBS sources. The FAP distribution in the region above the black horizontal line is artifically low, due to the lack of detected sources.* 73

5.8 *Total FAP distribution of the GBS sources. Around 90% of the sources have a final FAP < 0.1 and ∼79% have FAP < 0.03. These values are for the case presented in black. The red distribution shows the final FAP for sources where $FAP_{\rm random}$ was calculated using all the matches in VVV within 5 arcseconds of the X-ray positions.* . . . 75
5.9 *Number of VVV matches found in a 95% confidence interval (R_{95}) from each X-ray source. The median value of this distribution is 2, meaning that each GBS source had typically 2 potential NIR matches in its R_{95} positional error radius.* 76
5.10 Comparing FAP of closest and second closest NIR matches to GBS X-ray positions. 76
5.11 *$FAP_{\rm final}$ of four closest matches, within R_{95} of the X-ray position. Panels (a), (b), (c) and (d) correspond to the distributions of $FAP_{\rm final}$ of the closest, the second closest, the third closest and the fourth closest matches to the X-ray position. The total number of sources clearly drops as we move away from the X-ray position.* 77
5.12 *(K_s) vs ($J - K_s$) colour-magnitude diagram of the VVV matches with $FAP_{\rm final} < 0.1$. The size of the circle is proportionate to the value of the $FAP_{\rm final}$ of the source. The larger the circle, the bigger the $FAP_{\rm final}$. The red and green crosses correspond to the hard and soft X-ray sources respectively. The pink squares are Hα emission line sources (AGN, M-stars, RS CVns) and the yellow squares are accreting binaries (Torres et al., 2014), all confirmed via spectroscopy. The black triangle corresponds to CX0093, a CV confirmed by Ratti et al. (2013) and the cyan triangles correspond to the CVs studied in Britt et al. (2013). The black arrow indicates the reddening for an extinction value of E(B - V) = 1.8.* 82
5.13 *Top panels: VVV K_s-band light curve and finder chart of CX1177. This source has a χ^2 = 30.070 and a p-value = 0.002. Bottom panels: VVV K_s-band light curve and finder chart of CX1074. This source has a χ^2 = 60.152 and a p-value = 0. This makes these two objects very interesting for follow-up. The cyan crosses indicate the Chandra X-ray positions, whereas the magenta crosses point at the centre of the NIR counterpart.* 86
5.14 *(a): P-value of all sources with VVV variability data. (b): χ^2 of all sources with VVV variability data. (c): P-value of all sources within the range of 0 to 0.1. (d): χ^2 of all sources with p-value < 0.1.* . . 87
5.15 *Top panels: VVV K_s-band light curve and finder chart of CX0750. This source has a χ^2 = 7.564 and a p-value = 0.671. Despite its high FAP and high p-value, we clearly see from its K_s-band light curve that it is variable. Bottom panel: Optical MOSAIC-II light of CX0750 which also shows its variable nature. The cyan cross indicates the X-ray position, and the magenta cross indicates the NIR variable source considered here.* 89

5.16 *Colour-magnitude diagram of sources with $FAP_{\rm final} < 0.1$. The size of the circle is proportionate to the value of the $FAP_{\rm final}$ of the source. The larger the circle, the bigger the $FAP_{\rm final}$.The pink circles correspond to the selected Hα emission line sources. The black line is the fit to the main locus of stars and the yellow line corresponds to the 5σ limit above the fit. We also show in cyan the colours and magnitudes of the sources presented in Torres et al. (2014).* 91
5.17 *Optical spectra of CX0128 (top) and CX0794 (bottom) taken from Torres et al. (2014).* 92
5.18 *Colour-magnitude diagram of sources with $FAP_{\rm final} < 0.1$. The size of the circle is proportionate to the value of the $FAP_{\rm final}$ of the source. The larger the circle, the bigger the $FAP_{\rm final}$. The pink squares correspond to the selected Hα emission line sources and the yellow squares are the VVV variable sources.* 93
5.19 *Top panel: VVV K_s-band light curve and finder chart of CX0084. This source has a χ^2 = 2.894 and a p-value = 0.984. These values are not within the limits set to select variables yet we clearly see from the optical data that it is a variable source. The cyan and magenta crosses indicate the X-ray and NIR positions respectively. Middle panel: Optical MOSAIC-II light curve of CX0084. Bottom panel: GMOS spectrum of CX0084.* 95
5.20 *Flow chart summary. It is important to note that the optical MOSAIC-II variability data yielding 167 variable sources only covered 75% of the GBS fields.* 98

6.1 *($U-g$, $g-r$) (top) and ($r-$Hα, $r-i$) (bottom) colour-colour diagrams of stellar sources from the Kepler-INT survey (gray scale), and log $g = 8$ DA WD cooling tracks (dashed line). The dotted line indicates the Pickles main sequence tracks taken from Groot et al. (2009). Narrowing our colour selection around the first ZZ Ceti in the field identified by Hermes et al. (2011) leaves ∼ 60 WD candidates (open circles). The filled squares correspond to the ZZ Ceti stars we discovered in the Kepler field. The vertical dashed lines mark the empirical ($T_{\rm eff}$, log g) instability strip (Gianninas et al., 2011) projected into ($U-g, g-r$) space.* 100
6.2 *The WHT/ISIS spectrum of KIC 11911480 (gray) obtained in August 2012 confirming the star to be a DA WD. The best-fit atmosphere parameters are $T_{\rm eff}$ = 12 350 ± 250 K and* $\log g = 7.96 \pm 0.01$, *which places the star within the empirical ZZ Ceti instability strip.* 104

6.3 *($T_{\rm eff}$, $\log g$) diagram of all the WDs we observed with ISIS. The cyan circles correspond to the four ZZ Ceti stars we observed with Kepler. The red circles are the additional two new ZZ Ceti stars we confirmed using ground-based time-series photometry. The blue squares are the ZZ Ceti candidates chosen on the basis of their multiple KIS observations. The black dotted lines correspond to the boundaries of the empirical ZZ Ceti instability strip (Gianninas et al., 2011). The sources with very large error bars are planned to be re-observed in an observing run on the WHT, end of July 2014.* 105
6.4 *RATS-Kepler amplitude power spectra of KISJ1920+5017 (KIC 11911480), KISJ1917+4413 (KIC 08293193), KISJ1917+3927 (KIC 04357037) and KISJ1908+4316 (KIC 07594781). The bottom panel shows the spectral window of the RATS-Kepler data.* 109
6.5 *McDonald observatory amplitude power spectra of KISJ1913+4709 (KIC 10132702) and KISJ1923+3929 (KIC 04362927). The bottom panel shows the spectral window of the McDonald data.* 110
6.6 *Amplitude power spectrum of KIC 11911480 from the Q12 (top) and Q16 (bottom) data. The Xs above certain frequencies indicate the Kepler spurious frequencies and the dashed horizontal line corresponds to the 3σ threshold limit. The values noted above each significant frequency corresponds to period (in seconds) of the given pulsation mode.* 115
6.7 *Kepler amplitude power spectra of KIC 11911480, our first ZZ Ceti discovered in the Kepler field from KIS. The panels on the left correspond to the Q12 data, whereas the ones on the right correspond to the Q16 data. The dashed lines correspond to the 3σ significance threshold in each dataset. The top left hand-side of each panel gives the corresponding period (in seconds). The bottom panels in both columns show the spectral window of each quarter. Splitting of the modes is a direct indication of the star's rotation (note that it is common that not all modes of a multiplet are detected at a particular epoch, see e.g. Table 5 of Kepler et al. 2003).* 117
6.8 *Amplitude power spectrum of KIC 10132702 from Q15. The dashed horizontal line corresponds to the $4\langle \mathrm{A} \rangle$ threshold limit.* 120
6.9 *Amplitude power spectrum of KIC 04357037 from the Q16 data.* . . 121
6.10 *Amplitude power spectrum of KIC 07594781 from the Q16 data.* . . 125
6.11 *Distribution of the rotation rates of isolated WDs. The red histogram corresponds to upper limits of the projected rotational velocities of single non-pulsating WDs taken from Karl et al. (2005), whereas the black dashed histogram shows the rotation rate of ZZ Ceti stars taken from Fontaine & Brassard (2008) as well as our sample.* 126
6.12 *Weight function of the five identified pulsation modes of KIC 11911480 as a function of* $\log q$. 129

6.13 *Logarithm of merit function S^2 in terms of rotation period in hours. the red horizontal dotted lines indicate the 1σ, 2σ and 3σ limits (from bottom to top). The minimum value for* $\log S^2$ *is for P_{rot} = 78.63 $\pm$ 3.6 h.* 130
6.14 *Observed (red) and computed (blue) frequencies of KIC 11911480. The widths represent the 1σ errors on each frequency.* 131
6.15 *Rotation kernels of the five modes as a function of the normalized radius.* 132
6.16 *Internal rotation profile of KIC 11911480 in the form of a contour map of the logarithm of the merit function S^2 as a function of depth and rotation period of the star. The white curve indicates the solution of the rotation period and the dotted white lines are the 1, 2 and 3σ contours. The vertical dotted-dashed line indicates the exact solution for solid-body rotation.* 133

Acknowledgments

There are also celestial bodies and terrestrial bodies; but the glory of the celestial is one, and the glory of the terrestrial is another. There is one glory of the Sun, another glory of the Moon, and another glory of the stars; for one star differs from another star in glory. (I Corinthians 15:40, 41) - It may be unusual to find a Bible verse in a Physics PhD Thesis but I could not help quote this one in my acknowledgments. I feel truly blessed and grateful to have made this far and this is why I begin my Thesis with this very relevant verse. Indeed, all stars are unique and glorious in their own way.

I would like to begin by thanking my supervisors Prof. Boris Gänsicke and Dr. Danny Steeghs for their constant guidance, patience, advice and time ever since I moved to England in 2009. From my MSc up to now, they've shown me immense support, without which I would have never been able to make it this far in life. I still remember the first day that I arrived at The University of Warwick and the excitement I felt to begin my research 'career'. With very basic knowledge in Astronomy & Astrophysics, they patiently taught me how to become the successful researcher I am today. There is no doubt that they are behind all my achievements in the past four years and I can not be more grateful to anyone else.

I am also grateful for the guidance of many of my collabortors, including Peter Jonker, Manuel Torres and Tom Maccarone. Gilles Fontaine and Noemi Giammichele, thank you for your warm welcome in Montreal, for the funny stories you shared with me and for the inspiring science you taught me. You made me love my research more than I already do.

It comes without saying that I could not have made it to England without the support of my parents, Amany and Magdy. They have never stopped believing in me and never doubted any decision I took in life. I am truly blessed with amazing, loving and caring parents and siblings. Miriam, Tony and Michael, thank you for supporting your 'crazy and weird' sister. Even though none of you understand the career choice I made in life, you have always respected me and are constantly proud of me. I would also like to thank Iman, my second mother, for all the love and care you've given me since I moved to Europe. You are the strongest woman I know. Meena, Ramy, Maryam, Marina, Lolly and Rourou you've made me feel like I have a home and family here from day one. Caleb, you are the reason I smile again. Khalo, my guardian angel, I know you're proud of me. To all my friends

and extended family, thank you for all the support good times - Amrita, Cynthia, Leene, Alia, Karen, Veronica and John.

I would also like to thank my examiners, Professor Phil Charles and Dr. Elizabeth Stanway for their useful comments, and the surprisingly enjoyable viva.

Life as a student is fun thanks to the other students that surround you. It is crazy how quickly time flies, yet I still remember my favourite moments with Lieke, Joao, Jonathan, Rachel, Simon, Steven and Stelios in my first year here. You warmly welcomed me to the group and were there to help me with Python, Linux, observing, as well as fun times. Phil, Penelope, Madelon, John and Nicola, you made PS.004 the best office to work in during my PhD. Merci!

Last but not least, to the one person who's had to put up with my stressful and sleepless nights writing this Thesis, I thank God for the day I met you. I would have never been able to survive another day in England if it weren't for you. From sleepless nights because of proposal deadlines, to weeks apart for observing trips and conferences, you've shown me nothing less than support and love. You remind me every day of how proud of are of me and this is what keeps me going. Youssef, marrying you was the best decision I made in my life.

Declarations

This thesis is the sole work of Sandra Magdy Kamel Greiss, all other works and contributions are acknowledged. This work has not been submitted to any other university or for the purpose of any other degree or qualification. The following Sections are based on refereed articles that were submitted during my PhD:

Section 4.3 is based on: Greiss, S., Steeghs, D., Gänsicke, B. T., Martín, E. L., Groot, P. J., Irwin, M. J., González-Solares, E., Greimel, R., Knigge, C., Østensen, R. H., Verbeek, K., Drew, J. E., Drake, J., Jonker, P. G., Ripepi, V., Scaringi, S., Southworth, J., Still, M., Wright, N. J., Farnhill, H., van Haaften, L. M., and Shah, S., *Initial Data Release of the Kepler-INT Survey*, AJ, 144, 24 (2012)

Sections 4.1, 4.2, 5.1 to 5.4 are based on: Greiss, S., Steeghs, D., Jonker, P. G., Torres, M. A. P., Maccarone, T. J., Hynes, R. I., Britt, C. T., Nelemans, G., and Gänsicke, B. T., *Near-infrared counterparts to the Galactic Bulge Survey X-ray source population*, MNRAS, 438, 2839 (2014)

Section 6.4.1 is based on: Greiss, S., Gänsicke, B. T., Hermes, J. J., Steeghs, D., Koester, D., Ramsay, G., Barclay, T., and Townsley, D. M., *KIC 11911480: the second ZZ Ceti in the Kepler field*, MNRAS, 438, 3086 (2014)

Section 6.5 is based on: Giammichele, N., Greiss, S., Fontaine, G., Charpinet, S., Brassard, P., and Gänsicke, B. T., *Asteroseismic model of KIC 11911480*, in prep.

Abstract

Multi-wavelength astronomical surveys have revolutionised the field. They have dramatically changed the way we search for sources, as well as the way we analyse their data. In this thesis, we focus on the search for compact objects using different photometric surveys, from X-rays to near-infrared, including the optical bands. Compact sources are the end points of stellar evolution. They consist of white dwarfs, neutron stars and black holes.

This thesis consists of two key parts. The first concerns the exploitation of three near-infrared surveys of the Galactic Bulge in order to find the counterparts of 1658 X-ray sources detected with NASA's *Chandra* satellite. These sources are the focus of the Galactic Bulge Survey (GBS), which has a main goal to find low-mass X-ray binaries, composed of neutron stars or stellar-mass black holes accreting material from a low-mass companion. We present all viable counterpart candidates and associate a false alarm probability (FAP) to each near-infrared match in order to identify the most likely counterparts. The FAP takes into account a statistical study involving a chance alignment test, as well as considering the positional accuracy of the individual X-ray sources. We find that although the star density in the Bulge is very high, $\sim$90% of our sources have a FAP $< 10\%$, indicating that for most X-ray sources, viable near-infrared counterparts candidates can be identified. In addition to the FAP, we provide positional and photometric information for candidate counterparts to $\sim$95% of the GBS X-ray sources. This information in combination with optical photometry, spectroscopy and variability constraints will be crucial to characterize and classify secure counterparts. We also present the available GBS optical photometry, near-infrared as well as optical variability data, and some initial spectroscopic results.

In the second part, we search for white dwarfs in a region of the sky known as the *Kepler* field. The *Kepler* mission provides superior time series photometry of a 116 deg^2 field. In order to search for white dwarfs, we carried out our own survey, the *Kepler*-INT Survey (KIS), using the U, g, r, i and Hα filters, reaching down to $\sim 20^{th}$ mag. Our second data release catalogue contained $\sim$14.5 million sources and covered $\sim$97% of the field. Using KIS, we selected white dwarf candidates on the basis of their colours, which were then confirmed via optical spectroscopy. We discovered 43 new white dwarfs, including six pulsating hydrogen-atmosphere white dwarfs. Asteroseismology is the only way to probe the interiors of the stars thus finding more pulsators is crucial. We obtained short-cadence *Kepler* observations of four of our pulsating white dwarfs: KIC 11911480, KIC 10132702, KIC 0435037 and KIC 07594781. All four have pulsation periods within the expected range for this type of variable white dwarfs. They also all confirm that white dwarfs are slow rotators, with rotation periods in the order of days. We end this Thesis with the full asteroseismic analysis of KIC 11911480, our first ZZ Ceti in the *Kepler* field.

Chapter 1

Motivation

What are compact stars? How are they formed? Why should we search for them in our Milky Way? What importance do they have on our understanding of our Universe? We can ask ourselves many questions by simply reading the title of this Thesis. The term compact objects is used to refer to white dwarfs, neutron stars and black holes: the end points of stellar evolution. Therefore, it is needless to emphasize their importance since *all* stars will evolve into one of these forms.

There exist many techniques and approaches to search for stellar remnants; yet the most rewarding one consists of exploiting multi-wavelength surveys of the sky. Compact objects have distinct physical properties setting them apart from normal stars, making them more or less easy to find when using the correct techniques and information. In this Thesis, we make use of a number of astronomical surveys to search for these stellar remnants. Multi-wavelength surveys have dramatically increased the number of detected compact sources, which has an implication on theoretical models predicting their existence and space density. The more white dwarfs, neutron stars and black holes we find, the better their statistical analyses. Also, we are more likely to cover a wider range of their different sub-classes when compiling a larger and complete sample.

For many years, Galactic X-ray point sources have been a mystery to most astronomers due to the extreme difficulty in identifying them, the large uncertainty in their positions and the actual origin of the X-rays. In our Milky Way, multi-wavelength studies of X-ray source populations have mainly been carried out in the Galactic Centre (Muno et al., 2004, 2009; DeWitt et al., 2010; Mauerhan et al., 2009) and the Galactic Plane (Grindlay et al., 2005; Servillat et al., 2012; van den Berg et al., 2012; Nebot Gómez-Morán et al., 2013) by exploiting the *Chandra* X-ray Observatory's excellent spatial resolution. The Centre suffers from extremely high extinction and crowding, making multi-wavelength follow-up of the X-ray sources very difficult. In most studies, it was found that a simple astrometric and photometric matching was not enough to find the true counterparts to the X-ray sources and additional photometric and spectroscopic data were required to confidently find the real matches. Moreover, the main focus so far has been on systems bright in the optical and/or NIR, making most confirmed sources giant stars, high-mass X-ray

binaries which contain early-type mass donors and cataclysmic variables. The extinction drops off rapidly away from the Galactic Centre making the follow-up study of X-ray sources considerably less challenging in the rest of the Galactic Plane and Bulge. The Galactic Bulge, also highly populated with X-ray sources due to the fact that it contains about 14% of the mass of the Milky Way (McMillan, 2011), suffers from three times less extinction in E(B-V) than the Centre, making it a more practical region to study the Galactic X-ray population. Besides their detection, the identification of X-ray sources is crucial in these surveys. With this in mind, the Galactic Bulge Survey was designed (GBS, Jonker et al. 2011). An interesting class of X-ray sources are the X-ray binaries, consisting of a normal star and a collapsed stellar remnant, which could be a neutron star or a black hole. A binary star system contains two stars which orbit around their common centre of mass. These pairs of stars produce X-rays if the stars are close enough such that the material is transferred from the normal star (the donor) to the dense collapsed one, known as the accretor or compact object. This process, called accretion, heats the material to very high temperatures and consequently releases photons of very high energies at very short wavelengths (King, 2003; Lewin & van der Klis, 2006). In this process, potential energy is converted into thermal and kinetic energies; producing very hot plasma near the compact object. The X-rays come from the area around the collapsed star: the inner accretion disc.

The reason why such interacting binaries are very important to detect and study is because they provide information on the physics of accretion and on the properties of neutron stars and black holes (King, 2003; Lewin & van der Klis, 2006; Carroll & Ostlie, 2006). In fact, it is only possible to deduce the mass, radius and velocity of each star when they belong to a binary system rather than as single stars in the sky (Hynes, 2010; Ozel et al., 2010). The equation of state for a neutron star is still not known. Several equations of state have been proposed, which can be ruled out or confirmed by measuring the masses and radii of observed neutron stars. Also, all of the known stellar mass black holes are in binary systems (Remillard & McClintock, 2006; Ozel et al., 2010), which motivates us to search for more X-ray binaries, in order to broaden our knowledge about black holes. Moreover, such sources allow us to understand accretion discs better, which are important in many other environments such as protostars or AGN (Active Galactic Nuclei) or star formation. Finally, assessing their properties in a statistical sense should help us better analyse their evolution and characteristics.

The Galactic Bulge Survey (GBS) combines sensitivity for faint X-ray sources, the astrometric accuracy of the *Chandra* X-ray Observatory, with a complementary photometric optical r', i' and Hα survey (Jonker et al., 2011). The main goals of the GBS are to discover accreting compact objects, more specifically low-mass X-ray binaries (LMXBs, which contain a neutron star or a black hole accreting matter from a low-mass companion with $M<2M_{\odot}$) and ultra-compact X-ray binaries (UCXBs, which are LMXBs with orbital periods shorter than one hour). Binary systems are crucial for the determination of masses of compact objects, offering strong constraints on stellar evolution. In terms of our understanding of binary evolution,

the common envelope phase is not yet well understood, therefore finding compact binary sources which have undergone one or two common-envelope phases will help us further understand that crucial evolutionary phase. The common envelope phase usually occurs when the mass transfer is unstable (Tauris & van den Heuvel, 2006). The more massive star fills its Roche-lobe first and starts mass transfer, which will lead to the orbit shrinking while the star continues to expand. The Roche-lobe volume decreases with the orbital shrinkage and the star continues growing, yet the mass transfer accelerates. All this causes both the orbit to shrink and the donor to expand faster, which is a very unstable mass transfer. The name of common envelope comes from the fact that the donor's envelope expands fast and engulfs the companion star. This short-lived phase in binary evolution is usually found in the case where the donor is a giant star, with a large convective envelope, and the accretor is a compact star with a degenerate core.

The more binary systems we find in a well controlled sample, the better our constraints of binary formation and evolution can be. This can be done by comparing robust samples against predictions from population synthesis calculations. Such samples can be constructed by counting the number of sources of a given class in a well controlled volume. This results in a necessary tool in the study of X-ray sources; the need to classify sources. Although the X-rays allow us to pinpoint possible accreting objects, more detailed follow-up through the detection of coincident counterparts at other wavelengths is necessary. Thus multi-wavelength studies of the GBS X-ray sources, as well as spectroscopic follow-up form a key component of the strategy of the GBS collaboration (radio: Maccarone et al. 2012; optical: Hynes et al. 2012; optical variability: Britt et al. 2014, spectroscopic: Ratti et al. 2013; Britt et al. 2013; Torres et al. 2014).

Besides X-ray binaries, single white dwarfs are important to many fields of astronomy, mainly because they are the end points of more than 95% of stars, including our Sun. Studying the galactic population of white dwarfs offers insight into the star formation history of our Galaxy. White dwarfs have electron degenerate cores with very diverse non-degenerate envelopes, making their structures very different to main-sequence stars. They can be found in single or binary systems, and their study is hence central to a global understanding of stellar evolution. Accreting white dwarfs are also believed to be the progenitors of Type Ia supernovae, making them excellent laboratories to probe the nature of dark energy. As white dwarfs cool, they all evolve through instability strips, exhibiting periodic variations about the mean intensity of their light. Four classes of pulsating white dwarfs are known, each mainly depending on the composition of their envelopes: the hot pre-white dwarfs (PG 1159 or DOV stars), warm helium-atmosphere white dwarfs (V777 Her or DBV stars, $T_{\rm eff} \simeq 22\,000 - 29\,000\,{\rm K}$), cool hydrogen-atmosphere white dwarfs (ZZ Ceti or DAV stars, $T_{\rm eff} \simeq 10\,900 - 12\,300\,{\rm K}$), and the recently discovered carbon-atmosphere white dwarfs (DQV, $T_{\rm eff} \simeq 20000\,{\rm K}$, Dufour et al. 2008). Precision asteroseismology of white dwarfs has the tantalising potential to probe the masses and compositions of their electron-degenerate cores, as well as of their non-degenerate envelopes (e.g. Winget & Kepler, 2008; Fontaine & Brassard, 2008), to determine their internal

rotation profiles (Charpinet et al., 2009), to measure weak magnetic fields (Winget et al., 1991), to detect the presence of planetary companions via pulse timing variations (Mullally et al., 2008), and to constrain nuclear reaction rates (Metcalfe et al., 2002). A full understanding of white dwarf structure and evolution will require a large sample of targets, spanning different masses, effective temperatures and compositions.

In Chapter 2 of this thesis, we briefly describe stellar evolution and present the basic properties of compact stars. Chapter 3 outlines the basic methods and tools used to find the objects introduced in Chapter 2. In Chapter 4, we describe the different surveys exploited for those projects. This Thesis essentially presents two different projects, which make use of very similar methods and tools. On the one hand, in Chapter 5, we focus on a small area of the Galactic Bulge, and analyse the near-infrared data of X-ray sources in two specific strips of that region. The main focus of this Chapter is the search for X-ray binary candidates. On the other hand, in Chapter 6, we search for white dwarfs in an area of the sky known as the *Kepler* field. The ultimate goal of both projects is to discover compact objects, which are candidates for spectroscopic follow-up to confirm their identities and obtain their parameters.

Chapter 2

Compact stars

2.1 The Hertzsprung-Russell diagram

One of the most useful and powerful plots in astrophysics is the Hertzsprung-Russell diagram (also known as the H-R diagram). It originated in 1911 when the Danish astronomer, Ejnar Hertzsprung, plotted the absolute magnitude of stars against their colour (indicative of their effective temperatures). Independently, in 1913 the American astronomer Henry Norris Russell used spectral class against absolute magnitude. Their resultant plots showed that the relationship between temperature and luminosity of a star was not random but instead appeared to fall into distinct groups. These are seen in the H-R diagram shown in Figure 2.1[1]. The 'theoretical' H-R diagram is a plot of luminosity against effective temperature of stars. They are not randomly distributed but fall in different areas of the diagram depending on the stage of their lives. Hot luminous stars are found at the upper left hand side of the diagram, whereas cool dim stars are in the lower right side. Note that temperature increases to the left, rather than to the right. The Sun lies almost in the middle of the big diagonal line in the centre of the diagram, the main-sequence. It is the most densely populated region of the figure because it is the stage where stars spend most of their lives.

The H-R diagram is a snapshot of the evolutionary states of many stars. In the following Section, we explain the different stages of stellar evolution seen in the diagram.

2.2 Stellar evolution in a nutshell

2.2.1 Nuclear processes

The nuclear fusion processes which go on in the cores of stars are different when comparing low ($M < 10\ M_{\odot}$) and high-mass ($M > 10\ M_{\odot}$) stars. They determine the evolutionary timescale of a star. In fact, in the core of a star with comparable or lower mass than the Sun, hydrogen is converted to helium by the proton-proton

[1]The diagram was taken from
http://www.atnf.csiro.au/outreach/education/senior/astrophysics/stellarevolution_hrintro.html

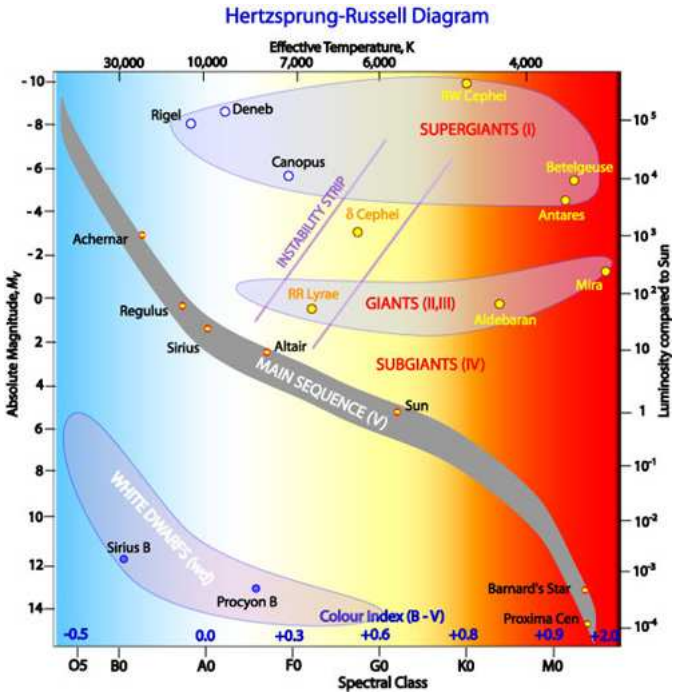

Figure 2.1: *The Hertzsprung-Russell diagram, showing the locii of the main-sequence where most stars actually lie, as well as other phases. The positions of some specific stars are also inlcuded in this sketch.*

chain (Prialnik, 2000), which consists of two protons fusing to form heavy hydrogen, to which a third hydrogen is added to make ^{3}He. The ^{3}He then fuses to form ^{4}He. Low-mass stars are not well-mixed, meaning that the produced helium in the core remains confined to that inner region and material in the outer layers - the envelope - retains its original chemical composition. This is mainly due to the fact that low-mass stars have radiative cores, surrounded by convective envelopes.

However, in a star more massive than the Sun, the proton-proton chain can still occur but the conversion of hydrogen to helium predominantly takes place by means of the CNO (Carbon-Nitrogen-Oxygen) cycle (Prialnik, 2000). These *metals* are already found in the cores of all types of stars - excluding the first generation of stars - however the core temperature of low-mass stars is not high enough to initiate the CNO cycle at a high rate. The CNO cycle is much more temperature dependent than the proton-proton chain(T^{17} vs T^4). Photons are unable to carry this huge amount of energy from small volumes, thus the gas in the core begins to rise in irregular clumps and carries the heat outward by convection. These currents do not extend close enough to the star's surface to allow hydrogen-rich gas from the outer layers to mix into the core and replenish the core's depleted fuel. Only very low-mass stars, with masses less than 0.3 $M_\odot$ are fully convective.

A star's MS lifetime depends on its mass and luminosity. Its mass determines

how much fuel it has and its luminosity determines how rapidly the fuel is burned. Therefore, in order to calculate a star's MS lifetime, we simply need to divide the amount of fuel by the rate at which it is consumed. The nuclear timescale of a star, which can also be considered as its MS lifetime, is the nuclear energy of the star divided by its luminosity. The latter is the rate at which the star loses energy. The luminosity L of a star is roughly proportionate to M^3, meaning that higher mass stars are much more luminous than lower mass stars, due to the much stronger dependence on temperature in the CNO cycle compared to the proton-proton cycle, leading to faster nuclear reaction rates. The nuclear energy of a star is proportional to Mc^2, therefore the MS lifetime of a star is $\tau_{MS} \propto M^{-2}$ (Prialnik, 2000).

2.2.2 Shell-hydrogen burning and red-giant phase

When a low-mass MS star has consumed a fraction of the hydrogen ($\sim$10% in solar-mass) in its core, the mean molecular mass and core temperature increase. As its temperature rises, hydrogen begins burning outside the core in what is called the shell source (Prialnik, 2000), a narrow shell of hot material located between the already-burnt helium core and the yet-to-be-burnt hydrogen envelope (Ryan & Norton, 2010). Core contraction is followed by the expansion of the envelope. Heat from the shell source and the core raises the pressure around the core. That stronger pressure pushes the surrounding gas outward, making its radius expand. The star maintains its luminosity during this expansion and hence moves horizontally across the H-R diagram, towards larger radii (Ryan & Norton, 2010). This short period, known as the subgiant phase, leads to a gap in the H-R diagram since not many stars are seen in this stage of evolution (see Figure 2.2[2]). The factor by which the star grows depends on its mass.

However, this expansion cools the outer layers, thus the star becomes what is called a red giant (Prialnik, 2000). Its name comes from the fact that it cools and therefore radiates more strongly at long (red) wavelengths and its radius can grow up to several hundred times larger. During the red-giant phase, the core mass steadily increases as the shell source continues to burn hydrogen into helium. This leads to an increase of the luminosity of the star. Since the envelope of a giant is fully convective, the energy can escape far more easily than during the MS phase. This increase in luminosity moves the star almost vertically onto the red-giant branch (RGB) on the H-R diagram (Ryan & Norton, 2010).

The evolutionary path the star takes as it moves along the RGB depends on the mass of the star. Some of the energy continues to come from burning hydrogen but many stars switch to a new energy supply: helium burning. The core temperature becomes high enough for helium to ignite (Prialnik, 2000). This nuclear reaction combines three ^{4}He into a ^{12}C. Helium nuclei are sometimes called 'alpha particles' by nuclear physicists, which explains why this process is sometimes referred to as 'the triple alpha process', or simply 'helium burning' (Prialnik, 2000).

[2]This diagram is taken from:
http://www.atnf.csiro.au/outreach/education/senior/astrophysics/stellarevolution_postmain.html

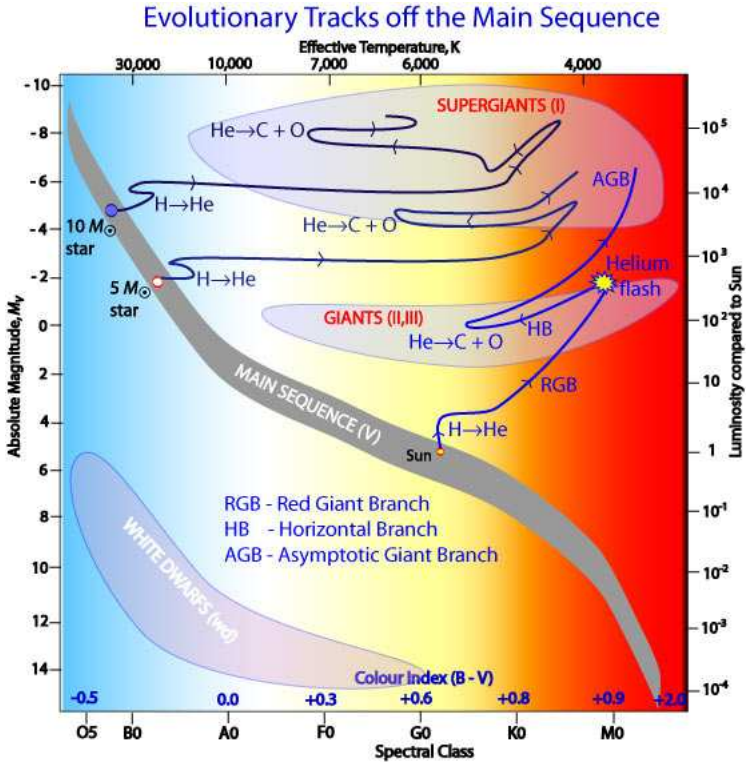

Figure 2.2: *The H-R diagram with evolutionary tracks of stars with different main-sequence masses.*

A low-mass star such as the Sun, however, must compress its core enormously to make it hot enough for helium to begin burning. The compression of such a star packs its gas atoms so closely that they no longer behave like an ordinary gas. Such a gas is called a degenerate gas.

In a degenerate gas, the matter is so densely packed that the electrons act according to the laws of quantum physics. No more than two electrons of the same energy can be found in the same volume, meaning they cannot occupy the same energy level, which is the Pauli exclusion law. In a normal gas, the energy released from nuclear fusion heats the gas and increases its pressure, which leads to its expansion. When the gas expands, it then cools down and reduces the rate of nuclear burning and less energy is therefore released. In normal stars, this mechanism keeps them from collapsing or exploding. In the case of a normal gas, it satisfies the ideal gas law. However, in the case of a degenerate gas, the pressure is written as (Prialnik, 2000):

$$P = \frac{h^2}{20 m_e m_p^{5/3}} \left(\frac{3}{\pi}\right)^{2/3} \left(\frac{\rho}{\mu_e}\right)^{5/3} \tag{2.1}$$

where ρ is the density and $\mu_e = \frac{N_e}{N_p}$ is the ratio of electron number to proton number. This formula is only valid in non-relativistic cases. When particle energies reach

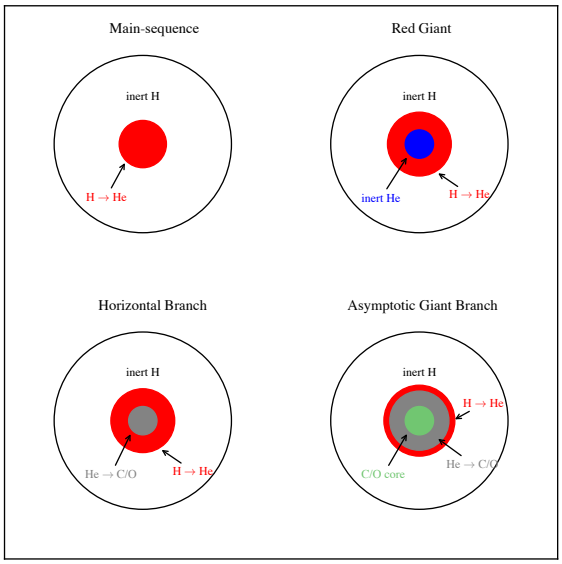

Figure 2.3: *Sketch of the stellar composition during different stages of its stellar evolution.*

relativistic levels, the degeneracy pressure is proportional to $\left(\frac{\rho}{\mu_e}\right)^{4/3}$. In this case, the pressure only depends on the density of the gas and **not** on the temperature.

When nuclear burning begins in a low-mass star with a degenerate core, the energy released does not raise the pressure because it does not depend on the temperature anymore but only on the density of the star (Equation 2.1). Nuclear burning in degenerate material is thermally unstable (Prialnik, 2000). The gas gets hotter and in only a few minutes it releases several thousand times more energy than in non-degenerate material, which leads to what is termed a *helium flash*. This happens when the mass of the core reaches 0.5 $M_\odot$ (Prialnik, 2000). The energy released heats the core enough for it to become a normal gas once again. With its degeneracy removed, the gas can now expand and adjust the star's outer layers by shrinking, compressing and heating them. High-mass stars do not have a helium flash, but instead have a steady helium burning phase (Prialnik, 2000).

2.2.3 Death of stars like the Sun

A star like the Sun will spend about 10 billion years on the MS, before becoming a red giant. However, it will spend less than 1% of that time, about 100 million years, consuming its helium. The evolution is faster, because helium releases less energy per unit mass than hydrogen-burning.

The helium flash marks the end of the RGB evolution of stars with $M < 2.5$ $M_\odot$ (Ryan & Norton, 2010). In this case, the low-mass star burns the helium in its core and becomes a red-giant clump star if its metallicity is similar to that of the Sun, or a horizontal branch star if it is metal-poor. Stars with $M > 2.5$ $M_\odot$ do not undergo helium flashes, but instead experience the expansion of their cores and

hydrogen-burning shells once helium burning begins.

Similarly to the formation of the hydrogen shell around the helium core at the beginning of the RGB phase, a helium-burning shell develops around the new carbon core. At the same time, the hydrogen-burning shell moves outwards towards the surface of the star, leading to its expansion and cooling. At this point, the star moves onto the asymptotic giant branch (AGB), a second red-giant phase. For low-mass stars, the temperature of the core does not reach the limit to burn carbon, but the compression does make it hot enough to increase significantly the rate at which the helium burns. The quicker the fuel is consumed, the more luminous the star gets and its expansion reaches a larger radius than before, making it a supergiant.

The gas shell then expands and becomes transparent, allowing us to see through to the star's hot core. Because it is so hot, the core's radiation is rich in ultraviolet light, which heats and ionizes the shell around it. Such bright objects are called planetary nebulae. The shell contains about 0.25 $M_\odot$ of glowing gas but may have as much as several solar masses of cooler, non-luminous gas around it. The shell eventually grows so big that the gas ends up in the interstellar medium. However, the core of the star remains behind as a tiny, glowing star, called a *white dwarf*. We discuss these compact stellar remnants in more detail in Section 2.3. A very different ending awaits a more massive star. Also, it is important to note that a star's rotation and its presence in a binary system can strongly affect its evolution (Ryan & Norton, 2010).

2.2.4 Death of massive stars

Massive stars do not become planetary nebulae or white dwarfs because their great mass compresses and heats up their cores enough to ignite carbon and allows them to keep burning when their helium is gone. Oxygen, neon, magnesium, and eventually silicon are formed. Silicon burning forms an iron core, which signals the end point of a massive star. The core becomes electron degenerate, similarly to white dwarfs, but once it reaches 1.4 $M_\odot$ and continues to increase in mass, electron pressure can no longer withstand gravity. The star's core pressure drops and its interior begins to collapse. The core shrinks enough to press the iron nuclei so tightly that protons and electrons merge to form neutrons. Therefore, such stars end up with neutron cores, which leads to catastrophic results because most of the pressure which supported the core is now replaced with neutron degenerate pressure (Prialnik, 2000). In less than a second, the core is transformed from an iron ball the size of the Earth to a ball of neutrons about 10 kilometers in radius. The outer layers of the star continue to crush the core and heat the infalling gas to billions of degrees. The pressure rises and lifts the outer layers away from the star in a recoil of the infalling material: a supernova.

A supernova explosion marks the death of a massive star. Gas ejected by the supernova explosion travels through the interstellar medium, mixing with other gas it encounters. The cloud of stellar debris, known as a supernova remnant, continues to expand. Eventually, the supernova remnant slows down and cools. However, the

Table 2.1: *Stellar evolution end-states as a function of initial masse (Tauris & van den Heuvel, 2006)*

Initial mass	He-core	Single star	Binary star
< 2.3 $M_\odot$	< 0.45 $M_\odot$	CO white dwarf	He white dwarf
2.3 - 6 $M_\odot$	0.5 - 1.9 $M_\odot$	CO white dwarf	CO white dwarf
6 - 8 $M_\odot$	1.9 - 2.1 $M_\odot$	O-Ne white dwarf or C-deflagration SN?	O-Ne white dwarf
8 - 12 $M_\odot$	2.1 - 2.8 $M_\odot$	neutron star	O-Ne white dwarf
12 - 25 $M_\odot$	2.8 - 8 $M_\odot$	neutron star	neutron star
> 25 $M_\odot$	> 8 $M_\odot$	black hole	black hole

remnant's gas is rich in heavy elements, therefore when the remnant mixes with an interstellar cloud, the latter is also enriched in heavy elements (Prialnik, 2000). Such a cloud can collapse and form a new generation of stars, which will contain more heavy elements than the previous generation. Such a supernova is known as supernova Type II, Ib or Ic. It leaves behind either a neutron star or a stellar mass black hole. It shows hydrogen in its visible spectrum and is associated with young stellar populations.

2.3 White Dwarfs

White dwarfs (WDs) are the end products of at least 95% of the stars in our Universe, including our Sun (Koester, 2013). They have masses ranging between $0.2M_\odot$ and $1.2M_\odot$ but with diameters of the order of 0.01 $R_\odot$, making them very dense, with interior densities of the order of 10^6 g.cm^{-3} (Koester, 2013), a million times more dense than the Sun. Due to their small surface area, WDs are dim stars - with the exception of hot, young WDs, which have a surface temperature ranging between ∼150 000 K and ∼4 000 K (Fontaine et al., 2001).

Since WDs are formed from low to intermediate-mass stars (0.07 $M_\odot$ $<$ $M < 8$ $M_\odot$), their cores are mainly composed of oxygen and carbon formed from hydrogen and helium burning. It is worth noting that the Universe is still too young to have formed WDs from stars with $M < 0.8$ $M_\odot$ but these stars will eventually become WDs. The exact proportions of carbon and oxygen are unknown because of uncertainties in the nuclear rates of helium burning (Fontaine et al., 2001). WDs are stratified objects, with typical masses ~ 0.6 $M_\odot$, consisting of a carbon-oxygen core containing more than 99% of their total mass, surrounded by a thin helium-rich envelope itself surrounded by a hydrogen-rich layer (Fontaine et al., 2001).

WDs are in hydrostatic equilibrium, just like normal stars, however it is important to note that their pressure is provided by degeneracy. In fact, they no longer undergo nuclear burning in their cores but are sustained by electron degeneracy (see Section 2.2.3). This has an important consequence on WD cooling: as the pressure

and temperature are decoupled, its pressure is unchanged and so is its radius. Also, as WDs cool, their luminosities decrease as $L \propto M \times t^{-7/5}$ (Mestel, 1952), where L and M are in solar units, and t in Gyrs. This relation leads to a crucial advantage in WD studies: the age of a WD can be deduced from its luminosity, meaning that WDs can be used as cosmic chronometers (Fontaine et al., 2001). A relation between the mass and radius of a WD can be derived (Chandrasekhar, 1939): $\mathrm{R} \propto \mathrm{M}^{-1/3}$. This indicates that more massive WDs have smaller radii.

WDs can therefore be considered as cosmic laboratories with physical conditions that cannot be achieved on Earth. The study of their structure and evolution tests our understanding of the equation of state under these extreme conditions. This also applies for neutron stars, however the physics in this case is far more uncertain.

2.3.1 Spectral types

WDs are mainly classified under two categories, depending on their spectra: they either have hydrogen-rich atmospheres, known as DA WDs, or their atmospheres are hydrogen deficient and are mainly constituted of helium. In Table 2.2, we show the different types of WD spectral types, their characteristics and temperature range. It is important to note that ∼80% of WDs are hydrogen-rich. In Figure 2.4, we show SDSS spectra of DA, DB, DO and DQ WDs. Their different characteristics are clearly visible in this Figure.

2.3.2 Mass distribution

Before analysing the mass distribution it is important to mention the limiting mass of WDs, known as the Chandrasekhar mass (Chandrasekhar, 1931). When the gravitational potential overcomes the electron degeneracy of a WD (when mass is added onto the WD surface for instance), the electrons become relativistic. The core density in such a case becomes very large as the mass increases. As such, there exists a limiting mass of WDs, known as the Chandrasekhar mass (it was discovered by the Indian astrophysicist Subrahmanyan Chandrasekhar, who won the Nobel Prize in 1983 for his theoretical calculations on the limiting mass of WDs). For a typical WD, this limiting mass is about 1.4 $\mathrm{M}_{\odot}$ (Prialnik, 2000). In Table 2.1, we give the different types of WDs that can be formed, depending on the initial mass of the main sequence star.

We mentioned above that the typical WD mass is ∼0.6 $\mathrm{M}_{\odot}$ which can be seen in Figure 2.5. More recent studies also confirm this typical WD mass value, whether in the case of DA or DB WDs (Bergeron et al., 2011; Tremblay et al., 2013).

2.3.3 Why are they useful?

WDs are of interest in a wide range of astrophysical topics. Here we summarise the main benefits of studying WDs:

Table 2.2: *White dwarf spectral types (Koester, 2013).*

Spectral type	Characteristics	Temperature range
DA	Only Balmer lines, no HeI or metals present in the spectra	6 000 - 100 000 K
DB	HeI lines; no H or metals present	10 000 - 30 000 K
DC	Continuous spectrum, no lines deeper than 5% in any part of the electromagnetic spectrum	$< 10\,000$ K
DO	HeII strong; HeI or H present	$> 45\,000$ K
DZ	Metal lines only; no H or He lines	
DQ	Carbon features, either atomic or molecular (more particularly the molecular C_2 Swan bands) in any part of the electromagnetic spectrum	$< 11\,000$ K
hot DQ	Atomic carbon lines are the dominant feature in the electromagnetic spectrum	18 000 - 24 000 K
P (suffix)	Magnetic white dwarfs with detected polarization	
H (suffix)	Magnetic white dwarfs with Zeeman splitting in the spectra	
X (suffix)	Peculiar or unclassifiable spectrum	
E (suffix)	Emission lines are present	
? (suffix)	Uncertain assigned classification; a colon (:) may also be used	
V (suffix)	Symbol to denote variability	

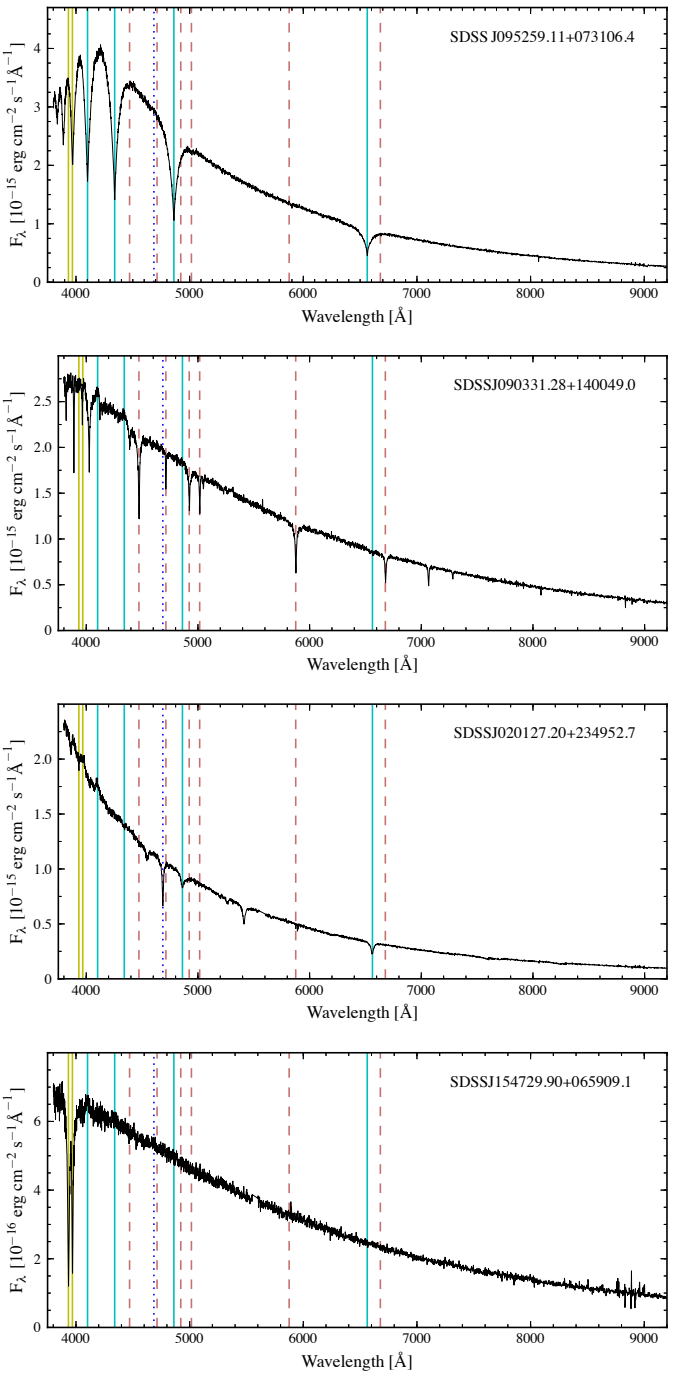

Figure 2.4: *SDSS DA, DB, DAO and DZ spectra of white dwarf stars (top to bottom). The legend for the lines is the following: cyan ≡ H, pink dashed ≡ HeI, blue dotted ≡ HeII, yellow ≡ CaII.*

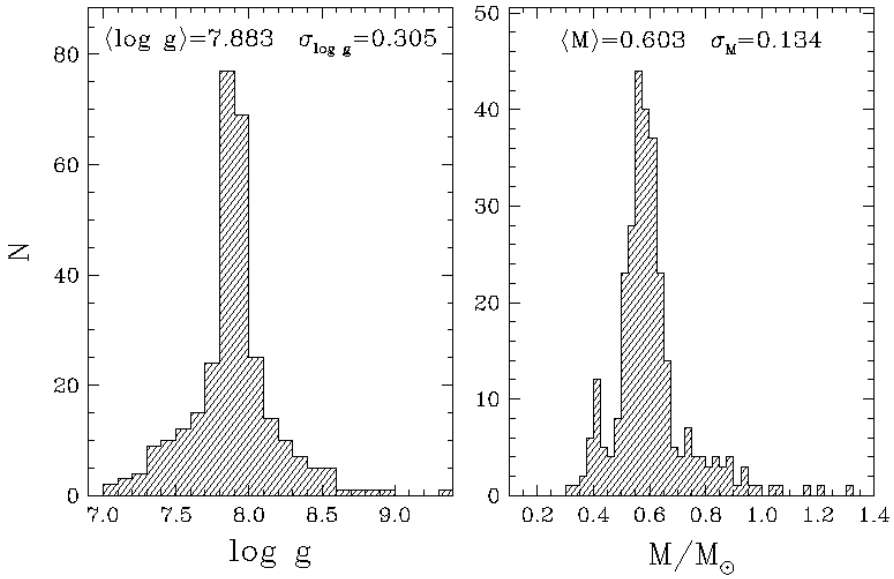

Figure 2.5: *Surface gravity and mass distribution of DA WD stars with $T_{\rm eff}$ >13 000 K from the Palomar Green survey (Liebert et al., 2005). The mean values and standard deviations of both distributions are given at the top of each panel.*

- Since more than 95% of stars will end their lives as WDs, they can be considered as a boundary condition for stellar evolution. The extreme difference between the initial MS masses and the final WD masses highlights the role that mass-loss plays during the AGB phase.
- WDs can be used as laboratories for the study of the physics of matter under extreme conditions, i.e. densities, temperatures, and magnetic fields, due to their electron degenerate cores, since those conditions cannot be attained on Earth.
- WDs are Galactic chronometers, thanks to the straightforward relation between the age of a WD and its luminosity. This allows for a determination of the age and history of the Galactic disk and halo.
- Accreting WDs are believed to be the progenitors of Type Ia supernovae. An understanding of their structure and dynamical properties may improve our understanding of the resultant supernova events. Supernovae Type Ia are most probably due to carbon-oxygen WDs accreting material from a companion such that it then exceeds the Chandrasekhar limit. These supernovae show no hydrogen in their visible spectra and are associated with old stellar populations.

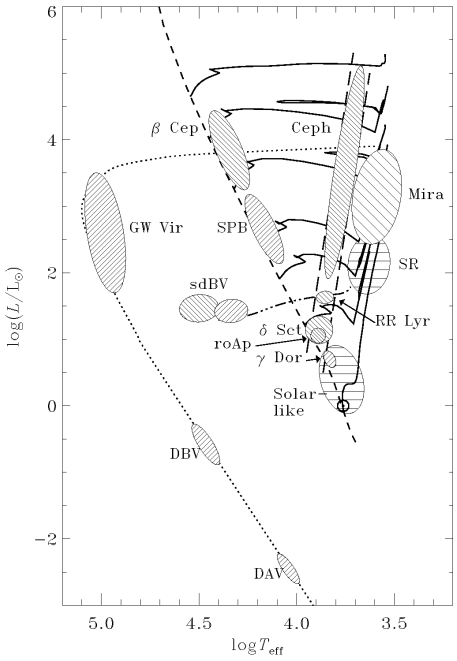

Figure 2.6: *A pulsation H-R diagram showing different classes of pulsating stars, taken from Aerts et al. (2010).*

2.3.4 Pulsating white dwarfs

As WDs cool, they all evolve eventually through instability strips, exhibiting periodic brightness variations about their mean intensity. These multi-periodic pulsations are due to non-radial gravity waves (Winget & Kepler, 2008; Fontaine & Brassard, 2008). There are four classes of pulsating WDs, mainly divided according to spectral type, leading to different envelope compositions and structures. In Figure 2.6, we show different types of pulsating stars, including three of the WD classes. The most numerous class is the variable hydrogen-dominated atmosphere WD, known as the DAV or ZZ Ceti star. The first one, HL Tau, was discovered by Landolt (1968) but this category of pulsating WDs is named after the second DAV discovered, Ross 548 also known as ZZ Ceti (Lasker & Hesser, 1971). The pulsations are explained by the partial ionization (recombination) of hydrogen in the envelope of the cooling DA WD, which is responsible for the excitation of low-degree, low-order g-modes (Fontaine & Brassard, 2008). ZZ Ceti stars occupy a narrow strip in effective temperature-surface gravity space with $11\,000$ K $\lesssim T_{\rm eff} \lesssim 12\,500$ K. At the end of Chapter 6, we provide a detailed description of ZZ Ceti stars. It is worth pointing out that very recently, Hermes et al. (2013) discovered extremely low-mass WDs with helium cores and hydrogen atmospheres that also show g-mode pulsations.

In 1979, pulsations were detected in PG1159-035 by John T. McGraw and collaborators (McGraw, 1979). This star was a pre-WD since it was at a stage of

stellar evolution between the AGB phase and the WD one. This formed a new class of pulsating WDs known as the GW Vir or PG1159 stars, named after its prototype. These objects are hot, with 75 000 K $\lesssim T_{\rm eff} \lesssim$ 200 000 K, and have atmospheres composed of helium, carbon and oxygen in roughly comparable proportions. In fact, these pulsators are born after a violent mixing event is induced by a late helium flash in the post-AGB phase of stellar evolution (for more details on this and the class of PG 1159 stars and related objects, see Werner & Herwig 2006). It is believed that this class of pulsators will eventually cool and become DO WDs. Here, the excitation mechanism is caused by the so-called κ-mechanism associated with ionized carbon and oxygen in their envelopes (Quirion et al., 2007).

In 1981, Don Winget and collaborators predicted the existence of variable helium-dominated atmosphere WDs, where in this case the pulsations are explained by the partial ionization of helium in their atmospheres. In 1982, they found the first DBV (Winget et al., 1982), GD 348 and also known as V777 Her, hence pulsating DB WDs are called DBVs or V777 Her stars. These stars have effective temperatures ranging from ∼22 000 K to ∼29 000 K.

Recently, in 2007, a new class of carbon-dominated atmosphere WDs with luminosity variability was found (Montgomery et al., 2008; Dufour et al., 2007). These are also known as the hot DQV stars. They are all found together in a narrow range of effective temperature centered around 20 000 K (Dufour et al., 2008).

Precision asteroseismology of WDs has the tantalising potential to probe the masses and compositions of their electron-degenerate cores, as well as their non-degenerate envelopes (e.g. Winget & Kepler, 2008; Fontaine & Brassard, 2008), to determine their internal rotation profiles (Charpinet et al., 2009), to measure weak magnetic fields (Winget et al., 1991), to search for planetary companions via pulse timing variations (Mullally et al., 2008), and to constrain nuclear reaction rates (e.g. $^{12}\mathrm{C}(\alpha,\gamma)^{16}\mathrm{O}$, Metcalfe et al. 2002). WD parameters (effective temperature and surface gravity) are traditionally inferred from model fits to spectra which only analyse their thin atmospheres but asteroseismology can probe deeper in the core of the stars. Here we give in more detail the theoretical background on the asteroseismology of ZZ Ceti stars.

2.3.4.1 Theoretical context

Stars are not homogeneous in their composition, making the waves that travel through them subject to specific boundary conditions at the centre and at the surface of the stars. A typical DA WD consists of a C/O core containing over 99% of the mass, a thin He envelope surrounding the core, containing less than 1% of the mass, itself surrounded by a pure H layer that contains less than 0.01% of the total mass of the star. The outer layers of a ZZ Ceti star play a major role in its temporal behaviour, as we will show later that the nonradial pulsations in this case only propagate in the envelope. Pulsation modes are sensitive to the chemical stratification above the core and this produces a highly nonuniform power spectrum of the star. The chemical composition of a typical ZZ Ceti is shown in Figure 2.7. The

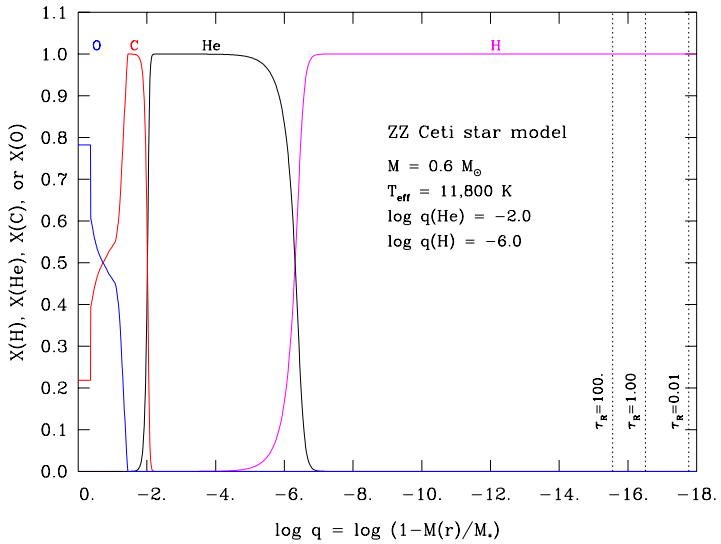

Figure 2.7: *Chemical composition of ZZ Ceti model (taken from Fontaine & Brassard 2008). The x-axis corresponds to the logarithm of the fractional mass depth, a scale chosen to emphasize the outer layers of the star, where most of the 'action' takes place.*

x-axis corresponds to the logarithm of the fractional mass depth, a scale chosen to emphasize the outer layers where most of the 'action' is happening. The atmosphere of a ZZ Ceti star contains less than 10^{-15} of the total mass and it is the only region that is directly observable (Fontaine & Brassard, 2008).

From a theoretical point of view, these waves can be modeled/described by a set of four linear differential equations with real variables: the equation of motion, the equation of continuity and Poisson's equation that relates the gravitational potential with the density distribution of matter. In order to obtain four linear equations one should only consider small perturbations. Also, the *adiabatic approximation* should be considered: there is no energy exchange between the environment and the macroscopic fluid motions during a pulsation cycle. This approximation only takes into account the mechanical behaviour of the oscillations and can be used to compute the required frequencies with enough precision to obtain a reliable asteroseismic model. Due to the boundary conditions mentioned above, only certain solutions (the modes) corresponding to specific values of the oscillation frequency σ are permitted.

A variable star has oscillation modes that have nodes in three orthogonal directions, thus a stellar pulsation mode is defined in terms of three discrete numbers: k, l and m. The index k is known as the *radial order or overtone* and gives the number of nodes in the radial direction ($k \in \mathbb{N}$). The index l is called the *degree* of

the mode and gives the total number of nodal planes that divide the stellar sphere ($l \in \mathbb{N}$). The number m is called the *azimuthal order* and m gives the number of surface nodes that are lines of longitude, meaning the number of nodal planes that divide the stellar sphere perpendicular to the equator while going through the poles. It is possible for m to have values ranging from $-l$ to $+l$, leading to $2l + 1$ modes for each degree l.

The waves that propagate in stars have two distinct but related origins: either they are acoustic waves, or they are related to the action of gravity. Once a region of a star is perturbed from its equilibrium state, the gas oscillates and is restored through different types of forces. The modes of vibration of acoustic waves are known as *pressure* (or p-) modes since the restoring force of the pulsation is gas pressure. The second group of waves have *gravity* (or g-) modes and the restoring force in this case is buoyancy. In both cases, it is important to note that they are non-radial pulsation modes. These waves oscillate at specific frequencies known as the Lamb (for p-modes) and Brunt-Väisälä (for g-modes) frequencies. The latter is defined by,

$$N^2 \equiv g\left(\frac{1}{\Gamma_1}\frac{d\ln P}{dr} - \frac{d\ln \rho}{dr}\right) \tag{2.2}$$

and the Lamb frequency is defined by,

$$L^2 \equiv \frac{l(l+1)c^2}{r^2} \quad with \quad c^2 = \frac{\Gamma_1 P}{\rho} \tag{2.3}$$

where g is the gravitational acceleration, Γ_1 is an adiabatic exponent, P is the pressure and ρ the density of the gas (they are functions of r).

In Figure 2.8, we show the profile of the square of the Brunt-Väisälä and Lamb frequencies in the case of a typical ZZ Ceti model with l=1 pulsation modes. The Lamb frequency profile is plotted with a dotted line and clearly propagates mostly in the core/interior of the ZZ Ceti star. The solid line corresponds to the Brunt-Väisälä frequency, where the well, at -17< $\log q$ <-14, indicates the superficial convection zone caused by the partial ionization of H in the outer layer of the star. The 'bumps' in the Brunt-Väisälä profile correspond to the regions where the chemical composition of the WD changes: the $\log q \simeq$ -6 bump is associated with the H/He compositional transition zone, and the $\log q \simeq$ -3 bump is associated with the He/C transition zone. These compositional features are important as they produce mode trapping and more confinement, which leads to nonuniform period distributions. This concept of mode trapping/confinement must be seen as a result of partial wave reflection in the transition layers, allowing the confined mode to extend above the transition region, and the trapped mode to extend below that.

The ZZ Ceti phase is a natural phase in the evolution of DA WDs during which the hydrogen in the outer layer recombines around $T_{\rm eff} \sim 12\,000$ K, leading to a large increase in the opacity of the envelope, which in turn strangles the flow of radiation and ultimately causes pulsational instabilities against g-modes. This driving mechanism is also known as the κ-mechanism and it occurs in the hydrogen

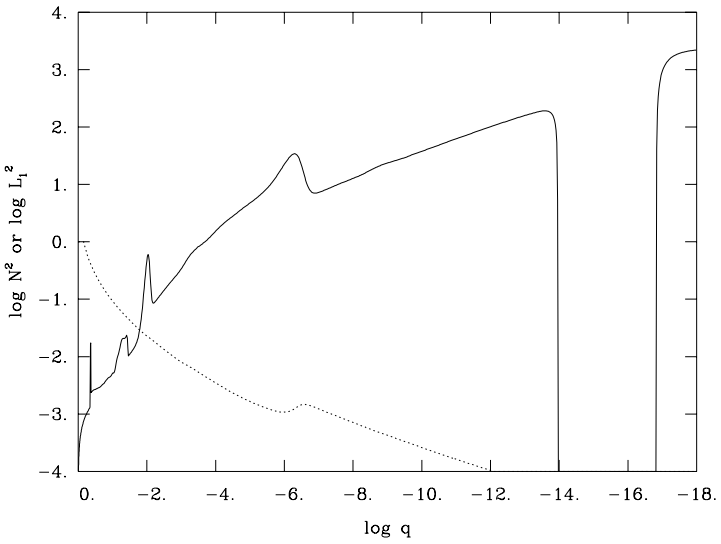

Figure 2.8: *Profiles of the Lamb (dotted) and Brunt-Väisälä (solid) frequencies in a typical ZZ Ceti model (taken from Fontaine & Brassard 2008).*

partial ionization zone.

According to detailed numerical computations taking into account the four linear differential equations, as well as the definitions of the Lamb and Brunt-Väisälä frequencies, we can predict where the nodes of the p and g-modes are in a given stellar model. Their locations indicate where a given pulsation mode can propagate in a star. In fact, it can be shown that p-modes propagate when $\sigma^2 > L^2, N^2$, while g-modes do when $\sigma^2 < L^2, N^2$. It is also important to note that in the case of WDs, low-order p-modes propagate in much deeper layers than low-order g-modes. These propagate in the outer layers of the stars, probing only their thin envelopes. This is not the case for main-sequence stars and it is due to the fact that WDs have degenerate cores and very large surface gravities. In fact, the region of g-mode formation is pushed outwards as the overall degeneracy of a WD model increases. This is not the case for p-modes.

Kinetic energy. The kinetic energy, E_{kin}, of a pulsation mode is defined by

$$E_{kin} \equiv \frac{1}{2} \int_V \rho v^2 dV \quad , \tag{2.4}$$

where V corresponds to the total volume of the star.

The kinetic energies of p-modes are much larger than those of g-modes, mainly due to the fact that the p-modes propagate in the core of WDs, where the densities are much higher than in their envelopes.

Weight function. In the case of a purely spherical model, the square of the frequency can be written as (Lynden-Bell & Ostriker, 1967):

$$\sigma^2 = \frac{D}{A} \quad , \tag{2.5}$$

where D and A are two integral expressions over the stellar model. A is proportionate to the kinetic energy, while D provides a measure of the contribution of each shell in the stellar model. D is often known as the *weight function* of the mode and is very useful for inferring which regions of the star contribute most to the formation of a mode. We will show below the weight functions of the theoretically detected pulsation modes of KIC 11911480.

Rotational splitting. According to many observational results, isolated WDs have been found to be *slow rotators*, meaning that $\Omega \ll \sigma$ where Ω is the rotation frequency of the star. This fact remains an unresolved mystery in the theory of WDs, as it is not yet understood where the angular momentum from the AGB phase of the star has gone. Nevertheless, asteroseismology can provide an accurate estimate of the rotation period of the WD since the main effect of slow rotation destroys the spherical symmetry of the star. Assuming that the angular rotation frequency is a function of depth $\Omega(r)$, the frequency of a mode is given to a first order approximation by,

$$\sigma_{klm} \simeq \sigma_{kl} - m \int_0^R \Omega(r) K_{kl}(r) dr \quad , \tag{2.6}$$

where σ_{kl} is the frequency of the mode in absence of rotation and the second term on the right is the first order correction to that frequency. $K_{kl}(r)$ is the first order rotation kernel, and plays the role of a weight function in the regions contributing to the frequency splitting due to rotation.
If we assume that the star rotates as a solid body as opposed to having a differential rotation, the angular rotation frequency is no longer a function of depth and the previous equation can be simplified to,

$$\sigma_{klm} \simeq \sigma_{kl} - m\Omega(1 - C_{kl}) \tag{2.7}$$

where C_{kl} is a dimensionless quantity known as the first-order solid body rotation coefficient. For a given mode, this leads to a set of equally spaced frequencies with a splitting between adjacent frequency components equal to,

$$\Delta\sigma = \Omega(1 - C_{kl}) \tag{2.8}$$

In the asymptotic limit of high radial order, the values of C_{kl} become very small compared to 1 for p-modes, whereas they converge towards $1/(l(l+1))$ for g-

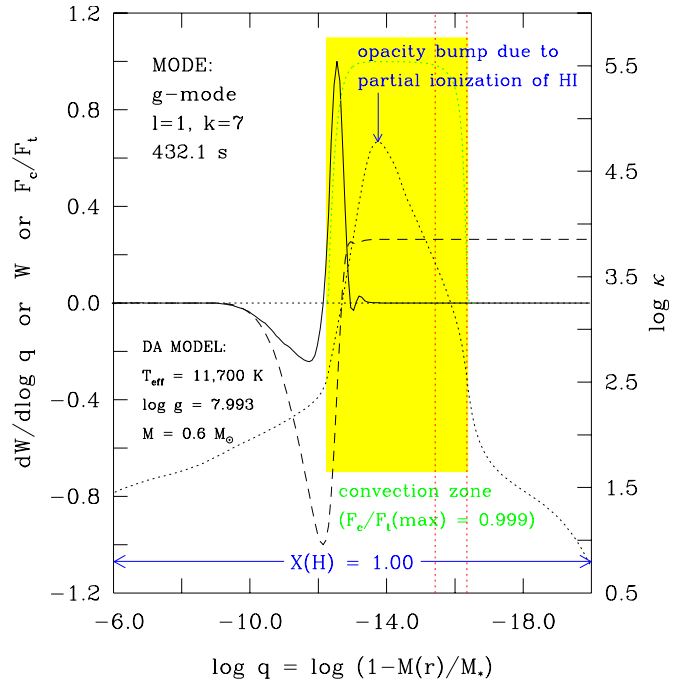

Figure 2.9: *Typical ZZ Ceti model with excited mode l=1, k=1 (taken from Fontaine & Brassard 2008). For the explanation of curves, see Section 2.3.4.1.*

modes. In the case of low radial order in g-modes, the values of C_{kl} from one mode to the other are significantly different, making it an additional way to constrain the radial order of a mode versus another one in the presence of rotational splitting.

The nonadiabatic approach. At the start of this section, we made the assumption that there was no exchange of energy between the environment and the macroscopic fluid motions during a pulsation cycle. However, in reality, this is not the case. If we now consider the full nonadiabatic approach, two more hydrodynamic equations must be taken into account of the nonadiabatic model. This leads to 6 (no longer 4) linear differential equations with 6 dependent *complex* eigenfunctions. This approach must be considered in order to verify if a pulsation mode is excited or not in a stellar model.

In this case, the eigenfrequency σ of a mode is a complex number obeying

$$e^{i\sigma t} \quad = \quad e^{i(\sigma_R + i\sigma_I)t} \quad = \quad e^{i\sigma_R t - \sigma_I t} \tag{2.9}$$

where σ_R is the angular oscillation frequency of the mode and σ_I is directly related to the so-called e-folding time of the mode defined by $\tau_e = -1/\sigma_I$. As mentioned above, the main purpose of considering the nonadiabatic approach is to check if a mode is excited or not. When $\sigma_I > 0$, the mode is stable, damped, not excited and it is not expected to be observable. However, when $\sigma_I < 0$, the mode is unstable,

driven, excited and expected to be observable.

For ZZ Ceti stars, the κ-mechanism is the driving mechanism of their pulsation modes. It involves the modulations of the radiative and convective flux around an opacity bump in the envelope. These WDs have developed extensive superficial convective zones that interact with the pulsations. A time-dependent treatment of convection in a WD context is now available and taken into account in the latest models (Dupret et al., 2008; Quirion et al., 2008; Van Grootel et al., 2012), which is a crucial addition as convection plays a significant role in the pulsation of ZZ Ceti stars. We show a typical model of a pulsating DA WD in Figure 2.9, which illustrates the driving/damping region in the star. The x-axis corresponds to the logarithm of the fractional mass depth as in Figure 2.7. The first vertical dotted red line on the right corresponds to the location of the photosphere and the second vertical dotted red line indicates the base of the atmosphere of the star. The dotted black curve shows the profile of the opacity, with its legend given on the right-hand y-axis. For the particular mode considered in this Figure, the solid curve corresponds to the arbitrarily normalized integrand $dW/d\log q$ of the work integral. This integrand indicates which regions of a stellar model contribute to the driving of a pulsation mode, and which regions contribute to damping. A negative value of this quantity means that the mode is locally damped, whereas a positive value means that it is driven. Finally, the dashed curve corresponds to the running work integral W. A final positive value of W at the surface of the star means that the mode is globally excited and that it is possibly observable. In Chapter 6, we describe the method used to obtain an asteroseismic solution and show an example for a ZZ Ceti star we found.

2.4 Neutron Stars

When the collapsed core of a massive star ($M \gtrsim 11\ M_\odot$) is of a certain high density, the star's protons and electrons merge together into neutrons. So long as there is one proton and one electron for every 200 neutrons, the neutrons are prevented from decaying. In such conditions, a neutron star is formed, as it remains supported by the pressure of degenerate neutrons. This happens when the pressure of the degenerate electrons is no longer sufficient to sustain the gravitational force, which is one reason why most neutron stars are born with masses $\sim 1.4 M_\odot$, corresponding to just above the Chandrasekhar mass for WDs. They have radii of about 10 kilometers, thus they are extremely dense objects. The predicted maximum mass of a neutron star is $\sim 3\ M_\odot$, based on stellar models (Prialnik, 2000). However, it is crucial to mention again that the equation of state of a neutron star remains uncertain until today. As can be seen in Figure 2.10, there exist many possibilities for the equation of state of neutron stars, which can only be constrained by the observational determination of their masses and radii.

Neutron stars are formed from the collapse of massive stars, which generally explode as supernovae. Their core radii are tiny, especially compared to that of

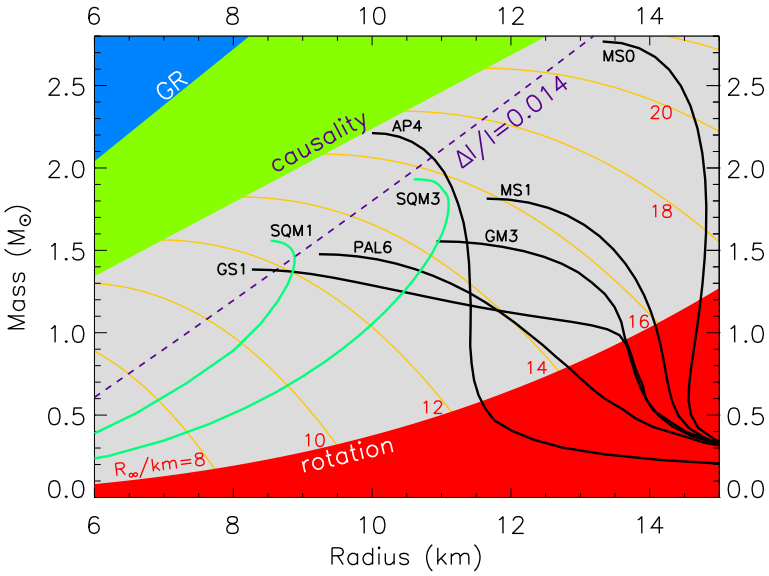

Figure 2.10: *Mass-radius diagram for neutron stars, taken from Lattimer & Prakash 2004. The black and green curves are for different equations of state of neutron stars. Regions excluded by general relativity (GR), causality, and rotation constraints are also indicated.*

their progenitors. By taking into account the conservation of angular momentum, the neutron star must therefore spin faster when it shrinks. Their typical rotation period ranges from about 1.4 ms to 30 seconds (Haensel et al., 2007). It also creates a very strong magnetic field. Such neutrons stars are known as pulsars and have extremely strong magnetic fields. In combination with their rapid rotation, they produce narrow beams of charged particles at their magnetic poles (Carroll & Ostlie, 2006). The emission created by the accelerating charges does not depend on the temperature of the heated gas but rather on the magnetic field and spin period. The pulsar emission extracts kinetic energy, which slows the neutron star down until the point that the pulsar mechanism breaks down. This explains why we have only detected a very small fraction of neutron stars in the Galaxy. For most pulsars, the charges generate low-energy radiation, which is why they were detected at radio wavelengths. This does not preclude the possibility that they can also be detected at much higher energy wavelengths such as visible light and γ-rays.

Stellar models and calculations show that neutron stars have three separate regions: a thin, outer gaseous atmosphere about 1 millimeter thick; a solid crust a few hundred meters thick; and the core of the star composed of neutrons lying below the crust. Even though neutron stars have been found in binary systems and as radio pulsars, they remain difficult and rare to detect as the pulsar mechanism eventually switches off when the neutron star spins down.

2.5 Black holes

When a star with an initial mass larger than $\sim$25 $M_\odot$ collapses, it leaves behind a black hole. In order to understand the properties of black holes, we must remember the concept of escape velocity. This is the speed a mass requires to be free from another object's gravitational attraction. The escape velocity for an object of mass M and radius R is:

$$V = \sqrt{\frac{2GM}{R}} \tag{2.10}$$

where G is the gravitational constant. This equation shows that for a given mass, the smaller radius it is compressed to, the larger its escape velocity.

For a body to be a black hole, the escape velocity is equated to the speed of light, because it is known that no light can escape from a black hole (Prialnik, 2000):

$$V = c = \sqrt{\frac{2GM}{R}} \qquad \text{therefore} \qquad R = \frac{2GM}{c^2} \tag{2.11}$$

This equation determining the radius of a black hole is called the Schwarzschild radius, named after the German astrophysicist who discovered it.

General relativity shows that gravity is related to the curvature of space and a black hole forms where the curvature is very extreme. According to general relativity, mass creates a curvature of space and as the bodies move in straight lines along the curvature, gravitational motion occurs. In the case of a black hole, the reason why light cannot escape from it is its extreme curvature. Astronomers call its boundary the *event horizon*. Its mass is one of the few properties of a black hole that can be determined (Carroll & Ostlie, 2006).

Since black holes do not emit light or any sort of electromagnetic radiation, it is impossible to observe them directly. However, they are detected in binary systems where the initial star which evolved had a mass of at least $\sim$25 $M_\odot$ and exploded as a supernova leaving behind a black hole. The process of accretion draws gas from the companion star to the compact object and forms a ring of gas around the black hole. Since the material in the disc orbits nearly at the speed of light, the friction of the gas heats it to millions of degrees or even higher, making it emit in X-rays and γ-rays. Also, in the case of binaries, it is possible to calculate the masses of the stars in the system (Steeghs et al., 2013), confirming that the primary component of the binary systems are black holes. If the mass of the accretor is larger than 3 to 5 $M_\odot$, it is definitely a black hole since it cannot be a neutron star (Carroll & Ostlie, 2006; Ryan & Norton, 2010).

2.6 Compact binary systems

It is estimated that about half of all stars belong to binary systems, containing two stars orbiting around their common centre of mass, held together as pairs by their mutual gravitational attraction. Such systems are very interesting because they

provide information on stellar mass and evolution. By using Kepler's third law, we can determine the system's mass (Carroll & Ostlie, 2006):

$$P_{orb}^2 = \frac{4\pi^2 a^3}{G(M_1 + M_2)} \tag{2.12}$$

where M_1 and M_2 are the masses of both stars and a is the binary separation.
Many types of compact binary systems that emit X-rays have been found. However, the main ones described here are the cataclysmic variables and the low-mass X-ray binaries. The compact object in those systems accretes matter through Roche-lobe overflow.
The effective gravitational potential in a binary system, also known as the Roche potential, takes into account the gravitational potential of each star and the centrifugal potential of the system since it is rotating (Tauris & van den Heuvel, 2006):

$$\Phi = -\frac{GM_1}{r_1} - \frac{GM_2}{r_2} - \frac{\Omega^2 r_3^2}{2} \tag{2.13}$$

where r_1 and r_2 are the distances from each star to the centre of mass, r_3 is the distance to the rotational axis of the binary and Ω is the orbital angular velocity.

We assume that the stars revolve in circular orbits and it is therefore simple to determine fixed equipotential surfaces to the stars. Such surfaces are calculated by taking $\nabla\Phi = 0$, thus Φ a constant. Five solutions to $\nabla\Phi = 0$ are found making equilibrium points and are called the Lagrangian points. In Figure 2.11, the equipotential lines and Lagrangian points are plotted for two stars with masses $M_1 = 15\ M_\odot$ and $M_2 = 7\ M_\odot$. L_1, Lagrangian point 1, is in between the two stars and matter can flow freely from one star to another through this point. It also defines the 'pear-shaped' Roche-lobe (RL) of the stars, surfaces which have L_1 as a contact point. L_2 and L_3 are on opposite sides of the secondary and primary stars respectively. Finally, L_4 and L_5 are found in lobes perpendicular to the line joining the binary. It is important to note that $L_{1,2,3}$ are unstable points, which means that a small perturbation will lead to material leaving the L-point, whereas $L_{4,5}$ are stable (Tauris & van den Heuvel, 2006).
In this example, the donor is more massive than the accretor, which is not necessarily the usual case. Since L_1 is unstable, if the more massive star evolves to fill its Roche-lobe mass transfer will occur onto the less massive star. This process is called Roche-lobe overflow (RLO). The size of the RL of the accretor is a function of the orbital separation and the mass ratio of the binary components.

2.6.1 Cataclysmic variables

In binary systems, WD progenitors and WDs evolve differently to when they are isolated. A binary system containing a WD accreting material from a MS star, of spectral type G or later, is known as a cataclysmic variable (CV). Due to the conservation of angular momentum of the system, an accretion disc is formed around the

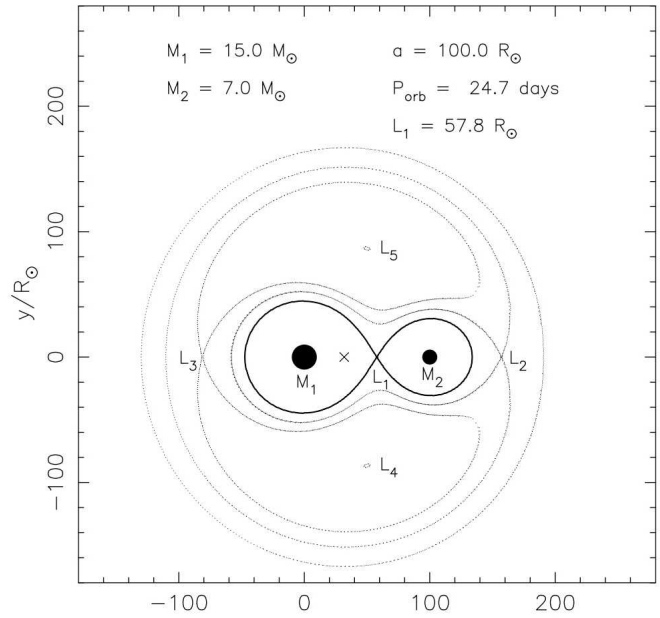

Figure 2.11: *Equipotential lines in a binary system, also indicating the five Lagrangian points of potential equilibrium (Tauris & van den Heuvel, 2006).*

WD. When in an interacting binary system, the WD could lead the system to evolve into a dwarf nova, a classical nova or a supernova. In the case of a dwarf or classical nova, the outburst process recurs, unlike in a supernova where the WD is completely disrupted. In a dwarf nova, the 'outburst' can begin in the outer, cooler part of the disc and then spreads to the hotter, inner regions, or the other way round. In fact, outbursts are caused by a thermal instability in the disc, which is believed to be caused by the hydrogen partial ionisation zone at a temperature of 10 000 K (Carroll & Ostlie, 2006). A WD in a close binary system accreting enough material from the secondary star to surpass the Chandrasekhar limit leads to a Type Ia supernova.

In CVs, the typical mass of the WD is 0.85 $M_\odot$, which is larger than the typical mass of a single WD ($\sim$0.6 $M_\odot$) (Carroll & Ostlie, 2006). Similarly to all binary systems with accretion discs, the light detected comes primarily from the disc around the compact star. CVs are also known to show X-ray emission, which is generated from the accretion disc. They are however weak X-ray emitters, compared to the low-mass X-ray binaries presented in the following Section. In some cases, the WDs have magnetic fields that are strong enough to prevent the formation of an accretion disc, instead the material follows the magnetic lines, falling onto the magnetic poles of the WD. Usually magnetic X-ray emitting CVs are subdivided in Polars or AM Her systems, Intermediate polars (IPs) and DQ Herculis systems, depending on the geometry of the accretion flow (Warner, 1995). Dwarf Novae, i.e. non-magnetic systems, also show low amplitude quasi-coherent X-ray oscillations in

outburst.

CVs have periods ranging from 48 min to 5.7 days (Ritter & Kolb, 2003; Sekiguchi, 1992), even though most of them have periods of less than 8 hours. An interesting observational fact of CVs is that out of the $\sim$ 1166 known systems, few of them have periods between 2.25 and 2.83 hours, known as the 'period gap' (Ritter & Kolb, 1992; Carroll & Ostlie, 2006; Gänsicke, 2005).

2.6.2 Low-mass X-ray binaries

A low-mass X-ray binary (LMXB) is a binary star where one of the components is either a black hole or neutron star accreting matter from a low-mass ($M \leq 2$ $M_{\odot}$) companion through Roche-lobe overflow(Kolb, 2010). A typical low-mass X-ray binary emits almost all of its radiation in X-rays, and typically less than one percent in visible light, so they are among the brightest objects in the X-ray sky, but relatively faint in visible light. The brightest part of the system is the accretion disc around the compact object. This is due to the fact that the accretion efficiency scales with M/R of the accretor. There is an orbital period division of LMXBs which can lead to different types of systems. On the one hand, a binary system can be formed because the orbital period decreases until the donor becomes degenerate and the system becomes an ultracompact binary. On the other hand, when the orbital period increases, so does the binary separation, which leads to a diverging system. In this case, the orbital period increases until the donor has lost its envelope and the binary separation grows enough to obtain a wide detached binary system (Tauris & van den Heuvel, 2006).

Most black hole X-ray binaries are discovered when they first go into outburst and are then monitored daily by satellites and wide-field X-ray cameras (Remillard & McClintock, 2006). X-ray outbursts which last between 20 days and many months are usually explained by an instability which occurs in the accretion disc, similarly to the case of dwarf novae.

Over 187 LMXBs have been detected in our Galaxy, the Large Magenallic Cloud and the Small Magenallic Cloud (Liu et al., 2007). Their orbital periods range from 11 minutes to 17 days. It is very difficult to obtain the spectrum of the companions in these systems because the observed spectrum is usually dominated by the accretion disc during active phases of accretion, and they remain very faint when they are in low accretion states. However, advances in the field and the exploitation of multi-wavelength photometric and spectroscopic data of X-ray transient sources in particular, have enabled the study of both components of the LMXB systems (Charles & Coe, 2006). Such studies remain crucial as they are necessary for the determination of the masses of the binary components. In the case of persistent X-ray sources, methods based on the irradiation of the donor star have enabled us to *see* the donor star for the first time and to derive dynamical information and mass constraints in such systems (Steeghs & Casares, 2002; Casares & Charles, 2006).

In this Chapter, we went through the major phases of stellar evolution and

Table 2.3: *Observational properties of LMXBs (Tauris & van den Heuvel, 2006)*

X-ray spectra	$kT \leq 10$ keV (soft)
Type of time variability	only a very few pulsars, often X-ray bursts
Accretion process	Roche-lobe overflow
Timescale of accretion	10^7-10^9 yr
Accreting compact star	low-magnetic field NS (or BH)
Spatial distribution	Galactic centre and around the plane
Stellar population	old, age $> 10^9$ yr
Companion stars	faint, L_{opt} / $L_x \ll 0.1$, blue optical counterparts

presented the three types of compact objects found at the end of a star's life. We also briefly described some of the relevant (for this work) binary systems they can be found in. In the following Chapter, we present the astronomical tools and methods we used to observe, find and study these compact sources in our Milky Way.

Chapter 3

Astronomical tools and methods

3.1 Charge-coupled devices

Charge-coupled devices (CCDs) are the most essential piece of technology in modern astronomy. They have dramatically increased the precision, as well as the amount of astronomical data available. Their high quantum efficiency (QE), linear response and low noise level make them an astronomer's favourite tool. Their concept is fairly simple. A CCD is a grid of metal-oxide semiconductor (MOS) capacitors, more commonly known as pixels (in fact, one pixel corresponds to three capacitors). The pixels are typically 15 to 25 microns in size. During an exposure, the incoming photons hit a pixel and generate free electrons via the photoelectric effect. This produces a charge in the pixel, which corresponds to a measure of the number of photons which hit it. A typical modern CCD is 90% efficient at this capture. This is called the QE of the device. The free electrons are trapped in each pixel until the exposure is completed. The readout process is achieved by 'shifting' charges across the columns, one at a time, towards the serial register located on the far end of the array. From the serial register, the electrons are moved to the sense node where they are converted into a digital value, giving them analog-to-digital units (ADUs). This 'shifting' process continues until all the columns are read out. The CCD's concept is illustrated in Figure 3.1.

3.2 Photometry

Nowadays, most astronomers use multi-wavelength surveys to understand and classify stellar populations. These surveys provide information on stellar objects, such as their brightness, as well as digital images in different wavebands. Astronomers measure the brightness of a star in magnitudes. This value is derived from the brightness of a star on a logarithmic scale, which is measured in a specific passband by the use of filters.

Stellar flux is the power received per unit area radiated from an object. It is written in W m^{-2}. The flux of a star at its surface depends only on its effective

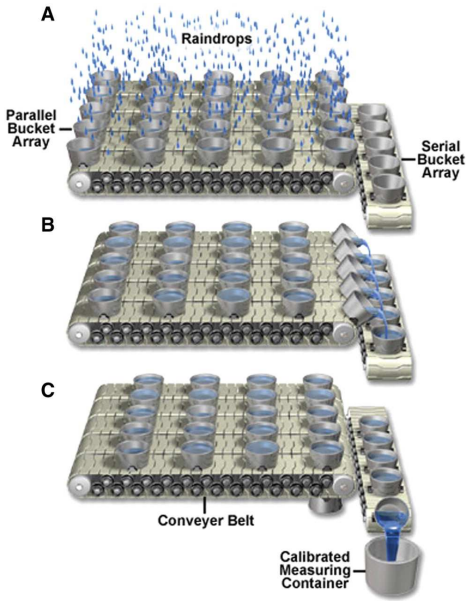

Figure 3.1: *Illustration of the concept of a CCD where the 'raindrops' are actually the photons. Image found on: http://www.microscopyu.com/articles/digitalimaging/ccdintro.html .*

temperature, according to the Stefan-Boltzmann Law:

$$F = \sigma T_{\text{eff}}^4 \tag{3.1}$$

where σ is the Stefan-Boltzmann constant and is equal to 5.67×10^{-8} W m^{-2} K^{-4}.

There are several types of magnitudes. The most widely used is the apparent Vega magnitude, which corresponds to the brightness of a star with respect to its observed flux. Since it is a relative definition, meaning a star's magnitude is always calculated with respect to another known star. A commonly used reference star is Vega, also known as α Lyr. Therefore, $m_{\text{Vega}} \equiv 0$ and the apparent magnitude can therefore be calculated by:

$$m_{\text{star}} = -2.5 \times \log\left(\frac{F_{\text{star}}}{F_{\text{Vega}}}\right) = 2.5 \times (\log F_{\text{Vega}} - \log F_{\text{star}}) \tag{3.2}$$

where F_{Vega} and F_{star} are the respective fluxes of Vega and the star in consideration. This definition of apparent magnitude is known as the Vega system magnitude.

There exists another commonly used apparent magnitude system known as the AB magnitude system, where the reference object is a hypothetical flat spectrum source. In this case, no relative reference object is used and the zero-point is set to 3631 Jansky, where 1 Jansky $= 10^{-23}$ erg s^{-1} Hz^{-1} cm^{-2}:

$$m_{\text{AB}} = -\frac{5}{2}\log 10 f_\nu - 48.6 \tag{3.3}$$

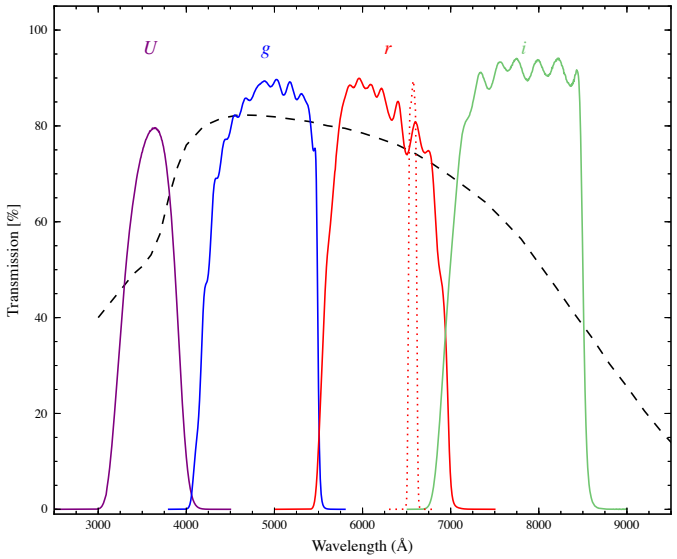

Figure 3.2: *Filter curves and the WFC's quantum efficiency transmission curve (black dashed line) of the five filters (purple: U, blue: g, red: r, green: i, red dotted:* Hα*) used for the Kepler-INT Survey observations (see Chapter 4).*

if f_ν is in erg s^{-1} Hz^{-1} cm^{-2} (not Jansky). Both Vega and AB systems differ in their reference source but practically speaking, their zero points are different. Also, the spectrum of Vega is nearly flat in f_λ, whereas the AB reference object is flat in f_ν. Both systems are defined to match in the optical but diverge elsewhere.

There are two important facts about the magnitude system which should be noted. Firstly, the scale is 'backward' in the sense that the brighter the star, the smaller the magnitude. Secondly, the difference between magnitudes of two stars corresponds to the logarithm of the ratio of their fluxes. Hence, the magnitude scales are logarithmic units and one magnitude difference is equal to a brightness variation of about 2.512 times (the 5th root of 100). This scale was chosen in order to maintain as much consistency as possible with the original system and catalogue of stars produced by Hipparchus himself. All the work and results described in the coming thesis refer to apparent magnitudes in the Vega system.

Astronomers use CCDs, attached to instruments, in order to image the sky. The definitions given above can be generalised to represent the flux in a given filter pass-band. Each filter is designed to transmit only light within a specific wavelength range. As will be seen later in this chapter, astronomical surveys use different filters in order to integrate the total light obtained from stars at different wavelengths. We show in Figure 3.2 filter curves of the ones used for the *Kepler*-INT Survey which is presented in the following Chapter.

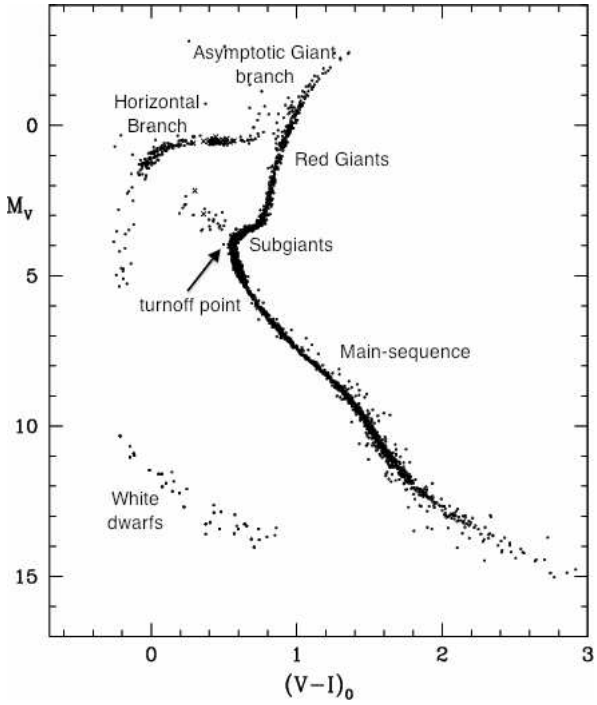

Figure 3.3: *Schematic colour-magnitude diagram for a globular cluster produced from selected stars of several galactic globular clusters (Harris, 2003). The different stages of stellar evolution are indicated. This diagram is equivalent to the 'observers' H-R diagram.*

3.2.1 Colour-colour and colour-magnitude diagrams

The colour of a star in astronomy is the difference in magnitude between any two filters, where the longer wavelength magnitude is generally subtracted from the shorter one. It is however not restricted to visual/optical wavelength ranges. A star's optical colour can provide rough indications on its average effective temperature. When the temperature of the star's surface increases, the star's spectrum peaks at shorter wavelengths. This crucial property of stars can be deduced from data obtained from astronomical surveys, making the colours of stars a *cheap* proxy for their effective temperatures. As seen previously, fluxes are measured in magnitudes. If the star is 'hot', it will emit more light at shorter wavelengths and therefore its magnitudes will be smaller in bluer filters leading to it having negative colours if it is hotter than Vega ($\sim$9 600 K), whereas the 'cooler' sources will have positive colours.

Colour-colour and magnitude-colour diagrams are important tools in modern astronomy as they enable the selection of specific types of stars, given the correct use of colour combinations, which will be demonstrated in Chapters 5 and 6. Here we show an example of a colour-magnitude diagram produced from several galactic globular clusters in Figure 3.3. The different stages of stellar evolution are indicated and can clearly be distinguished.

3.2.2 Time-series photometry

Obtaining many consecutive short exposures of a target can provide what astronomers call the light curve: the magnitude of the star as a function of time. Such data is useful in the case of variable sources, where their light intensity is not constant with time. There are many different types of variable sources, with a wide range of periods. For this reason, the time-series photometry of a given source must be tailored to its variation period: long period variables can be observed with longer cadences whereas short period variables must have short enough cadences to detect the fluctuations in their magnitudes.

A reliable method to confirm a periodic variable source is the use of the Fourier Transform (FT) of its light curve. The FT is a mathematical concept that transforms signals from time domain to frequency domain. It is based on the concept that the light curve can be decomposed into the sum of simple sinusoids with different frequencies. In practice, we use the Discrete Fourier Transform (DFT) of the time series photometric signals, due to the gaps in the data sets. The amplitude of each sine wave is determined by its relative contribution to the observed time-variable signal. A power spectrum, or periodogram, is a plot of these amplitudes against frequency. The periodic signals in the light curve will translate into the form of peaks at their given frequencies. We show in Figure 3.4 an example of a light curve and associated DFT of a pulsating WD star.

It is important to note that the quality or precision of the power spectrum of a light curve depends on the duration of the observation. The longer the data set, the more accurately the period can be determined, due to the higher frequency

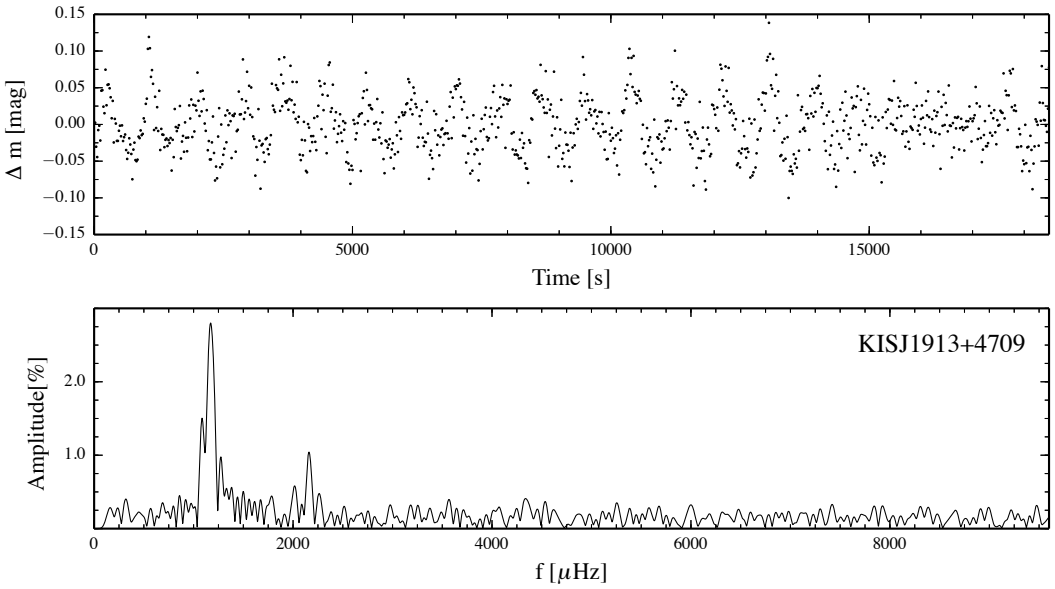

Figure 3.4: *Light curve (top) and amplitude power spectrum (bottom) of a pulsating WD in the Kepler field.*

resolution and stronger peaks. Also, gaps in the observations can affect the quality of the data and introduce what is known as 'aliases', the appearance of several 'fake' peaks either side of the 'real' peak in the periodogram. In order to reduce such alias confusion, the problem of interrupted data has been solved from the ground with the Whole Earth Telescope (WET) project introduced by Nather et al. (1990). Carefully coordinated observations of given targets from both hemispheres lead to their continuous observations for days to weeks. Fortunately, we use space-based observations which suffer much less from gaps in the data set than ground-based data.

In time series photometry, it is worth defining some terms which are required for the data analysis. The sampling rate of an observation is the frequency at which the observations are taken: $\nu = \frac{1}{T}$, where T is the exposure time in seconds. The *Nyquist frequency* is equal to half the sampling rate and corresponds to the highest frequency at which a complete study of the signal can be done. This value defines the largest frequency for which the DFT should be calculated. For instance, if a time series data set has a sequence of consecutive 60 second exposures, the sampling rate of this data set would be $\nu \simeq 0.0167$ Hz and $f_{Nyq} \simeq 0.0083$ Hz.

We use the TSA package within MIDAS written by Schwarzenberg-Czerny (1993), which is very useful for the straightforward calculation of DFTs and the amplitude of the peaks in the generated power spectra. These amplitudes are calculated using least-squares sinusoidal fits to the peaks in the power spectra.

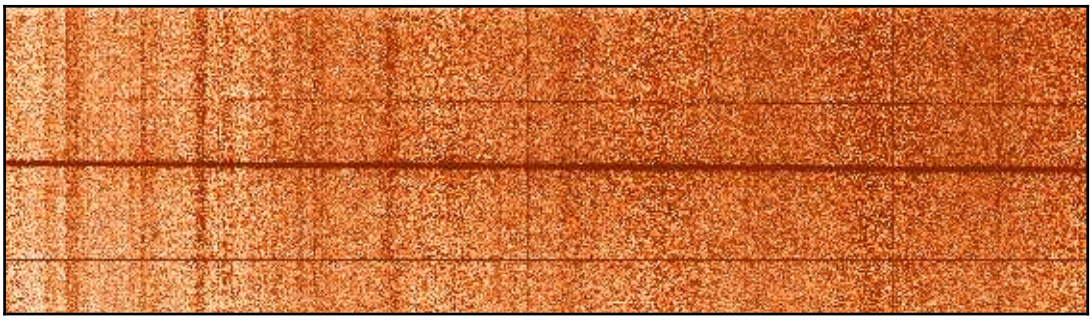

Figure 3.5: *Typical (raw) 2D spectrum of a source observed with ISIS on the WHT. The x axis corresponds to the spectral direction whereas the y-axis is the spatial direction. The latter is always aligned with the slit. The black horizontal lines indicate the spectra of observed stars whereas the dark vertical lines correspond to sky lines.*

3.3 Spectroscopy

A star's spectrum is a measure of its light intensity as a function of wavelength. It is also known as the spectral energy distribution (SED) of the star. There are different types of stellar spectra found, because stars have different properties (temperature, radius, luminosity, chemical composition, etc). Along the main sequence, the main reason for different spectral appearance is the mass of the star, which translates into its effective temperature. In the spectra of stars, we often find absorption lines which are produced when photons travels through a cooler gas before reaching the observer (usually the star's atmosphere). Photons are therefore absorbed by the atoms in the gas through what is known as bound-bound transitions. These are discrete and narrow energy electron transitions, which are reflected through lines in the spectra of stars.

In order to record a spectrum, an adjustable slit is placed at the focus of the telescope. The light from the source passes through the slit, and is then transformed into a thin beam of parallel rays by the use of a collimating lens or mirror. The light is then focused onto a diffraction or reflective grating, which is then sent to a detector, usually a CCD. The final raw data is a 2D image with a spatial and a spectral axis (see Figure 3.5). The basic steps to reduce spectroscopic raw data are the following: bias removal and flat fielding of the raw frame, extraction of the spectrum and wavelength and flux calibration of the extracted spectrum.

3.3.1 Bias removal

A bias frame is taken with no exposure time (zero seconds) and quantifies the electronic response of the CCD. It corresponds to an offset level introduced when the detector is read out. Also, the conversion from analog-to-digital units during the readout stage produces a small amount of noise. This noise is found in the

bias frame so one should acquire several bias 'exposures' and the average of all the frames should yield a good 'master bias frame' which will be used to de-bias all the other images. This averaging process should avoid introducing additional noise to the science frames, as well as eliminate spurious pixels in individual frames. Also, one can use the bias to calculate the readout noise, by taking its root-mean-square.

3.3.2 Flat Fielding

Each pixel in a CCD has a different sensitivity. This is explained by two main factors. The optics of the telescope can lead to nonuniform light transmission across the entire field of view which can be explained by either the presence of dust on the CCD or by vignetting. Also, the QE of individual pixels varies across the CCD, leading to variations in sensitivity. For these reasons, one must correct these effects by acquiring flat-field images. In our case, we use a Tungsten lamp located inside the spectrograph. Other observers choose to obtain dome or twilight flats as well. The smooth Tungsten spectrum is collapsed to a 1D spectrum along the spatial direction and fitted with a high order polynomial. The 2D master flat frame is then divided by the polynomial and applied to the science frames.

3.3.3 Spectrum extraction

Due to tilts introduced by the optics, the spectrum of the observed target can also be curved in the raw frames. For this reason, one must 'track' the spectrum by fitting it with a low order polynomial. Selecting two small regions either side of the spectrum defines the sky or background level (see Figure 3.5), which is required during the extraction of the spectrum. The sky regions are also fitted with polynomials, which will be subtracted from the target's spectrum during its extraction. In our study, we use the optimal extraction method outlined by Marsh (1989) and made available through the PAMELA software. Optimal extraction is designed to achieve the best possible signal-to-noise ratio with CCD spectral data.

3.3.4 Wavelength calibration

Once a 1D optimally extracted spectrum is obtained, the next step is to wavelength calibrate it. Arc lamp exposures, typically copper-argon, copper-neon or thorium-argon, are taken throughout the observations. These lamps have specific emission lines, where the expected wavelength positions of these lines are precisely known. An arc line map must be constructed from the observations and reference data, as it relates pixel position to wavelength, and then applied to the science spectra.

3.3.5 Flux calibration

Spectrophotometric flux standard stars must be observed in order to carry out the flux calibration stage. These stars have been carefully and precisely studied and have tabulated values of their fluxes as a function of wavelength. The difference between the template and the spectrum of the standard star is fitted with a spline,

which is then applied to the science spectra. It is important to note that flux calibration is not usually very accurate, especially in spectral regions with many spectral lines. Also, the Earth's atmosphere becomes less transparent at redder wavelengths, leading to forests of absorption lines, known as telluric lines. These can be approximately removed by creating a telluric-correction spectrum and subtracting it from the science spectra. A rather more important effect is the differential atmospheric refraction, which corresponds to the deviation of light from a straight line as it passes through the atmosphere due to the variation in air density as a function of altitude. Differential atmospheric refraction effects are more pronounced at shorter (i.e bluer) wavelengths.

3.4 Summary

We have briefly described the tools and methods we have used in the data analysis and studies described in the following Chapters. Achieving high quality observational data is becoming standard in astronomy, yet all the *truth* lies within the quality of their reduction. Each step of the bias removal, flat fielding, extraction and calibration must be done with precision and care in order to trust the final results. The astronomical surveys used in my studies are presented in the following Chapter.

Chapter 4

Large Sky Surveys

In order to obtain multiwavelength information on given sources, one must cross-correlate astronomical surveys covering different wavelength ranges. In all our studies, we match catalogues by calculating the angular distances between the sources. The angular distance, θ, between two stars is determined by the following equation:

$$cos(\theta) = sin(\delta_1) \times sin(\delta_2) + cos(\delta_1) \times cos(\delta_2) \times cos(\alpha_1 - \alpha_2) \tag{4.1}$$

where (α_1, δ_1) correspond to the right ascension and declination of the first star and similarly (α_2, δ_2) are the coordinates of the second star. Here, α and δ are in radians.
When matching catalogues, we set a search radius in which the sources should be found. This radius usually depends on the astrometric precision of the given catalogues, as well as the density of sources. A too small matching radius could lead to not matching the same sources, while a too large radius could lead to false matches. Below we describe all the surveys we have made use of for the search for compact sources.

In this Chapter, we describe the surveys we used in our projects. The surveys which have public data access are simply summarised here, with no details on how the data analyses were done. In such cases, we point to the website where the data were downloaded. However, in the cases where I was involved in the data calibration or analyses, a more thorough description is given (i.e. VVV and KIS).

4.1 X-ray survey

4.1.1 Galactic Bulge Survey (GBS)

The Galactic Bulge Survey combines sensitivity for faint X-ray sources and the astrometric accuracy of the *Chandra* X-ray Observatory, with a complementary photometric optical r', i' and Hα survey (Jonker et al., 2011). The GBS has several goals which will mainly be accomplished with the discovery of accreting compact objects. Detecting a large, homogeneous sample of X-ray emitting accreting objects

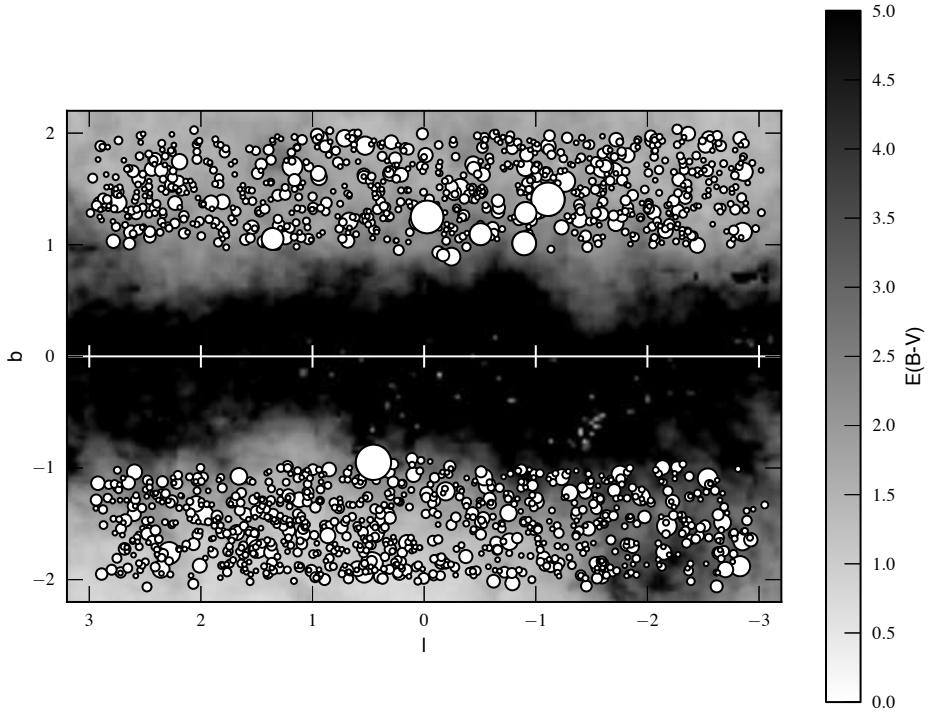

Figure 4.1: *The GBS coverage in galactic coordinates. The grey scale image depicts the total absorption E(B-V), estimated from the extinction maps from the VVV (Gonzalez et al., 2011). The overplotted white circles indicate the positions of the 1658 Xray sources detected in the GBS. The size of the white circles is proportional to the number of Chandra counts detected for the given source. (see Section 5.2 for more details).*

is necessary in order to understand binary formation and evolution (see Chapter 1).

The area of the sky covered in this survey is two rectangles of $l \times b = 6^\circ \times 1^\circ$, centred at $b = \pm 1.5^\circ$ (see Figure 4.1). These two strips were chosen in order to avoid the Galactic Centre region ($|b| < 1^\circ$), which suffers from extremely high extinction and source confusion, but just above and below the midplane, where the source density is still high. The GBS is a shallow X-ray survey, of 2 ksec exposures, in order to maximize the fraction of sources that are LMXBs, while also ensuring that a large fraction of the detected sample of flux limited sources are suitable for spectroscopic follow-up. Theoretical calculations from Jonker et al. (2011) predict the detection of $\sim$ 1600 X-ray sources in the survey region, out of which $\sim$ 700 are expected to be coronally active late-type stars (single and binaries) or binary systems such as RS Canum Venaticorum (RS CVn) or W Ursae Majoris (W UMa) systems, $\sim$ 600 are CVs and $\sim$ 300 are LMXBs.

The GBS completed the total 12 deg^2 area of the survey in both the X-ray and optical bands. Two separate X-ray energy bands (0.3-2.5 keV and 2.5-8 keV) were used to distinguish between soft and hard X-ray sources. A total of 1658 X-ray sources, with more than 3 X-ray counts, were found in the total area covered by the *Chandra* X-ray Observatory (see Figure 4.1). Jonker et al. (2011) published the initial list of X-ray sources detected between 2009 and 2010, containing 1234 sources. In 2011-2012, *Chandra* observed the remainder of the survey, adding another 424 X-ray sources to the list (Jonker et al., 2014). We use the source list and same naming convention as in Jonker et al. (2014). It is important to note that out of the initial list of published objects in Jonker et al. (2011), Hynes et al. (2012) found 18 duplicates, meaning that our catalogue actually contains 1640 unique X-ray sources. The main reason why duplicate sources were found in the catalogue was due to the fact that they were faint and off-axis, leading to a large PSF and poor centroiding. In our study of the GBS sources, we will use the catalogue of 1658 objects and comment on the duplicates in our final table containing the NIR data of their matches.

4.2 The near-infrared surveys

We exploit NIR data of the Bulge region in order to find the counterparts of the GBS X-ray sources. Here we present three NIR surveys which nominally cover the GBS fields: 2MASS, UKIDSS GPS and VVV. All three surveys have a different depth and coverage, each offering specific advantages in the search for the NIR counterparts of the GBS sources.

4.2.1 The Two Micron All Sky Survey (2MASS)

2MASS is a NIR survey, using J, H and K_s filters, which began in June 1997 and was completed in February 2001, covering 99.998% of the celestial sphere (Skrutskie et al., 2006). It produced a Point Source Catalog containing 471 million sources and an Extended Source Catalogue of 1.7 million sources. In order to map out the entire sky, 2MASS required telescope facilities in both hemispheres. Two identical 1.3m equatorial telescopes were constructed for the survey's observations. The northern telescope is located at the Whipple Observatory at Mount Hopkins in Arizona (USA) and the southern telescope was constructed at the Cerro Tololo Inter-American Observatory at Cerro Tololo in Chile. An automated software pipeline, the 2MASS Production Pipeline System (2MAPPS), reduced each night's raw data and produced astrometrically and photometrically calibrated images and tables. The entire 2MASS data set was processed twice. The average pixel scale is 2 arcseconds per pixel. The astrometric accuracy of the 2MASS catalogue is better than 0.1 arcseconds for sources with $K_s < 14$ (Skrutskie et al., 2006). We obtained the 2MASS data from the Infrared Processing and Analysis Center (IPAC, http:www.ipac.caltech.edu), in the form of reduced catalogues with coordinates, magnitudes and errors.

This survey is reliable for sources with magnitudes up to 15.8, 15.1 and 14.3

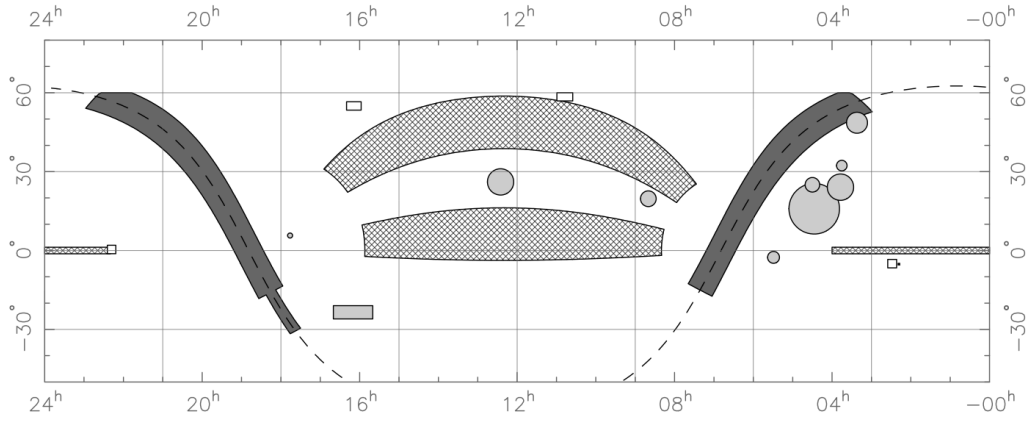

Figure 4.2: *Planned final UKIDSS coverage (Lawrence et al., 2007). The colour-code is the following: dark grey for the Galactic Plane Survey, light grey for the Galactic Clusters Survey, cross-hatched for the Large Area Survey and white for the Deep Extragalactic Survey. The dashed curve corresponds to the Galactic Plane.*

in J, H and K_s respectively (Skrutskie et al., 2006), in regions which do not suffer from high densities of sources. In the Bulge, the depth is around 1.5 magnitudes shallower (see Table 4.1). For this reason, we use 2MASS magnitudes solely in the case of bright sources ($K_s < 11.5$) where the other deeper NIR surveys saturate. The effective wavelengths of the JHK_s filters used in 2MASS are given in Table 4.1.

4.2.2 UKIDSS Galactic Plane Survey (GPS)

UKIDSS is the UKIRT (United Kingdom Infrared Telescope) Deep Sky Survey, which began in May 2005. It consists of five different surveys, each covering different areas of the sky, with the use of five near-infrared broadband filters ($ZYJHK$) as well as a narrowband one (H_2), and with a total area of 7500 deg^2 (see Figure 4.2, Lawrence et al. 2007). These surveys all use the Wide Field Camera (WFCAM), mounted on UKIRT, a 3.8 metre infrared reflecting telescope located on Mauna Kea in Hawaii. The projected pixel size is 0.4 arcseconds and the total field of view is 0.207 deg^2 per exposure. The data are reduced and calibrated at the Cambridge Astronomical Survey Unit (CASU), using a dedicated software pipeline. They are then transferred to the WFCAM Science Archive in Edinburgh[1]. The nominal positional accuracy of UKIDSS is $\sim$ 0.1 arcseconds but this deteriorates to 0.3 arcseconds near the Bulge (Lucas et al., 2008).

The GPS maps the Galactic Plane in JHK to a latitude of $\pm$ 5°. The effective wavelengths of the filters used in the GPS are given in Table 4.1. The Galactic longitude limits are $15° < l < 107°$ and $142° < l < 230°$. An additional narrow region, with $|b| < 2°$ and $-2° < l < 15°$, will also be mapped in GPS. Thus the UKIDSS GPS overlaps fully with the GBS fields. However, coverage is not as

[1]The data can be found on: http://surveys.roe.ac.uk/wsa/

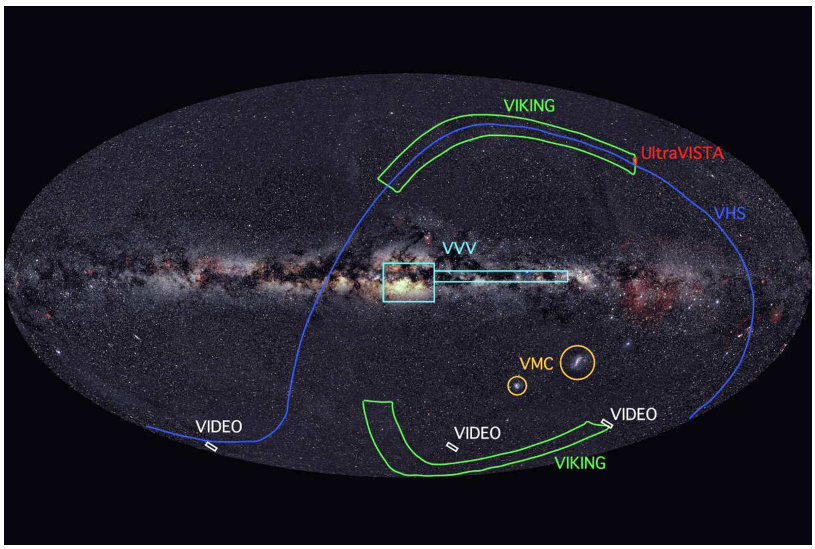

Figure 4.3: *VISTA surveys coverage (taken from the ESO website: https://www.eso.org/public/teles-instr/surveytelescopes/vista/surveys/).*

complete as originally intended. We use data from DR8 of GPS, where the coverage in the K-band is about 65% complete, whereas the J and H bands are still at about 35% complete. The total survey area of GPS is 1800 deg^2, in JHK to a depth $K \sim 18$ (Lucas et al., 2008). This 5σ limiting magnitude is given for non-crowded regions. In the Galactic Centre and Bulge, the depth of the survey is shallower (see Table 4.1). UKIDSS GPS data saturates when the magnitudes in JHK reach $J < 12.75$, $H < 12.25$ and $K < 11.5$ (Lucas et al., 2008).

4.2.3 VISTA Variables in the Via Lactea (VVV)

VISTA (Visible and Infrared Survey Telescope for Astronomy) is a 4m class wide-field telescope, located at the Cerro Paranal Observatory in Chile. Its main purpose is to conduct large-scale surveys of the southern sky, in the NIR wavelength range. It is currently used for the observations for six different surveys: VVV, VIKING, VIDEO, UltraVISTA, VHS and VMC (see Figure 4.3). The camera mounted on VISTA is VIRCAM, which is a wide-field NIR camera with an average pixel scale of 0.34 arcseconds per pixel. The total effective field of view of the camera is 1.1 $\times$ 1.5 deg^2. The broadband filters used are Z, Y, J, H, and K_s, with bandpasses ranging from 0.8 to 2.5 μm (Minniti et al., 2010; Saito et al., 2012).

VVV is a public NIR European Southern Observatory (ESO) survey and includes a variability component. Its main goal is to construct the first precise 3-D map of the Galactic Bulge by using variable stars such as RR Lyrae stars and Cepheids (Minniti et al., 2010; Saito et al., 2012), which are accurate primary distance indicators. The survey plan is to cover 520 deg^2 of the Galactic Bulge and an adjacent section of the mid-Plane in $ZYJHK_s$ (see Table 4.1 for their effective

wavelengths). The Milky Way Bulge area which will be covered expands from $l < |10|^\circ$ and -10° < b < +5°, thus covering the GBS area. In our study, we use data from all five filters provided in VVV. The depth and exposure times in each band are given in Table 4.1. The pipeline used to process the VVV data is based at CASU[2] and delivers reduced and calibrated images, as well as the aperture photometry for the VVV fields. I was in charge of the NIR study of the GBS X-ray sources so I was given early access to the VVV data, which I describe in this thesis.

We used VVV data from observations taken between March 2010 and September 2011, using version 1.1 of the photometric catalogues. The average seeing per night was typically 0.8 arcseconds (Saito et al., 2012). We calculate the magnitudes using the following equation:

$$m = ZP - 2.5 \times \log(\frac{f}{exptime}) - apcor - percorr \tag{4.2}$$

where ZP is the zero-point magnitude of the given VVV tile as derived from standard star observations obtained during the same night, f is the flux given in ADU, *exptime* corresponds to the exposure time in the given filter, *apcor* is the stellar aperture correction and *percor* is the sky calibration correction. All these values are taken from the headers of the downloaded catalogues and are calculated during pipeline processing. The errors on the magnitudes were also calculated, using the following equation:

$$\sigma_m = \frac{2.5}{\ln 10} \frac{\sigma_f}{f} \tag{4.3}$$

where σ_f is the error on the flux (f).

We merged all the Z, Y, J, H and K_s catalogues for each GBS source in order to work on the magnitudes and colours of any possible matches located near the X-ray positions. In order to test the quality of the photometry of the VVV data, we plot the magnitude errors against magnitudes of the nearest VVV match to the GBS sources, in all five filters (Figure 4.4). This gives us an indication of the limiting magnitudes of the VVV pointings we are using. Due to the dense fields of the Bulge, the actual depth is sensitive to seeing and thus covers a range around the nominal depth quoted in Table 4.1. Note that VVV data saturates at $K_s < 11.5$.

In summary, UKIDSS GPS and VVV have very similar resolution, whereas 2MASS has a much larger pixel scale (of 2 arcseconds per pixel). Also, the UKIDSS GPS observations have the longest exposure times (see Table 4.1), making it the deepest NIR survey out of the three, whereas 2MASS has the shortest exposures times, making it ideal for bright sources. In the following Chapter, we show how each survey was used in our search for the NIR counterparts to the GBS X-ray

[2]This project was an official VVV thesis project, allowing us full access to the data before its public release. We downloaded the VVV images and catalogues from http://apm49.ast.cam.ac.uk/vistasp/imgquery/search

Table 4.1: *Exposure times and 5σ limiting magnitudes in all three NIR surveys used in this paper. The GPS integration times are longer than those applied in VVV, allowing for deeper observations of the Bulge than VVV. The magnitude limits given here are for fields that are moderately crowded similar to the GBS areas.*

Survey	Filters	$\lambda_{\rm eff}$ (μm)	Exposure time (s)	Depth (mag)
2MASS	J	1.25	7.8	14.3
	H	1.65	7.8	13.6
	K_s	2.16	7.8	12.8
UKIDSS GPS	J	1.248	80	18.5
	H	1.631	80	17.5
	K	2.201	40	16.5
VVV	Z	0.878	40	18
	Y	1.021	40	18
	J	1.254	48	17
	H	1.646	16	16.5
	K_s	2.149	16	16

sources.

4.3 Optical survey: The *Kepler*-INT Survey

4.3.1 *Kepler* mission

NASA's *Kepler* spacecraft, which was launched in March 2009, contains a differential broadband optical (4 200 - 9 000Å) CCD array with a wide field of view (FoV) of 116 deg^2, mounted on a modified 0.95m Schmidt telescope continuously observing a region in the Cygnus and Lyra constellations. The *Kepler* mission's (Borucki et al., 2010) main goal is to discover Earth-size planets within the habitable zones of Sun-like stars. Due to the onboard storage and telemetry bandwidth limitation, only 170 000 sources, out of the millions present within the FoV, can be observed and downloaded to Earth at any given time. Therefore, the targets must be selected prior to the observations.

Kepler provides uninterrupted time series photometry that is superior to any previous ground-based study. Although *Kepler* was designed for the detection of exoplanets, its high-quality light curves hold an enormous potential for other astrophysical domains such as asteroseismology (Chaplin et al., 2010), stellar activity (Basri et al., 2011), star spot monitoring (Llama et al., 2012), eclipsing and close binary systems (Prša et al., 2011; Coughlin et al., 2011; Bloemen et al., 2011), gyrochronology (Meibom et al., 2011), accreting WDs (Fontaine et al., 2011; Still et al., 2010; Wood et al., 2011), the study of RR Lyrae stars (Benkő et al., 2010; Nemec et al., 2011) as well as systems showing stochastic behaviour in the variability

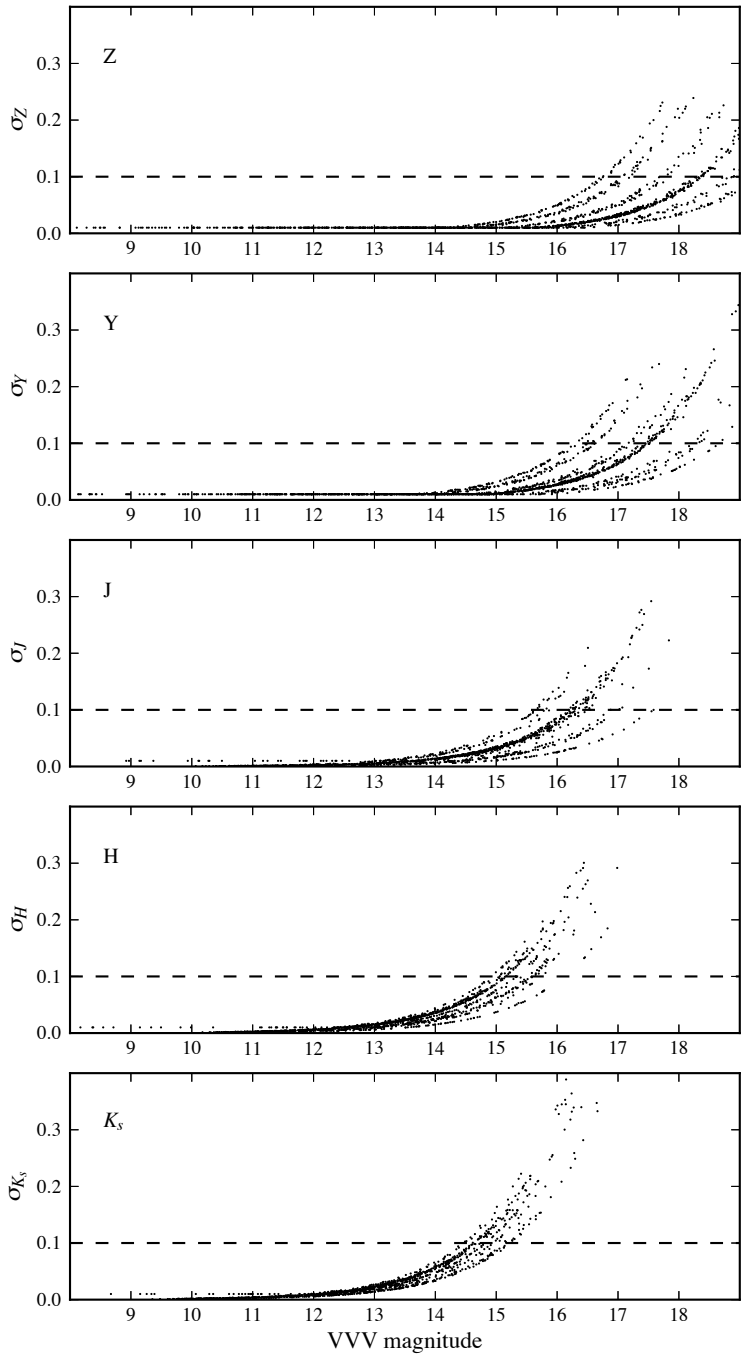

Figure 4.4: *We plot the magnitude against its uncertainty for different VVV fields. The typical 5σ limits of sources located in the Galactic Bulge are given in Table 4.1. It is clear that the different VVV fields do not have the same depth due to seeing variations from observations taken on different nights. This explains the large spread seen in the limiting magnitude values.*

of their fluxes (Mushotzky et al., 2011; Scaringi et al., 2012). *Kepler* data has also enabled the first determination of radial velocity amplitudes of binary systems through Doppler boosting (van Kerkwijk et al., 2010).

Kepler operates two types of observation modes: the short (one minute) and long (30 minutes) cadence modes. The Guest Observer (GO) program offers a yearly opportunity for the observation of 5,000 long cadence targets per quarter and 40 short cadence targets per month, through a peer-reviewed competition, which is open for all astrophysical domains. Every 3 months, the *Kepler* mission also offers the opportunity for a few dozen targets to be observed through Director's Discretionary Time (DDT) Proposals. Finally, every quarter, the *Kepler* Asteroseismology Science Consortium (KASC) can bid for more than $\sim$ 1,700 targets in order to study stellar pulsations.

It is therefore clear that the short cadence mode slots are very limited, thus a target must be well studied from the ground in order to justify required time with *Kepler*. In order to observe candidate planet hosts, mainly G-M type main-sequence stars, the *Kepler* team created the Stellar Classification Project (SCP), with a main goal to prevent the selection of non-main-sequence stars, by providing important stellar parameters (radius, effective temperature, apparent magnitude, etc) of the sources in the *Kepler* FoV. A photometric study of the *Kepler* field, mainly using $griz$ broadband filters was produced and stored in what is known as the *Kepler* Input Catalog (Brown et al., 2011). Since the main purpose of the KIC was to pre-select bright solar-like stars in order to detect Earth-like planets around them, the reliable depth of this survey is $g \sim 16$ and there was no need to include a filter bluer than the g-band. However, it is clear that many fainter objects within the *Kepler* FoV, which cannot be selected using KIC data, are of interest to non-exoplanet science such as cataclysmic variables (Wood et al., 2011), pulsating WDs (Østensen et al., 2011a; Hermes et al., 2011) and active galactic nuclei (Mushotzky et al., 2011).

The Guest Observer and *Kepler* Asteroseismic Science Consortium programs show that there is a large interest in fainter and bluer objects. In order to pre-select other, rarer types of targets such as hot, young, or active stars, WDs or subdwarfs, and accreting objects, a deeper optical survey of the *Kepler* field, including a filter bluer than g, was required. Also, the addition of an Hα filter would be useful to detect emission line objects, as well as strong Hα deficit sources such as hydrogen-rich WDs. Therefore, the INT Photometric Hα Survey of the Northern Galactic Plane (IPHAS, Drew et al. 2005) and the UV-Excess Survey of the Northern Galactic Plane(UVEX, Groot et al. 2009) collaborations made use of their available data reduction pipeline and observation strategy to obtain a homogeneous $Ugri$ and Hα catalogue of the *Kepler* FoV, down to $\sim 20^{th}$ mag in all five filters. All magnitudes are given in the Vega system (Morgan et al., 1953). We have named this effort the Kepler-INT Survey (KIS). KIS should be useful not only because it can identify UV-excess objects and Hα emitters, but also because it goes much deeper than KIC. Even though other collaborations are also conducting optical surveys of the *Kepler* field, such as the UBV Photometric Survey of the *Kepler* field (Everett et al., 2012), only KIS provides the critical deep U-band and Hα imaging.

Table 4.2: *Filter parameters of INT observations (González-Solares et al., 2008; Groot et al., 2009)*

Filters	Central wavelength (Å)	FWHM (Å)
U	3581	638
g	4846	1285
r	6240	1347
i	7743	1519
Hα	6568	95

KIS was designed and began observations during the second year of my PhD. As I was already experienced with working on CASU catalogues from the INT, I was given the task to calibrate the KIS data and release the catalogue. Here I explain the details of this work.

4.3.2 Survey imaging with the Isaac Newton Telescope

The 2.5m Isaac Newton Telescope (INT) is located in the Roque de los Muchachos Observatory on La Palma. The Wide Field Camera (WFC), mounted in its prime focus, is an optical imager consisting of 4 anti-reflective-coated 2048 $\times$ 4096 pixel CCDs, arranged in an L-shape. It has a pixel scale of 0.333 arcsec and a field of view of 0.29 deg^2 (González-Solares et al., 2008).

Four broadband filters ($Ugri$) and one narrowband filter (Hα) were used to obtain the INT data. The filter characteristics are provided in Table 4.2. Unlike g, r and i which are SDSS-like filters, the U-band is a non-standard U filter and it is affected by the CCD detector response dropping towards its blue edge. For more information on the U filter, see Verbeek et al. (2012).

The wealth of the available IPHAS and UVEX data has been used to develop selection methods to detect objects of special interest such as Hα emitters (Witham et al., 2006), cataclysmic variables (Witham et al., 2007), planetary nebulae (Viironen et al., 2009), symbiotic stars (Corradi et al., 2008), early-A stars (Drew et al., 2008), extremely red stellar objects, including mainly Asymptotic Giant Branch stars, and S-type stars (Wright et al., 2008, 2009), very low-mass accreting stars and brown dwarfs (Valdivielso et al., 2009) and UV-Excess sources (Verbeek et al., 2012). Candidates were primarily selected through the use of colour-colour diagrams. Their nature and the efficiency of the associated selection methods were then confirmed using spectroscopic data. Surveys such as IPHAS and UVEX have enabled the development of automated searches of a large number of unusual and 'exotic' objects.

4.3.3 INT observations and data

4.3.3.1 Observations

As our data processing recipe is identical to that of the IPHAS and UVEX surveys, we refer to Drew et al. (2005), González-Solares et al. (2008) and Groot et al. (2009) for details. The observing strategy consists of dividing the entire survey region into fields, each of them corresponding to the area of the WFC's FoV. A five percent overlap is included between adjacent pointings. Also, in order to cover the gaps between the four detectors, comprising ~ 12 arcmin^2, each field is observed in pairs with an offset of 5 arcmin North and 5 arcmin East between the pointings. This leads to at least two detections of most objects observed.

In order to balance the survey progress with the calibration quality of the data, approximately five observations of standards fields are taken throughout each night. These observations allow us to derive accurate zero-point magnitudes (ZPs) for each broadband filter per night without using too much of the allocated time on the telescope. The zero-point RMS of each night allows one to assess whether a night is considered 'photometric' (González-Solares et al., 2008).

4.3.3.2 Data

The data processing is described in detail in Section 3 of González-Solares et al. (2008). The final data products consist of band-merged catalogues with equatorial positions tied to 2MASS, Vega magnitudes and errors in all five filters and morphological flags (see Table 4.3). Further information on each detected object, such as CCD pixel coordinates in each waveband and the CCD in which the source was detected, are also provided in the catalogues. The astrometric precision of the end product is better than 100 mas across all four CCDs (González-Solares et al., 2008).

In the UVEX data reduction pipeline, the U-band zero-point (ZP) magnitudes are tied to the g-band ones with a fixed offset of (ZP_g - ZP_U) = 2.1 mag, similar to the case of the Hα ZPs in IPHAS (Drew et al., 2005) which are tied to the r-band via a fixed offset of 3.14 mag. The nightly g-band zero-points are derived from the standards observed throughout each night. However, in the KIS, we depart from the UVEX strategy in the U-band by using actual standard star ZPs to obtain U-band magnitudes, in the same way as we do for g, r and i (see Section 4.3.3.4 for more details). The Hα zero-points for each night remain tied to the r-band ones, as is done in IPHAS (Drew et al., 2005), since there are no Hα standards available.

A bubble in the U filter was discovered that was visibly affecting a corner of the U-band images, and a red leak is also known to exist in the filter (Verbeek et al., 2012). The bubble was fixed on 15 Jun 2011. However, Calima - dust winds which originate in the Saharan desert - was strongly present during that period of the observations. This affected the pre-June 20^{th} U-band data in particular. The derived U-band ZPs taken from the standards observations of those nights have an RMS of ~ 0.3 mag, about three times larger than the quality control threshold set for this survey and are thus not included in this release.

Table 4.3: *Morphological flags*

Flags	Definition
-9	saturated
-8	poor match
-7	contains bad pixels
-1	stellar
-2	probably stellar
-3	compact but probably not stellar
1	non-stellar (e.g. a galaxy)
0	no detection

4.3.3.3 Quality control flags

During the 2011 observing season, a total of 742 INT pointings, consisting of fields and offsets, were observed. However, not all of them pass the quality control threshold set for this survey. We only select fields which were observed under reasonably clear conditions where the RMS on the derived nightly zero-points must be smaller than 0.10 mag. Additional quality control tests related to the observing conditions include selecting pointings which have r-band seeing < 2 arcsec and r and g-band sky background values < 2000 ADUs, to remove observations done too close to the Moon. The distribution of seeing in the r-band, for all 742 pointings, is shown in Figure 4.5. Also, we use an additional measurement, the ellipticity, which is a detector-averaged PSF property that flags any tracking and focussing issues of the telescope that were possibly encountered on a given night. It must not be confused with a shape measurement for each source. We keep fields with mean r-band ellipticity values below 0.2 and any larger value would trigger a re-observation.

Out of all the observed fields in 2011 and 2012, 1159 pointings pass our quality control tests, which covers $\sim 97\%$ of the *Kepler* FoV. This number includes an additional quality control criterion described in the following Section. In Figure 4.6, we overplot the centres of these *good* INT pointings on the *Kepler* FoV. We indicate the boundaries of the sky footprints of the CCDs on the *Kepler* satellite. Note that our images include the gaps in between the *Kepler* CCDs. Thus not all objects in our catalogues will land on-chip. In 2013, we observed the remaining $\sim 3\%$ of the *Kepler* FoV and we are currently preparing the final data release of the catalogue.

4.3.3.4 Photometric calibration

For the KIS catalogue, we start by calibrating $Ugri$ to the standards observed each night by taking the average nightly ZPs in each filter, while the Hα ZP is tied to the nightly r-band ZP by a fixed offset. This calibration can introduce ZP errors if the

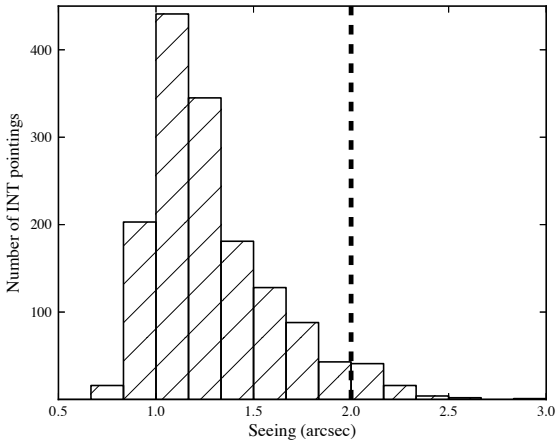

Figure 4.5: *r-band seeing in arcseconds of all INT pointings. Fields observed under seeing conditions worse than 2 arcsec were not included in the data release catalogues.*

night is not reasonably clear since all pointings in a given night employ the same ZPs. As mentioned previously, we reject the nights that have ZP RMS deviations larger than 0.10 mag.

Given the existence of the well-calibrated KIC catalogue, which has served as the principal survey for selecting *Kepler* targets, we decided to tie our absolute photometric calibration to the KIC broad-band magnitudes.

KIC contains over 13 million detected objects. A full explanation of the catalogue production can be found in Brown et al. (2011), but we provide a brief description of it here. The KIC photometric data were placed as close as possible to the Sloan photometric system (Brown et al., 2011), by selecting 8 fields outside the *Kepler* FoV, which overlap with SDSS DR1 (Stoughton et al., 2002) and which are used as photometric standards. Spanning a wide range of RA around the *Kepler* field, 316 primary standard stars were chosen. Each night, standards were taken on an hourly basis in order to calculate the transformations between the KIC and SDSS magnitudes. A specially designed pipeline was used to reduce the image data to catalogues of star positions and apparent magnitudes. The photometric calibrations were done using the time-averaged extinction-corrected magnitudes from the standards stars (Brown et al., 2011). The photometric precision of the KIC sources is expected to be $\sim 1.5\%$. However, it is important to note that out of the ~ 13 million detected objects, less than 3 million have g-band magnitudes < 16. The rest are either fainter than 16^{th} mag or are not provided with a magnitude value but only with their coordinates.

Given that the astrometry of both the KIS and KIC catalogues are based on well-resolved CCD data, we used a matching radius of 1 arcsec. Additional

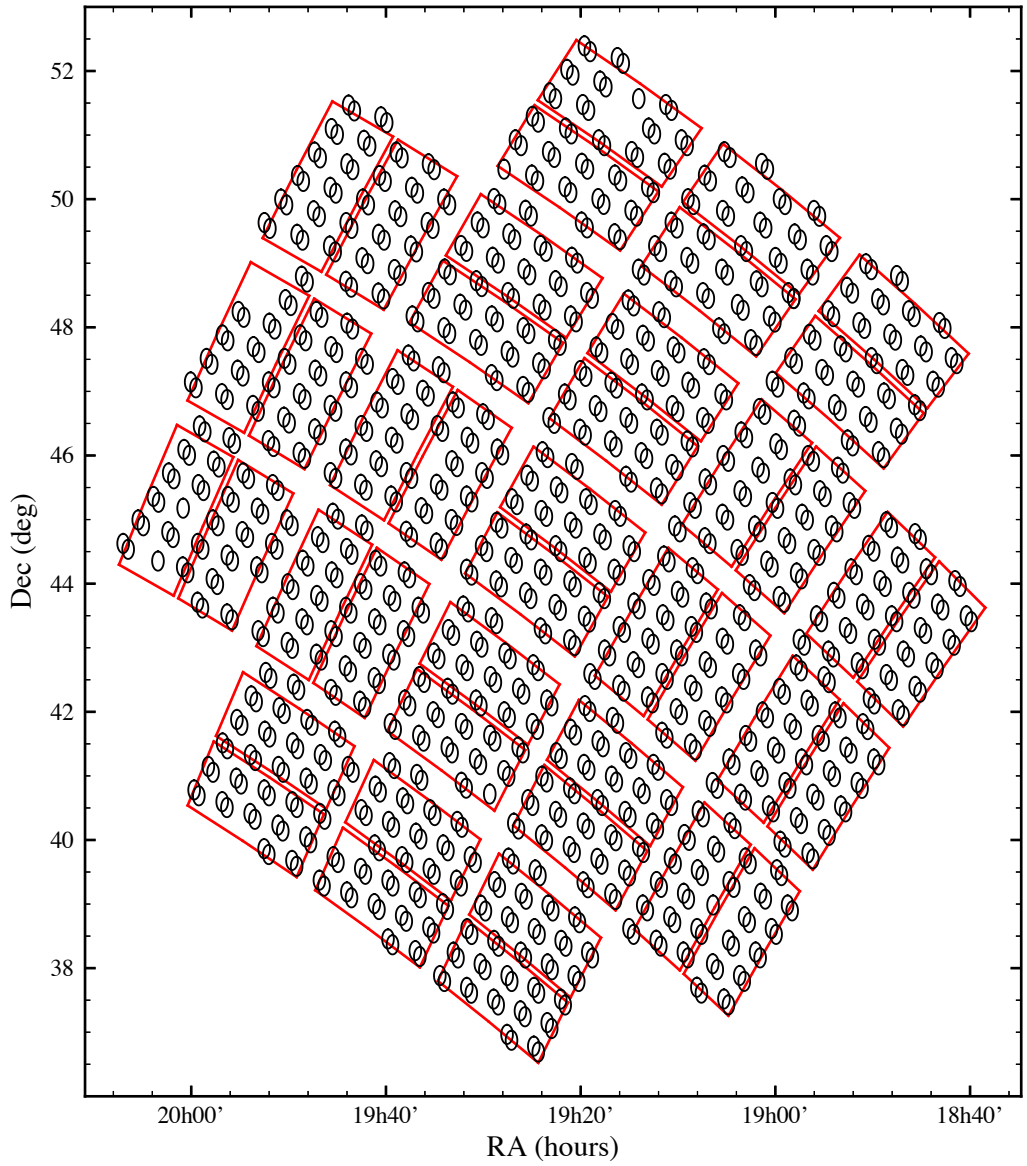

Figure 4.6: *INT coverage of Kepler fields. The open circles correspond to the centres of the INT pointings which passed our quality control tests and are part of the released catalogues. The boundaries of the sky footprints of the CCDs on the Kepler satellite are shown in red.*

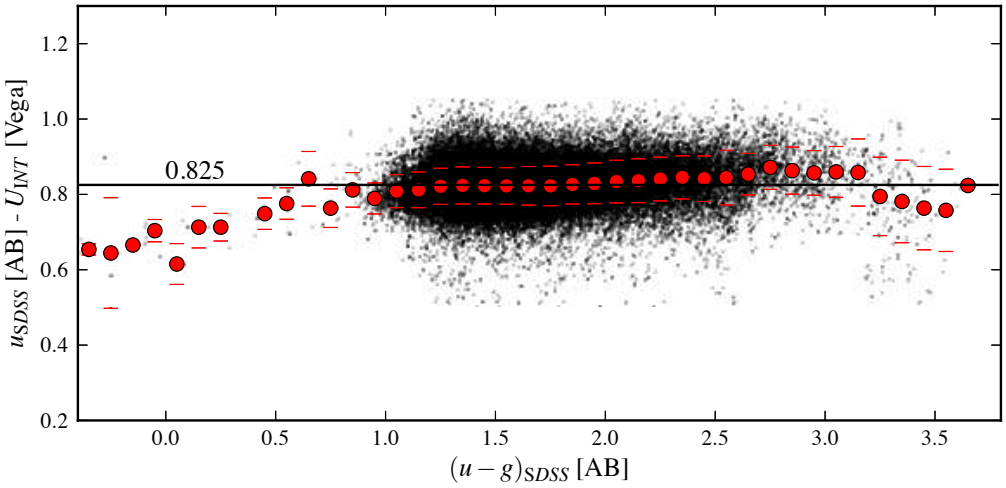

Figure 4.7: *Difference between u from SDSS (AB system) and U from KIS (Vega system) against $(u-g)$ from SDSS (AB system), showing that the transformations from AB to Vega (and vice versa) are more colour-dependent when looking at non-main-sequence stars. The red points correspond to the medians of $(u-U)$ over 0.1 magnitude bins in $(u-g)$[AB]. The median of $(u-U)$ is 0.825, a value close to the fixed term found in Equations 4.4. The data points with no error bars simply mean that only one data point was used to determine the median.*

information on the KIC astrometry can be found on the *Kepler* webpage[3]. Since the KIC photometry is based on the AB system (Oke & Gunn, 1983) and the INT data is all in the Vega magnitude system, we converted the KIC data to the Vega system using the transformations from González-Solares et al. (2011):

$$\begin{aligned} U_{\rm WFC} &= u_{\rm SDSS} - 0.833 - 0.009 \times (u_{\rm SDSS} - g_{\rm SDSS}) \\ g_{\rm WFC} &= g_{\rm SDSS} + 0.060 - 0.136 \times (g_{\rm SDSS} - r_{\rm SDSS}) \\ r_{\rm WFC} &= r_{\rm SDSS} - 0.144 + 0.006 \times (g_{\rm SDSS} - r_{\rm SDSS}) \\ i_{\rm WFC} &= i_{\rm SDSS} - 0.411 - 0.073 \times (r_{\rm SDSS} - i_{\rm SDSS}) \end{aligned} \tag{4.4}$$

We stress that these transformations are reliable for main-sequence stars but diverge for blue objects which have a negative $(U-g)$ colour. In order to verify this, we cross-match the KIS data with Sloan Digital Sky Survey (SDSS, Abazajian et al. 2009) and select matches with r-band magnitudes ranging from 15 to 18. Only $\sim$ 25% of the KIS pointings overlap with SDSS and therefore this test is only used to determine the range over which these transformations are valid. The transformations taken from González-Solares et al. (2011) were derived using a more robust algorithm.

In our test, we plot the difference between SDSS and KIS magnitudes in U against $(u-g)$ colours from SDSS (see Figure 4.7). We bin the data in colour bins

[3]http://keplergo.arc.nasa.gov/Documentation.shtml

Table 4.4: $\Delta\{filter\}$ *is the median offset between the KIC and KIS magnitudes (see Section 4.3.3.4). The standard deviations of the distributions in each filter are also given here* ($\sigma_{\{filter\}}$). *The distributions are shown in Figure 4.8.*

	g	r	i
$\Delta\{filter\}$	0.012	0.004	0.044
$\sigma_{\{filter\}}$	0.040	0.042	0.053

of 0.1 mag and calculate the median of the difference between the SDSS and KIS magnitudes. These values correspond to the red circles. The error bars are the standard deviations of the binned data. As we can see, the transformations provided by González-Solares et al. (2011) are confirmed for objects within $1 < (u-g)$ [AB] < 3. At both the red and blue ends of the plots, the data points do not follow the linear fit for the main locus of stars. For the purpose of our photometric calibration, this is not an issue.

As mentioned earlier, we use the KIC to calibrate the photometric data of KIS. By placing the KIS ZPs as close to the KIC ones as possible, we can improve our photometric calibration on a pointing by pointing basis. We calculate the difference between the KIC magnitudes and the KIS ones for sources between $g \sim 13$ and 15. These limits were chosen because KIS magnitudes smaller than $\sim 12^{th}$ mag become less reliable due to saturation and the photometric accuracy of KIC deteriorates above $\sim 16^{th}$ mag. We plot the distribution of the offsets in the g, r and i bands in Figure 4.8 (Δg, Δr and Δi). The median values of these offsets corresponding to the centre of their distributions, as well as the standard deviations of these distributions, are given in Table 4.4. As can be seen, the values of these offsets were typically a few percent, rarely exceeding 5% for fields passing the quality control threshold. The applied offset values are provided in the final catalogue of the *Kepler*-INT Survey.

We also make use of the KIC to set an additional quality control criterion: we only select fields which have a median offset with respect to KIC in each waveband within $\pm$ 0.2 mag of the values given in Table 4.4. Only 34 fields fail this criterion. In general, the systematic offset between the KIC and KIS magnitudes are within 0.1 mag.

The KIC contains g, r and i - band magnitudes for a large number of sources. For these bands, our photometric corrections are thus simply:

$$\begin{aligned} \Delta g &= g_{\rm WFC} - g_{\rm KIC} \\ \Delta r &= r_{\rm WFC} - r_{\rm KIC} \\ \Delta i &= i_{\rm WFC} - i_{\rm KIC} \end{aligned} \tag{4.5}$$

In order to have a more accurate calibration, we calculated these offsets for each WFC CCD separately. In general, all four CCDs behaved the same way. For each KIS field, we calculate the median of the offsets of all matched sources in each

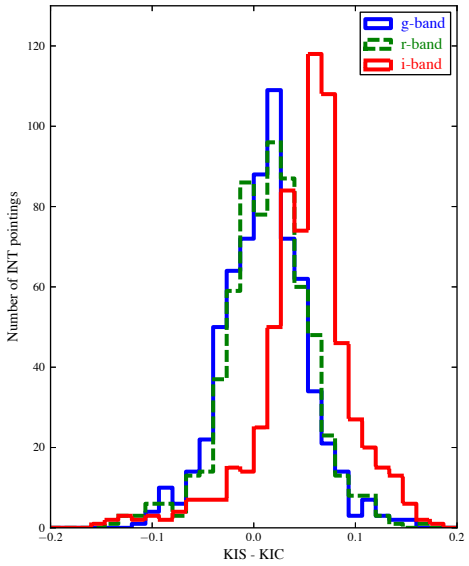

Figure 4.8: *Distribution of Δg, Δr and Δi, for all pointings, where $\Delta\{filter\}$ is the offset between the KIC and KIS magnitudes (see Section 4.3.3.4). Fields with offsets > 0.2 mag from the median are not included in the final catalogues.*

passband for each WFC CCD (for instance, median($\Delta g_{\rm CCD1}$), median($\Delta g_{\rm CCD2}$),median($\Delta g_{\rm CCD3}$), median($\Delta g_{\rm CCD4}$), and similarly for the r and i bands).

As KIC lacks u-band data, the KIS U-band cannot have an absolute calibration as for the case of g, r and i. For two main reasons, we decided to use the g-band offset also for U: to conserve the $U-g$ colours of the KIS sources and to minimise any wavelength dependent effects by using the nearest KIC broadband, which is the g-band. This introduces a systematic error in the U-band photometry of up to ~ 0.05 mag.

In summary, to calibrate the INT photometry, we applied the following equations to the sources in each INT pointing and CCD:

$$\begin{aligned} U'_{\rm WFC} &= U_{\rm WFC} - \Delta g_{\rm CCD\#} \\ g'_{\rm WFC} &= g_{\rm WFC} - \Delta g_{\rm CCD\#} \\ r'_{\rm WFC} &= r_{\rm WFC} - \Delta r_{\rm CCD\#} \\ i'_{\rm WFC} &= i_{\rm WFC} - \Delta i_{\rm CCD\#} \\ H\alpha'_{\rm WFC} &= H\alpha_{\rm WFC} - \Delta r_{\rm CCD\#} \end{aligned} \tag{4.6}$$

where the prime indicates the calibrated magnitudes.

4.3.3.5 Catalogue description

In the Initial Data Release (IDR) catalogue, 511 INT fields were classified as reliable and observed during reasonably clear nights between June and August 2011. The second data release catalogue contained an additional 648 fields, all observed between May and August 2012. In total, we covered ∼97% of the *Kepler* FoV.

We plotted individual ($U-g$, $g-r$) and ($r-\mathrm{H}\alpha$, $r-i$) colour-colour diagrams of each INT pointing in order to assess the state of the data by considering Pickles (1998) main-sequence tracks, as well as DA (hydrogen-rich) WD tracks from Koester models (Koester, 2010), taken from Drew et al. (2005); Groot et al. (2009) and Verbeek et al. (2012). A stacked colour-colour diagram of all the INT pointings from the IDR catalogue is shown in Figure 4.9, where the model tracks and the stellar content of KIS are in good agreement.

With all reliable pointings at hand, we produced the KIS initial and second data release catalogues. The IDR catalogue contained $\sim$ 6 million sources. Out of these sources, $\sim$ 2.1 million of them are also unique detections in KIC. However, only $\sim$ 280 000 of those $\sim$ 2.1 million objects have KIC magnitudes between 12 and 16. Therefore, we provide 'reliable' magnitudes to $\sim$ 1.3 million sources already existing in KIC. With KIS, we detect an additional $\sim$ 2.4 million unique objects in the field, since around 25% of the sources in KIS have another detection from overlapping regions between different pointings. The second data release catalogue contains an additional ∼8.5 million sources. Once again, these are not all unique sources and similarly to the IDR catalogue, around 25% of them will be duplicates. The data is available for download from the KIS webpage (www.astro.warwick.ac.uk/research/kis/), as well as from the Kepler Target Search page at MAST (http://archdev.stsci.edu/kepler/kepler fov/search.php).

We produce two versions of the catalogue: a standard version and an extended one. A description of the columns of the catalogue is given in Table 4.5 and an example of a few lines taken from the standard version is shown in Table 4.6. It contains the positions of the sources in degrees, their magnitudes and errors, as well as their morphological classes in each waveband (see Table 4.3 for more details). We also give each KIS source an ID, found in the first column of the tables. It simply corresponds to the 'KISJ' prefix, followed by the object's KIS coordinate given in sexagesimal notation. Finally, when a KIS object had a match in the *Kepler* Input Catalog within 1 arcsec, we added the *Kepler* ID of that match in the final column of the table. If no match was found, the *Kepler* ID is equal to 0.

The extended catalogue contains further information on each source, such as the CCD in which it was detected, its CCD pixel coordinates, the seeing, ellipticity and modified Julian date in each filter and the offsets between the KIS and KIC magnitudes which were used to calibrate the KIS catalogue. The seeing and ellipticity values given for each source are average values for the given INT pointing in which the object was detected.

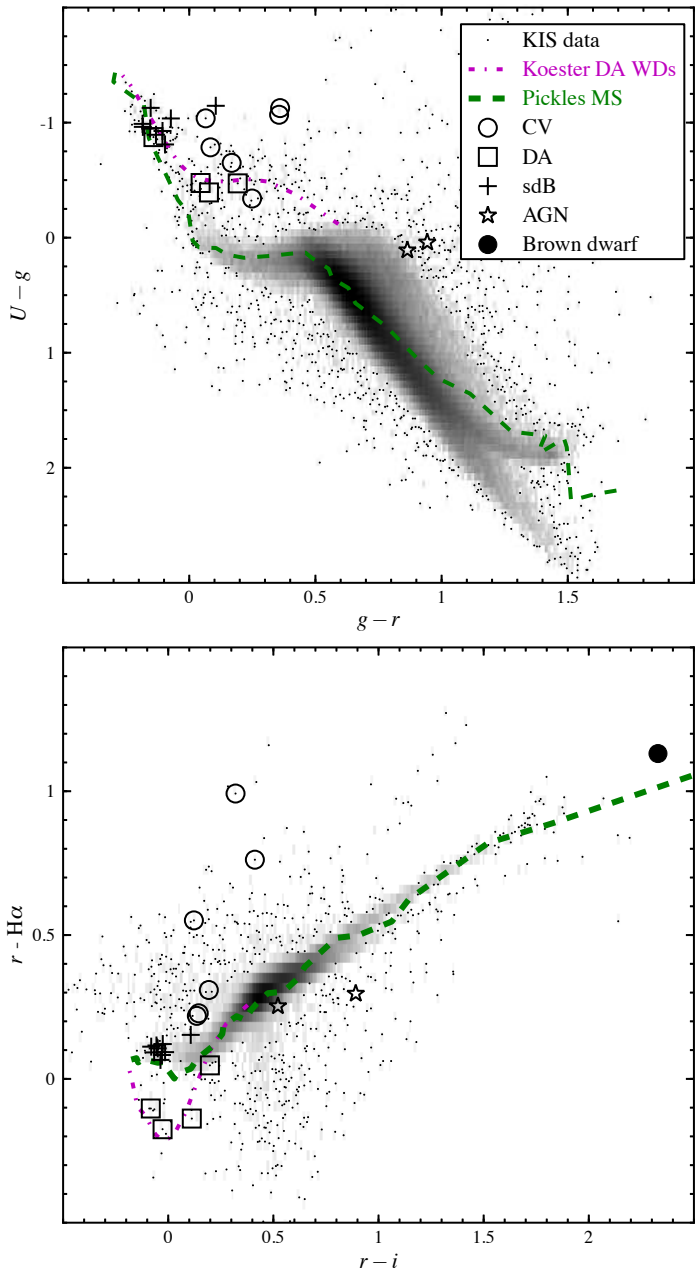

Figure 4.9: *Colour-colour diagrams of some of the published pulsators, WDs, CVs, ultra-cool dwarfs and AGNs in the Kepler field. The Pickles tracks are taken from Drew et al. (2005) in the lower panel, and from Groot et al. (2009) in the top panel. The magenta tracks in both panels correspond to Koester models of DA WDs with constant surface gravity, log g = 8, taken from Verbeek et al. (2012). The grey scale and black points are stellar objects taken from the KIS catalogue which have photometric errors smaller than 0.02 mag in all five filters, as well as r-band magnitudes between 12 and 20. The grey scale shows the densest region of the colour-colour diagrams using a logarithmic scale.*

Many sources had two detections, therefore the magnitude and errors provided in the catalogue are mean values, calculated from the magnitudes and errors of detections of the same source found in an INT and its paired field. The reason why we allow for a mean value to be calculated in this case is because the paired fields are observed one after the other, under very similar conditions. We also compute the deviation of the magnitudes for each source in order to compare the difference between the magnitudes in both detections, within their error bars. If the value of the calculated deviation is large with respect to the errors, it would imply either short timescale variability or non-ideal observing conditions. In the case of a single detection, the deviation is set to -1. The overlap between non-paired pointings was not taken into account for the search of duplicates, therefore the final catalogue will still contain two detections of the same source for $\sim 25\%$ of the sources.

The limiting magnitudes in each filter can be seen in Figure 4.10, where we plot only 'stellar' objects in all five bands independently, for sources fainter than 12^{th} mag in each filter. We also only plot significant detections, by setting the S/N threshold to values above ~ 10, in order to avoid being misled by spurious detections. The figure shows that the depth of the ongoing survey is $\sim 20^{th}$ mag in the Vega system. Sources brighter than $\sim 12^{th}$ magnitude are saturated and their magnitudes should not be considered reliable. This figure also gives an indication of the photometric errors in the catalogue, as a function of magnitude. At $\sim 20^{th}$ magnitude, the random photometric errors are $\sim 10\%$, except in the case of the U-band where the errors can be larger. Errors of around 10% are within the quality target of our catalogue. Note, the random photometric errors are obtained from the pipeline product and do not include systematic effects, e.g. related to the offset applied to calibrate KIS against KIC. The systematic errors (up to 5%) may dominate at the bright end.

We show the distribution of the number of detected sources as a function of magnitudes in Figure 4.11. Similarly to Figure 4.10, we select 'stellar' objects in all five bands independently and set the same S/N limit. As can be seen, the g and r-bands go slightly deeper than the other filters and the number of detected objects in the U-band is much smaller than in the other bands.

In order to test the potential of the KIS catalogue to identify rare and unusual objects in the *Kepler* field, we cross-match KIS with known published sources within the *Kepler* FoV such as the pulsating subdwarfs and WDs from Østensen et al. (2010, 2011b,a); Hermes et al. (2011), the CVs from Williams et al. (2010); Wood et al. (2011); Fontaine et al. (2011) and the AGN from Mushotzky et al. (2011). The objects which had matches in KIS are plotted in colour space (Figure 4.9). We also include a recently spectroscopically confirmed ultra-cool dwarf (R. Tata, E. L. Martín & E. Martioli, private communication) in the (r- Hα, $r - i$) colour-colour diagram of Figure 4.9, which did not have a U-band detection. We see that the different types of objects fall within their expected locations in colour-space. The CVs are indeed found in the ($U - g$, $g - r$) colour-colour diagram with $(U - g) < 0$ and they also stand out as Hα emitters in the ($r - H\alpha$, $r - i$) diagram. Also,

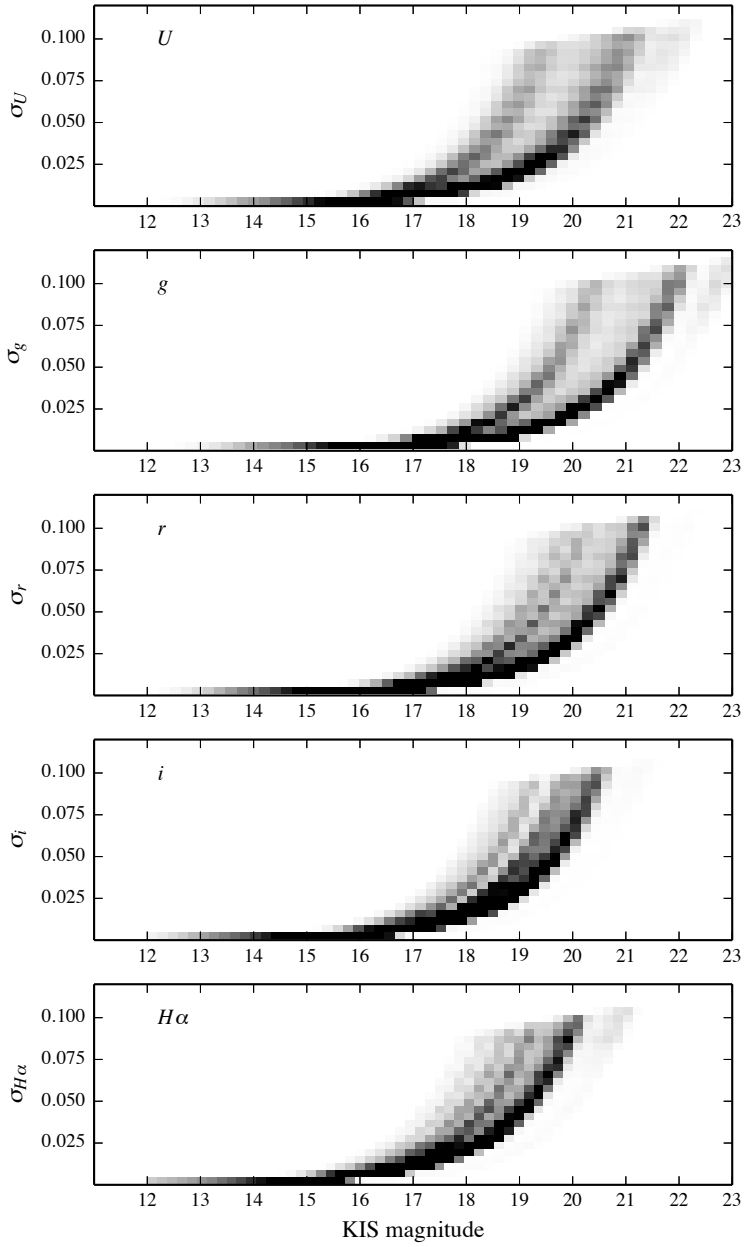

Figure 4.10: *Limiting magnitudes in all five bands. Sources with magnitudes smaller than 12^{th} mag are detected but not shown because they are not considered reliable. The survey depth is $\sim 20^{th}$ mag in all filters. We use a linear scale in order to show the densest regions of the plots.*

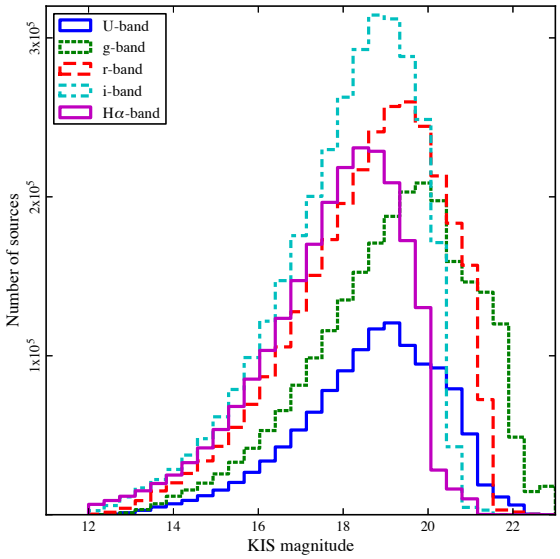

Figure 4.11: *Distribution of the number of sources as a function of KIS magnitudes. The objects taken into account are those classified as 'stellar' in all five filters independently.*

the DA WDs are known to be Hα deficit objects due to strong broad Balmer line absorption, which can be seen in the bottom panel of Figure 4.9.

4.4 Summary

In this Chapter, we have described the surveys which we exploited for the search of exotic, rare and interesting compact sources. In the following Chapters, we explain our methods used to mine these surveys for such objects. First, we focus on the search for the counterparts of the 1658 X-ray GBS sources in the NIR surveys we mentioned here, then we move onto the search for pulsating WDs in the *Kepler* field. In each study, the methods used were based on photometric data, which then relied on spectroscopy to confirm the identities of the objects we chose for follow-up. Nevertheless, we point out that the techniques we developed in each study are different to one another.

Table 4.5: *Description of columns in KIS catalogue*

Column name	Description
KIS_ID	KIS ID containing the coordinate of the source, in sexagesimal notation.
RA	Right Ascension (J2000), in degrees.
Dec	Declination (J2000), in degrees.
mean_U, mean_g, mean_r, mean_i, mean_Hα	Magnitudes of sources, given in the Vega system. In the case of two detections, the mean value is given.
U_err, g_err, r_err, i_err, Hα_err	Magnitude errors. In the case of two detections, the mean error is given.
rms_$U^\star$, rms_$g^\star$, rms_$r^\star$, rms_i^star, rms_H$\alpha^\star$	Root-mean-square (rms) deviation of magnitudes of sources with two detections. In the case of a single detection, the rms deviation value is set to -1.
x_$U^\star$, x_$g^\star$, x_$r^\star$, x_$i^\star$, x_H$\alpha^\star$	X pixel coordinate of source.
y_$U^\star$, y_$g^\star$, y_$r^\star$, y_$i^\star$, y_H$\alpha^\star$	Y pixel coordinate of source.
class_U, class_g, class_r, class_i, class_Hα	Morphological class of source (see Table 4.3).
CCD*	WFC's CCD in which the source was detected.
seeing_$U^\star$, seeing_$g^\star$, seeing_$r^\star$, seeing_$i^\star$, seeing_H$\alpha^\star$	Average seeing of the INT pointing, given in arcsec.
ellipticity_$U^\star$, ellipticity_$g^\star$, ellipticity_$r^\star$, ellipticity_$i^\star$, ellipticity_H$\alpha^\star$	Average ellipticity of the night.
MJD_$U^\star$, MJD_$g^\star$, MJD_$r^\star$, MJD_$i^\star$, MJD_H$\alpha^\star$	Modified julian date of observation.
delta_$U^\star$, delta_$g^\star$, delta_$r^\star$, delta_$i^\star$, delta_H$\alpha^\star$	Difference between KIS and KIC magnitudes applied to calibrate KIS data.
KIC_ID	KIC ID of source. If it does not have a KIC match within 1 arcsec, the value is set to 0.

* These values are only available in the extended catalogue.

Table 4.6: *Example of light version of the KIS catalogue*

KIS ID	RA	Dec	U	σ_u	cls U	g	σ_g	cls g	r	σ_r	cls r	i	σ_i	cls i	Hα	$\sigma_{H\alpha}$	cls Hα	KIC ID
KISJ183904.45+472458.6	279.768542	47.416278	20.892	0.150	-1	18.811	0.014	-1	17.754	0.000	-1	17.110	0.000	-1	0.000	0.000	0	10316732
KISJ183904.53+471612.6	279.768875	47.270167	0.000	0.000	0	21.395	0.120	-1	0.000	0.000	0	0.000	0.000	0	0.000	0.000	0	0
KISJ183904.68+471532.8	279.769500	47.259111	0.000	0.000	0	13.499	0.001	-1	12.888	0.001	-9	12.489	0.001	-1	0.000	0.000	0	0
KISJ183904.68+471625.6	279.769500	47.273778	0.000	0.000	0	21.955	0.193	-1	20.490	0.073	1	18.921	0.033	1	19.699	0.091	1	0
KISJ183904.73+473001.1	279.769708	47.500306	0.000	0.000	0	0.000	0.000	0	21.326	0.148	-1	19.421	0.050	-1	20.253	0.145	-1	0
KISJ183904.76+471636.7	279.769833	47.276861	0.000	0.000	0	0.000	0.000	0	21.789	0.219	-1	20.332	0.110	1	0.000	0.000	0	0
KISJ183904.79+472829.3	279.769958	47.474806	18.758	0.025	-1	18.042	0.000	-1	17.274	0.006	-1	16.821	0.007	-1	16.964	0.011	-1	10316736
KISJ183904.85+472027.0	279.770208	47.340833	18.010	0.014	-1	17.571	0.006	-1	16.931	0.005	-1	16.486	0.006	-1	16.623	0.009	-1	10250924
KISJ183904.88+473120.4	279.770333	47.522333	16.383	0.005	-1	0.000	0.000	0	15.481	0.002	-1	0.000	0.000	0	0.000	0.000	0	10382031
KISJ183904.93+472511.8	279.770542	47.419944	19.668	0.053	-1	18.530	0.011	-1	17.582	0.007	-1	16.981	0.000	-1	17.181	0.013	-1	10316737
KISJ183904.97+470905.8	279.770708	47.151611	0.000	0.000	0	21.745	0.160	-7	0.000	0.000	0	0.000	0.000	0	0.000	0.000	0	0
KISJ183904.98+471902.8	279.770750	47.317444	12.859	0.001	-9	11.694	0.001	-9	10.531	0.001	-9	10.252	0.001	-9	10.519	0.001	-9	0
KISJ183905.04+472525.8	279.771000	47.423833	0.000	0.000	0	0.000	0.000	0	21.540	0.178	-1	19.505	0.054	1	0.000	0.000	0	0
KISJ183915.68+472135.5	279.815333	47.359861	15.487	0.003	-1	14.960	0.001	-1	14.315	0.001	-1	13.880	0.001	-1	14.024	0.002	-1	10250986
KISJ183915.74+472239.7	279.815583	47.377694	0.000	0.000	0	0.000	0.000	0	21.466	0.168	-1	21.016	0.197	1	0.000	0.000	0	0
KISJ183915.77+472054.0	279.815708	47.348333	19.701	0.055	-1	18.899	0.015	-1	18.130	0.011	-1	17.598	0.012	-1	17.759	0.020	-1	10250987
KISJ183916.12+472412.8	279.817167	47.403556	19.686	0.054	-1	18.102	0.000	-1	17.000	0.005	-1	16.390	0.005	-1	16.613	0.009	-1	10316799
KISJ183916.16+472140.4	279.817333	47.361222	16.751	0.006	-1	16.443	0.003	-1	15.871	0.003	-1	15.459	0.003	-1	15.597	0.005	-1	10250990
KISJ1839163+472143.4	279.817625	47.362056	19.078	0.032	1	18.633	0.012	1	18.026	0.010	-1	17.560	0.011	-1	17.720	0.019	-1	0
KISJ183916.33+472123.7	279.818042	47.356583	19.360	0.041	-1	18.687	0.013	-1	17.957	0.010	-1	17.428	0.010	-1	17.601	0.017	-1	10250993
KISJ183916.35+472130.3	279.818125	47.358417	20.833	0.144	-1	18.616	0.012	-1	17.088	0.005	-1	15.156	0.003	-1	16.070	0.007	-1	0
KISJ183916.40+471515.6	279.818333	47.254333	15.715	0.003	-1	14.878	0.001	-1	14.131	0.001	-1	13.675	0.001	-1	13.812	0.002	-1	10184560
KISJ183916.47+471621.6	279.818625	47.272667	18.240	0.017	-1	16.727	0.004	-1	15.673	0.002	-1	15.065	0.002	-1	15.274	0.004	-1	10184561
KISJ183916.79+471239.7	279.819958	47.211028	20.413	0.100	-1	20.341	0.049	-2	19.823	0.041	-1	19.318	0.046	1	19.494	0.077	-1	10184563
KISJ183916.83+472018.8	279.820125	47.338556	19.927	0.066	-1	19.143	0.018	-1	18.330	0.013	-1	17.758	0.013	-1	18.000	0.023	-1	10250996

Chapter 5

Near-infrared and optical study of the GBS sources

5.1 Near-infrared coverage of the Bulge

We begin by comparing the NIR surveys we introduced in Section 4.2 for the study of likely counterparts to our *Chandra* X-ray sources. 2MASS will be useful in the case of sources saturated in VVV and UKIDSS GPS. We also show that UKIDSS GPS goes deeper than VVV, yet it does not cover the entire GBS area, making VVV the data set with the most uniform coverage, in terms of both survey area and depth.

5.1.1 Coverage

We cross-match the positions of the GBS X-ray sources with the positions of the detected stars in all three NIR surveys and compare the results we obtain from each one. To do this, we need to consider all sources of error that contribute to the absolute positional uncertainty. In Table 5.1, we give the number of matches found within respectively 5 arcseconds and 2.8 arcseconds of the X-ray position, in each filter of each survey. Those radii were chosen because 2.8 arcseconds represents the median positional uncertainty of the GBS X-ray sources corresponding to a 95% confidence interval. The statistical component to the *Chandra* positional inaccuracies P is calculated for each source individually using Equation 4 from Evans et al. (2010) which takes into account the number of X-ray counts and off-axis angles of each GBS source:

$$log\ P = \begin{cases} 0.1145\theta - 0.4957\ log\ C + 0.1932, \\ \qquad\qquad\qquad\qquad \text{if } 0.000 < log\ \mathrm{C} < 2.1393 \\ 0.0968\theta - 0.2064\ log\ C - 0.4260, \\ \qquad\qquad\qquad\qquad \text{if } 2.1393 < log\ \mathrm{C} < 3.300 \end{cases} \tag{5.1}$$

where θ is the off-axis angle in arcminutes and C is the number of X-ray counts detected. This positional error, given in arcseconds, corresponds to a 95% confidence

interval. We mention once again that we use ACIS-I and most X-ray sources detected have a few counts (less than 10) so many *Chandra* positions can be uncertain by several times the size of the *Chandra* on-axis PSF. In addition to this component, several other terms contribute to the total positional uncertainty. One is due to some uncertainty in the spacecraft pointing, which can introduce a positional offset. The distribution of this offset reaches 0.7 arcseconds at the 95% confidence limit[1]. Since we cannot derive this offset from our data due to the low number of sources in one pointing, we must add a term for it. However, it is important to note that for most sources the positional error is not dominated by this absolute correction but instead the low count rate and significant off-axis angles. Most GBS sources will have typically 5 X-ray counts and an off-axis angle of 4.5 arcminutes, leading to a positional uncertainty of 2.3 arcseconds. Primini et al. (2011) statistically characterised the positional uncertainties of *Chandra* Source Catalogue objects by cross-matching these to SDSS. They found residual offsets suggesting that another component contributes to the total absolute positional accuracy. Since the radial position offset is distributed according to a Rayleigh function, the 95% error from Eq. 5.1 can be converted to an equivalent 1σ error by multiplying by 0.4085 (the 95% confidence interval for a Rayleigh PDF corresponds to a radius of $2.448 \times \sigma$). Primini et al. (2011) show that a term of 0.16" should be added in quadrature to this 1σ error. Finally, the NIR positional uncertainty for VVV amounts to 0.08" at the 1σ level[2]. All these error terms are added in quadrature to obtain the total 1σ absolute positional uncertainty R_σ that incorporates all contributions:

$$R_\sigma = \sqrt{(0.4085 \times P)^2 + (0.4085 \times 0.7)^2 + 0.16^2 + 0.08^2} \tag{5.2}$$

We show the distribution of the 95% percentile uncertainty (R_{95}) across the GBS sample in Figure 5.1. The median value of this distribution for all GBS sources is 2.8 arcesonds. Also, more than 90% of them have a positional uncertainty smaller than 5 arcseconds. Beyond that value, it is difficult to select the real counterpart to the X-ray position due to the high density of sources in that region (see Figure 5.1).

We now turn to compare the NIR matches found in 2MASS and GPS with the VVV matches, since the latter is the most complete survey out of the three in terms of coverage.

5.1.2 VVV vs 2MASS

When comparing the magnitudes of the closest matches within 5 arcseconds of the X-ray positions in 2MASS and VVV, we find a small magnitude range where both surveys are in agreement. The J and H-band magnitudes agree between $\sim$12 and $\sim$14, the K_s-band ones between $\sim$11.5 and $\sim$13. However, 2MASS is more reliable at the bright end, for magnitudes < 12 in J and H and < 11.5 in K_s, whereas VVV is more reliable in the case of fainter magnitudes. Therefore, in the case of bright

[1] http://cxc.harvard.edu/cal/ASPECT/celmon/ - Note that we consider the ACIS-S value since it is the best determined one, with most observations taken into account for its study. This is a spacecraft correction and should not depend on the instruments on board.

[2] http://apm49.ast.cam.ac.uk/surveys-projects/vista/technical/astrometric-properties

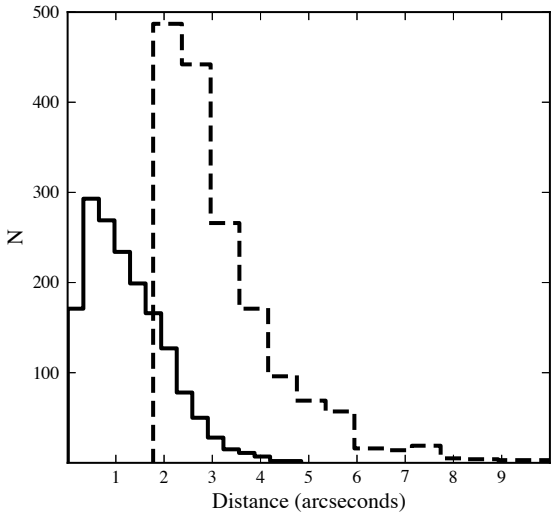

Figure 5.1: *Distribution of distances to the closest VVV matches within 5 arcseconds of the X-ray position (solid) and the 95% confidence positional X-ray uncertainty of each GBS source (dashed). It is clear that the positional uncertainity can become very large in some cases making it impossible to choose the correct NIR match from positional coincidence alone.*

Table 5.1: *Percentage of total number of GBS X-ray sources with possible counterparts found within a 5 arcseconds (upper section) radius and 2.8 arcseconds (lower section) of the X-ray positions, in 2MASS, UKIDSS GPS (DR8) and VVV*

Survey	Z	Y	J	H	K	$J, H\&K$
2MASS	-	-	74.7	74.7	74.7	74.7
UKIDSS GPS	-	-	34.9	35.2	63.8	31.5
VVV	98.1	98.7	99.3	99.5	99.5	99.2
2MASS	-	-	48.7	48.7	48.7	48.7
UKIDSS GPS	-	-	34.3	34.6	61.5	31.1
VVV	85.3	86.9	91.3	92.2	91.7	88.4

sources, we use 2MASS when their NIR magnitudes are available (see Table 5.1 for the fraction of sources with 2MASS data).

5.1.3 VVV vs UKIDSS GPS

Similarly to the work done with 2MASS, we compare the VVV matches of the GBS sources with those found in GPS. The magnitudes seem to agree in the ranges of ∼12 to ∼15 in all three bands (see Figure 5.2). Bright sources in both surveys do not agree due to saturation problems. On the fainter end, VVV becomes less reliable and therefore starts to deviate from UKIDSS. The scattered points seen between both surveys can be explained by several reasons: many sources in the intermediate magnitude range are probably blended objects or possibly variable sources. Variable sources will be followed up in detail in a future paper. The different pipelines, filter sets and photometric systems used can also contribute towards the offsets between both surveys (clearest in the K_s-band), indicated with the horizontal lines in Figure 5.2[3]. However, GPS is not yet complete and only contains matches to ∼35% of the X-ray sources in J, H and K, whereas VVV covers over ∼99% of the GBS fields.

As seen in Table 4.1 GPS goes deeper than VVV. In order to confirm this statement as well as the nominal depth given in Table 4.1 for VVV, we show in Figure 5.3 the distribution of the fraction of number of sources detected in GPS and VVV, as a function of K_s-band magnitude. For each GBS source that has both UKIDSS GPS and VVV coverage, we look for the number of GPS detections (N_{GPS}) and the number of VVV detections (N_{VVV}) within a given K_s-band magnitude bin. We then calculate $\Delta_N = N_{GPS}$ - N_{VVV}, for each source, and divide by N_{GPS}. Finally we take the mean value of all $\frac{\Delta_N}{N_{GPS}}$ in a given magnitude bin (shown in Figure 5.3). When the fraction is negative, this indicates that there are more VVV detections in the considered K_s-band magnitude bin. When $\Delta_N \sim 0$, both surveys are in agreement and when the fraction reaches 1, GPS dominates over VVV. We see that both surveys are on par until $K_s \sim 16$, where the VVV source catalogues become significantly incomplete, at least in the Galactic Bulge regions considered here.

Because we wish to have a consistent photometric system which covers a broad range of wavelengths and almost the entire solid angle of the GBS, we primarily use VVV for the search of the NIR counterparts to the X-ray sources in GBS, and use 2MASS in the case of bright matches. Our comparison shows that this gives us a secure picture of all viable counterparts down to K∼ 16. We also report on any UKIDSS GPS detections with K_s >16 (see Section 5.3.6). Note that the comparison between VVV and other NIR surveys was only possible in the JHK_s bands since those were the only filters in common with 2MASS and UKIDSS GPS.

[3]For more information on the photometric systems, see: http://apm49.ast.cam.ac.uk/surveys-projects/vista/technical/photometric-properties

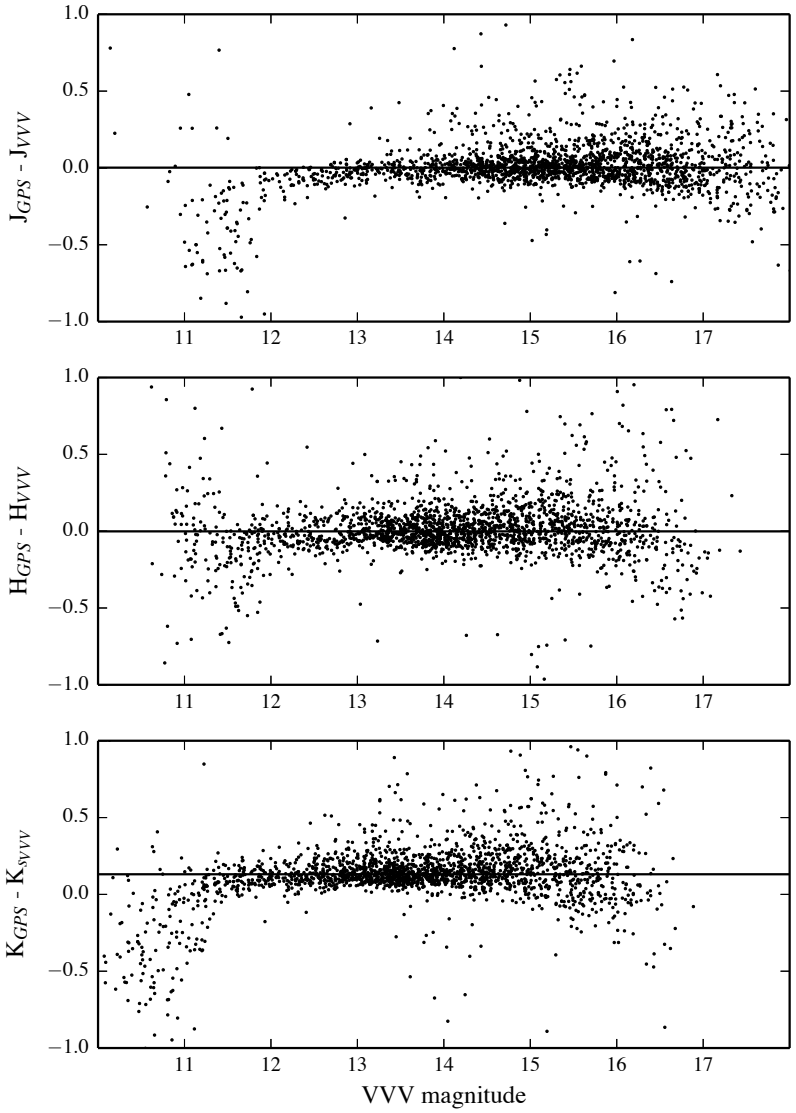

Figure 5.2: *Difference between the VVV and UKIDSS GPS magnitudes against magnitudes in J, H and K_s. The solid horizontal lines correspond to the median of the difference in magnitudes between both surveys.*

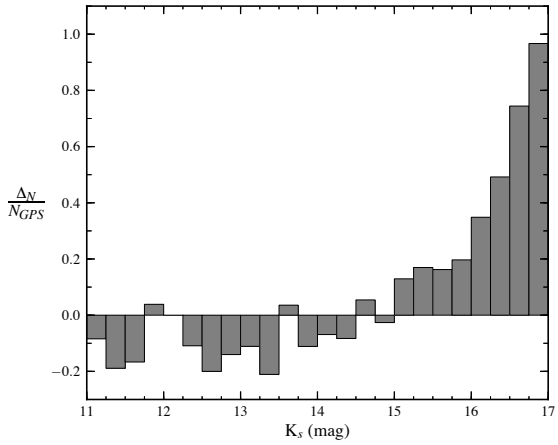

Figure 5.3: *Distribution of the fraction of detected sources UKIDSS GPS (N_{GPS}) and VVV (N_{VVV}) as a function of K_s magnitude. Δ_N corresponds to (N_{GPS} - N_{VVV}). From the increase towards 1 in the ratio towards fainter magnitudes, we conclude that the UKIDSS GPS limiting magnitude is fainter than that of VVV (see text for more details). We further conclude that crowding is not a limiting factor over the whole GBS area given that the median seeing of the GPS is 1 arcseconds (Lucas et al., 2008) whereas that of the VVV is 0.8 arcseconds.*

5.2 Extinction

Due to the large variations on small angular scales, low spatial resolution reddening maps (Schlegel et al., 1998) are not reliable in the Galactic Plane and Bulge region. We obtain the reddening values for all our GBS sources from Gonzalez et al. (2011)'s method which uses red clump (RC) giants to map the extinction towards the Bulge. They use the VVV data of the Bulge and take a 10' × 10' field, centered at (l = 1.14, b = -4.18) as their reference window (Baade's Window). It is an area close to the Galactic Centre which suffers from relatively low amounts of reddening. The extinction towards that field is $E(B-V) = 0.55$ mag (Gonzalez et al., 2011). The relation established to obtain the extinction values is:

$$E(B-V) = E(B-V)_{BW} - \frac{\Delta(J-K_s)_{RC}}{(0.87-0.35)} \tag{5.3}$$

where $E(B-V)_{BW}$ is the extinction towards the chosen Baade's Window, and $\Delta(J-K_s)_{RC}$ is the difference between the $(J-K_s)$ colour of the RC giants found in the field of unknown extinction and the $(J-K_s)$ colour of the RC giants in Baade's Window. The reddening values towards the GBS sources were calculated for a spatial resolution of 1.1' × 1.1' the lowest achievable with this method. The distribution of their values can be seen in Figure 4.1, where we plot the extinction in the K_s-band (A_{K_s}) of the sources in Galactic coordinates. As expected, the closer the sources are to the centre, the higher the extinction is. We also notice a region of the southern strip, with l < -1° which suffers from the highest reddening in the

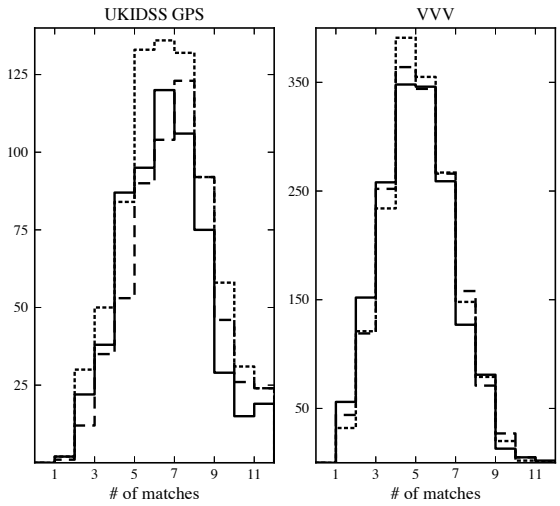

Figure 5.4: *Distribution of the number of matches found in UKIDSS GPS (left panel) and VVV (right panel) within 5 arcseconds of the X-ray position out of the total number of 1658 GBS X-ray sources. The solid line corresponds to the J-band, the dashed line to the H-band and the dotted line to the K-band. Note that the reason why the total number of sources (y-axis) in GPS is smaller than in VVV is due to the larger coverage in VVV.*

GBS region.

The typical $E(B-V)$ value towards the GBS fields is ~ 1.8, clearly indicating that the survey region suffers from high extinction. We note that the measured E(B-V) by Gonzalez et al. (2011) is integrated to the typical distance of RC stars. Therefore, for each GBS source, the returned $E(B-V)$ value can be lower or higher, depending on its distance.

5.3 Results

For 99.6% of the GBS sources, we now have NIR data from VVV in Z, Y, J, H and K_s. When data were available, we created a small catalogue with all the NIR objects found within 10 arcseconds of the X-ray position. Most sources returned over 10 neighbours, which clearly reflects on the multiple possible matches found for each X-ray source (see Figure 5.4-right). We also have an approximate reddening value for most GBS sources (see Figure 4.1), as well as their X-ray properties from Jonker et al. (2011). For each *Chandra* source, we created a postage stamp with five VVV finder charts (10 x 10 arcseconds^2), one in each filter, as well as three colour-colour diagrams: $(Z-Y,\ Y-J)$, $(Y-J,\ J-H)$ and $(J-H,\ H-K_s)$ (see Figure 5.5). We included $ZYJHK_s$ isochrones[4] in the VISTA photometric system (Vega-based system), in order to know where the un-reddened main-sequence stars lie. These colour-colour diagrams and postage stamps were used by us to identify possible

[4]The values were given by Stefano Rubele and Leo Girardi, members of the VVV team

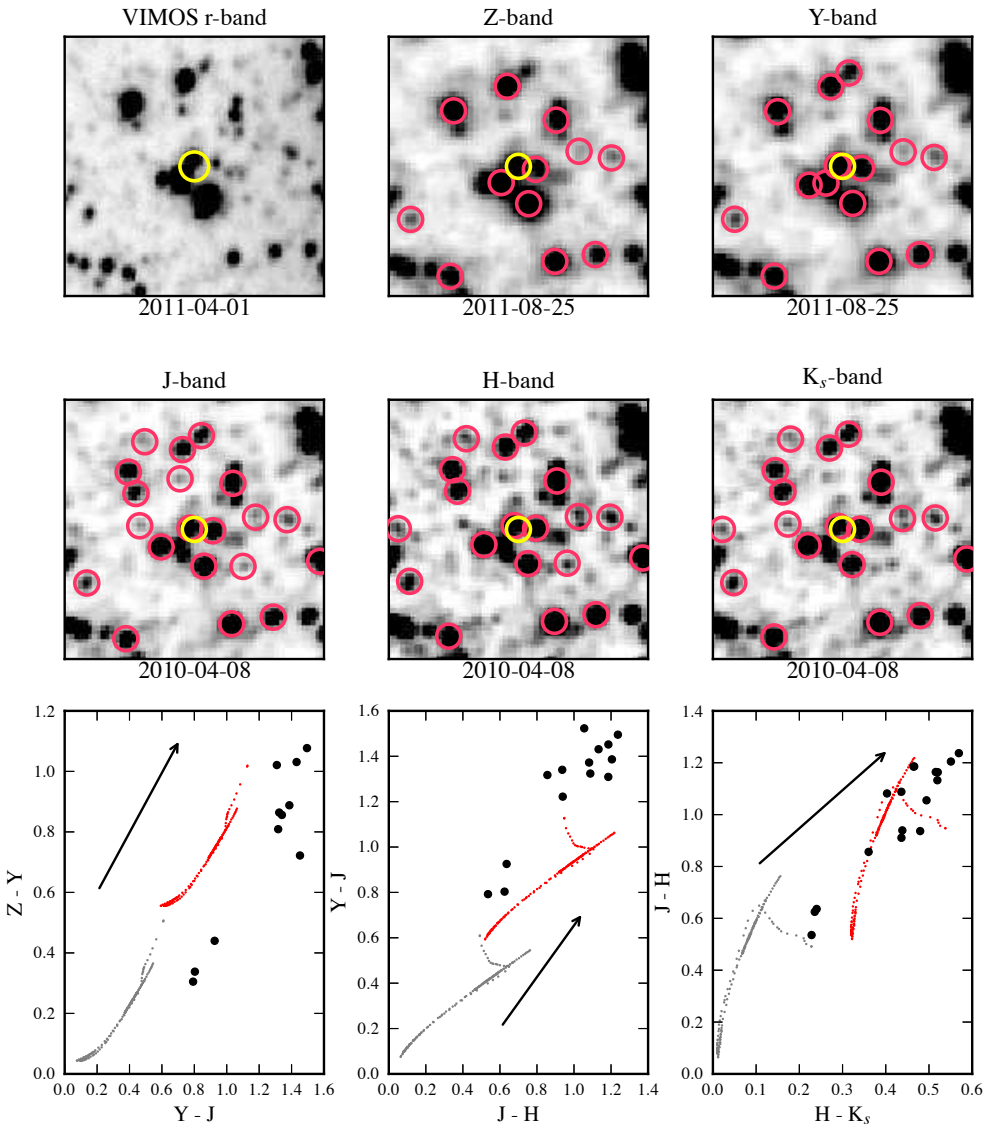

Figure 5.5: *Postage stamps of CX0377 (Wu et al. 2014, submitted), illustrating the high density of sources within 5 arcseconds of the X-ray position plotted in yellow. The red circles correspond to the VVV sources detected in each band separately. We also plot 3 colour-colour diagrams ($Z-Y$ vs $Y-J$, $Y-J$ vs $J-H$, $J-H$ vs $H-K_s$) with the VVV matches found in each case. We add reddened and unreddened synthetic tracks of main-sequence stars, in red and grey respectively, as well as a reddening vector (with E(B-V) = 1.53 in this case). The high number of possible matches is due to the very large qualitative uncertainties in the X-ray position. Many sources suffer from blending and they only become clearer in the K_s-band (the seeing gets better at longer wavelengths, but not necessarily the PSF). We also notice the non-detection of some objects in the given filters, despite their clear presence in the images. This is probably due to issues with the crowding and sky subtraction in the pipeline.*

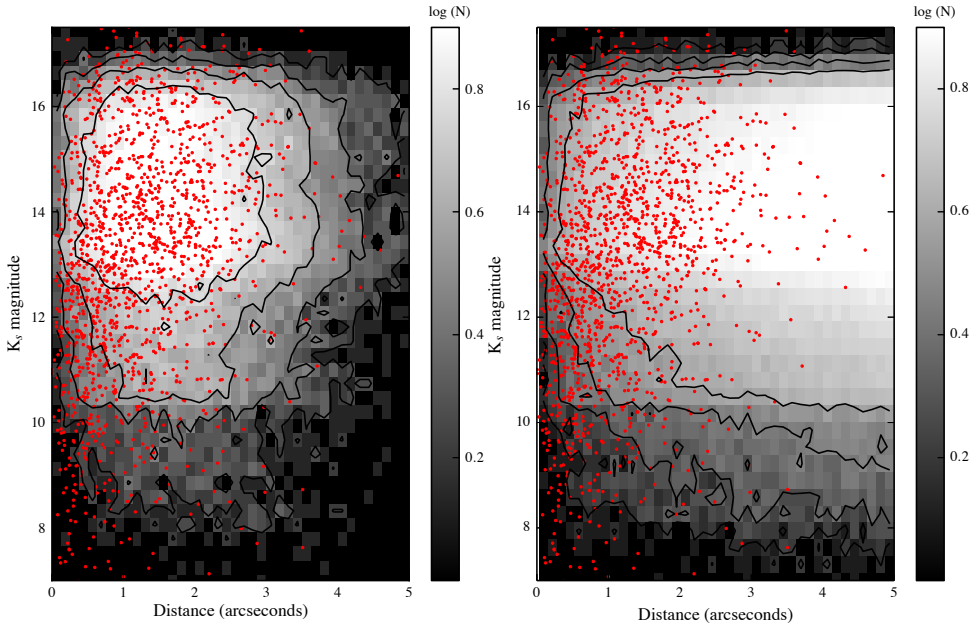

Figure 5.6: *Left: Density plot of the K_s-band magnitudes of the nearest VVV matches of $\sim$ 40 000 generated sources in the Bulge against their distances to the corresponding sources. The grey scale is a normalized logarithmic scale. The red dots correspond to the nearest VVV matches to the GBS sources. Sources brighter than 8^{th} magnitude are not included in this figure because they are the main focus of the study carried out by Hynes et al. (2012). Right: Same as left hand side but with all matches within 5 arcseconds of the random positions.*

targets for spectroscopic follow-up in order to classify likely counterpart candidates. More details on the spectroscopic component of the GBS is given in Torres et al. (2014). While these individual data sheets offer detailed insights into the specific environments around our X-ray sources, we now turn to a more robust statistical study of the counterpart candidates detected in the NIR in order to identify those that may be considered genuine NIR matches.

5.3.1 Quantifying the false alarm rate

The goal of this study is to quantify the false alarm rate when matching the GBS X-ray sources with NIR surveys of the Bulge given the large stellar densities. Not only do we take into account the positional uncertainties of each GBS source, we also calculate a statistical false alarm probability (FAP) based on the brightness of the NIR match as well as its distance from the X-ray position.

5.3.2 Random matching

In order to quantify the false alarm rate of our VVV matches, we generate a catalogue containing ∼40 000 random positions near the GBS source positions. In order to avoid duplicates, the sources in the generated catalogues are at least 10 arcseconds away from each other and fall in regions with $0.5^\circ < |b| < 3^\circ$ and $-3^\circ < l < 4^\circ$. We cross-match those random positions with the positions of stars detected in VVV and search for their nearest NIR counterparts. Such a random test preserves the specific environments our GBS sources are detected in, and also carries with it any source detection biases the survey may have. In this way it self-calibrates and is preferred over analytic estimates based on stellar densities. In the left-hand panel of Figure 5.6, we show a density map (in K_s vs distance) of the background field population of sources which could lead to false matches, and overplot in red dots the K_s-band magnitudes of each VVV closest match to the GBS sources against their separation from them. We notice that the counterparts of the GBS sources do not follow the same distribution as the generated sources, where the bulk of random sources fall within a defined region in the figure. This is an indication that in many cases (e.g. sources with $K_s < 12$), the VVV matches of the GBS are not random sources.

We repeat this study by cross-matching the random positions with VVV and select all the matches within a 5 arcseconds radius. Due to the much larger number of sources considered in this case, the density plot looks different to previously (see right-hand panel of Figure 5.6). This does not change our conclusion that in the case of sources brighter than 12^{th} magnitude, the VVV matches of the GBS sources are not random.

We continued quantifying the false alarm rate by using this density map to create a cumulative FAP map as a function of the source's K_s-band magnitude and distance to it (see Figure 5.7). This was done by binning in both distance and K_s-band directions and adding the number of sources found in each bin as we looped over our range of distances and magnitudes. The grey dots in Figure 5.7 correspond to the GBS counterparts. It is important to remember that objects fainter than K_s ∼16 were not detected reliably, even if there is evidence for those sources in the VVV images (see Section. 5.1.3). Therefore the FAP distribution in the region above the black horizontal line in Figure 5.7 is artifically low, due to the lack of detected sources. Only a handful of sources have matches fainter than $K_s \sim 16$, but in this regime we extrapolate our FAP distribution for the GPS counterparts. Note that this analysis can be done in any filter and we illustrate it here in the K_s-band since it has the best coverage and suffers from lower extinction and thus tends to have the highest source densities.The panels of Figure 5.7 come from the different cases considered in Figure 5.6.

With such a cumulative distribution at hand, we calculate the FAP ($FAP_{\rm random}$) for each GBS counterpart by interpolating across both source magnitude and separation to find the FAP value for that counterpart. Therefore, each NIR match within R_{95} of a GBS source will have an associated FAP, which depends on its magnitude

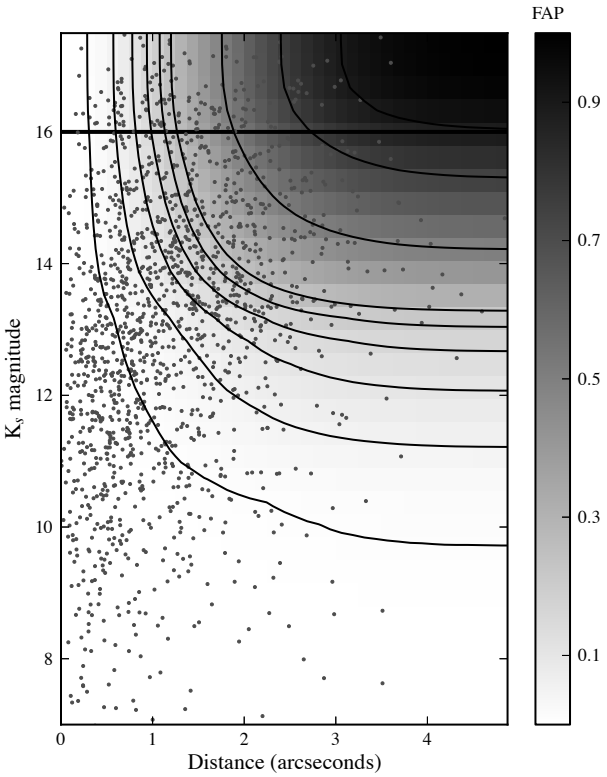

Figure 5.7: *Cummulative distribution of the FAP of having the real VVV match. The contours indicate false alarm probabilities at 0.01, 0.05, 0.1, 0.15, 0.25, 0.5, 0.75 and 0.9. The grey dots correspond to the nearest VVV counterparts of the GBS sources. The FAP distribution in the region above the black horizontal line is artifically low, due to the lack of detected sources.*

and distance to its NIR match and reflects the density of field sources near GBS sources.

5.3.3 Positional uncertainties

In order to determine the final FAP for each NIR counterpart to the GBS sources, we need to take into account the total positional uncertainties of each GBS source as these vary considerably from source to source (see Section 5.1.1). In each case, we calculate the cumulative density function (CDF) of the positional error, assuming it has a Rayleigh distribution:

$$\frac{1}{\sigma^2}\int_0^{R_\sigma} \mathrm{e}^{-\frac{r^2}{2\sigma^2}}\, r dr \tag{5.4}$$

with $\sigma = 1$, R_σ the 1σ positional error and $r = \frac{d}{R_\sigma}$, d = distance to NIR match. The FAP based on the position of the NIR match with regards to the positional uncertainty of each source is $FAP_{\mathrm{position}} = \mathrm{CDF(r)}$.

5.3.4 Total FAP

We assign a final FAP (FAP_{final}) to each matched source by taking into account the FAP calculated through the cross-matching of random sources in the GBS area with VVV and the FAP based on the positional uncertainties of the GBS sources: $FAP_{\mathrm{final}} = FAP_{\mathrm{position}} \times FAP_{\mathrm{random}}$. We calculate the final FAP for both cases considered in FAP_{random} and show them in Figure 5.8. We notice that for the closest matches to the GBS X-ray positions, both distributions are very similar. Since we published this study using the first case (i.e. random positions were matched with their nearest VVV detection) we choose to analyse our results for this case only. We find that $\sim$90% (1490 sources) of the GBS sources have a final FAP $< 10\%$ and $\sim$79% of them have a final FAP $< 3\%$. Even though 10% remains a high value in terms of false alarm probabilities, it nonetheless confirms that we are not dominated by false matches to field stars and that the NIR matches found for most of the GBS sources are genuine counterpart candidates. About $\sim$3% of the sources in the VVV NIR K_s band catalogue did not have a valid K_s-band magnitude within R_{95}, so they could not have a final FAP assigned to them.

5.3.5 Multiple matches

Our $FAP_{\mathrm{final}} = FAP_{\mathrm{position}} \times FAP_{\mathrm{random}}$ combines the fact that for larger source distances, FAP rates are higher due to field star contamination, but at the same time the probability that these are genuine matches is reduced. More than one match may be consistent with our GBS source position and the closest match is not necessarily the best match. In order to identify the most likely counterpart to the X-ray source (i.e. the match with the lowest FAP_{final}), we repeat the same process of calculating FAP_{position} and FAP_{random} for all the NIR matches within R_{95} of the total positional uncertainty of the source. We show in Figure 5.9 that typically, the

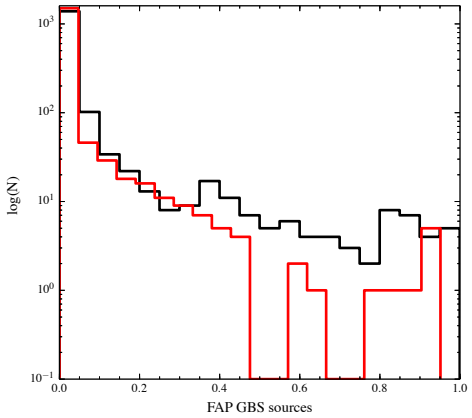

Figure 5.8: *Total FAP distribution of the GBS sources. Around 90% of the sources have a final FAP < 0.1 and ∼79% have FAP < 0.03. These values are for the case presented in black. The red distribution shows the final FAP for sources where* $FAP_{\rm random}$ *was calculated using all the matches in VVV within 5 arcseconds of the X-ray positions.*

GBS sources have 2 possible matches within R_{95}. This value comes from the median of the distribution shown in Figure 5.9.

In Figure 5.11, we show the $FAP_{\rm final}$ for the nearest VVV matches (panel *a*), as well as the second (panel *b*), third (panel *c*) and fourth (panel *d*) closest matches within R_{95}. We clearly see that the $FAP_{\rm final}$ increases as we move further away from the X-ray position. This indicates that the closest match has the most likely chance of being a real match, since the fourth closest VVV match has a typical $FAP_{\rm final}$ of 80%. In addition, the number of sources with a fourth match within R_{95} decreases. Even though it is clear that the closest match is most likely to be the one with the lowest $FAP_{\rm final}$, we found that in 50 cases, the second closest match had a lower $FAP_{\rm final}$ than the nearest one. This only represents ∼3% of the sources but it is important to note. In such cases, the distances between the closest and second closest matches are similar yet the second closest match is brighter than the nearest one, making it a statistically more likely real counterpart to the X-ray source. Another way to compare the $FAP_{\rm final}$ of the closest and second closest matches to the X-ray positions is shown in Figure 5.10. We clearly see what it most cases, the closest match has lower $FAP_{\rm final}$. The right-hand panel of Figure 5.10 shows that the second closest match has a significantly larger $FAP_{\rm final}$ the further away the source is from the X-ray position.

To illustrate this, we consider CX0013 as an example. In this case, we find 4 matches within its R_{95} (see Figure associated with Table 5.3). As we move further away from the X-ray position, the final FAP does increase dramatically making the closest match the preferred choice. However, upon inspection of the images, we notice a very faint object even closer to the X-ray position. This source is too faint to make it into the NIR source catalogues considered in this study. This is an important reminder that despite our analysis, we must always consider the possibility of even

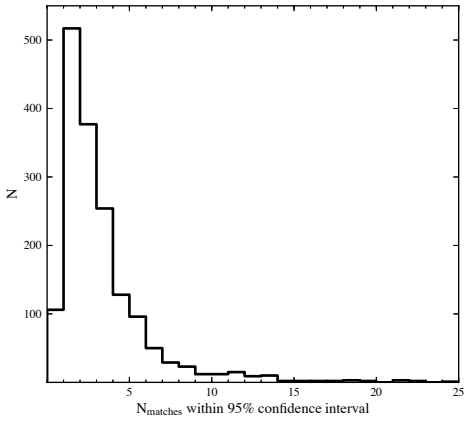

Figure 5.9: *Number of VVV matches found in a 95% confidence interval (R_{95}) from each X-ray source. The median value of this distribution is 2, meaning that each GBS source had typically 2 potential NIR matches in its R_{95} positional error radius.*

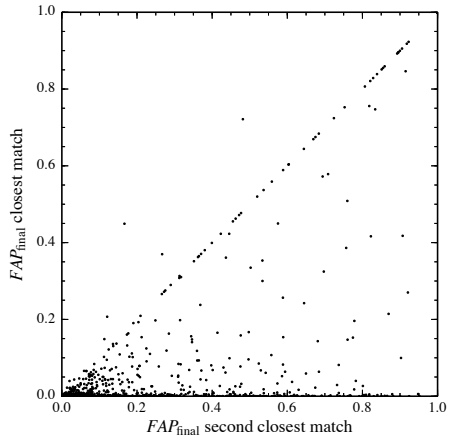

Figure 5.10: Comparing FAP of closest and second closest NIR matches to GBS X-ray positions.

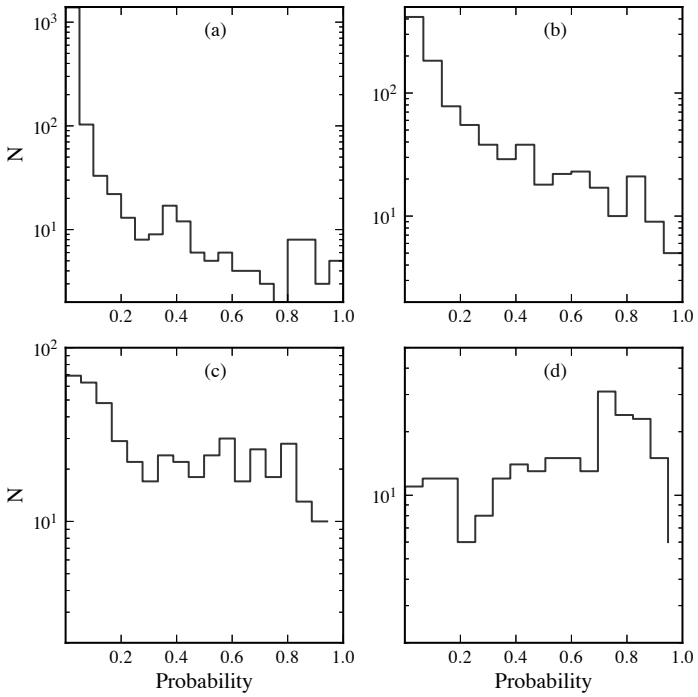

Figure 5.11: *$FAP_{\rm final}$ of four closest matches, within R_{95} of the X-ray position. Panels (a), (b), (c) and (d) correspond to the distributions of $FAP_{\rm final}$ of the closest, the second closest, the third closest and the fourth closest matches to the X-ray position. The total number of sources clearly drops as we move away from the X-ray position.*

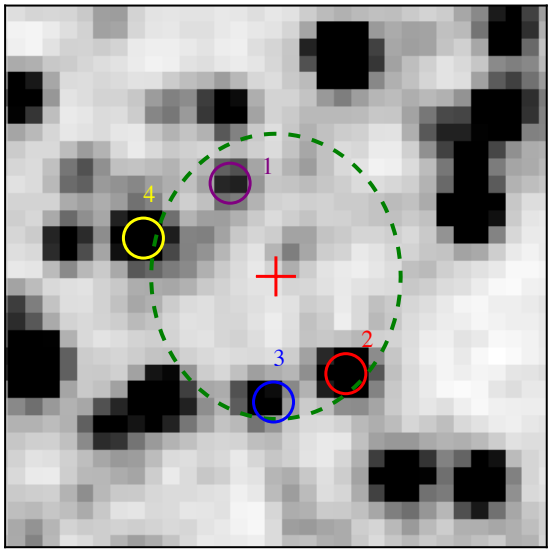

Table 5.2: *Positions of the 4 closest matches of CX0013 found within R_{95} in VVV. The red cross indicates the X-ray position and the large dashed green circle indicates the R_{95} boundary of 2.84 arcseconds in this case. The table below provides information on their magnitudes and false alarm probabilities.*

Source	Distance	K_s	$FAP_{\rm final}$
1	2.07	15.60	0.069
2	2.40	14.36	0.138
3	2.50	15.38	0.188
4	2.75	14.02	0.349

Table 5.3: *Four closest VVV matches to CX0013.*

fainter sources not detected in VVV. Our source table identifies the most likely counterpart among the *detected* sources in VVV, 2MASS and UKIDSS GPS.

5.3.6 Final table

To assist the characterization of the GBS source population, we provide in Table 5.4 the NIR positions, magnitudes and calculated K_s-band FAP$_{final}$ for detected sources within R_{95} of the GBS X-ray positions. Such a Table presents a useful resource to anyone interested in studying the GBS sources, in particular at longer wavelengths and can be downloaded through the following link:
http://mnras.oxfordjournals.org/content/438/4/2839/suppl/DC1.
Here we only show the results for the first 30 brightest sources as an example of the full table, which contains 4 661 entries.

Table 5.4: *Table containing all NIR data and FAP of matches within* R_{95}

CX ID	RA GBS	Dec GBS	RA NIR	Dec NIR	Offset	J mag	σ_J	H mag	σ_H	K mag	σ_K	Survey	$FAP_{\rm final}$	Comments
1	17 50 24.44	-29 02 16.4	17 50 24.55	-29 02 15.6	1.793	15.908	0.027	13.284	0.028	12.374	0.033	2MASS	3.161e-02	-
2	17 37 28.39	-29 08 02.0	17 37 28.39	-29 08 02.1	0.034	13.633	0.056	12.257	0.054	11.187	0.059	2MASS	2.851e-09	(a)
3	17 40 42.81	-28 18 08.0	17 40 42.96	-28 18 11.5	3.998	9.075	0.214	7.598	0.212	6.947	0.254	2MASS	2.176e-02	-
4	17 39 31.22	-29 09 52.8	17 39 31.22	-29 09 53.3	0.515	7.209	0.001	6.566	0.003	6.384	0.004	2MASS	1.369e-08	(b)
5	17 40 09.13	-28 47 25.6	17 40 09.21	-28 47 25.9	0.977	15.459	0.047	14.451	0.018	13.858	0.02	VVV	1.759e-03	(c)
6	17 44 45.78	-27 13 44.5	17 44 45.77	-27 13 44.4	0.112	7.054	0.057	6.843	0.051	6.507	0.055	2MASS	8.455e-11	(b)
6	17 44 45.78	-27 13 44.5	17 44 45.85	-27 13 45.0	1.109	-	-	-	-	10.501	0.002	VVV	1.548e-03	-
6	17 44 45.78	-27 13 44.5	17 44 45.70	-27 13 45.1	1.302	10.927	0.001	-	-	10.46	0.002	VVV	3.104e-03	-
7	17 38 26.18	-29 01 49.4	17 38 26.21	-29 01 49.5	0.323	9.388	0.006	8.916	0.011	8.823	0.017	2MASS	6.359e-09	(b)
8	17 35 08.28	-29 29 57.9	17 35 08.24	-29 29 58.2	0.556	-	-	-	-	10.665	0.002	VVV	7.200e-06	-
9	17 35 08.40	-29 23 28.4	17 35 08.42	-29 23 28.3	0.169	10.162	0.006	9.828	-	9.659	0.006	2MASS	4.857e-09	(b)
10	17 36 29.04	-29 10 28.8	17 36 29.06	-29 10 29.1	0.470	7.967	0.019	7.464	0.021	7.264	0.025	2MASS	3.453e-07	(b)
11	17 41 51.30	-27 02 23.5	17 41 51.42	-27 02 23.8	1.705	15.146	0.014	14.04	0.012	13.505	0.013	VVV	1.957e-02	-
12	17 43 47.24	-31 40 25.2	17 43 47.26	-31 40 25.2	0.411	6.998	0.001	6.364	0.001	6.165	0.001	2MASS	3.020e-08	(b)
13	17 50 29.13	-29 00 02.3	17 50 29.20	-29 00 00.5	2.066	-	-	-	-	15.599	-	VVV	6.935e-02	-
13	17 50 29.13	-29 00 02.3	17 50 29.03	-29 00 04.3	2.402	16.587	0.11	14.92	0.076	14.363	0.074	VVV	1.380e-01	-
13	17 50 29.13	-29 00 02.3	17 50 29.14	-29 00 04.8	2.500	17.253	0.194	-	-	15.376	0.179	VVV	1.880e-01	-
13	17 50 29.13	-29 00 02.3	17 50 29.33	-29 00 01.6	2.745	16.203	0.078	14.58	0.056	14.02	0.055	VVV	3.349e-01	-
14	17 46 23.67	-31 35 00.8	17 46 23.69	-31 35 00.6	0.191	9.962	0.33	9.262	-	9.119	-	2MASS	1.355e-09	-
15	17 46 46.17	-25 52 17.5	17 46 46.25	-25 52 17.5	0.948	16.198	0.23	15.571	0.409	15.392	-	VVV	1.381e-03	-
16	17 55 45.83	-27 58 14.0	17 55 45.84	-27 58 13.8	0.288	12.908	-	12.104	-	11.72	0.499	2MASS	3.330e-07	-
16	17 55 45.83	-27 58 14.0	17 55 45.84	-27 58 15.8	1.843	15.269	0.017	-	-	14.036	0.036	VVV	4.314e-02	-
17	17 52 53.02	-29 22 09.1	17 52 52.96	-29 22 08.0	1.383	-	-	13.778	-	13.538	-	VVV	7.763e-03	-
17	17 52 53.02	-29 22 09.1	17 52 53.14	-29 22 09.4	1.631	12.437	0.036	11.27	0.031	10.893	0.069	2MASS	1.124e-02	-
18	17 39 35.77	-27 29 35.9	17 39 35.76	-27 29 36.0	0.142	15.702	0.001	14.93	0.001	14.601	0.001	VVV	2.422e-08	(c)
19	17 49 54.57	-29 43 35.4	17 49 54.53	-29 43 35.8	0.745	11.989	-	10.432	-	9.93	0.046	2MASS	5.201e-05	-
20	17 38 59.68	-28 24 49.1	17 38 59.66	-28 24 49.5	0.407	15.768	0.018	15.117	0.015	14.636	0.016	VVV	7.970e-06	-
21	17 41 33.76	-28 40 33.8	17 41 33.79	-28 40 34.5	0.890	17.284	0.093	16.849	0.055	16.447	0.058	UKIDSS	8.253e-04	-

(a) Maccarone et al. (2012), (b) Hynes et al. (2012), (c) Britt et al. (2013), (d) Ratti et al. (2013)

5.3.7 Influence of the hardness of the X-ray sources

Since for most GBS sources, only a few counts are detected across the full 0.3 to 8 keV energy band, we have hardness ratios only for the 164 brightest X-ray sources in GBS. For the remaining GBS objects, we can consider the energy range over which the sources were detected. Therefore they can be given, when available, a hardness classification: *soft* X-ray sources are detected in the 0.3 to 2.5 keV band, while *hard* X-ray sources are detected solely in the 2.5 to 8 keV band.

We find that 327 sources are detected in the *soft* band, 444 are *hard* and the rest do not have a classification. In order to see if there is a correlation between the hardness of the X-ray sources, their NIR colours and the reddening towards the GBS fields, we plot a ($J - K_s$, K_s) colour-magnitude diagram of the closest VVV matches to the GBS sources (see Figure 5.12). These sources are then colour-coded according to the X-ray hardness of the X-ray source, where red and green crosses correspond to *hard* and *soft* sources respectively. We also add a reddening vector with E(B-V) = 1.8, since it corresponds to the typical extinction value towards the GBS region. Looking at the colour-magnitude diagram, we notice that *soft* sources are less affected by reddening than hard X-ray sources. This is an indication that the *soft* X-ray sources are more likely to be foreground objects whereas *hard* X-ray sources are probably reddened sources lying behind significant layers of extinction. In fact, *hard* X-ray sources are intrinsically blue. Also most *soft* sources seem to have bright NIR matches, making them foreground sources and most probably the real matches. In order to confirm this result, we look at the $FAP_{\rm final}$ values of the *soft* and *hard* sources. We find that 90% of the *soft* sources have a $FAP_{\rm final} < 3\%$, whereas this is the case for only 68% of the *hard* sources. This indicates that we have probably found the real (foreground) NIR counterparts to the *soft* GBS sources.

5.4 Near-infrared photometry discussion

The combination of the NIR colours with the hardness of X-ray sources can provide additional information on the nature of the object beyond its proximity to the X-ray source. However, given the FAP for even the best matches, additional data is desirable. Indeed an optical component is a key part of the GBS strategy. This consists of optical imaging as well as spectroscopy. Here we briefly compare the NIR colour of some confirmed Hα emission line objects.

5.4.1 NIR colours of Hα emission line objects

In Figure 5.12, we show in pink squares some of the confirmed Hα emission line sources in the GBS catalogue such as AGN, single M-stars and RS CVn systems. Also, Torres et al. (2014) have obtained spectra for several GBS sources and 23 objects show Hα emission in their spectra, as well as accretion signatures. These types of X-ray binaries are our principle science targets and are plotted in yellow squares. As can be seen, many Hα emission line objects fall in the region populated

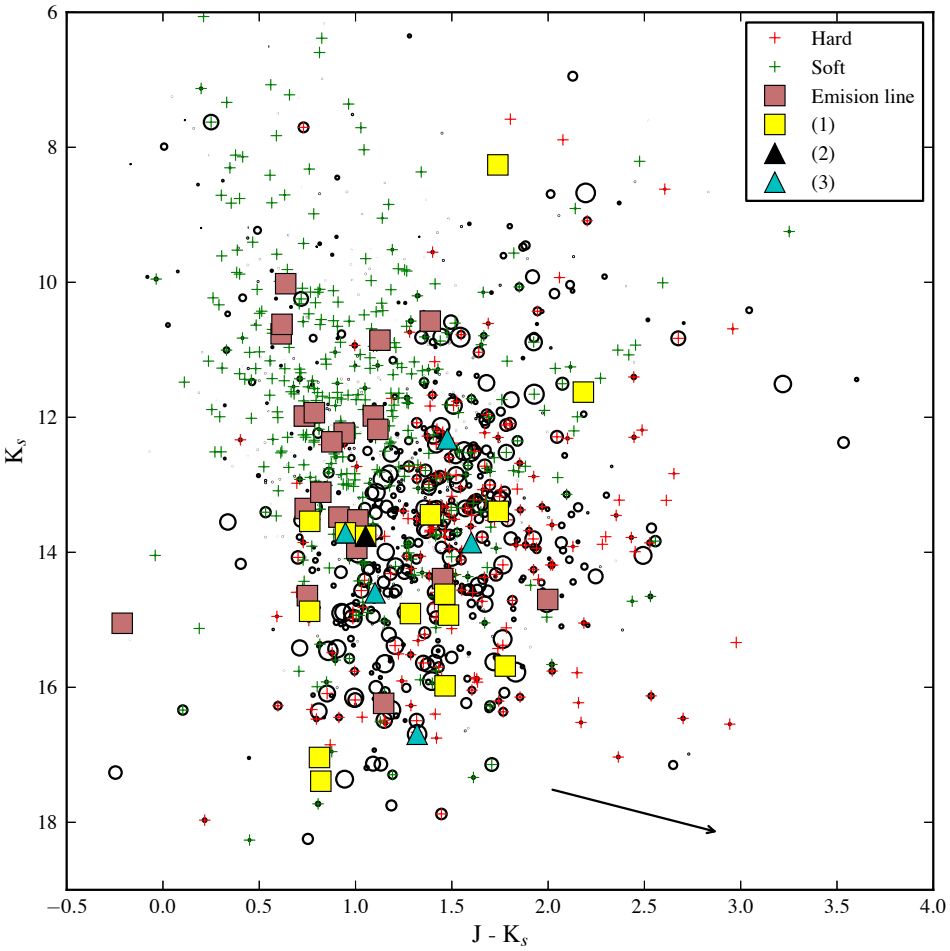

Figure 5.12: *(K_s) vs ($J - K_s$) colour-magnitude diagram of the VVV matches with $FAP_{\rm final} < 0.1$. The size of the circle is proportionate to the value of the $FAP_{\rm final}$ of the source. The larger the circle, the bigger the $FAP_{\rm final}$. The red and green crosses correspond to the hard and soft X-ray sources respectively. The pink squares are Hα emission line sources (AGN, M-stars, RS CVns) and the yellow squares are accreting binaries (Torres et al., 2014), all confirmed via spectroscopy. The black triangle corresponds to CX0093, a CV confirmed by Ratti et al. (2013) and the cyan triangles correspond to the CVs studied in Britt et al. (2013). The black arrow indicates the reddening for an extinction value of E(B - V) = 1.8.*

by the soft X-ray sources, possibly indicating that they are not Bulge sources. We also notice that most X-ray binary systems occupy the same region as the hard X-ray sources. However, they do not occupy a very distinct region of the diagram, making the source classification difficult when using NIR colours alone. The black triangle corresponds to CX0093 (also known as CX0153), a CV studied by Ratti et al. (2013), and the cyan triangles are the CVs published by Britt et al. (2013).

5.4.2 Towards the identification of key GBS source classes

Despite the various studies of Galactic Centre X-ray sources using NIR photometry and spectroscopy, classifying objects on the basis of their colours alone is difficult. The Galactic Centre and Bulge suffer from different amounts of extinction, which in itself varies on very small scales, greatly altering the colours. Therefore, strategies driven by a source's position in a colour-colour or colour-magnitude diagram, cannot be directly employed in these environments even though such methods are highly effective at high Galactic latitudes.

In addition to the effects of reddening, the intrinsic colours of the sources expected in the GBS show great diversity. The key source types include LMXBs, CVs, UCXBs, RS CVn stars, W UMa and Be X-ray binaries. In the case of quiescent LMXBs, one may expect the companion stars to dominate the SED in the NIR. As these are typically late-type dwarfs, such objects may have colours very similar to reddened field dwarfs. Comparison with theoretical colours of main-sequence and giant stars, as well as the correct reddening (and distance) towards the line of sight of the X-ray source, can then help with the identification of potential NIR counterparts to the GBS sources. However, the presence of accretion continuum sources such as from accretion discs and jets will alter the colours. This diversity even among one subclass of, for example LMXBs, means that the NIR colours need complimentary constraints from other wavelength studies for a reliable classification of sources.

Previous work suggests that the NIR colours of CVs are similar to F-K main-sequence stars (Hoard et al., 2002). Since most CVs are foreground objects, they do not suffer from the same amount of reddening as potential Bulge LMXBs. Note that this does not mean that their donor stars have spectral types of F-K as also in CVs accretion components will contribute. Knigge et al. (2011) also found that NIR colours of CVs were dominated by the donor star, except for systems close to the period minimum where contributions from the WD were beginning to be more significant. Indeed, the majority of these systems have optical spectra dominated by the WD (Gänsicke et al., 2009). Given their very low mass donors, the NIR colours of such systems thus no longer track a simple donor star sequence. It is also important to note that $\sim 20\%$ of CVs contain a magnetic WD (polars or intermediate polars). It has been found that they contribute towards a large fraction of the hard X-ray sources in the Galactic Centre (Muno et al., 2004; Hong, 2012; Britt et al., 2013) since their X-ray luminosities are significantly higher than those of non-magnetic CVs. Luminosity ratios such as L_{opt}/L_X can often be used as a crude discriminant between some of these source classes that otherwise may have similar NIR colours.

Due to the fact that the GBS is a shallow survey, with 2ks exposures, most detected sources have typically less than ten X-ray counts, leading to very poorly constrained X-ray fluxes. Another contribution to the large uncertainty of the X-ray flux, F_X, comes from the fact that the reddening towards the GBS X-ray sources is unknown. The VVV extinction maps yield a maximum limit to A_{Ks}, making it difficult to determine the actual X-ray flux of our sources. For this reason, we are unable to calculate reliable F_X/F_{NIR} in order to identify key GBS source classes.

RS CVn stars, a type of close detached binary stars, are known to be variable due to cool stellar spots present on the surfaces. A good way to select them is by exploiting the NIR variability information which is now available in VVV and which we present in the following Section of this Chapter.

The work presented here allows us to prioritize those proposed counterparts with lowest $FAP_{\rm final}$ for spectroscopic or photometric follow-up and also assess the impact of false matches. The false alarm probability study is most reliable in the near-infrared (mainly in the K_s-band) since we can probe through the dust and detect more Bulge sources. With the final table presented in this study, which contains the most likely NIR counterparts to the GBS X-ray sources, we are now able to move on to the next stage of the GBS strategy, which is to use optical photometric and variability data to select the objects for spectroscopic follow-up. This has been demonstrated with the results found by Torres et al. (2014), where key GBS source classes have been identified via spectroscopy. The addition of optical data will enable us to disentangle the effects of reddening towards the GBS fields and separate the field CVs from the Bulge LMXBs. The NIR variability information discussed next and provided via VVV in the K_s-band will also help us in selecting those viable counterparts that show evidence for variability, as would be expected for the majority of our objects. True secure classification, however, is best achieved through spectroscopy (Britt et al. 2013; Ratti et al. 2013; Torres et al. 2014, Wu et al. 2014 submitted). In fact, the spectroscopic results of GBS sources have found a total of 45 accreting X-ray sources, most of which are CVs. In some cases, it has not been possible to determine the nature of the compact sources and more spectroscopic data are required in order to estimate the mass of the accreting object. This remains an ongoing effort within the GBS collaboration. My main contribution to the spectroscopy studies was the selection of targets on the basis of NIR data. I was also able to go on an observing run at the Southern Astrophysical Research Telescope (SOAR) in Cerro Pachón, Chile.

5.5 VVV Variability

As mentioned in the previous Section, the VVV survey has a K_s-band variability component to the project, which aims to cover the entire survey region. Unfortunately, the observing strategy is not fixed and the fields are not observed on a regular cadence. Nevertheless, many fields in the Galactic Bulge have repeat coverage over the span of two years, making it possible to search for and identify variable sources. Here we describe our method used to select variable sources from the VVV data and provide examples of light curves. The key GBS sources are LMXBs, which should

show variability in their light curves, either through outbursts due to instabilities in their accretion discs, or through orbital period modulations. For this reason, additional variability information will help us prioritise LMXB or CV candidates for additional follow-up, by assuming that non-variable sources are more likely to be foreground contaminants.

We calculated the available K_s magnitudes of all the sources in our final NIR catalogue described in the previous section. In order to generate an automated search for variability in the VVV light curves, we do a χ^2 statistical test against a non-variable model (in our case the median value of the data is taken as the constant magnitude of the source). We calculate the χ^2 for each light curve using the following equation:

$$\chi^2 = \frac{1}{N} \sum_{i=1}^{N} \left(\frac{X_i - \mu}{\sigma_i} \right)^2 \tag{5.5}$$

where X_i and σ_i correspond to the K_s magnitude and error of the source from a given exposure, μ is the median of all the K_s magnitudes of a light curve.

Since the observations of the variability survey are randomly chosen, we set criteria to select the most *reliable* variable sources in our sample. For each calculated χ^2, we can associate a probability based on a statistical significance test using the CDF of the χ^2 distribution as a function of the correct number of degrees of freedom which differs from source to source. The final probability which decides on the significance of the deviation from a neutral hypothesis (in our case this corresponds to the hypothesis that the source is constant) is known as the p-value and corresponds to 1 - CDF. A low p-value in this case would indicate that the source is variable, whereas a constant source would have a large p-value. In most statistical studies, a p-value > 0.1 cannot give any information on the deviation from the neutral hypothesis. In fact, a p-value of 0.1 corresponds to a 90% confidence interval, which is equivalent to 1.64σ.

In our search for variable sources in the VVV data, we excluded sources with K_s <11.5 in order to avoid any unreliable data from saturated objects, as well as those with $\chi^2 < 1$. Out of the 4 661 sources from our NIR catalogue, 1504 pass these criteria. It is important to note that these do not correspond to 1504 unique GBS counterparts. In fact, out of these 1504 objects 939 have unique GBS IDs, meaning that some GBS sources have more than one variable counterpart candidate.

For each source, we plotted the VVV light curve, along with a finder chart (see Figure 5.13). In Figure 5.14, we show the distribution of the p-value probability associated with the calculated χ^2. We see that most sources have a p-value > 0.1, making the VVV variability study of limited value. We set a limit to select variable sources on the basis of a p-value < 0.1, leading to 249 candidates out of 1504. We find that the sources with p-values < 0.1 have a $\chi^2 > 5$ (see panel (d) of Figure 5.14). A natural instinct would be to set the variability threshold at sources with a $\chi^2 > 5$ but it is not as straightforward since the p-value depends on the number of degrees of freedom, as well as the associated χ^2.

We visually classified each of the 1504 produced light curves in order to have a clearer idea of the quality of the VVV data. In many cases, bright nearby

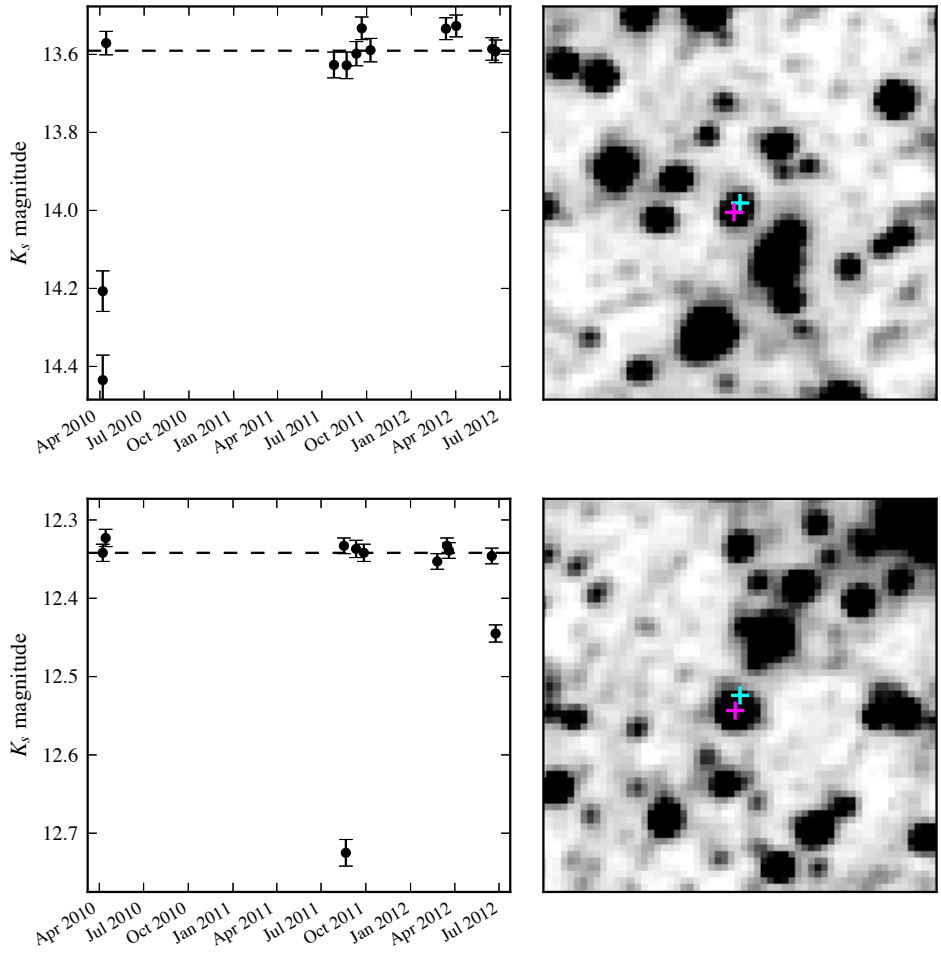

Figure 5.13: *Top panels: VVV K_s-band light curve and finder chart of CX1177. This source has a χ^2 = 30.070 and a p-value = 0.002. Bottom panels: VVV K_s-band light curve and finder chart of CX1074. This source has a χ^2 = 60.152 and a p-value = 0. This makes these two objects very interesting for follow-up. The cyan crosses indicate the Chandra X-ray positions, whereas the magenta crosses point at the centre of the NIR counterpart.*

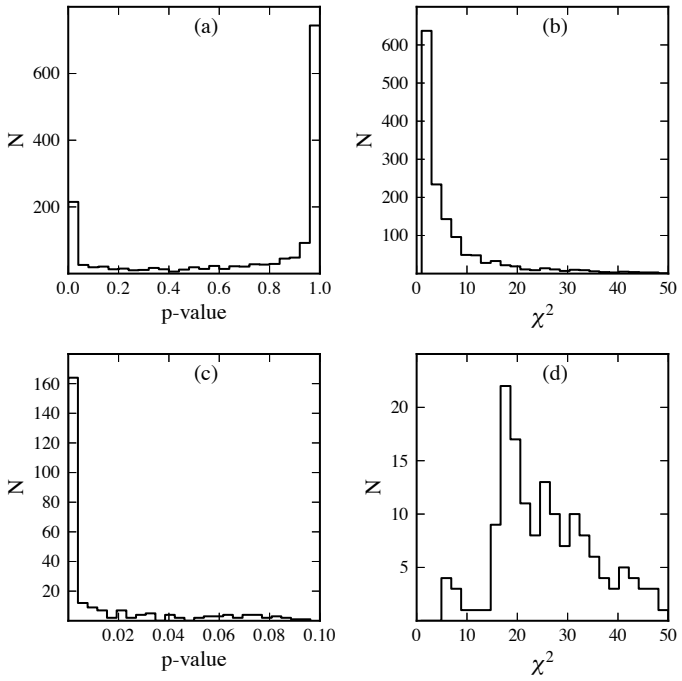

Figure 5.14: *(a): P-value of all sources with VVV variability data. (b): χ^2 of all sources with VVV variability data. (c): P-value of all sources within the range of 0 to 0.1. (d): χ^2 of all sources with p-value < 0.1.*

sources affected the photometry of neighbouring sources, leading to their spuriously high χ^2 values. These would normally have been classified as *variable* under all the previously mentioned criteria. The sources affected by blending or unreliable photometry were classified as *non-statistically significant variables*. In order to have a clearer view of the VVV variability study, we provide a few numbers from our results:

- 1504 sources have VVV variability data and fall under the following criteria: $\chi^2 > 1$ and $K_s > 11.5$
- 249 (16.6%) of these 1504 have a p-value < 0.1 and $\chi^2 > 5$.
- 104 of these 249 sources are visually confirmed and classified as *variable*.

Our following step was to analyse the variable sources which also had a FAP < 0.1 as determined previously. In total, out of the 1504 sources, we find 816 (54.3%) of them have a FAP < 0.1. Out of these, only 167 have a p-value < 0.1. The next natural stage would be to obtain spectra of these objects in order to identify them. Classifying them as variable sources using NIR data makes them somewhat more peculiar and interesting to follow-up. We intend to propose for such spectroscopic observations in order to identify these selected sources.

Also, we identify a case where the source is variable in both the VVV and optical data, but it is not the source with the lowest associated FAP_{final}: CX0750 (Figure 5.15). The main reason why it has a large FAP_{final} (~ 0.6) is because it is 6.7 arcseconds away from the *Chandra* X-ray position. This shows that the source with the lowest FAP_{final} is not always necessarily the one with the most interesting features. This source seems to be a candidate eclipsing quiescent LMXB or CV, based on its optical variability data (see Section 5.7; Britt et al. 2014). Therefore, one must keep an open mind when exploiting all the available data around the X-ray positions and not restrict the study to the nearest counterpart detected.

5.6 Mosaic optical data

In the early days of the GBS project, we obtained optical data of the survey area using the Mosaic CCD camera on the 4-metre Blanco telescope located at the Cerro Tololo Inter-American Observatory (Jonker et al., 2011). The filters we used for our observations were r, i and a narrow-band Hα one. Our final products are band-merged catalogues down to $r \sim$23, reduced at CASU. Due to the lack of standard stars in the Hα band, we have had to set a fixed offset between the r and Hα-band ZPs, on the basis of their filter profiles.

We begin by searching for all the optical counterparts within R_{95} of the X-ray positions, in the same manner as we did for the NIR study. In total, we find 3 952 sources. This is less than the total number of NIR matches detected within the same radii (4 661), but we will show later that these are not of less value or importance. In fact, when cross-matching both the optical and NIR catalogues, we only find 2 774 objects in common. This means that there are many sources detected in the

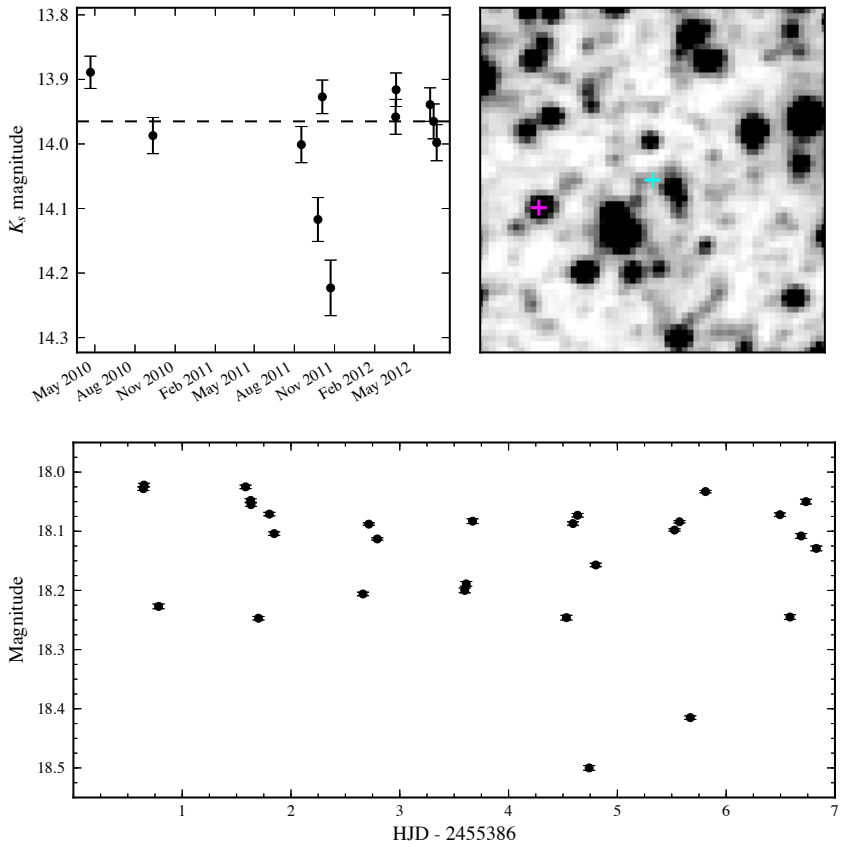

Figure 5.15: *Top panels: VVV K_s-band light curve and finder chart of CX0750. This source has a $\chi^2 = 7.564$ and a p-value = 0.671. Despite its high FAP and high p-value, we clearly see from its K_s-band light curve that it is variable. Bottom panel: Optical MOSAIC-II light of CX0750 which also shows its variable nature. The cyan cross indicates the X-ray position, and the magenta cross indicates the NIR variable source considered here.*

optical bands that are not found in the NIR surveys, and vice versa. This is a clear manifestation of the reddening towards the Bulge, as optical sources without NIR data correspond to foreground objects whereas NIR sources with no optical data are often very reddened objects. Each catalogue brings valuable information on the possible counterparts to the GBS X-ray sources, making them useful in their own way.

With the r and Hα photometry at hand, we can select Hα emission line sources using the $(r, r - \mathrm{H}\alpha)$ colour-magnitude diagram of all sources shown in Figure 5.16. The black open circles correspond to objects with a $\mathrm{FAP}_{final} < 0.1$, with the sizes of the circles indicating the value of the associated FAP_{final} of the sources. We fitted the main locus of stars (the main-sequence) with a straight line, shown in black, and selected all the Hα emission line sources as objects that fell above 5σ of the fitted line. This limit is plotted in a yellow line. The pink circles correspond to the 161 Hα emitters we have found in the optical catalogue. When matching these sources with our final NIR table, we only find 66 objects in common. For this reason, we choose to select Hα emission line objects on the basis of their optical photometry only. When available, we appreciate any additional information but we do not limit our search to sources with both optical and NIR photometry. In order to confirm our selection of Hα emission line sources, we look for those which have optical spectra and find that Torres et al. (2014) present the spectra of CX0128 and CX0794, which also fall in our list of selected sources. We show their optical spectra in Figure 5.17 and clearly see the very strong Hα emission lines in both cases. These systems have their spectra dominated by the accretion disk and explains why they can also be easily selected on the basis of their optical photometry.

In order to assess the effects of reddening, we plot the $(r, r - K_s)$ colour-magnitude diagram (Figures 5.18). In black open circles we show the colours and magnitudes of all the sources with low FAPs (< 0.1). We overplot Hα emission line objects (in pink squares), as well as variables sources from the VVV survey (with a p-value < 0.1). We notice that all the Hα emission line sources are reddened. The VVV variable sources with $r < 15$ are probably foreground active stars or CVs. A reddening vector is also plotted for the typical extinction towards the GBS fields (E(B - V) = 1.8). We clearly see that the bulk of the sources in the colour-magnitude diagram are reddened, as they are separated from the foreground objects. Also, the brightest and less reddened sources are those with the lowest FAPs.

It is important to note that this optical survey was specifically designed for the GBS project, unlike the NIR surveys we exploited. Had the VVV photometry gone deeper, we would have probably been able to detect more sources in common (since the optical data goes down to $r \sim 23$). It is not obvious whether an even deeper optical survey would be more valuable than a deeper NIR one. Due to the large amount of extinction, it may seem more natural to require deeper NIR images of the GBS fields since the ultimate goal of the GBS is to find and study LMXBs in the Galactic Bulge. An optical survey would inevitably be biased towards foreground sources.

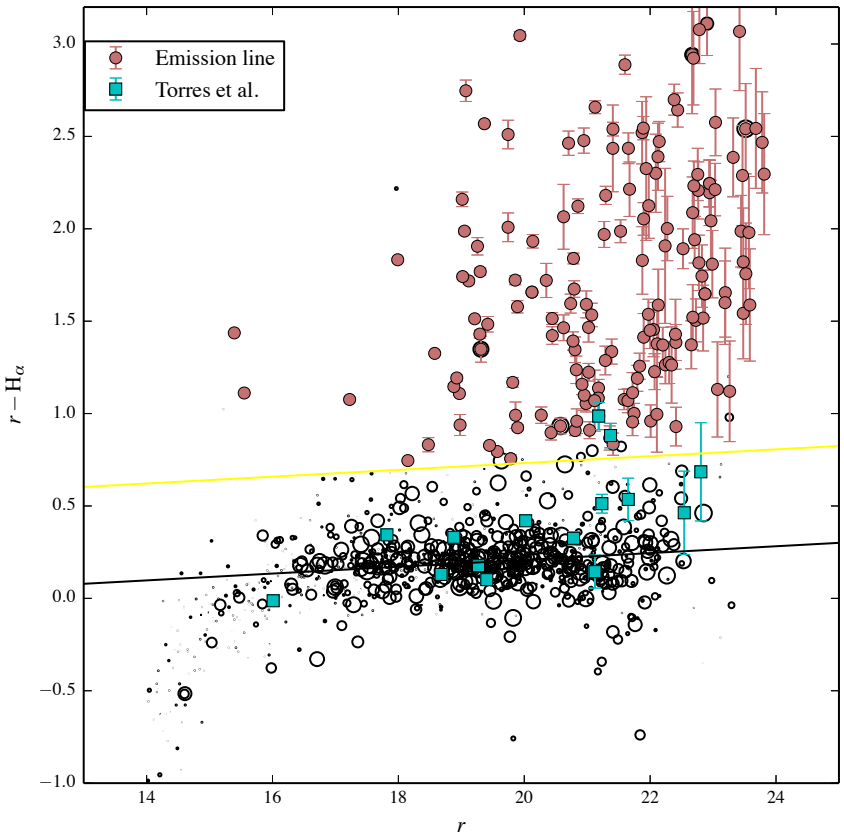

Figure 5.16: *Colour-magnitude diagram of sources with* $FAP_{\mathrm{final}} < 0.1$*. The size of the circle is proportionate to the value of the* FAP_{final} *of the source. The larger the circle, the bigger the* FAP_{final}*.The pink circles correspond to the selected H*α *emission line sources. The black line is the fit to the main locus of stars and the yellow line corresponds to the* 5σ *limit above the fit. We also show in cyan the colours and magnitudes of the sources presented in Torres et al. (2014).*

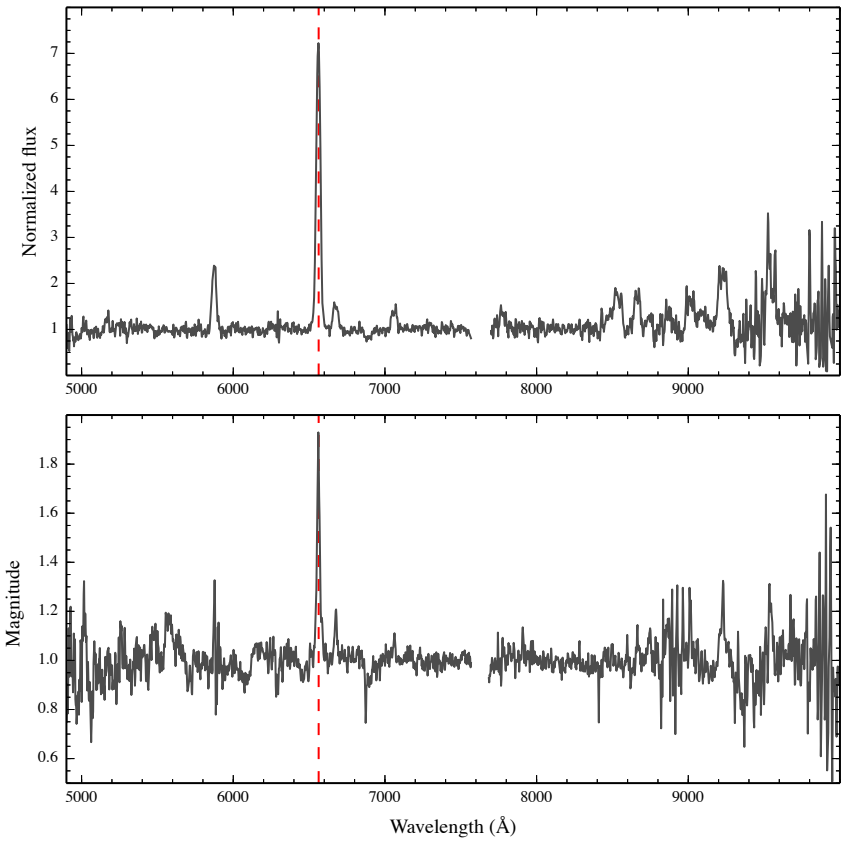

Figure 5.17: *Optical spectra of CX0128 (top) and CX0794 (bottom) taken from Torres et al. (2014).*

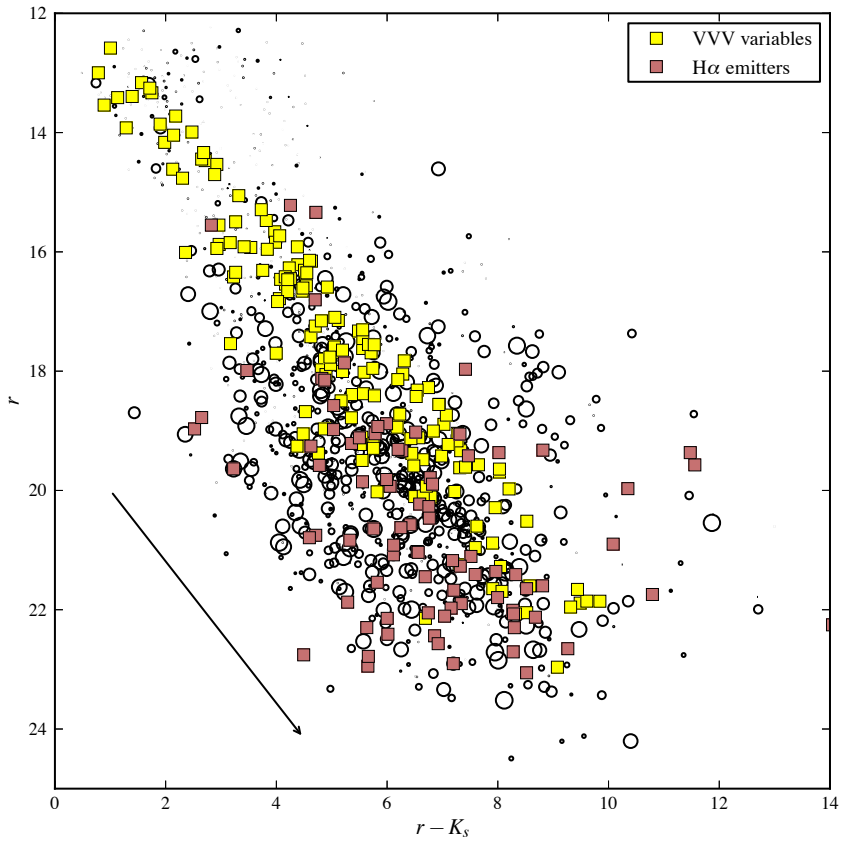

Figure 5.18: *Colour-magnitude diagram of sources with* $FAP_{\rm final} < 0.1$*. The size of the circle is proportionate to the value of the* $FAP_{\rm final}$ *of the source. The larger the circle, the bigger the* $FAP_{\rm final}$*. The pink squares correspond to the selected Hα emission line sources and the yellow squares are the VVV variable sources.*

5.7 Optical Variability

In parallel to the optical and NIR data we presented in the previous paragraph, other members of the GBS team have carried out a *variability* study of the GBS region in the r-band using the Mosaic-II CCD camera on the Blanco telescope. In total, Britt et al. (2014) acquired 8 nights in July 2010 to cover 9 deg^2 of the total GBS area. Typically sources were observed on timescales of $\sim$2 h to 8 days, with 120 s exposure times in the r-band. The remaining 25% of the optical variability survey of the GBS area will be presented in a later study as the data are still being reduced.

Another variability survey of the Galactic Bulge area has been carried out by the Optical Gravitational Lensing Experiment (OGLE[5]) team. This is a Polish project which began in 1992 and is led by Professor Andrzej Udalski at the University of Warsaw. Its main goal is to discover dark matter using the microlensing technique. The observations are mostly focused on the Galactic Bulge and the Magellanic clouds. The OGLE-III Catalog of Variable Stars[6] (Soszyński et al., 2011a,b; Szymański et al., 2011), found that $\sim$98% of field stars towards the Bulge are non-variable. However, we expect many X-ray sources to show some optical variability in their light curves. Udalski et al. (2012) and Hynes et al. (2012) focus on the bright optical counterparts to the GBS sources, by searching for any optical variability information in OGLE IV and the All Sky Automated Survey (ASAS, Pojmanski 1997). These bright sources were not studied by Britt et al. (2014) since our goal is to find LMXBs in the Bulge and thus we focus on the fainter objects since they are typically fainter than $r \sim 18$ (Ritter & Kolb, 2003).

The shape of the light curves of sources can provide clues on their nature and possibly on the parameters of the systems such as their orbital periods and inclinations. Eclipsing systems have the additional advantage of enabling the determination of accurate masses of the systems since their inclinations are better constrained. RS CVns and coronally active M-dwarfs can show sinusoidal variations with a period of days due to star spots. In the case of quiescent LMXBs and CVs, their light curves can differ significantly depending on the donor star: main-sequence donors will yield variability in the light curves on the periods of hours, whereas evolved donors would have periods greater than a day. The light curves of dwarf novae outbursts are also easily spotted. Quiescent systems have a large portion of their light contributed by the donor star. In the case of systems where the donor has filled its Roche Lobe, its effective surface area changes due to tidal distortion, which leads to ellipsoidal modulations in the light curves of these systems. However, in the case of binaries with higher accretion rates, the emission is dominated by the accretion disk, where irregular flickering is expected to be seen in their light curves. Flickering on time scales of seconds to minutes is commonly observed in soft and hard X-rays from polars which varies around the orbit in a way associated with emission from accretion zones.

Britt et al. (2014) searched for all the variable counterparts to the GBS

[5]http://ogle.astrouw.edu.pl/

[6]http://ogledb.astrouw.edu.pl/ ogle/CVS/

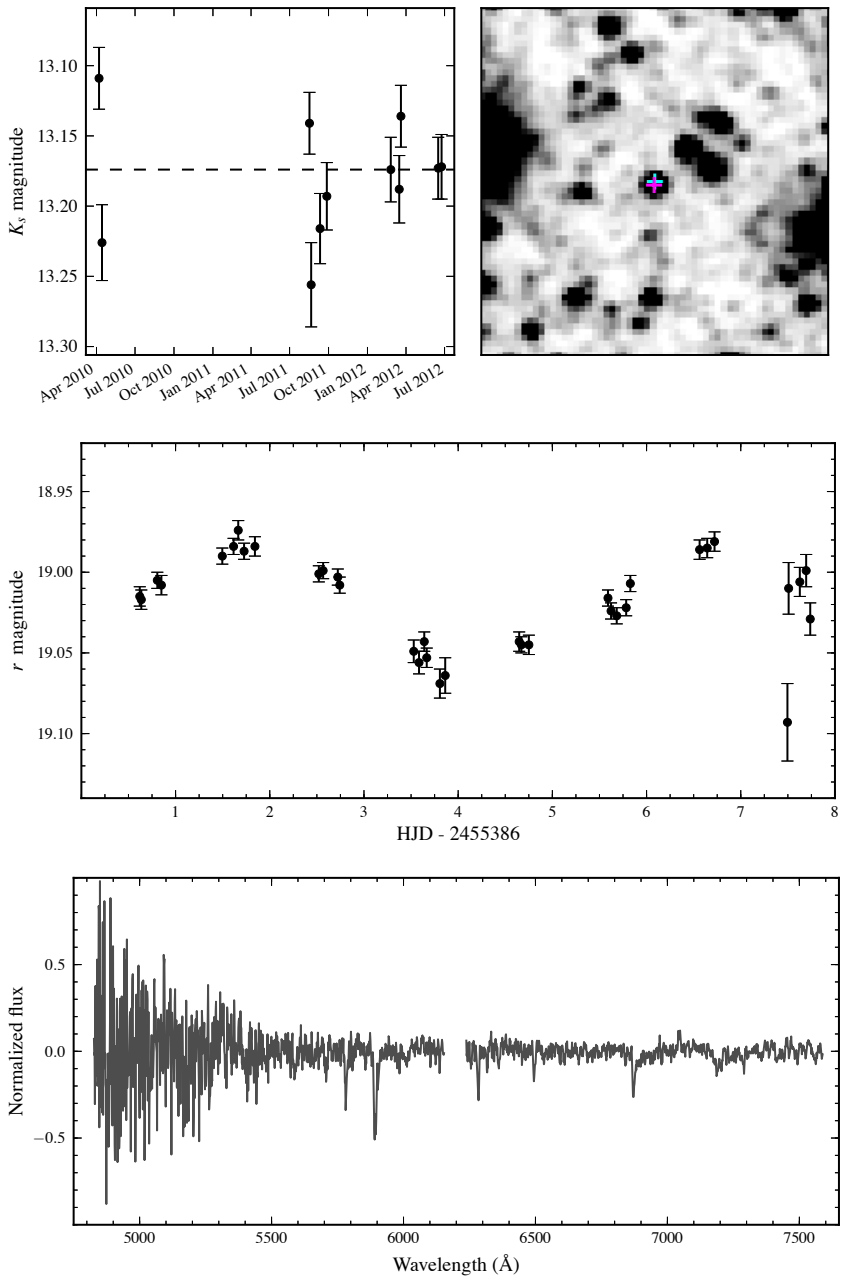

Figure 5.19: *Top panel: VVV K_s-band light curve and finder chart of CX0084. This source has a χ^2 = 2.894 and a p-value = 0.984. These values are not within the limits set to select variables yet we clearly see from the optical data that it is a variable source. The cyan and magenta crosses indicate the X-ray and NIR positions respectively. Middle panel: Optical MOSAIC-II light curve of CX0084. Bottom panel: GMOS spectrum of CX0084.*

sources, in a 9 deg^2 (i.e. 75%) region of the total GBS area. They found 167 variables and are in the process of identifying them with deeper X-ray images and optical spectroscopy. We cross-match his list of optical variable sources with ours from the VVV study and find 20 sources in common. However, 4 of these 20 sources have their VVV light curves affected by nearby bright stars, leaving the reliable number of variable objects in common 16. We show an example of the optical Mosaic II light curve of the variable source CX0084, which also shows some variability in the VVV data even though it did not pass the NIR variability criteria threshold (see Figure 5.19). This shows that one must keep an open mind when selecting sources for follow-up as they may show variability in some data sets better than in others. According to the optical data, CX0084 has a suspected period of 4.67 days, with an amplitude of variations of 0.1 mag, which is consistent with ellipsoidal variations from accreting binaries. Britt et al. (2014) think it is probably a CV or quiescent LMXB with an evolved donor star. We have also obtained optical spectra of this object (Wu et al. 2014, submitted) and it has been classified as a G9 star. Using tabulated values of the absolute magnitudes of a subgiant G9 star, $M_r = 2.5$, we can estimate the distance to the object. We find that $D \simeq 3.4 \pm 0.7$ kpc. In Figure 5.19, we show the optical spectrum of CX0084, taken with GMOS (Gemini Multi-Object Spectrograph; Davies et al. 1997) mounted on the Gemini-South Telescope in Chile. The spectroscopic data also reveals that this object has a radial velocity variation of ~ 100 km.s^{-1}.

5.8 Summary

In this Chapter, we demonstrated how exploiting multi-wavelength surveys can help us identify certain classes of sources. We began with the search for the NIR counterparts of 1658 X-ray sources in the GBS area. We used 2MASS for the bright sources and UKIDSS GPS for the fainter end (when it was available). The majority of the counterparts however, were found using the VVV survey. In order to find the most likely counterpart out of the typically 2-3 sources found within the 95% error radius, we associate a false alarm probability based on the K_s-band magnitude of the sources, its distance to the X-ray position and the source density around the X-ray positions. We find that around 79% of the GBS sources have a NIR counterpart with a FAP $< 3\%$.

The next step in our aim to identify these X-ray sources was to exploit the K_s-band variability part of the VVV survey. The photometric variability data was not taken regularly and therefore each source had a random number of observations over the span of two years. It cannot yield periods or any physical parameters of variable sources but we attempted to select those which showed variability in their light curves. For this, we associated a probability (p-value) to the calculated χ^2 of each light curve. A p-value < 0.1 meant that the source was very likely to be variable. In total, we find 249 sources with p-value < 0.1. Out of these, only 104 of them were visually classified as probably variable (the rest had their photometric data affected by nearby saturated stars). As mentioned earlier in this Chapter,

spectroscopy is ultimately the only way to identify and classify sources. However, by exploiting all the available photometric information we have on the GBS X-ray sources, we can prioritise the objects for spectroscopic follow-up.

Since our ultimate goal is to detect as many LMXBs in the Bulge as possible, the GBS project also has a deep optical photometric survey of its area. The addition of the Hα filter in this survey is necessary to select accreting objects that show strong Hα emission coming from the accretion disk. We used a $(r, r - \mathrm{H}\alpha)$ colour-magnitude diagram to select strong Hα emitters. In total, we find 161 possible counterparts to the GBS sources that stand out in colour-magnitude space. It is important to remember that active single low-mass dwarfs can also have strong Hα emission, which can lead to the selection of many of these types of sources in this study. However, with the combination of this optical data, as well as the NIR information, we can select those which are not too bright, since the latter are probably foreground active stars. In our selection of Hα emitters, we recovered two sources that indeed have strong Hα emission lines in their spectra: CX0128 and CX0794. These are binary systems, with their optical spectra dominated by the emission from the accretion disk.

The final available set of data consists of a deep optical variability survey using the r-band, specially designed to search for any variable counterparts to the GBS X-ray sources (Britt et al., 2014). The study yielded 167 variable sources in a region covering 75% of the total GBS area. Out of these, only 20 are in common with the VVV variable sources making each survey an additional asset to the study of the GBS X-ray sources. Since this optical survey was purposely carried out to fulfill the goals of the GBS, it is difficult to compare its findings directly to the NIR results. We were still able to select many variable NIR sources, which have not been found in the optical study. Since the K_s filter probes the most through the large amount of extinction towards the Bulge, possibly deeper NIR images of the GBS fields could be the next step forward in the study of the GBS sources. Given the range of diagnostics available to us, many combinations of constraints are possible. We attempt to visualise this complexity using a flowchart shown in Figure 5.20.

Ultimately, spectroscopy is the only way we can confidently identify and classify sources. We are currently analysing optical spectra of many sources that have been observed with several telescopes in Chile (NTT, Gemini, VLT). A number of results have been presented by Ratti et al. (2013), Torres et al. (2014), Britt et al. (2013), Wu et al. (2014, submitted). The large amount of data at hand will help us prioritize the sources to be followed-up in our next round of spectroscopic observations. This project is still ongoing, with many unexploited and undiscovered systems awaiting to be found.

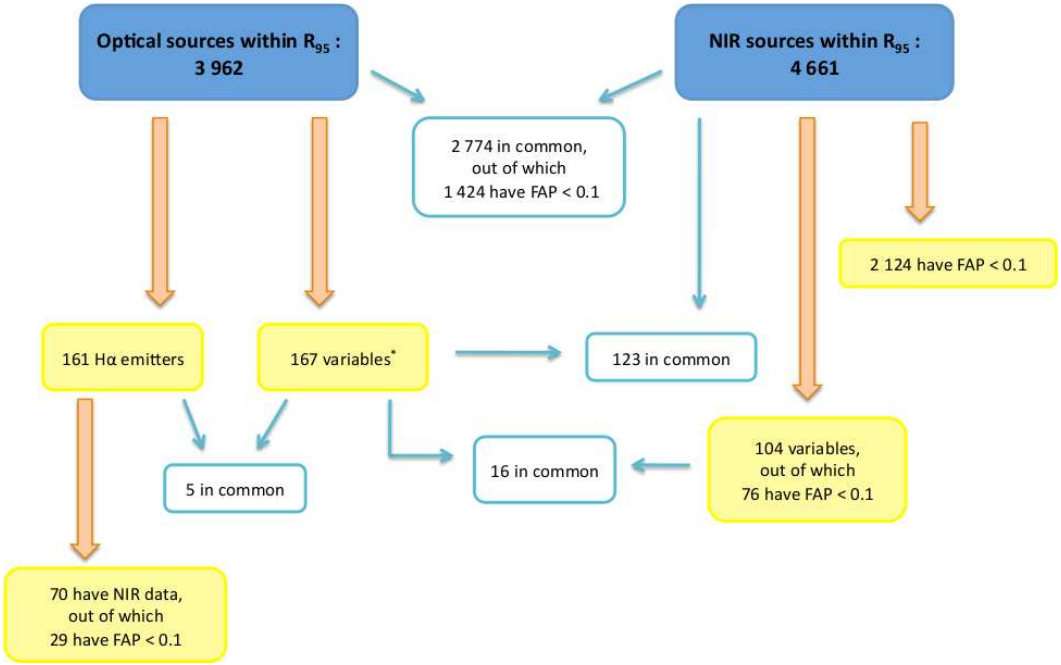

Figure 5.20: *Flow chart summary. It is important to note that the optical MOSAIC-II variability data yielding 167 variable sources only covered 75% of the GBS fields.*

Chapter 6

White dwarfs in the *Kepler* field

In this Chapter, we move away from the Galactic Bulge region and focus on a region of the sky, in the Cygnus and Lyra constellations, known as the *Kepler* field. As part of an ongoing project, we developed a method using our very own KIS catalogue to select WDs in the field, and more particularly, pulsating ones. Here we present our selection method, our discoveries and the type of exciting science that can be done with such objects.

6.1 Searching for white dwarfs in the *Kepler* field

We selected our WD candidates using ($U-g$, $g-r$) and ($r-\mathrm{H}\alpha$, $r-i$) colour-colour diagrams from KIS (see Figure 6.1). We remind the reader that KIS is a deep optical survey of the *Kepler* field, using four broadband filters, U, g, r, i and one narrowband filter, Hα, down to $\sim 20^{th}$ mag in the Vega system (see Section 4.3). As of December 2012, we have covered 97% of the *Kepler* field (Greiss et al., 2012). WDs are bluer than main-sequence stars and most single DA WDs also have strong Hα absorption lines, leading to $r - \mathrm{H}\alpha < 0$ (see bottom panel of Figure 6.1), which makes the KIS filter set ideal for their search.

In our photometric selection, we recovered KIC 4552982, the first ZZ Ceti star in the *Kepler* field found by Hermes et al. (2011). We narrowed down our selection to a small region in colour-space centred on KIC 4552982 and to candidates in, or close to the empirical (T_{eff}, log g) instability strip (Gianninas et al., 2011) projected into ($U-g, g-r$) space using the cooling models presented in Tremblay & Bergeron (2009). This left $\sim$60 WD candidates, $\sim$50% of which were ZZ Ceti candidates. Our next step was to confirm their identities via spectroscopy and to search for the variable stars amongst our candidates.

6.2 Spectroscopy

We were awarded a total of six nights on the William Herschel Telescope (WHT) in 2012 and 2013, where we obtained intermediate resolution spectra of 44 of our

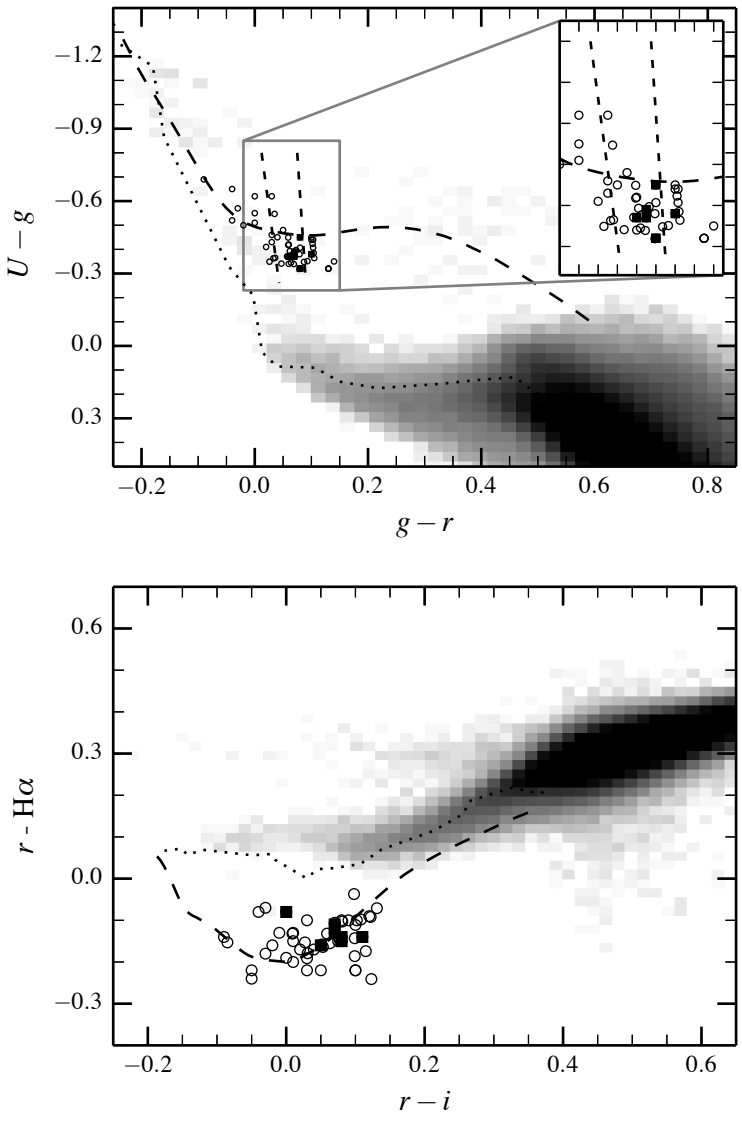

Figure 6.1: *$(U-g,\ g-r)$ (top) and $(r-\mathrm{H}\alpha,\ r-i)$ (bottom) colour-colour diagrams of stellar sources from the Kepler-INT survey (gray scale), and $\log g = 8$ DA WD cooling tracks (dashed line). The dotted line indicates the Pickles main sequence tracks taken from Groot et al. (2009). Narrowing our colour selection around the first ZZ Ceti in the field identified by Hermes et al. (2011) leaves $\sim$ 60 WD candidates (open circles). The filled squares correspond to the ZZ Ceti stars we discovered in the Kepler field. The vertical dashed lines mark the empirical ($T_{\rm eff}$, $\log g$) instability strip (Gianninas et al., 2011) projected into $(U-g, g-r)$ space.*

candidates in order to confirm their identities as WD stars and to measure their atmospheric parameters ($T_{\rm eff}$ and log g). We used the Intermediate dispersion Spectrograph and Imaging System[1] (ISIS), with the R600R and R600B gratings on the red and blue arms respectively and a 1" slit during our June 2013 run. Bad weather in our three-night run in August 2012 led to the use of a wider slit at 1.2" on the final night when we could carry out most of our observations. The blue arm was centred at 4351Å and the red arm at 6562Å. The blue spectra covered a total wavelength range from ∼3800Å to ∼5100Å, and the red spectra ranged from ∼5600Å to ∼7100Å (see Figure 6.2). The resolution of the spectra in the red arm is ∼2Å and ∼1.8Å in the blue arm.

All our spectra were de-biased and flat-fielded using the standard STARLINK[2] packages KAPPA, FIGARO and CONVERT. They were then optimally extracted using PAMELA[3] (Marsh, 1989). As we were not after very accurate wavelength calibrations, copper-argon arc lamp exposures were taken at the start and end of each night for the wavelength calibration of the spectra. We identified around 10 to 15 arc lines in each arm, which we fitted with fourth order polynomials. We also observed several standard stars at the beginning, middle and end of each night: Feige 34, Grw+70 5824, LB 1240, G191-B2B and L1512-34. We used MOLLY[4] for the wavelength and flux calibration of the extracted 1-D spectra obtained. For more details on the data reduction, see Section 3.3.

In total, we observed 44 sources with ISIS and all were confirmed to be DA WDs. This validates our colour cuts used to select the WD candidates. We provide the coordinates and magnitudes of all the WDs we confirmed in Table 6.1. KISJ1909+4717, also known as KIC 10198116, was previously found by Østensen et al. (2011b), which leads to our discovery of 43 new WDs from KIS.

[1] http://www.ing.iac.es/Astronomy/instruments/isis/

[2] The STARLINK Software Group homepage website is http://starlink.jach.hawaii.edu/starlink.

[3] PAMELA was written by T. R. Marsh and can be found in the STARLINK distribution Hawaiki and later releases.

[4] MOLLY was written by T. R. Marsh and is available from http://www.warwick.ac.uk/go/trmarsh/software.

Table 6.1: *Summary of photometric data of our WD candidates selected for spectroscopic follow-up.*

KIS ID	RA	Dec	U	g	r	i	Hα	KIC ID	Comment
KISJ1846+4157	18:46:35.96	+41:57:07.6	17.96 (2)	18.31 (1)	18.22 (1)	18.14 (2)	18.33 (3)	-	-
KISJ1848+4225	18:48:30.83	+42:25:15.5	18.02 (1)	18.36 (1)	18.32 (1)	18.29 (2)	18.51 (4)	6923777	-
KISJ1851+4506	18:51:01.28	+45:06:49.5	18.51 (4)	18.92 (3)	18.81 (3)	18.72 (4)	18.96 (9)	-	-
KISJ1857+4908	18:57:30.66	+49:08:36.2	18.34 (1)	18.79 (1)	18.75 (1)	18.74 (2)	18.90 (3)	11337510	-
KISJ1858+4613	18:58:10.23	+46:13:07.9	18.31 (2)	18.77 (1)	18.74 (2)	18.79 (4)	18.98 (5)	9573820	-
KISJ1859+4842	18:59:01.98	+48:42:38.3	18.57 (1)	19.02 (1)	18.92 (1)	18.88 (1)	19.09 (2)	11125021	-
KISJ1902+4223	19:02:07.12	+42:23:25.5	18.67 (1)	18.99 (1)	18.86 (2)	18.76 (3)	19.08 (5)	-	-
KISJ1904+4130	19:04:50.16	+41:30:16.7	17.03 (2)	17.45 (1)	17.39 (1)	17.36 (1)	17.54 (3)	-	-
KISJ1904+4245	19:04:26.62	+42:45:48.7	18.21 (1)	18.78 (1)	18.81 (1)	18.83 (3)	18.97 (4)	7184288	-
KISJ1906+4354	19:06:31.31	+43:54:48.8	18.67 (2)	19.01 (1)	18.95 (2)	19.00 (4)	19.17 (6)	8084967	-
KISJ1906+5002	19:06:34.71	+50:02:17.0	18.73 (3)	19.28 (2)	19.24 (3)	19.33 (5)	19.39 (8)	11805054	-
KISJ1908+4316	19:08:35.91	+43:16:42.3	17.84 (1)	18.16 (1)	18.08 (1)	18.00 (1)	18.23 (2)	7594781	ZZ Ceti; ground-based confirmation; observed with *Kepler*
KISJ1908+4619	19:08:25.69	+46:19:35.4	18.03 (2)	18.45 (1)	18.39 (2)	18.42 (2)	18.46 (4)	9639485	-
KISJ1909+4717	19:09:59.36	+47:17:09.5	15.82 (1)	16.30 (1)	16.25 (1)	16.28 (1)	16.43 (1)	10198116	(a)
KISJ1911+4543	19:11:33.53	+45:43:46.1	18.26 (2)	18.67 (2)	18.65 (2)	18.69 (3)	18.73 (5)	9272512	-
KISJ1913+4709	19:13:40.87	+47:09:30.6	18.71 (3)	19.08 (3)	19.01 (3)	18.93 (4)	19.15 (8)	10132702	ZZ Ceti; ground-based confirmation; observed with *Kepler*
KISJ1917+3927	19:17:19.17	+39:27:18.2	17.91 (1)	18.28 (1)	18.22 (1)	18.17 (2)	18.38 (3)	4357037	ZZ Ceti; ground-based confirmation; observed with *Kepler*
KISJ1917+4413	19:17:55.28	+44:13:26.2	18.10 (2)	18.42 (1)	18.34 (2)	18.27 (3)	18.47 (4)	8293193	ZZ Ceti; ground-based confirmation
KISJ1918+3914	19:18:54.33	+39:14:32.9	18.36 (1)	18.72 (1)	18.62 (1)	18.49 (2)	18.69 (3)	-	-
KISJ1918+4533	19:18:30.15	+45:33:13.0	17.80 (2)	18.42 (2)	18.42 (2)	18.42 (4)	18.61 (7)	9149300	-
KISJ1919+4247	19:19:55.09	+42:47:23.1	17.36 (1)	18.05 (1)	18.14 (1)	18.23 (2)	18.28 (3)	-	-
KISJ1919+4712	19:19:52.92	+47:12:56.3	17.73 (2)	18.16 (2)	18.13 (2)	18.11 (2)	18.30 (5)	10203164	-
KISJ1919+4957	19:19:12.21	+49:57:51.3	17.40 (1)	17.92 (1)	17.96 (2)	17.93 (3)	18.18 (6)	11759570	-
KISJ1920+4338	19:20:18.87	+43:38:32.4	18.52 (3)	18.84 (2)	18.71 (2)	18.66 (3)	18.93 (5)	7885860	-
KISJ1920+5017	19:20:24.87	+50:17:22.1	17.68 (2)	18.13 (2)	18.05 (2)	18.05 (4)	18.13 (6)	11911480	ZZ Ceti; ground-based confirmation; observed with *Kepler* (b)
KISJ1922+4807	19:22:48.86	+48:07:21.4	18.05 (2)	18.70 (2)	18.74 (3)	18.71 (4)	18.84 (7)	107944390	-
KISJ1923+3929	19:23:48.76	+39:29:33.1	19.05 (2)	19.43 (1)	19.33 (2)	19.26 (3)	19.44 (6)	4362927	ZZ Ceti; ground-based confirmation
KISJ1924+3655	19:24:08.27	+36:55:18.4	17.53 (1)	18.15 (1)	18.12 (1)	18.13 (2)	18.25 (3)	1293071	-
KISJ1926+3703	19:26:03.05	+37:03:16.4	18.49 (1)	19.04 (1)	19.04 (2)	19.03 (3)	19.24 (5)	1432852	-
KISJ1928+3929	19:28:14.16	+39:29:54.8	18.16 (1)	18.66 (1)	18.68 (1)	18.67 (2)	18.81 (4)	-	-
KISJ1929+3857	19:29:52.07	+38:57:50.0	18.20 (1)	18.55 (1)	18.41 (1)	18.33 (2)	18.51 (3)	3854110	-
KISJ1929+4302	19:29:12.27	+43:02:52.1	18.01 (3)	18.45 (2)	18.35 (2)	18.23 (3)	18.44 (5)	-	-
KISJ1932+4210	19:32:12.04	+42:10:53.5	18.36 (4)	18.87 (3)	18.87 (3)	18.78 (4)	18.97 (8)	6695659	-
KISJ1933+4753	19:33:55.22	+47:53:02.4	18.71 (3)	19.13 (2)	19.03 (2)	18.92 (4)	19.13 (7)	10604007	-
KISJ1935+4237	19:35:34.63	+42:37:41.7	17.31 (1)	17.76 (1)	17.70 (1)	17.69 (2)	17.83 (3)	7124835	-
KISJ1935+4634	19:35:06.67	+46:34:59.1	17.88 (1)	18.28 (1)	18.20 (1)	18.15 (2)	18.36 (3)	9775198	-
KISJ1939+4533	19:39:07.15	+45:33:33.9	18.15 (2)	18.51 (1)	18.48 (2)	18.36 (2)	18.65 (5)	9162396	-
KISJ1943+4538	19:43:02.67	+45:38:42.4	16.93 (1)	17.30 (1)	17.26 (1)	17.23 (1)	17.44 (2)	-	-
KISJ1943+5011	19:43:31.92	+50:11:45.8	16.77 (1)	17.12 (1)	17.03 (1)	16.93 (1)	17.13 (2)	-	-
KISJ1944+4327	19:44:05.85	+43:27:21.7	16.41 (1)	16.76 (1)	16.73 (1)	16.67 (1)	16.86 (1)	7766212	-
KISJ1945+4348	19:45:59.25	+43:48:45.3	17.26 (1)	17.61 (1)	17.55 (1)	17.45 (1)	17.58 (2)	8043166	-
KISJ1945+4455	19:45:42.30	+44:55:10.6	16.82 (1)	17.16 (1)	17.09 (1)	16.99 (1)	17.20 (2)	-	-
KISJ1945+5051	19:45:03.58	+50:51:39.7	18.73 (2)	19.11 (2)	19.05 (2)	18.93 (4)	19.29 (9)	12217892	-
KISJ1956+4447	19:56:16.98	+44:47:53.4	18.49 (3)	18.88 (2)	18.81 (2)	18.71 (4)	19.00 (8)	-	-

(a) Østensen et al. (2011b); (b) Greiss et al. (2014)

Since we are interested in the ZZ Ceti stars within our DA WD sample, we fitted model atmospheres (Koester, 2010) to our spectra in order to obtain their effective temperatures and surface gravities. It is known that ZZ Ceti stars occupy a specific instability strip in ($T_{\rm eff}$, log g) space (Gianninas et al., 2011), making it possible to select ZZ Ceti candidates from our sample of WDs on the basis of those parameters. When several exposures were taken for a given star, we calculated the average spectrum using the individual spectra obtained. The normalised Balmer line profiles in the average spectrum were then fitted using the WD models of Koester (2010), following the procedure described in Homeier et al. (1998). For the computation of the models, we used the Stark-broadened Balmer line profiles of Tremblay & Bergeron (2009) and adopted the ML2/α = 0.8 prescription for convection. In model atmospheres, convection has been described with the mixing length theory (Böhm-Vitense, 1958), and ML2/α (α is the mixing length to pressure scale height ratio) is a parametrisation typically used for WD atmospheres (Tassoul et al., 1990).

In Figure 6.2, we show the spectrum of KIC 11911480 as an example of the data we obtained and method we used to fit the spectrum. We overplot the best model fit, which returned the following parameters for this DA WD: $T_{\rm eff}$ = 12 350 ± 250 K and log g = 7.96 ± 0.01. The uncertainties in the atmospheric parameters were estimated from fitting the three individual 20 min WHT spectra and taking the root mean square (RMS). These values place KIC 11911480 close to the blue edge of the empirical boundaries of the ZZ Ceti instability strip (Gianninas et al., 2011). Using a mass-radius relation and the evolutionary cooling models from Fontaine et al. (2001) with a carbon-oxygen core (Bergeron et al., 2001)[5], we obtain a mass estimate of our ZZ Ceti star: $M_{\rm WD}$ = 0.58 ± 0.06 $M_{\odot}$. However, we note that this may be a slight overestimate of the true WD mass, as it is now well established that the spectroscopically determined surface gravities, and hence the masses, of WDs with temperatures < 13 000 K, are systematically too high (see e.g. Bergeron et al. 1990; Gianninas et al. 2011; Koester et al. 2009, for a discussion). The most likely explanation for this problem is that 1-D mixing length theory does not properly account for the effects of convection on the temperature structure of the atmosphere (Tremblay et al., 2011a). For completeness, we adopt the 3-D model corrections of Tremblay et al. (2013) in the case of KIC 11911480 and find $T_{\rm eff}$ = 12 160 ± 250 K and log g = 7.94 ± 0.01, corresponding to $M_{\rm WD}$ = 0.57 ± 0.06 $M_{\odot}$. The differences in our case are negligibly small, yet we adopt the corrected values for our study.

The results from the fits to our spectra are given in Table 6.2. These parameters have also been corrected using the 3-D models of Tremblay et al. (2013). In Figure 6.3, we plot the results from the fits for all our WDs. Out of the 43 new WDs we found in the *Kepler* field, ∼20 are strong ZZ Ceti candidates. We use two methods to select the strong ZZ Ceti candidates from our observed WDs. In one case, the atmospheric parameters of half of them place them in or very close to the empirical

[5]The cooling models can be found on http://www.astro.umontreal.ca/∼bergeron/CoolingModels/. Also refer to Holberg & Bergeron (2006); Tremblay et al. (2011b); Bergeron et al. (2011) for colour and model calculations.

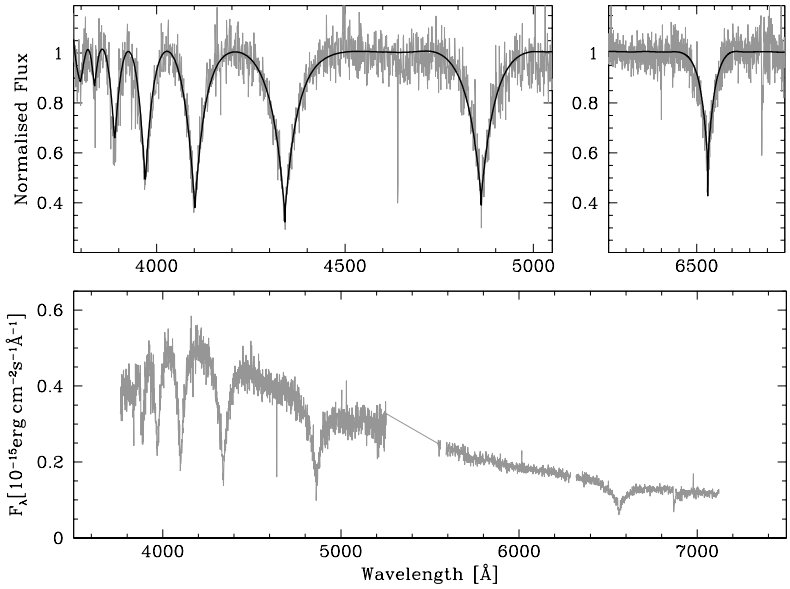

Figure 6.2: *The WHT/ISIS spectrum of KIC 11911480 (gray) obtained in August 2012 confirming the star to be a DA WD. The best-fit atmosphere parameters are* $T_{\rm eff} = 12\,350 \pm 250$ *K and* $\log g = 7.96 \pm 0.01$*, which places the star within the empirical ZZ Ceti instability strip.*

instability strip of ZZ Ceti stars (Gianninas et al. 2011, see Figure 6.3). In the case of the other half, we make use of the fact that we have multiple KIS observations of a large fraction of the stars in the catalogue. For sources with two entries in the KIS catalogue, we select those that have their magnitudes varying significantly or that are inconsistent with regards to their photometric errors. These are shown in blue squares in Figure 6.3. The cyan circles correspond to the four ZZ Ceti stars observed with the *Kepler* spacecraft and the two additional red circles are also confirmed pulsators using ground-based data. In fact, we made use of ground-based time series photometry to confirm the variable nature of six of these ZZ Ceti star candidates.

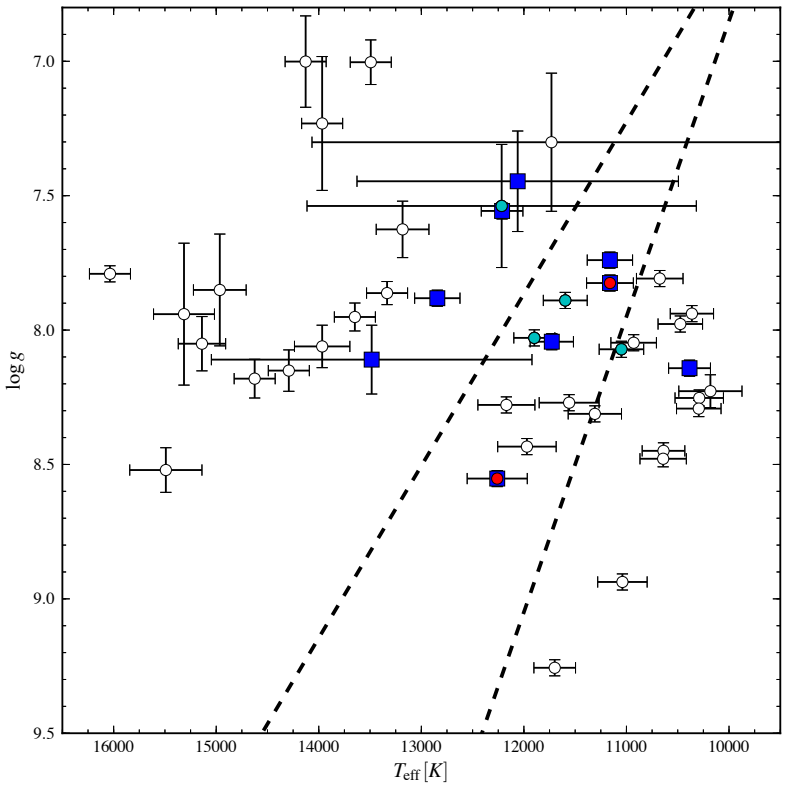

Figure 6.3: *($T_{\rm eff}$, $\log g$) diagram of all the WDs we observed with ISIS. The cyan circles correspond to the four ZZ Ceti stars we observed with Kepler. The red circles are the additional two new ZZ Ceti stars we confirmed using ground-based time-series photometry. The blue squares are the ZZ Ceti candidates chosen on the basis of their multiple KIS observations. The black dotted lines correspond to the boundaries of the empirical ZZ Ceti instability strip (Gianninas et al., 2011). The sources with very large error bars are planned to be re-observed in an observing run on the WHT, end of July 2014.*

Table 6.2: *Summary of spectroscopic observations and results from model atmosphere fits to the spectra.*

KIS ID	RA	Dec	Exposure time (s)	Obs date	$T_{\rm eff}$	$\log g$	Comment
KISJ1846+4157	18:46:35.96	+41:57:07.6	1 × 1200	07/06/2013	10 930 (222)	8.05 (0.03)	-
KISJ1848+4225	18:48:30.83	+42:25:15.5	1 × 1200	07/06/2013	12 060 (1567)	7.45 (0.19)	-
KISJ1851+4506	18:51:01.28	+45:06:49.5	1 × 1500	07/06/2013	19 058 (226)	7.30 (0.03)	-
KISJ1857+4908	18:57:30.66	+49:08:36.2	1 × 1500	11/08/2012	11 308 (260)	8.31 (0.03)	-
KISJ1858+4613	18:58:10.23	+46:13:07.9	1 × 1200	11/08/2012	15 139 (231)	8.05 (0.10)	-
KISJ1859+4842	18:59:01.98	+48:42:38.3	1 × 1200	11/08/2012	11 970 (285)	8.43 (0.03)	-
KISJ1902+4223	19:02:07.12	+42:23:25.5	1 × 1800	08/06/2013	10 639 (208)	8.45 (0.03)	-
KISJ1904+4130	19:04:50.16	+41:30:16.7	1 × 900	07/06/2013	13 967 (200)	7.23 (0.25)	-
KISJ1904+4245	19:04:26.62	+42:45:48.7	1 × 1200	11/08/2012	15 314 (297)	7.94 (0.26)	-
KISJ1906+4354	19:06:31.31	+43:54:48.8	1 × 1800	11/08/2012	13 967 (270)	8.06 (0.08)	-
KISJ1906+5002	19:06:34.71	+50:02:17.0	1 × 1800	08/06/2013	14 965 (257)	7.85 (0.21)	-
KISJ1908+4316	19:08:35.91	+43:16:42.3	3 × 1200	06/06/2013	12 217 (1 700)	7.54 (0.22)	ZZ Ceti; ground-based confirmation; observed with *Kepler*
KISJ1908+4619	19:08:25.69	+46:19:35.4	1 × 1200	11/08/2012	13 484 (1563)	8.11 (0.13)	-
KISJ1909+4717	19:09:59.36	+47:17:09.5	3 × 1500	09/08/2012	13 648 (200)	7.95 (0.05)	(a)
KISJ1911+4543	19:11:33.53	+45:43:46.1	1 × 1200	11/08/2012	14 292 (200)	8.15 (0.08)	-
KISJ1913+4709	19:13:40.87	+47:09:30.6	3 × 1500	06/06/2013	11 048 (217)	8.07 (0.03)	ZZ Ceti; ground-based confirmation; observed with *Kepler*
KISJ1917+3927	19:17:19.17	+39:27:18.2	3 × 1200	06/06/2013	11 898 (200)	8.03 (0.03)	ZZ Ceti; ground-based confirmation; observed with *Kepler*
KISJ1917+4413	19:17:55.28	+44:13:26.2	1 × 1200	11/08/2012	11 161 (228)	7.82 (0.03)	ZZ Ceti; ground-based confirmation
KISJ1918+3914	19:18:54.33	+39:14:32.9	1 × 1500	07/06/2013	10 474 (217)	7.98 (0.03)	-
KISJ1918+4533	19:18:30.15	+45:33:13.0	1 × 1200	11/08/2012	15 491 (352)	8.52 (0.08)	-
KISJ1919+4247	19:19:55.09	+42:47:23.1	1 × 1200	11/08/2012	11 039 (241)	8.94 (0.03)	-
KISJ1919+4712	19:19:52.92	+47:12:56.3	3 × 900	14/07/2012	11 699 (203)	9.26 (0.03)	-
KISJ1919+4957	19:19:12.21	+49:57:51.3	1 × 1275	10/08/2012	14 625 (200)	8.18 (0.07)	-
KISJ1920+4338	19:20:18.87	+43:38:32.4	1 × 1800	11/08/2012	10 290 (236)	8.25 (0.03)	-
KISJ1920+5017	19:20:24.87	+50:17:22.1	3 × 1200	07/06/2013	12 160 (250)	7.94 (0.01)	ZZ Ceti; ground-based confirmation; observed with *Kepler* (b)
KISJ1922+4807	19:22:48.86	+48:07:21.4	1 × 1200	11/08/2012	10 642 (226)	8.48 (0.03)	-
KISJ1923+3929	19:23:48.76	+39:29:33.1	1 × 1800	08/06/2013	12 260 (293)	8.55 (0.03)	ZZ Ceti; ground-based confirmation
KISJ1924+3655	19:24:08.27	+36:55:18.4	1 × 1200	11/08/2012	11 731 (2 135)	7.30 (0.26)	-
KISJ1926+3703	19:26:03.05	+37:03:16.4	1 × 1200	11/08/2012	14 128 (200)	7.00 (0.18)	-
KISJ1928+3929	19:28:14.16	+39:29:54.8	1 × 1500	08/06/2013	16 036 (200)	7.79 (0.03)	-
KISJ1929+3857	19:29:52.07	+38:57:50.0	1 × 1200	11/08/2012	10 675 (227)	7.81 (0.03)	-
KISJ1929+4302	19:29:12.27	+43:02:52.1	1 × 1200	11/08/2012	10 181 (308)	8.23 (0.06)	-
KISJ1932+4210	19:32:12.04	+42:10:53.5	1 × 1500	08/06/2013	11 559 (292)	8.27 (0.03)	-
KISJ1933+4753	19:33:55.22	+47:53:02.4	1 × 1500	07/06/2013	10 295 (217)	8.29 (0.03)	-
KISJ1935+4237	19:35:34.63	+42:37:41.7	1 × 900	08/06/2013	13 183 (257)	7.63 (0.11)	-
KISJ1935+4634	19:35:06.67	+46:34:59.1	1 × 1200	08/06/2013	12 171 (278)	8.28 (0.03)	-
KISJ1939+4533	19:39:07.15	+45:33:33.9	1 × 1200	07/06/2013	11 161 (221)	7.74 (0.03)	-
KISJ1943+4538	19:43:02.67	+45:38:42.4	1 × 900	08/06/2013	12 884 (221)	7.88 (0.03)	-
KISJ1943+5011	19:43:31.92	+50:11:45.8	1 × 900	06/06/2013	10 362 (211)	7.94 (0.03)	-
KISJ1944+4327	19:44:05.85	+43:27:21.7	1 × 900	06/06/2013	12 213 (203)	7.56 (0.03)	-
KISJ1945+4348	19:45:59.25	+43:48:45.3	1 × 900	08/06/2013	10 385 (204)	8.14 (0.03)	-
KISJ1945+4455	19:45:42.30	+44:55:10.6	1 × 900	07/06/2013	11 728 (211)	8.04 (0.03)	-
KISJ1945+5051	19:45:03.58	+50:51:39.7	1 × 1800	07/06/2013	13 493 (200)	7.00 (0.08)	-
KISJ1956+4447	19:56:16.98	+44:47:53.4	1 × 1500	07/06/2013	13 334 (200)	7.86 (0.04)	-

(a) Østensen et al. (2011b); (b) Greiss et al. (2014)

6.3 Ground-based confirmation of pulsators

We obtained ground-based optical time-series photometry for six of our ZZ Ceti candidates, in order to confirm their variable nature. The ground-based observations of four of our stars were obtained from the RATS-*Kepler* survey (Ramsay et al., 2013), which is a deep optical high-cadence survey of objects in the *Kepler* field using mostly the INT, as well as the 1.2m MDM telescope at Kitt Peak. The RATS-*Kepler* survey provides one hour-long sequences of 20 s g-band exposures of objects in the *Kepler* field. However, in our case we obtained data for several targets through private communication with the Princial Investigator of the survey (Gavin Ramsay) and the cadence of our observations were 48 s. We also obtained variability confirmation of two of our WDs from the McDonald Observatory (Hermes, private coomunication - see Figure 6.5). The McDonald observations were also 20 s exposures extending over ∼5 hours for each of the targets. We summarise in Table 6.3 the ground-based observations confirming the variability of our six WDs. It is important to note that these ground-based observations were only obtained in order to perform a qualitative study of the variability of the sources, hence the rather low-quality data shown in Figure 6.4.

The dominant periodicities found for all six ZZ Ceti stars are within the expected range for this class of pulsators (see Table 6.3). DAVs are known to pulsate within the range of 100 to 1000 s, with hot DAVs usually exhibiting short period pulsations between 100 to 300 s whereas the cooler ones have pulsation periods between 600 to 1000 s (Mukadam et al., 2006). This indicates that KISJ1917+4413 (KIC 08293193), KISJ1917+3927 (KIC 04357037), KISJ1908+4316 (KIC 07594781) and KISJ1920+5017 (KIC 11911480) belong to the hotter group of DAVs, whereas KISJ1913+4709 (KIC 10132702) and KISJ1923+3929 (KIC 04362927) are cooler. This is in agreement with their spectroscopic temperatures (see Table 6.3 and Figure 6.3).

Our next step was to obtain *Kepler* time-series photometry of as many DAVs as possible. Our main goal is to probe the structure and interior of a wide range of WDs by studying as many pulsating WDs in the *Kepler* field as possible. Asteroseismology has the potential to accurately measure the masses of WDs and to study their degenerate cores, which can never be done via spectroscopy. Our sample of ZZ Cetis should span a large range of effective temperatures and surface gravities in the instability strip. However, it is clear that all ZZ Cetis we discovered are faint (see Table. 6.1), therefore long, uninterrupted time-series photometry will improve the S/N and enable the detection of weak pulsation modes, which is not easily feasible through ground-based studies. Also, it is known that the pulsation properties of WDs change across the instability strip (e.g. Mukadam et al., 2004). For instance, the amplitudes of individual pulsation modes in cool ZZ Cetis can vary dramatically on time scales of days to weeks (e.g. G29-38, Kleinman et al., 1994, 1998). Therefore, only high-quality light curves, such as those obtained through *Kepler*, can overcome this effect. We obtained DDT *Kepler* observations of four of our ZZ Ceti stars: KISJ1920+5017 (KIC 11911480, Greiss

Table 6.3: *Summary of ground-based time-series data of six ZZ Ceti stars confirmed from our survey. The dominant periods and frequencies found in the amplitude power spectra of each source are given here.*

KIS ID	KIC ID	Period (s)	Frequency (μHz)	Telescope	Total time (hours)	Cadence (s)
KISJ1917+4413	KIC 08293193	310	3222	INT	1.03	48
KISJ1917+3927	KIC 04357037	323	3094	INT	1.03	48
KISJ1908+4316	KIC 07594781	284	3520	INT	0.93	44
KISJ1920+5017	KIC 11911480	291	3432	INT	1.10	49
KISJ1913+4709	KIC 10132702	854	1172	McDonald	5.13	20
KISJ1923+3929	KIC 04362927	724	1381	McDonald	4.63	20

et al. 2014), KISJ1908+4316 (KIC 07594781), KISJ1917+3927 (KIC 04357037) and KISJ1913+4709 (KIC 10132702) which we present in the following Section. In April 2012, our *Kepler* GO proposal to observe eight of our ZZ Ceti stars was approved but later canceled due to the failure of two reaction wheels on the *Kepler* spacecraft, forcing it to change its field of view towards the ecliptic.

6.4 *Kepler* data of four ZZ Ceti stars

In this Section, we discuss the analysis of the *Kepler* observations of four of our new ZZ Ceti stars: KIC 11911480 (KISJ1920+5017), KIC 10132702 (KISJ1913+4709), KIC 04357037 (KISJ1917+3927) and KIC 07594781 (KISJ1908+4316). We use their KIC IDs here since these are the IDs chosen and referred to by the *Kepler* team. The first one, KIC 11911480 was observed for nearly 6 months with the *Kepler* satellite, whereas the other three DAVs have one to three months of data. Each ZZ Ceti is presented separately and we give a summary of our results at the end of this Section.

The *Kepler* light curves, produced using simple aperture photometry and delivered by the *Kepler* Science Operations Center pipeline, were downloaded from the MAST website[6]. Details on the data handling, processing and releases can be found on the *Kepler* data analysis website[7]. In each case, we calculate the discrete Fourier Transforms (FT) of each set separately, using the TSA package within MIDAS written by Alex Schwarzenberg-Czerny. This is a standard signal processing method used to extract the periods (or frequencies) and amplitudes of the detected pulsation modes in a variable star. It transforms a signal form time domain to frequency domain.

6.4.1 KIC 11911480

After confirmation of its pulsating nature, we were awarded *Kepler* short-cadence mode observations of KIC 11911480 during Quarters 12 and 16 (Q12, Q16). *Kepler* operates in two modes: short and long cadence observations consisting of 58.89 s and 29.4 min exposures respectively. The Q12 observations were taken between

[6]http://archive.stsci.edu/kepler/publiclightcurves.html
[7]http://keplerscience.arc.nasa.gov/DataAnalysis.shtml

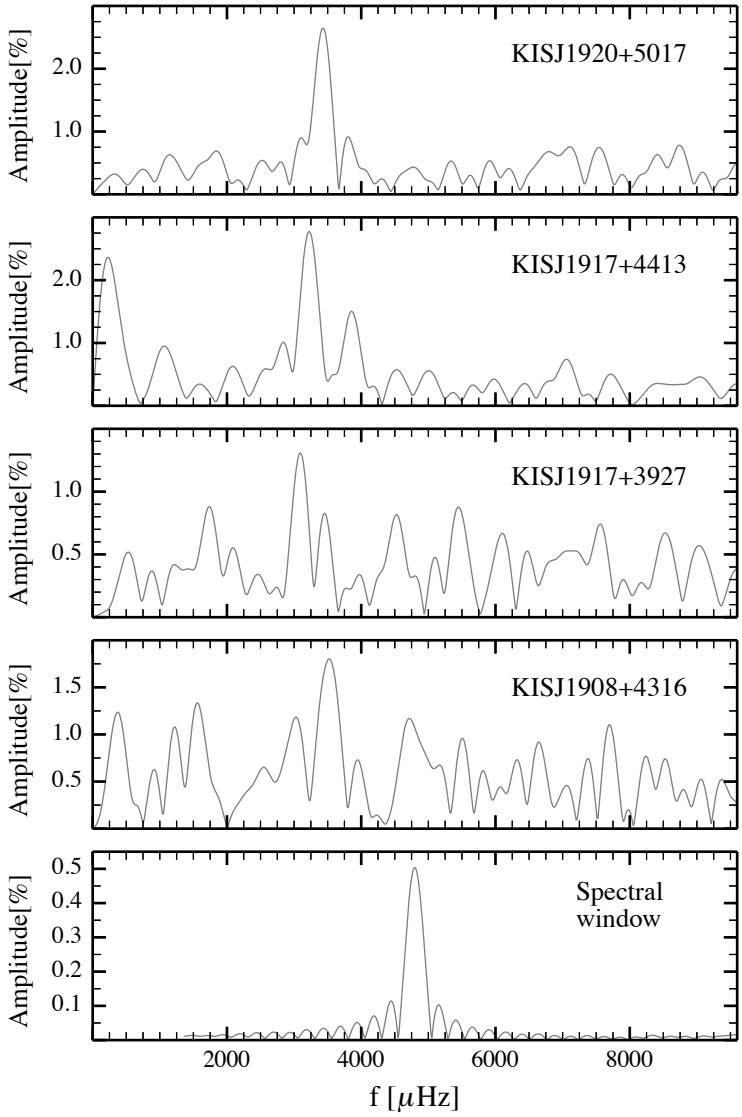

Figure 6.4: *RATS-Kepler amplitude power spectra of KISJ1920+5017 (KIC 11911480), KISJ1917+4413 (KIC 08293193), KISJ1917+3927 (KIC 04357037) and KISJ1908+4316 (KIC 07594781). The bottom panel shows the spectral window of the RATS-Kepler data.*

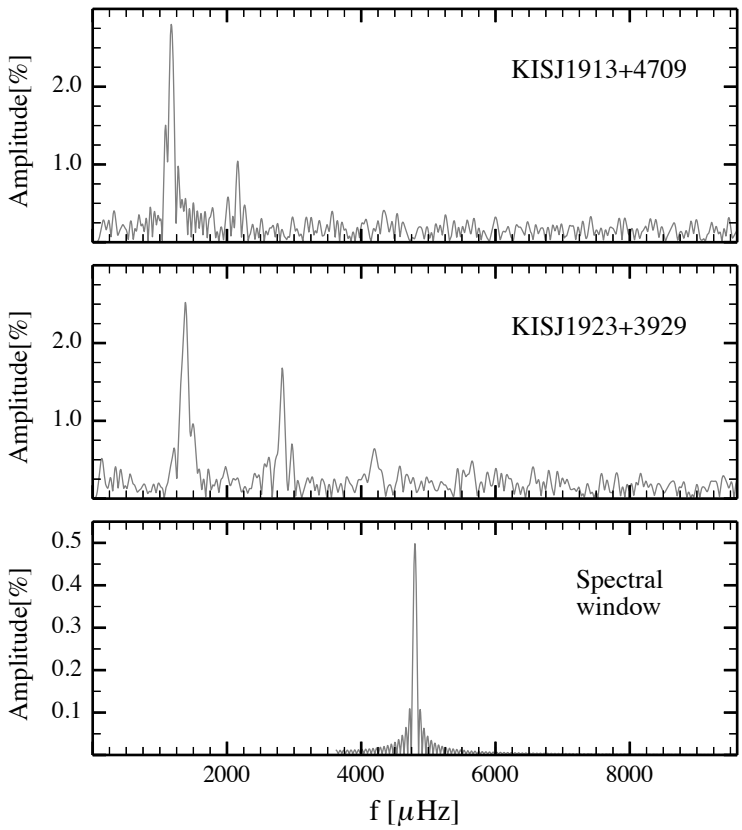

Figure 6.5: *McDonald observatory amplitude power spectra of KISJ1913+4709 (KIC 10132702) and KISJ1923+3929 (KIC 04362927). The bottom panel shows the spectral window of the McDonald data.*

Jan 4 - Mar 28, 2012 and Q16 spanned from Jan 11 - Apr 8, 2013. Each *Kepler* quarter corresponds to three months of observations. However, during Q12, a series of coronal mass ejections (CMEs) affected the run by bringing the duty cycle of Q12 down to 88.2%. The CMEs did not lead to any damage on the spacecraft but they did result in the loss of several days of data collected. During Q16, *Kepler* went into rest mode for 11.3 days, leading to a duty cycle of 84.8% for that quarter.
In the FT of KIC 11911480 (Figure 6.6), we observe optical variability in the *Kepler* data with periods ranging from 137.1 s to 519.6 s (see Table 6.4 for more details). These periods are within the expected range for ZZ Ceti stars, which are known to have g-mode pulsations ranging from 100 to 1000 s (Fontaine & Brassard, 2008), and match the pulsation periods of other known hot ZZ Ceti stars (Mukadam et al., 2004).

Table 6.4: *Pulsation frequencies of KIC 11911480 from the Q12 and Q16 data. The uncertainties are given in parentheses.* Δf *corresponds to the frequency spacing between two consecutive frequencies in the table*

	P [s]	f [μHz]	A [%]	Δf[μHz]	P [s]	f [μHz]	A [%]	Δf[μHz]
	Q12				Q16			
$f_{1,-}$	290.9664 (7)	3436.823 (8)	0.185		290.9675 (3)	3436.810 (4)	0.439	
$f_{1,o}$	290.8016 (1)	3438.770 (1)	1.187	1.947	290.8026 (6)	3438.759 (7)	2.175	1.949
$f_{1,+}$	290.6322 (4)	3440.775 (5)	0.368	2.005	290.6341 (2)	3440.753 (3)	0.641	1.994
$f_{2,-}$	259.3731 (2)	3855.451 (3)	0.501		259.3738 (1)	3855.440 (2)	0.997	
$f_{2,o}$	259.2531 (2)	3857.235 (3)	0.581	1.784	259.2538 (1)	3857.224 (2)	0.975	1.784
$f_{2,+}$	-	-	-	-	259.1352 (3)	3858.989 (4)	0.391	1.764
$f_{3,-}$	324.529 (1)	3081.39 (1)	0.169		324.5299 (6)	3081.381 (5)	0.321	
$f_{3,o}$	324.3152 (9)	3083.420 (9)	0.185	2.03	324.3175 (6)	3083.398 (6)	0.278	2.017
$f_{3,+}$	324.1032 (1)	3085.44 (2)	0.100 $\star$	2.02	-	-	-	-
$f_{4,-}$	172.9588 (4)	5781.72 (1)	0.086 $\star$		-	-	-	-
$f_{4,o}$	172.9003 (5)	5783.68 (1)	0.113 $\star$	1.96	172.9015 (3)	5783.64 (1)	0.149	
$f_{5,o}$	-	-	-	-	202.5687 (6)	4936.60 (1)	0.118 $\star$	
$f_{5,+}$	-	-	-	-	202.4873 (5)	4938.58 (1)	0.091 $\star$	1.98
$2\,f_{1,o}$	145.4007 (3)	6877.54 (1)	0.125		145.4013 (1)	6877.516 (6)	0.301	
$f_{1,o} + f_{2,o}$	137.0610 (2)	7296.02 (1)	0.158		137.0614 (1)	7295.999 (7)	0.234	
$f_{4,o} - f_{1,o}$	426.936 (3)	2342.27 (2)	0.085 $\star$		426.455 (2)	2344.91 (1)	0.140	
$f_{4,-} - f_{2,-}$	519.600 (4)	1924.56 (2)	0.078 $\star$		-	-	-	-
$f_{4,o} - f_{2,o}$	519.110 (4)	1926.37 (1)	0.078 $\star$	1.81	519.093 (4)	1926.440 (1)	0.119 $\star$	
$f_{4,+} - f_{2,+}$	-	-	-	-	518.636 (2)	1928.136 (7)	0.088 $\star$	1.696

$\star$ the frequency was detected below 3σ

6.4.1.1 Significance threshold

We adopted a randomisation technique to determine the detection thresholds for the *Kepler* light curve. In this process, we bootstrap the *Kepler* data, keeping the times of the individual observations in place, but randomise the sequence of the fluxes. For each of these randomised light curves we compute the discrete FT as described above and we record the highest amplitude from each of the randomisations. The process of randomising is repeated a large number of times, building up a smooth cumulative distribution of the highest recorded amplitudes, from which the 3σ threshold is determined, i.e. 99.7% of the highest amplitudes recorded in the randomised light curves fall below that threshold. We found that the 3σ threshold converges after about a thousand randomisations, and, to err on the side of caution, we used 3000 randomisations for the final calculation of the significance thresholds. In the case of each individual quarter, the $3\,\sigma$ threshold for Q12 is 0.138% and Q16 is 0.130%. Strictly speaking, this threshold only applies to the highest amplitude signal detected in the *Kepler* light curves, and the entire process would need to be repeated after pre-whitening the *Kepler* data with the highest amplitude signal, carrying on in an iterative fashion until no signal satisfies the $3\,\sigma$ threshold. However, we have experimented with a *Kepler* light curve that had all pulsation signals (Table 6.4) and spurious signals removed, and the resulting $3\,\sigma$ threshold is 0.132% in the case of the Q12 data. It is therefore not significantly different from that derived from the original *Kepler* light curve.

Note that this method yields more conservative significance thresholds than the more widely adopted method which uses $4\langle \mathrm{A} \rangle$ as the limit to consider significant peaks, where $\langle \mathrm{A} \rangle$ corresponds to the average amplitude of the amplitude power spectrum (see Section 5.4 of Aerts et al. 2010 and references therein). We find that $4\langle \mathrm{A} \rangle = 0.113\%$ for the Q12 run, and $4\langle \mathrm{A} \rangle = 0.099\%$ for Q16. As KIC 11911480 was the first ZZ Ceti we discovered, we used both methods to detect significant pulsation modes. However, in the case of the three other ZZ Cetis observed with *Kepler* and presented in the next section, we simply adopt the $4\langle \mathrm{A} \rangle$ method to determine their significant pulsation modes.

6.4.1.2 Pulsation modes of KIC 11911480

In the amplitude power spectra of KIC 11911480 (Figure 6.6), we mark the *Kepler* spurious frequencies taken from the Data Characteristic handbook[8]. These spurious frequencies are multiples of 1/LC period, where LC corresponds to long-cadence exposures of 29.4 min. Additional spurious frequencies, unrelated to the inverse of the LC period, have been detected from the analysis of many early *Kepler* quarters. Some components in the power spectrum of KIC 11911480 appear and disappear between both quarters and it is clear that the amplitudes of the detected frequencies are generally stronger in Q16 than in Q12 (see Figure 6.7). The error on the

[8]The Data Characteristic handbook can be downloaded from the following webpage: http://keplerscience.arc.nasa.gov/DataAnalysis.shtml

amplitudes is 0.028% (obtained using period analysis tools). This large overall amplitude variation between Q12 and Q16 may be explained by the fact that our target was observed with two different custom masks in both quarters, indicating that the amount of flux received in each quarter was different.

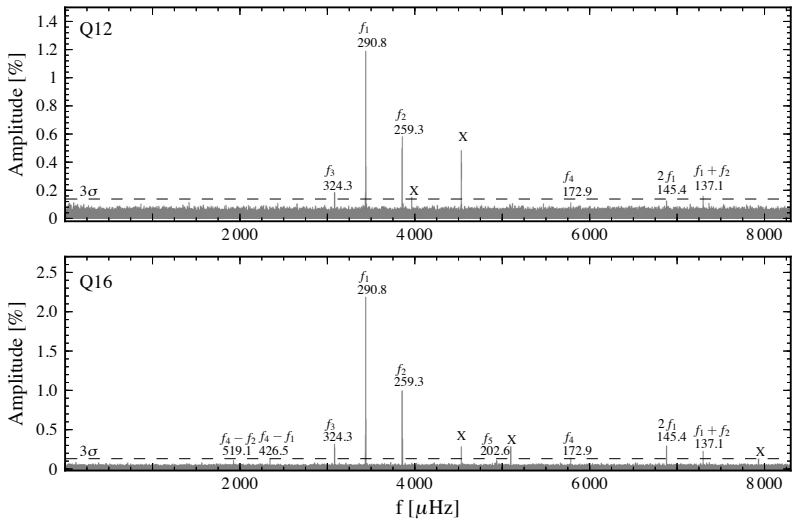

Figure 6.6: *Amplitude power spectrum of KIC 11911480 from the Q12 (top) and Q16 (bottom) data. The Xs above certain frequencies indicate the Kepler spurious frequencies and the dashed horizontal line corresponds to the 3σ threshold limit. The values noted above each significant frequency corresponds to period (in seconds) of the given pulsation mode.*

We calculate the frequencies and amplitudes of each significant peak, using a least-squares sine wave fitting routine at each individually selected peak from the FT. We find seven pulsation modes detected above the $3\,\sigma$ threshold in the Q16 data set, four of which are independent (Table 6.4). In the Q12 data, we find five pulsations modes above the $3\,\sigma$ threshold, out of which three are independent. The pulsation modes found in Q12 are all detected in Q16 as well. In Table 6.4, we also add two pulsation periods, f_5 and $f_4 - f_1$, which are not significantly detected in Q12 but they are very close to the Q16 $3\,\sigma$ threshold. Their amplitudes are larger than the $4\langle \mathrm{A} \rangle = 0.099\%$ for Q16. The main reason why we believe the detection of f_5 is because it shows splitting with the same frequency separation as the other significant modes. Also, $f_4 - f_1$ is a non-linear combination of two significant frequencies. In total, we find that KIC 11911480 has five independent pulsation modes and four combination frequencies. Non-linear combination frequencies are not generated by the same physical mechanism driving the pulsations of the star. Brickhill (1992) showed that these combination frequencies may come from the distortion of the sinusoidal waves associated to the normal modes travelling from the convective to the radiative zone of the star, where the heat transport changes dramatically at the base of the hydrogen ionization zone (see also Wu & Goldreich 1999; Vuille 2000; Wu 2001; Yeates et al. 2005). Their amplitudes can provide information on the physical conditions in the WD convection zone (Montgomery, 2005).

We notice splitting of some of the modes, which are denoted with '+' or '-' signs and placed next to the central component ('o') of each pulsation mode in Table 6.4. Not all components of a multiplet are always detected (see Figure 6.7). A full asteroseismic study is presented in the following Section, which was possible thanks to a collaboration with the Astronomy & Astrophysics group at the University of Montreal. Nevertheless, we have attempted to match the observed periods to adiabatic pulsation models with the constraints provided by our spectroscopic mass and temperature determinations. The models of Romero et al. (2012) of a 0.57 $\mathrm{M}_{\odot}$, 12 101 K WD with a thick ($10^{-3.82}$ M_{WD}) hydrogen layer mass are in agreement with the observed periods of f_1 to f_4 if these four modes have $\ell = 1$ and $k = 4, 3, 5, 2$, respectively. However, this is only a qualitative guess at a solution, and a full asteroseismic analysis is required to arrive at a more secure identification of these modes. We show in the following Section that indeed this qualitative guess does not correspond to the correct asteroseismic solution, yet remains very close to it.

6.4.1.3 Rotation rate of KIC 11911480

We see what appears to be multiplet splitting of some modes, which is a direct manifestation of the star's rotation rate (Figure 6.7). In the limit of slow rotation, the difference between the frequency of one mode of indices l, k, m ($\sigma_{k,lm}$) and the frequency in the non-rotating case ($\sigma_{k,l}$) is:

$$\sigma_{k,l,m} - \sigma_{k,l} = m(1 - C_{k,l})\Omega \tag{6.1}$$

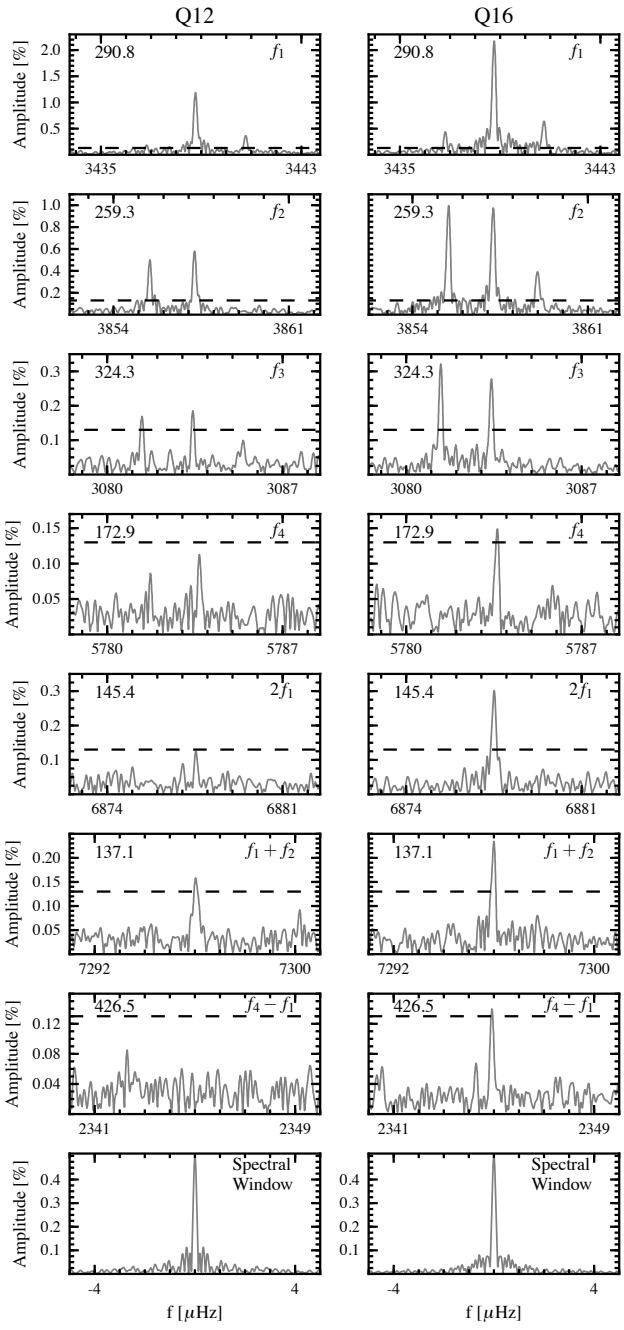

Figure 6.7: *Kepler amplitude power spectra of KIC 11911480, our first ZZ Ceti discovered in the Kepler field from KIS. The panels on the left correspond to the Q12 data, whereas the ones on the right correspond to the Q16 data. The dashed lines correspond to the 3σ significance threshold in each dataset. The top left hand-side of each panel gives the corresponding period (in seconds). The bottom panels in both columns show the spectral window of each quarter. Splitting of the modes is a direct indication of the star's rotation (note that it is common that not all modes of a multiplet are detected at a particular epoch, see e.g. Table 5 of Kepler et al. 2003).*

where $C_{k,l}$ comes from the Coriolis force term in the momentum equation and Ω is the rotation frequency (Winget et al., 1991; Vauclair, 1997). Note that this equation is the classical first order expansion. We provide a more detailed explanation of the effect of rotation on the power spectrum of a pulsating WD in the following Section. In the asymptotic limit for g-modes, meaning in the case of very large values of k, $C_{k,l}$ only depends on the degree of the mode: $C_{k,l} \simeq \frac{1}{l(l+1)}$. When a pulsating WD rotates, each mode of degree l can be split into $2l+1$ components. We see splitting into three components in several modes in the power spectrum of KIC 11911480 (see Figure 6.7), which likely corresponds to an $\ell = 1$ mode in those cases, leading to $C_{k,l} \simeq 0.5$. The frequency spacing between the split components of the modes is quite consistent, $1.93 \pm 0.10 \mu$Hz, suggesting these modes are all of the same spherical degree l. This corresponds to a rotation rate of 3.0 ± 0.2 days. However, f_1 to f_4 (with periods from $172.9 - 324.5$ s) are likely low-radial-order and far from the asymptotic limit, so their $C_{k,l}$ values should not be identical, and are not exactly 0.5. If we adopt the $C_{k,l}$ values of the model from Romero et al. (2012) discussed in the previous paragraph, we obtain a rotation rate of 3.5 ± 0.2 days. To best reflect the systematic uncertainties, we adopt a rotation rate of 3.5 ± 0.5 days. These values are in agreement with the initial assumption of *slow body* rotation.

6.4.2 KIC 10132702

We were awarded *Kepler* short-cadence mode observations of KIC 10132702 during Quarter 15 (Q15). The Q15 observations were taken between Oct 5, 2012 - Jan 11, 2013. However, during Q15, the satellite's fine-pointing was lost and it went into safe mode for around a week. This led to the duty cycle of Q15 to being 86.6%.

In the FT of KIC 10132702 (see Figure 6.8), we observe optical variability with periods ranging from 461.0 s to 977.1 s (see Table 6.5 for more details). These periods are within the expected values for ZZ Ceti stars and in this case match the pulsation periods of other known cool ZZ Ceti stars (Mukadam et al., 2004).

6.4.2.1 Pulsation modes of KIC 10132702

Similarly to KIC 11911480, we calculate the frequencies and amplitudes of each significant peak, using a least-squares sine wave fitting routine at each individually selected peak from the FT. We find 20 independent pulsation modes detected above the $4\langle A \rangle$ threshold in the Q15 data set (Table 6.5). The power spectrum of KIC 11911480 looks a lot 'messier' than our first ZZ Ceti. This is commonly seen in the case of cooler DAVs.

6.4.2.2 Rotation rate of KIC 10132702

Here, we also see multiplet splitting of some modes as in KIC 11911480. We use the same method to estimate the rotation rate KIC 10132702, assuming a slow rotation case. We see splitting into two or three components in several modes in the power spectrum of KIC 10132702 which have an average frequency spacing of 1.52 ± 0.33

Table 6.5: *Pulsation frequencies of KIC 10132702 from the Q15 data. Δf corresponds to the frequency spacing between two consecutive frequencies in the table*

	f [μHz]	f_{err} [μHz]	P [s]	P$_{err}$ [s]	A [%]	
$f_{1,-}$	1292.556	0.007	773.6611	0.0039	0.282	
$f_{1,o}$	1293.657	0.003	773.0025	0.0019	0.731	1.101
$f_{1,+}$	1294.795	0.007	772.3233	0.0043	0.298	1.138
$f_{1,++}$	1295.838	0.007	771.7012	0.0043	0.310	1.043
$f_{2,-}$	1228.849	0.008	813.7699	0.0053	0.417	
$f_{2,o}$	1230.795	0.003	812.4833	0.0019	0.727	1.946
$f_{2,+}$	1232.864	0.010	811.1192	0.0063	0.231	2.069
$f_{3,o}$	2169.016	0.005	461.03851	0.00097	0.468	
$f_{4,o}$	1378.895	0.005	725.2186	0.0026	0.451	
$f_{4,+}$	1381.096	0.011	724.0627	0.0057	0.187	2.201
$f_{5,o}$	1612.441	0.007	620.1776	0.0025	0.301	
$f_{6,-}$	1250.987	0.008	799.3689	0.0048	0.296	
$f_{6,o}$	1252.269	0.010	798.5512	0.0066	0.204	1.282
$f_{6,+}$	1253.511	0.009	797.7593	0.0059	0.201	1.242
$f_{7,o}$	1624.915	0.008	615.4168	0.0029	0.289	
$f_{8,o}$	1070.328	0.008	934.2927	0.0074	0.266	
$f_{9,-}$	1395.464	0.009	716.6075	0.0045	0.194	
$f_{9,o}$	1397.087	0.008	715.7752	0.0042	0.258	1.623
$f_{9,+}$	1398.686	0.011	714.9566	0.0056	0.199	1.599
$f_{10,o}$	1199.069	0.009	833.9805	0.0062	0.232	
$f_{10,+}$	1200.609	0.011	832.9109	0.0075	0.204	1.54
$f_{11,o}$	1023.451	0.008	977.0864	0.0081	0.231	
$f_{12,o}$	1547.189	0.010	646.3334	0.0041	0.218	
$f_{13,-}$	1204.101	0.009	830.4950	0.0065	0.178	
$f_{13,o}$	1206.226	0.009	829.0320	0.0064	0.209	2.125
$f_{14,-}$	1183.223	0.010	845.1492	0.0072	0.177	
$f_{14,o}$	1189.241	0.011	840.8722	0.0076	0.203	5.982
$f_{15,o}$	1465.971	0.011	682.1417	0.0052	0.198	
$f_{16,o}$	1167.049	0.010	856.8622	0.0071	0.194	
$f_{17,o}$	1135.467	0.010	880.6948	0.0076	0.192	
$f_{18,o}$	1315.722	0.011	760.0392	0.0063	0.189	
$f_{19,o}$	1256.908	0.011	795.6033	0.0073	0.187	
$f_{19,+}$	1258.523	0.011	794.5821	0.0072	0.182	1.615
$f_{20,-}$	1117.708	0.012	894.6880	0.0098	0.177	
$f_{20,o}$	1120.713	0.011	892.2888	0.0088	0.185	3.005

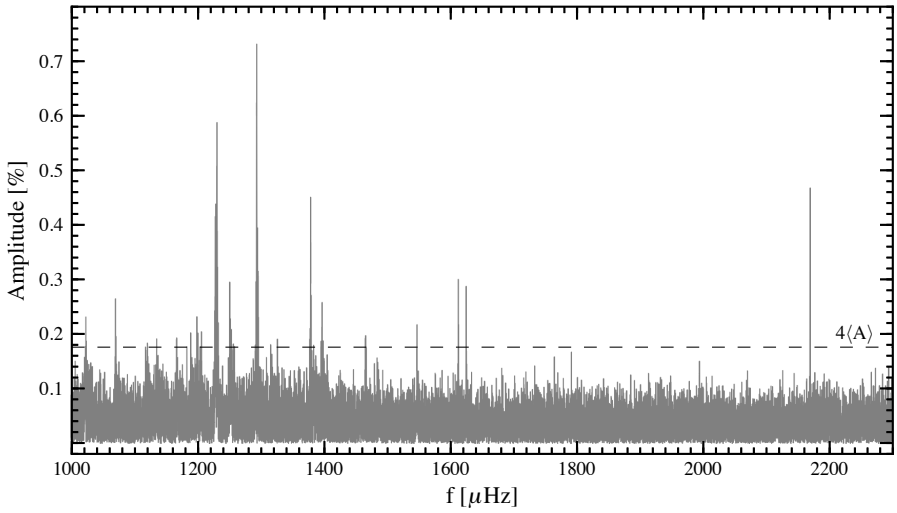

Figure 6.8: *Amplitude power spectrum of KIC 10132702 from Q15. The dashed horizontal line corresponds to the 4⟨A⟩ threshold limit.*

μHz. We assume that these correspond to an $\ell = 1$ mode, leading to $C_{k,l} \simeq 0.5$. This corresponds to a rotation rate of 3.8 $\pm$ 0.8 days. However, in the case of f_{14} and f_{20}, we notice that the frequency splitting is larger. If we assume that these two pulsation modes correspond to an $\ell = 2$ mode, with an average frequency spacing of 3.01 $\pm$ 0.01 μHz, this leads to a rotation rate of 3.2 $\pm$ 0.1 days.

In both cases, the calculated asteroseimic rotation rates are similar and agree with the assumption made of WDs being slow rotators (Kawaler & Hostler, 2005). However, a full asteroseismic analysis of the power spectrum of KIC 10132702 must be done in order to find the actual pulsation modes detected here and to calculate a more reliable rotation period of the star.

This DAV is much cooler than KIC 11911480, which can be seen in the period range of its pulsation modes as well as from the spectroscopic values: $T_{\rm eff,KIC119} =$ 12 160 $\pm$ 250 K vs $T_{\rm eff,KIC101} =$ 11 048 $\pm$ 217 K. Cool DAVs are expected to have periods ranging between 600 and 1000 s. This is indeed the case for all the periods detected here, except for f_3.

6.4.3 KIC 04357037

We were awarded *Kepler* short-cadence mode observations of KIC 04357037 during one month of Q16. In this case, the observations were taken between Jan 29 - Mar 6, 2013. The duty cycle was 99.02%.

In the FT of KIC 04357037 (Figure 6.9), we observe optical variability with periods ranging from 158.1 s to 956.1 s (see Table 6.6 for more details). These periods are once again within the expected values for ZZ Ceti stars. Simply looking

at the range over which pulsations are detected suggests that KIC 04357037 has an effective temperature between that of KIC 11911480 and KIC 10132702. It is indeed the case when inspecting the spectroscopic value: $T_{\rm eff,KIC119} = 12\,160 \pm 250$ K vs $T_{\rm eff,KIC101} = 11\,048 \pm 217$ K vs $T_{\rm eff,KIC043} = 11\,898 \pm 200$ K.

6.4.3.1 Pulsation modes of KIC 04357037

Similarly to the previous two DAVs, we calculate the frequencies and amplitudes of each significant peak, using a least-squares sine wave fitting routine at each individually selected peak from the FT. We find 12 independent pulsation modes detected above the $4\langle A\rangle$ threshold in the data set, as well as one non-linear combination frequency (Table 6.6). We show the detected frequencies in Figure 6.9.

6.4.3.2 Rotation rate of KIC 04357037

If we consider all triplets except for f_5 and f_7, we find an average frequency spacing of $\sim 6.89 \pm 0.53$ μHz, which leads to a rotation rate of 0.84 ± 0.06 days if we assume $\ell = 1$ mode and a rotation rate of 1.40 ± 0.11 days in the case of $\ell = 2$ modes. In the case of f_5, we find a frequency spacing of 4.62 ± 0.03 μHz, leading to a rotation period of 1.25 ± 0.01 days or 2.09 ± 0.01 days for $\ell = 1$ or $\ell = 2$ modes respectively. Finally, the frequency spacing in f_7 is 2.52 ± 0.02 μHz, which leads to a rotation rate of 2.30 ± 0.02 days or 3.83 ± 0.03 days for $\ell = 1$ or $\ell = 2$ modes respectively. Once again, a final rotation period determination has to await a full asteroseismic analysis of the power spectrum of KIC 04357037.

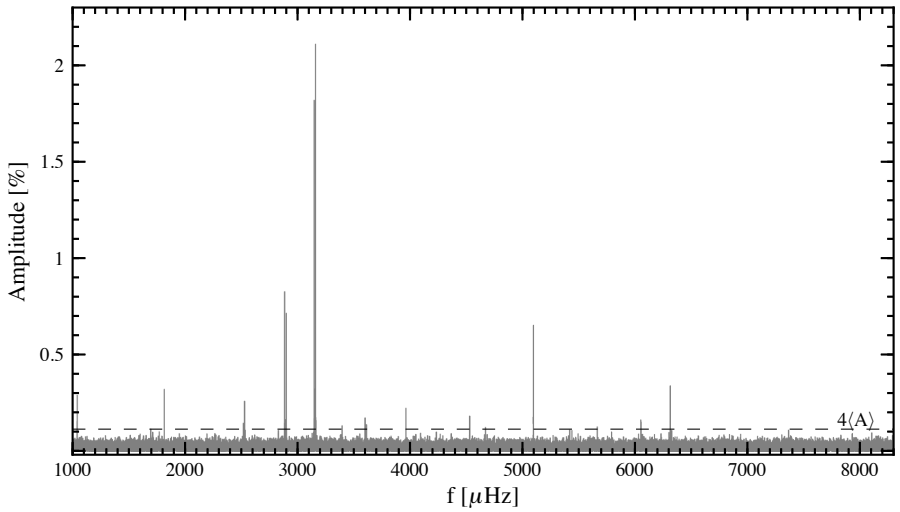

Figure 6.9: *Amplitude power spectrum of KIC 04357037 from the Q16 data.*

Table 6.6: *Pulsation frequencies of KIC 04357037 from one month of Q16 observations. Δf corresponds to the frequency spacing between two consecutive frequencies in the table*

	$f[\mu\text{Hz}]$	$f_{err}[\mu\text{Hz}]$	P [s]	P_{err} [s]	A [%]	Δ
$f_{1,-}$	3150.328	0.002	317.4273	0.0002	1.814	
$f_{1,o}$	3156.470	0.005	316.8096	0.0006	0.297	6.142
$f_{1,+}$	3162.629	0.002	316.1927	0.0002	2.085	6.159
$f_{2,-}$	2888.334	0.005	346.2203	0.0007	0.827	
$f_{2,o}$	2895.724	0.018	345.3368	0.0021	0.155	7.390
$f_{2,+}$	2903.131	0.006	344.4557	0.0007	0.716	7.407
$2\,f_{1,-}$	6300.598	0.044	158.7151	0.0011	0.097	
$2\,f_{1,o}$	6312.938	0.013	158.4048	0.0003	0.341	12.340
$2\,f_{1,+}\star$	6325.282	0.038	158.0957	0.0010	0.107	12.344
$f_{3,o}$	1819.110	0.014	549.7193	0.0042	0.323	
$f_{4,o}$	1045.881	0.015	956.132	0.014	0.292	
$f_{5,o}$	2531.930	0.016	394.9556	0.0025	0.261	
$f_{5,+}$	2536.554	0.035	394.2357	0.0054	0.108	4.624
$f_{6,o}$	3602.544	0.025	277.5816	0.0019	0.175	
$f_{7,o}$	6050.971	0.026	165.2627	0.0007	0.164	
$f_{7,+}$	6053.494	0.023	165.1939	0.0006	0.152	2.523
$f_{8,-}\star$	2513.726	0.051	397.8158	0.0081	0.079	
$f_{8,o}$	2520.777	0.027	396.7031	0.0042	0.148	7.051
$f_{9,o}$	3615.002	0.033	276.6250	0.0025	0.140	
$f_{10,-}\star$	4664.210	0.035	214.3986	0.0016	0.088	
$f_{10,o}$	4671.411	0.033	214.0681	0.0015	0.126	7.201
$f_{11,o}$	5420.110	0.027	184.4981	0.0009	0.113	
$f_{12,+}$	5439.649	0.036	183.8354	0.0012	0.110	

$\star$ the frequency was detected below $4\langle\text{A}\rangle$

6.4.4 KIC 07594781

6.4.4.1 Pulsation modes of KIC 07594781

At the same time as KIC 04357037, we were also awarded *Kepler* short-cadence mode observations of KIC 07594781 during one month of Q16. The observation dates and duty cycle are therefore identical to those of KIC 04357037.

In the FT of KIC 07594781 (Figure 6.10), we observe optical variability with periods ranging from 160.7 s to 1410.1 s (see Table 6.7 for more details). This ZZ Ceti has the largest range of observed periods out of all four presented here, yet the periods found are once again within the expected values for ZZ Ceti stars. The longest periods correspond to combination frequencies, and most of its independent periods range from ~ 161 s to ~ 684 s.

We calculate the frequencies and amplitudes of each significant peak, using a least-squares sine wave fitting routine at each individually selected peak from the FT. We find 22 independent pulsation modes detected above the $4\langle A\rangle$ threshold in the data set, as well as 13 non-linear combination frequencies (Table 6.6). We show the detected frequencies in Figure 6.10. KIC 07594781 has the richest amplitude power spectrum out of all the ZZ Ceti we observed with *Kepler*.

Table 6.7: *Pulsation frequencies of KIC 07594781 from one month of Q16 observations. Δf corresponds to the frequency spacing between two consecutive frequencies in the table*

	$f[\mu$Hz]	$f_{err}[\mu$Hz]	P [s]	P_{err} [s]	A [%]	Δ
f_1	3048.361	0.002	328.045	0.000	1.413	
f_2	3383.923	0.004	295.515	0.000	0.898	
$f_{3,-}$	2663.786	0.025	375.406	0.004	0.141	
$f_{3,o}$	2666.682	0.009	374.998	0.001	0.373	2.896
$f_{3,+}$	2669.210	0.005	374.643	0.001	0.567	2.528
f_4	3575.850	0.008	279.654	0.001	0.454	
$f_{5,o}$	3372.984	0.009	296.473	0.001	0.430	
$f_{5,+}$	3378.472	0.014	295.992	0.001	0.273	5.488
f_6	2854.443	0.011	350.331	0.001	0.376	
$f_{7,o}$	3554.655	0.012	281.321	0.001	0.317	
$f_{7,+}$	3560.080	0.035	280.893	0.003	0.094	5.425
$f_{8,o}$	2524.261	0.013	396.156	0.002	0.305	
$f_{8,+}$	2529.891	0.013	395.274	0.002	0.280	5.630
f_9	6096.714	0.013	164.023	0.000	0.291	
f_{10}	4835.143	0.015	206.819	0.001	0.261	
$f_{11,-}$	6222.011	0.034	160.720	0.001	0.078	

$f_{11,o}$	6223.929	0.021	160.670	0.001	0.184	1.918
f_{12}	2802.146	0.022	356.869	0.003	0.175	
$f_{13,o}$	6045.927	0.037	165.401	0.001	0.090	
$f_{13,+}$	6047.641	0.021	165.354	0.001	0.165	1.714
f_{14}	2081.828	0.024	480.347	0.005	0.158	
f_{15}	2162.817	0.033	462.360	0.007	0.115	
f_{16}	3828.219	0.032	261.218	0.002	0.114	
f_{17}	1462.089	0.034	683.953	0.016	0.111	
f_{18}	5471.447	0.036	182.767	0.001	0.103	
f_{19}	1521.665	0.035	657.175	0.015	0.103	
f_{20}	1243.682	0.032	804.064	0.021	0.102	
f_{21}	3740.007	0.036	267.379	0.003	0.101	
$f_{22,o}$	2288.705	0.041	436.928	0.008	0.089	
$f_{22,+}$	2290.050	0.040	436.672	0.008	0.091	1.354
$f_{1,} - f_{15}$	885.570	0.006	1129.216	0.007	0.649	
$f_{7,o} - f_{3,o}$	887.739	0.017	1126.457	0.021	0.220	
$2f_{3,+}$	5338.541	0.017	187.317	0.001	0.218	
$f_{10} - f_1$	1786.754	0.019	559.674	0.006	0.173	
$f_1 + f_6$	5902.799	0.024	169.411	0.001	0.161	
$f_1 + f_2$	6432.267	0.026	155.466	0.001	0.132	
$f_1 + f_{10}$	7883.516	0.031	126.847	0.001	0.124	
$f_{13,+} - 2f_{3,+}$	709.158	0.031	1410.122	0.062	0.112	
$f_{5,o} + f_{7,o}$	6933.137	0.034	144.235	0.001	0.110	
$f_9 - f_{7,o}$	2542.544	0.037	393.307	0.006	0.101	
$f_1 + f_{5,o}$	6421.369	0.039	155.730	0.001	0.091	
$f_1 + f_{7,o}$	5572.602	0.037	179.449	0.001	0.084	
$f_1 + f_4$	6624.263	0.044	150.960	0.001	0.075	

6.4.4.2 Rotation rate of KIC 07594781

If we suppose that the frequencies f_3, f_5, f_7 and f_8 correspond to l=2 modes, then the average frequency splitting is 2.75 $\pm$ 0.10 μHz, which leads to a rotation rate of 3.51 $\pm$ 0.13 days. We also notice narrower frequency splitting in f_{11}, f_{13} and f_{22} with an average value of 1.66 $\pm$ 0.23 μHz. If we suppose in this case that these correspond to l=1 modes, then this leads to a rotation rate of 3.48 $\pm$ 0.49 days. These two values are in very good agreement, but once again, it is impossible to confidently conclude on a precise rotation rate without a full asteroseismic study of this ZZ Ceti star.

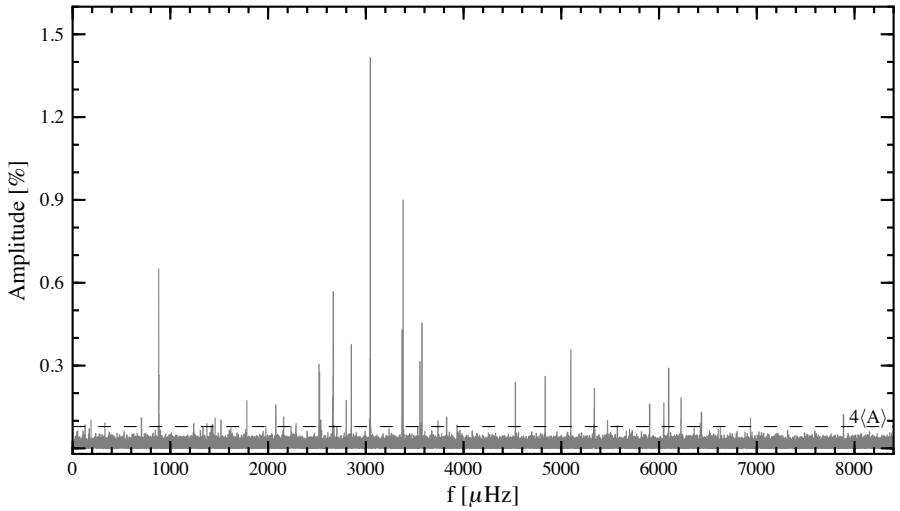

Figure 6.10: *Amplitude power spectrum of KIC 07594781 from the Q16 data.*

6.4.5 Summary

The asteroseismic studies of our four ZZ Ceti stars observed with *Kepler* have enabled us to confirm our spectroscopic findings, as well as estimate rotation rates based on the pulsation modes we detected in each case. The values found are in agreement with previous rotation frequencies found in ZZ Ceti stars. Fontaine & Brassard (2008) give an overview on pulsating WDs and provide the asteroseismic rotation rates of seven ZZ Ceti stars, spanning from 9 to 55 hours, i.e. 0.4 to 2.3 days. In the case of non-pulsating WDs, the sharp NLTE core of the Hα line in their spectra has been used in many studies to measure the projected rotation velocities of the stars (Heber et al., 1997; Koester et al., 1998; Karl et al., 2005). These are upper limits on the spin periods of the white dwarfs, indicating that they are probably spinning slower than determined using their projected rotational velocities. When comparing the asteroseismic rotation rates with those found for non-pulsating WDs, we notice that the latter are faster. We show in Figure 6.11 the distribution of the rotation rates in both cases. Under the asteroseismic rates, we include the values mentioned in Fontaine & Brassard (2008) as well as our results presented here. The projected rotation velocities are all taken from Karl et al. (2005). Despite the fact that one method delivers faster rotation rates than the other, we are able to conclude that: isolated WDs are generally *slow rotators*. This result can be justified by a rough estimation of the expected rotation period of WDs, assuming the conservation of angular momentum during the evolution of a Sun-like star to a WD. The angular momentum is $L = I \times \omega$, where I corresponds to the moment of inertia and is equal to $\frac{2}{5}MR^2$ assuming the star is a sphere, and ω is the angular velocity and can be written as $\frac{2\pi}{T}$ where T is the rotation period. If we consider conservation of angular momentum then we find $T_{WD} \simeq 0.6 \times 10^{-4} \times T_{\odot} \simeq 0.00152$ days.

This expected value is much faster than the rotation periods we find with

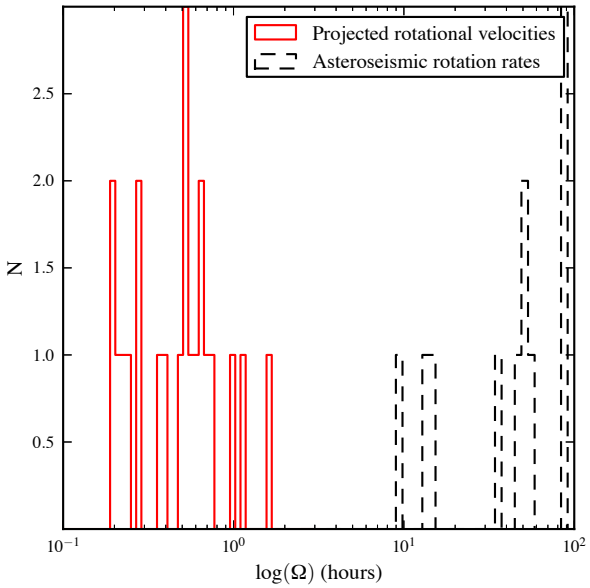

Figure 6.11: *Distribution of the rotation rates of isolated WDs. The red histogram corresponds to upper limits of the projected rotational velocities of single non-pulsating WDs taken from Karl et al. (2005), whereas the black dashed histogram shows the rotation rate of ZZ Ceti stars taken from Fontaine & Brassard (2008) as well as our sample.*

observational data. This shows that there is a loss of angular momentum at some stage of stellar evolution which is not yet very well explained. Our results show that WDs (whether pulsating or non-pulsating) are slow rotators, unlike what we expect from our rough theoretical calculation.

In the final three months of my PhD, I was granted a fellowship by the University of Warwick to visit my collaborators at the University of Montreal in Canada. Professor Gilles Fontaine and his PhD student Noemi Giammichele welcomed me for two weeks, to show me the method they developed to analyse asteroseimic data of ZZ Ceti stars. As new as the theoretical approach is to me, I attempt to summarize their method and present the results found for KIC 11911480 in the following Section. The results shown in this Section are obtained using their method. My contribution to this work consists of the observational data but the theoretical analysis is done by Noemi Giammichele. This following Section is part of an article in preparation by Giammichele et al. (2014).

6.5 Asteroseismic model of KIC 11911480

An asteroseismic model of a pulsating WD, if successfully determined, can provide its global structural parameters and information on its internal structure and evolu-

tionary state. The main goal of an asteroseismic exercise is to simultaneously match the observed pulsation periods with periods computed from stellar models, and obtain an optimal model which consists of a good physical solution of the star under consideration. Here we will briefly describe the different steps taken to obtain such a solution in the case of KIC 11911480. The method used here has been previously successful in many cases of hot pulsating subdwarf stars (Charpinet et al., 2009, 2011; Van Grootel et al., 2013).

6.5.1 Method

The method of asteroseismic analysis mainly consists of searching for a suitable model in parameter space which has a computed period spectrum that matches the observed one. For the comparison of the period data, we must consider the $m = 0$ (central) components of multiplets, as well as independent pulsation periods only (no nonlinear combination frequencies are taken into account in this exercise). It may seem a bit tricky to select the $m = 0$ components of pulsation modes, especially in the case of even number splittings, but this ambiguity does not cause significant problems at the level of accuracy with which the periods can be matched. In the case of KIC 11911480, we have five independent observed periods (P_{obs}) from the power spectrum (see Table 6.4).

The search for the optimal model is done using a double-optimization method, which at first calculates the best fit to the observed periods with the computed ones (from a given model) and then searches for the best-matching model in parameter space. At this stage, the computed periods of the models are obtained using the adiabatic approximation since it does not affect the calculated theoretical periods and significantly simplifies the problem compared to the nonadiabatic approach. The quality of the match between the observed and theoretical periods is tested with a merit function, similar to a χ^2, defined by,

$$S^2 = \sum_{i=1}^{N_{obs}} (P^i_{obs} - P^i_{theo})^2, \tag{6.2}$$

where $N_{obs} = 5$ in our case. Similarly to the χ^2 method, we are searching for the most realistic and credible (in a physical sense) model with the minimum S^2 in parameter space. In order to identify minimal values for S^2, a few million models and period spectra of WDs must be computed, which requires considerable computing resources.

The input parameters required to define a full WD model are: the effective temperature, the surface gravity, the thicknesses of the H and He layers, the core composition and the convective efficiency. It is important to note that the parameters describing the H and He layers not only take into account their total masses (ΔM(He) and ΔM(H)), but also the actual composition profiles in the transition zones themselves. In the current asteroseismological exercise, we used the following input parameter ranges: $11\,000$ K $\leq T_{\mathrm{eff}} \leq 13\,000$ K, $7.95 \leq \log g \leq 8.15$,

-8.0 $\leq \log \Delta M(\mathrm{H})/M \leq$ -2.0 and -4.0 $\leq \log \Delta M(\mathrm{He})/M \leq$ -1.5. Also the profiles of compositions of H and He in their respective transition zones are defined as A_H and A_{He}. We allow them to vary between 1 and 10 ($1 \leq \mathrm{A}_H \leq 10$ and $1 \leq \mathrm{A}_{He} \leq 10$) . These coefficients must be larger than 1 in order to indicate that the materials have been separated. The double-optimization procedure is done using a genetic algorithm developed by Charpinet et al. (2008). It is important to note that for this exercise to be valid, all observed periods must be fitted *simultaneously*. The final output of this exercise yields several fits with different values of S^2, T_{eff}, $\log g$, $\log \Delta M(\mathrm{H})/M$, $\log \Delta M(\mathrm{He})/M$, core composition, A_H, A_{He} and the mode identifications of the matched periods. The errors are also returned by the algorithm and 2 or 3D maps in any combination of parameter space can also be obtained.

6.5.2 Optimal model

In the case of KIC 11911480, the optimal model that was found had a merit function S^2 of 6.61×10^{-12}. The genetic algorithm returned the following results for the best parameters found: $T_{\mathrm{eff}} = 11\,694 \pm 100$ K, $\log g = 8.03 \pm 0.05$, $\log \Delta M(\mathrm{H})/M =$ -3.56 $\pm$ 0.16, $\log \Delta M(\mathrm{He})/M =$ -2.42 $\pm$ 0.13, Oxygen core composition = 43.4%, A_H = 1.39, A_{He} = 2.48. The values of T_{eff} and $\log g$ found for the optimal model are consistent with the spectroscopic measurements presented earlier in this Chapter.

The core of KIC 11911480 is made out of 43% O and 57% C, surrounded by a layer of He and itself surrounded by the pure H envelope. The chosen optimal model and fit also returned the mode identifications of the matched periods, which we provide in Table 6.8, along with their associated C_{kl} and $\log E_{kin}$ values. The identified modes are all consecutive radial order modes belonging to the family of degree $l = 1$. This result is consistent with the prediction from nonadiabatic theory that pulsation modes are excited in consecutive modes. In order to better visualise the propagation of each of these pulsation modes, we plot their normalized weight functions as a function of $\log q$ in Figure 6.12. It is clear that all the low-order g-modes only probe the envelope of KIC 11911480, except for the $k = 6$ one (purple), which propagates deeper in the star. This is the very first identification of a pulsation mode of a ZZ Ceti star probing a region deeper than the He envelope. We also clearly see from Figure 6.12 that some modes are partially confined below the H/He transition zone (where $\log q \simeq$ -3), while others are partially trapped above it. The modes obviously remain global but they are more sensitive to the conditions found above or below, depending on whether they are trapped or confined.

6.5.3 Stellar rotation

We repeat the same exercise as in the previous paragraph, using the same genetic algorithm, but this time we add a solid body rotation effect to the models and therefore include the periods of the multiplets detected in the power spectrum of KIC 11911480. There is no evidence that *all* WDs rotate as solid bodies but it has been seen in the case of a pulsating WD where the modes penetrated deep inside the star (Charpinet et al., 2009), therefore we assume a solid body rotation here. Despite the fact that the multiplet components of f_4 and f_5 have S/N < 4.5, their

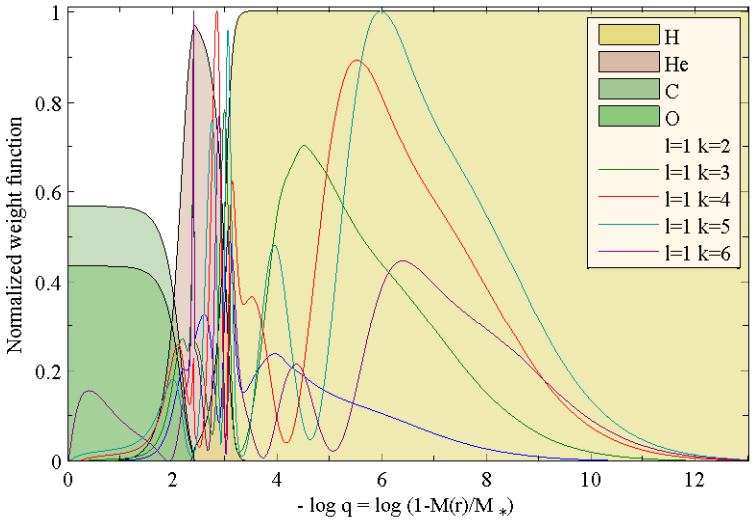

Figure 6.12: *Weight function of the five identified pulsation modes of KIC 11911480 as a function of* $\log q$.

Table 6.8: *Identified modes and their periods of optimal model of KIC 11911480.*

l	k	P_{obs} (s)	P_{theo} (s)	$\lvert\Delta P\rvert$ (s)	C_{kl}	$\log E_{kin}$
1	2	172.901	172.896	0.005	0.472	46.824
1	3	202.569	202.567	0.002	0.477	46.193
1	4	259.254	259.249	0.005	0.474	45.596
1	5	290.802	290.799	0.003	0.454	45.299
1	6	324.317	324.526	0.209	0.345	45.489

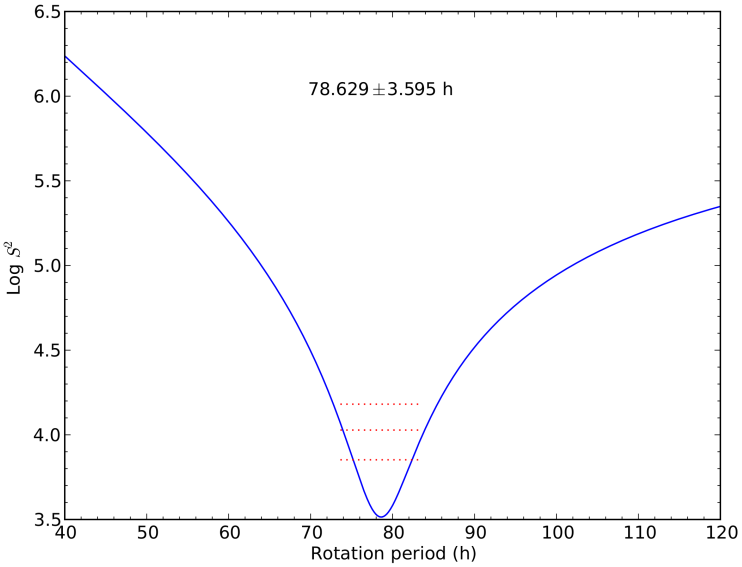

Figure 6.13: *Logarithm of merit function S^2 in terms of rotation period in hours. the red horizontal dotted lines indicate the 1σ, 2σ and 3σ limits (from bottom to top). The minimum value for* $\log S^2$ *is for P_{rot} = 78.63 ± 3.6 h.*

frequency splittings are consistent with those of the other more significant multiplets. Therefore we include them in this study and provide all the periods and frequencies in Table 6.9. This step of searching for the optimal model with the effect of rotation can be seen as a verification of the validity of the model previously obtained. We present our results in Table 6.9. We notice that the theoretical periods (frequencies) remain consistent with the observed ones and the identified pulsation modes are the same as those previously determined. In order to remain consistent, we choose to keep the values obtained using the adiabatic approach.

We can calculate the rotation period of KIC 11911480 using the C_{kl} values returned by the optimal model solution, in combination with Equation 2.8. Also, using a merit function S^2 in terms of the assumed rotation period can help us find its best value. We illustrate this in Figure 6.13 where the blue curve corresponds to the logarithm merit function as a function of the rotation period and the red horizontal dotted lines indicate the 1σ, 2σ and 3σ limits (from bottom to top). The final 'best' value of the rotation period of KIC 11911480 is clearly defined by a minimum value for $\log S^2$ at P_{rot} = 78.63 ± 3.6 h, which corresponds to P_{rot} = 3.28 ± 0.15 days. This confirms our initial assumption of *slow rotation* and also agrees with the rotation rate value of 3.5 ± 0.5 days, calculated using the frequency spacing between the splittings.

Figure 6.14 shows the agreement between the observed (red) and computed (blue) pulsation frequencies of KIC 11911480, when including the effect of solid body rotation. In addition, it is interesting to look at the rotation kernel of each of the five

Table 6.9: *Pulsation frequencies of KIC 11911480 from the combined Q12 and Q16 data (see Table 6.4). The uncertainties are given in between brackets. Δf corresponds to the frequency spacing between two consecutive frequencies in the table.*

	l	k	m	P ($P_{\rm err}$) (s)	f ($f_{\rm err}$) (μHz)	A (%)	Δf(μHz)	S/N
...	1	5	+1	290.9674 (3)	3436.811 (4)	0.442		19.4
f_1	1	5	0	290.8024 (1)	3438.761 (1)	2.272	1.949	99.7
...	1	5	-1	290.6341 (2)	3440.752 (2)	0.723	1.991	31.7
...	1	4	+1	259.3735 (1)	3855.444 (2)	1.030		44.9
f_2	1	4	0	259.2535 (1)	3857.229 (2)	1.044	1.784	45.5
...	1	4	-1	259.1341 (3)	3859.006 (4)	0.419	1.770	18.3
f_3	1	6	0	324.5301 (5)	3081.379 (5)	0.340		14.8
...	1	6	-1	324.3171 (6)	3083.402 (6)	0.295	2.023	12.8
f_4	1	2	-1	172.9013 (3)	5783.65 (1)	0.157		6.9
f_5	1	3	0	202.5691 (5)	4936.59 (1)	0.130		5.6

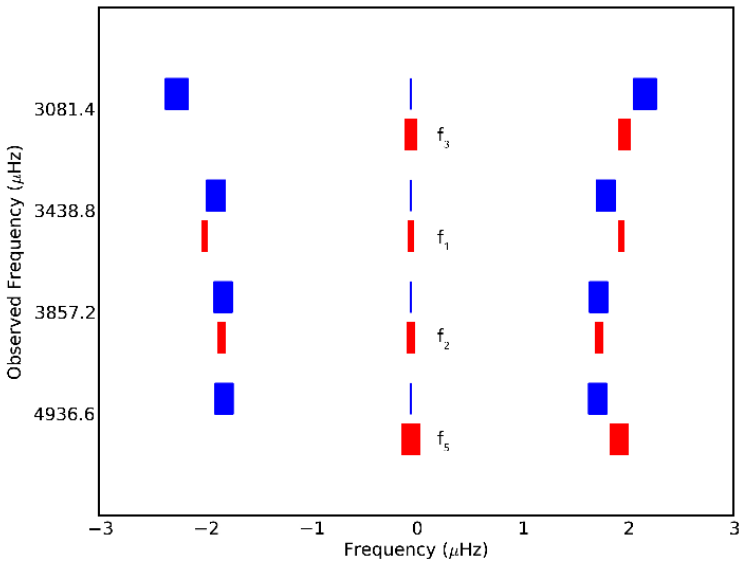

Figure 6.14: *Observed (red) and computed (blue) frequencies of KIC 11911480. The widths represent the 1σ errors on each frequency.*

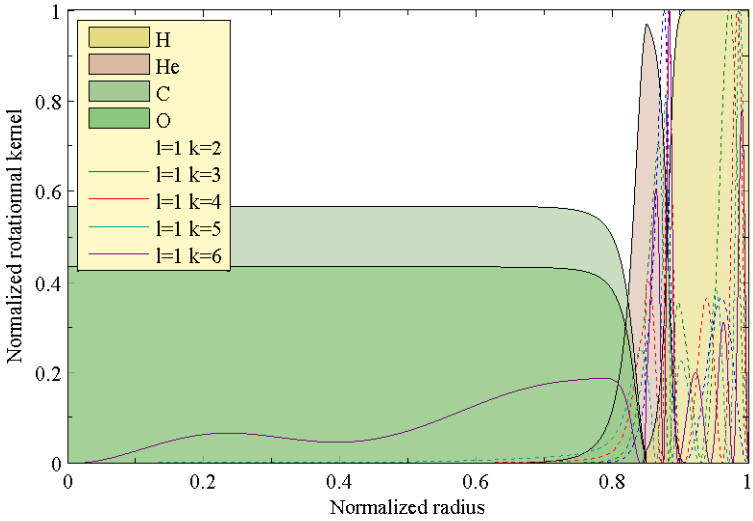

Figure 6.15: *Rotation kernels of the five modes as a function of the normalized radius.*

modes identified with observed multiplets. This is illustrated in Figure 6.15, where we plot the rotation kernels as a function of the radius of the star. We clearly see that all the modes, except for $k = 6$, are sensitive to the outer layer of KIC 11911480. For the first time ever in a ZZ Ceti star, we have been able to probe deeper into the core, thanks to the pulsation mode at $k = 6$. This has enabled a better estimate of the core composition in the case of this ZZ Ceti star.

Based on the optimal model of KIC 11911480, we have been able to determine its internal rotation profile, as shown in Figure 6.16. Once again, the g-modes only probe the outer 20% of the total radius of KIC 11911480, due to the degenerate core of ZZ Ceti stars. Nevertheless, we can still conclude from the internal rotation profile shown here that KIC 11911480 rotates as a solid body - at least within its outer 20% layer. Figure 6.16 is a contour map of the logarithm of the merit function S^2 in terms of depth and in terms of the rotation period. The nearly vertical white curve indicates the very well defined solution of the rotation period and the dotted white lines depict the 1, 2 and 3σ contours. In comparison, the vertical dotted-dashed white curve gives the exact solution for solid-body rotation. This Figure shows that KIC 11911480 rotates like a solid body at 78.63 $\pm$ 3.6 h over more than 20% of its radius.

6.5.4 Nonadiabatic approach

The main purpose of analysing the optimal model found with a nonadiabatic approach is to verify if the pulsation modes identified are indeed expected to be excited. We summarise in Table 6.10 the results obtained with the nonadiabatic pulsation code. The modes identified in this case are indeed consistent with the ones observed

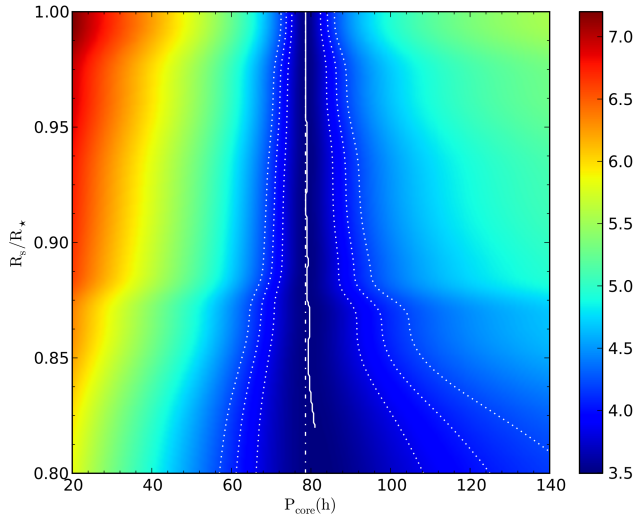

Figure 6.16: *Internal rotation profile of KIC 11911480 in the form of a contour map of the logarithm of the merit function S^2 as a function of depth and rotation period of the star. The white curve indicates the solution of the rotation period and the dotted white lines are the 1, 2 and 3σ contours. The vertical dotted-dashed line indicates the exact solution for solid-body rotation.*

Table 6.10: *Non adiabatic properties of the optimal model of KIC 11911480.*

l	k	P (s)	$\log E_{kin}$	C_{kl}	σ_I	σ_R
1	1	77.101	47.692	0.480	2.685E-15	-6.759E-16
1	2	174.259	46.786	0.472	-3.671E-14	-1.957E-13
1	3	203.586	46.216	0.476	-4.174E-13	-1.371E-12
1	4	259.693	45.626	0.473	-5.480E-12	-1.156E-11
1	5	290.824	45.334	0.454	-1.797E-11	-3.226E-11
1	6	325.969	45.556	0.339	-1.881E-11	-2.818E-11

in KIC 11911480 and with the optimal model found in the adiabatic approach. We provide the values of σ_I and σ_R returned for each pulsation mode. We recall that when $\sigma_I < 0$, the mode is unstable, driven whereas when $\sigma_I > 0$, the mode is stable, damped. We add the solution for the l =1 , $k = 1$ mode in Table 6.10 to show that in this case, $\sigma_I > 0$, and confirms the fact that we should not be detecting this given pulsation mode in the case of KIC 11911480. Once again, this is an independent result that confirms the validity of the optimal model found for KIC 11911480.

6.5.5 Asteroseismic properties of KIC 11911480

The main parameters derived from the detailed asteroseismic analysis of KIC 11911480 are the effective temperature $T_{\rm eff} = 11\,694 \pm 100$ K, the surface gravity $\log g = 8.03 \pm 0.05$. These parameters are in agreement with the spectroscopic values we found:

$T_{\rm eff}$ = 12 160 ± 250 K and $\log g$ = 7.94 ± 0.05. The asteroseismic analysis also enabled us to determine the fractional mass of the He layer $\log \Delta M(\mathrm{He})/M$ = -2.42 ± 0.13 and the fractional mass of the H envelope $\log \Delta M(\mathrm{H})/M$ = -3.46 ± 0.16. This value for the hydrogen envelope represents a thick hydrogen envelope, yet is still within the physical theoretical limit for DA WD stars. Given the mass-radius relationship of WDs, we can estimate the radius and mass of KIC 11911480 assuming these parameters: $M_{WD} = 0.645\ M_{\odot}$ and $R = 1.28 \times 10^{-2} R_{\odot}$. Finally, using the splitting in the power spectrum of KIC 11911480, we were able to derive a rotation period at P_{rot} = 3.28 ± 0.15 days.

Chapter 7

Conclusion and future work

In this thesis, we show how astronomical surveys can be exploited to search for, to find and to study compact stars in our Milky Way. Multi-wavelength surveys have revolutionised the field and dramatically changed the way we analyse astronomical data. In two separate projects, we use different surveys to search for LMXBs on the one hand, and for WDs on the other hand.

In Chapter 5, we look for the near-infrared counterparts of 1658 X-ray sources in the Galactic Bulge, detected with NASA's *Chandra* satellite. Due to the very high extinction and crowding in that region, the X-ray sources typically have multiple possible matches in the NIR catalogues we exploited. The 2MASS survey was used for bright sources and the UKIDSS GPS for faint ones. However, the VVV survey provided the majority of the NIR data we required in this study as it was the most complete survey of the Bulge. In order to find the most likely counterpart within the 95% positional error radius, we associate a false alarm probability based on the K_s-band magnitude of the sources, its distance to the X-ray position and the source density around the X-ray positions. We find that $\sim 79\%$ of the GBS sources have a NIR counterpart with a FAP $< 3\%$.

With the NIR photometric data at hand, as well as associated FAPs to each source, we move on to exploiting the K_s-band variability part of the VVV survey. This photometric variability data was not taken on a regular cadence, making it impossible to yield periods or any physical parameters of variable sources found. Nevertheless, we automate the search for variable sources by associating a probability (p-value) to the calculated χ^2 of each light curve we had. In total, we find 249 sources with high probability of being variable. Out of these, only 104 of them were visually classified as variable.

The GBS project also has a deep optical photometric survey of its area. This optical survey was done using the r, i and Hα filters. We used a $(r, r - \mathrm{H}\alpha)$ colour-magnitude diagram to select strong Hα emission line objects. In total, we find 161 possible counterparts to the GBS sources that stand out in colour-magnitude space. Combining these optical data with the NIR information we have on the sources, we can begin to characterize different types of objects.

Finally, we also have a deep optical variability survey using the r-band,

specially designed to search for any variable counterparts to the GBS X-ray sources (Britt et al., 2014). In a total area covering 75% of the GBS fields, 167 variable sources were found. Out of these, only 20 are in common with the VVV variable sources making each survey an additional asset to the study of the GBS X-ray sources.

Spectroscopy remains the only way to identify and classify sources. We are now in a strong position to sensibly select and prioritise the best targets for follow-up spectroscopy. The advance in technology and the number of multi-wavelength surveys providing crucial data for the GBS project are enabling us to move forward with the survey's goals, as well as to have a more convincing strategy with our target selection for follow-up. A few sources already have optical spectra taken on several telescopes in Chile, but no criterion other than optical brightness was used to select these sources. The spectroscopic results of the GBS X-ray sources have been presented by Ratti et al. (2013), Torres et al. (2014), Britt et al. (2013), Wu et al. (2014, submitted). So far, we have confirmed ∼30 CVs and are still searching for the LMXBs in our sample. This project is still ongoing, with many unexploited and undiscovered systems awaiting to be found. We recently requested a few nights on Gemini South using GMOS to follow-up bright NIR variable counterparts to the GBS X-ray sources, which were faint in the optical data. The GBS team is also following-up other individual sources using other instruments in other wavebands. Also, the optical variability data of the remaining 25% of the GBS area is being reduced and will reveal additional interesting objects that require further attention. Since the K_s filter probes the most through the large amount of extinction towards the Bulge, possibly deeper NIR images of the GBS fields could be the next step forward in the study of the GBS sources. Finally, in order to assess any flux ratios, whether optical to X-ray or NIR to X-ray, we will require deeper *Chandra* images of the GBS region.

In Chapter 6, we presented the method we developed to find WDs in the *Kepler* field. In order to achieve this goal, we carried the *Kepler*-INT Survey which we describe in Chapter 4.3. KIS is a deep optical survey of the *Kepler* field, using U, g, r, i and Hα filters on the INT. The addition of the U and Hα filters were crucial for our science goal since WDs are bluer than main-sequence stars and DA WDs have broad hydrogen absorption lines, making them Hα deficit sources in colour-space. We showed that we can successfully select WD candidates on the basis of their colours and have confirmed their identities using ISIS, an intermediate resolution spectrograph, on the WHT. We found 43 new WDs in the *Kepler* field.

In order to make the most of the unprecedented and high quality light curves of the *Kepler* spacecraft, we searched for the pulsating WDs in the field. Asteroseismology has the potential to probe their electron degenerate cores, unlike spectroscopy which only looks at their thin atmospheres. We selected our pulsating WD candidates using all the information we have: on one hand, sources that fell near the first ZZ Ceti (Hermes et al., 2011) and within the empirical $(T_{\rm eff}, \log g)$ instability strip boundaries plotted in colour-space were chosen for ground-based follow-up, as well as WDs with atmospheric parameters that placed them within the empirical

($T_{\rm eff}, \log g$) instability strip boundaries. We also made use of the fact that many sources had multiple KIS observations, helping us select possible variable sources using a reduced χ^2 test. The atmospheric parameters were obtained by fitting the optical spectra with WD model atmospheres. We confirmed six new ZZ Ceti stars in the *Kepler* field by using ground-based time-series photometry. We obtained *Kepler* short-cadence observations of four of them. The next step would be to follow-up the rest of the ZZ Ceti candidates we found, in order to see if they are variable and if they truly belong to the instability strip.

We present in Chapter 6.4 the preliminary asteroseismic analyses of the four ZZ Ceti stars observed with *Kepler*: KIC 11911480, KIC 10132702, KIC 0435037 and KIC 07594781. All four DAVs have pulsation periods within the expected range for this type of variable WD. They also all confirm that WDs are *slow rotators* with rotation periods in the order of days.

We also show the full asteroseismic analysis of KIC 11911480, our first ZZ Ceti in the *Kepler* field. The study consists of matching the observed power spectrum with modeled ones, using a genetic algorithm developed by Stephane Charpinet, Pierre Brassard and Gilles Fontaine. Our results were very surprising as this is the first ZZ Ceti which shows a mode that probes into the core, as g-modes usually only propagate in their surfaces. Our asteroseismic findings are also in agreement with the spectroscopic ones. These results are a clear example of what can be done with exceptional light curves and data. This also shows that theory and observations are in agreement in this case. The next step would be to perform similar asteroseismic studies of the rest of the ZZ Ceti stars for which we have *Kepler* short-cadence data. It is essential to study a large sample of WD targets in order to acquire a full understanding of their structure and evolution, as well as to probe the entire instability strip. With our current range of ZZ Ceti stars, we are on our way to fulfilling this goal.

As part of our project, we were also granted 3 HST COS orbits of one of our ZZ Ceti stars, in order to have a better constraint on its temperature and pulsation modes. The observations are scheduled for September 2014. These data will consist of three ultra-violet spectra of KIC 4552982. It has been proven by Allard & Koester (1992) that the detection of the H2/H2+ quasi-molecular satellites at 1400Å and 1600Å would improve the measured surface gravities and effective temperatures of WDs. They show that these lines are strongly dependant on surface gravity measurements, which would therefore provide a more accurate estimate of this parameter. In the case of optical spectra of WDs, the higher Balmer lines used to determine the star's atmospheric parameters over-estimate them. Therefore, UV spectra of WDs are crucial in our study. The general method in mode identification consists of fitting the observed light-curve to theoretical models based on stellar structure codes and pulsation codes. In the case of ZZ Ceti stars where the number of large-amplitude modes detected is low, the inaccuracies on the determined parameters can be large. A way to solve this problem is by obtaining the mode identifications (or pulsation indices) independently of stellar structure and pulsation codes. This can be done with UV data, since the pulsation amplitudes are larger in the UV wavelengths than in the optical. A limb darkening approach is used in this case and

is independent of pulsation theories and WD structure (see Robinson et al. 1995 for more details). A good determination of the pulsation indices will enable a more accurate measurement of the masses and effective temperatures of the WDs.

Finally, in May 2013, after our *Kepler* GO (Guest Observer) proposal to observe all our pulsating WDs in the field was approved, the reaction wheel #4 onboard the spacecraft failed. This resulted in having to move its pointing towards the ecliptic. The new mission, *Kepler*-2 (K2), will continuously observe 10 given fields in the ecliptic for ∼80 days at a time. The length of each run is good enough for us to undertake full asteroseismic studies of our pulsating WDs. Each K2 field has the same 116 $\deg^2$ field-of-view as the original one. As we were very successful in finding many ZZ Cetis in the *Kepler* field, we are restarting our project in the K2 mission. This should enable us to find and analyse many more pulsating WDs in order to probe the entire instability strip and broaden our understanding of the structure, composition and evolution of WDs. Selecting pulsating WDs in the K2 fields is turning out more challenging than in the original *Kepler* FoV since we no longer have KIS photometry to exploit, yet we are still able to find a handful in each K2 field, in order to carry on our project.

Abbreviations

2MASS	Two Micron All Sky Survey
AGN	Active Galactic Nuclei
CASU	Cambridge Astronomy Survey Unit
CV	Cataclysmic Variable
FAP	False Alarm Probability
GBS	Galactic Bulge Survey
GPS	Galactic Plane Survey
IDR	Initial Data Release
IPHAS	INT Photometric Hα Survey of the Northern Galactic Plane
INT	Isaac Newton Telescope
ISIS	Intermediate dispersion Spectrograph and Imaging System
KASC	*Kepler* Asteroseismic Science Consortium
KIS	*Kepler*-INT Survey
LMXB	Low Mass X-ray Binary
NIR	Near-InfraRed
RS CVn	RS Canum Venaticorum
SED	Spectral Energy Distribution
UCXB	Ultra-Compact X-ray Binary
UKIDSS	UKIRT Infrared Deep Sky Survey
UKIRT	UK InfraRed Telescope
UVEX	UV-Excess Survey of the Northern Galactic Plane
VVV	VISTA Variables in the Via Lactea
WD	White Dwarf
WFC	Wide Field Camera
WHT	William Herschel Telescope

Bibliography

Abazajian, K. N., et al., 2009, ApJS, 182, 543

Aerts, C., Christensen-Dalsgaard, J., Kurtz, D. W., 2010, Asteroseismology

Allard, N. F., Koester, D., 1992, A&A, 258, 464

Basri, G., et al., 2011, AJ, 141, 20

Benkő, J. M., et al., 2010, MNRAS, 409, 1585

Bergeron, P., Wesemael, F., Fontaine, G., Liebert, J., 1990, ApJ Lett., 351, L21

Bergeron, P., Leggett, S. K., Ruiz, M., 2001, ApJS, 133, 413

Bergeron, P., et al., 2011, ApJ, 737, 28

Bloemen, S., et al., 2011, MNRAS, 410, 1787

Böhm-Vitense, E., 1958, Zeitschrift für Astrophysik, 46, 108

Borucki, W. J., et al., 2010, Sci, 327, 977

Brickhill, A. J., 1992, MNRAS, 259, 529

Britt, C. T., et al., 2013, ApJ, 769, 120

Britt, C. T., et al., 2014, ApJS, 214, 10

Brown, T. M., Latham, D. W., Everett, M. E., Esquerdo, G. A., 2011, AJ, 142, 112

Carroll, B. W., Ostlie, D. A., 2006, An introduction to modern astrophysics and cosmology

Casares, J., Charles, P., 2006, Advances in Space Research, 38, 2731

Chandrasekhar, S., 1931, ApJ, 74, 81

Chandrasekhar, S., 1939, An introduction to the study of stellar structure

Chaplin, W. J., et al., 2010, ApJ Lett., 713, L169

Charles, P. A., Coe, M. J., 2006, Optical, ultraviolet and infrared observations of X-ray binaries, p. 215

Charpinet, S., Van Grootel, V., Reese, D., Fontaine, G., Green, E. M., Brassard, P., Chayer, P., 2008, A&A, 489, 377

Charpinet, S., Fontaine, G., Brassard, P., 2009, Nat, 461, 501

Charpinet, S., et al., 2011, A&A, 530, A3

Corradi, R. L. M., et al., 2008, A&A, 480, 409

Coughlin, J. L., López-Morales, M., Harrison, T. E., Ule, N., Hoffman, D. I., 2011, AJ, 141, 78

Davies, R. L., et al., 1997, in Ardeberg, A. L., ed., Optical Telescopes of Today and Tomorrow, vol. 2871 of *Society of Photo-Optical Instrumentation Engineers (SPIE) Conference Series*, p. 1099

DeWitt, C., Bandyopadhyay, R. M., Eikenberry, S. S., Blum, R., Olsen, K., Sellgren, K., Sarajedini, A., 2010, ApJ, 721, 1663

Drew, J. E., Greimel, R., Irwin, M. J., Sale, S. E., 2008, MNRAS, 386, 1761

Drew, J. E., et al., 2005, MNRAS, 362, 753

Dufour, P., Liebert, J., Fontaine, G., Behara, N., 2007, Nat, 450, 522

Dufour, P., Fontaine, G., Liebert, J., Williams, K., Lai, D. K., 2008, ApJ Lett., 683, L167

Dupret, M. A., Quirion, P. O., Fontaine, G., Brassard, P., Grigahcène, A., 2008, Journal of Physics Conference Series, 118, 012051

Evans, I. N., et al., 2010, ApJS, 189, 37

Everett, M. E., Howell, S. B., Kinemuchi, K., 2012, PASP, 124, 316

Fontaine, G., Brassard, P., 2008, PASP, 120, 1043

Fontaine, G., Brassard, P., Bergeron, P., 2001, PASP, 113, 409

Fontaine, G., et al., 2011, ApJ, 726, 92

Gänsicke, B. T., 2005, in J.-M. Hameury & J.-P. Lasota, ed., The Astrophysics of Cataclysmic Variables and Related Objects, vol. 330 of *Astronomical Society of the Pacific Conference Series*, p. 3

Gänsicke, B. T., et al., 2009, MNRAS, 397, 2170

Gianninas, A., Bergeron, P., Ruiz, M. T., 2011, ApJ, 743, 138

Gonzalez, O. A., Rejkuba, M., Zoccali, M., Valenti, E., Minniti, D., 2011, A&A, 534, A3

González-Solares, E. A., et al., 2008, MNRAS, 388, 89

González-Solares, E. A., et al., 2011, MNRAS, 416, 927

Greiss, S., Gänsicke, B. T., Hermes, J. J., Steeghs, D., Koester, D., Ramsay, G., Barclay, T., Townsley, D. M., 2014, MNRAS, 438, 3086

Greiss, S., et al., 2012, ArXiv e-print 1212.3613

Grindlay, J. E., et al., 2005, ApJ, 635, 920

Groot, P. J., et al., 2009, MNRAS, 399, 323

Haensel, P., Potekhin, A. Y., Yakovlev, D. G., eds., 2007, Neutron Stars 1 : Equation of State and Structure, vol. 326 of *Astrophysics and Space Science Library*

Harris, W. E., 2003, in Livio, M., Noll, K., Stiavelli, M., eds., A Decade of Hubble Space Telescope Science, p. 78

Heber, U., Napiwotzki, R., Reid, I. N., 1997, A&A, 323, 819

Hermes, J. J., et al., 2011, ApJ Lett., 741, L16

Hermes, J. J., et al., 2013, ApJ, 765, 102

Hoard, D. W., Szkody, P., Ishioka, R., Ferrario, L., Gänsicke, B. T., Schmidt, G. D., Kato, T., Uemura, M., 2002, AJ, 124, 2238

Holberg, J. B., Bergeron, P., 2006, AJ, 132, 1221

Homeier, D., Koester, D., Hagen, H. J., Jordan, S., Heber, U., Engels, D., Reimers, D., Dreizler, S., 1998, A&A, 338, 563

Hong, J., 2012, MNRAS, 427, 1633

Hynes, R. I., 2010, ArXiv e-print 1010.5770

Hynes, R. I., et al., 2012, ApJ, 761, 162

Jonker, P. G., et al., 2011, apjss, 194, 18

Jonker, P. G., et al., 2014, ApJS, 210, 18

Karl, C. A., Napiwotzki, R., Heber, U., Dreizler, S., Koester, D., Reid, I. N., 2005, A&A, 434, 637

Kawaler, S. D., Hostler, S. R., 2005, ApJ, 621, 432

King, A. R., 2003, ArXiv e-print 0301118

Kleinman, S. J., et al., 1994, ApJ, 436, 875

Kleinman, S. J., et al., 1998, ApJ, 495, 424

Knigge, C., Baraffe, I., Patterson, J., 2011, ApJS, 194, 28

Koester, D., 2010, Mem. Soc. Astron. Ital., 81, 921

Koester, D., 2013, White Dwarf Stars, p. 559

Koester, D., Dreizler, S., Weidemann, V., Allard, N. F., 1998, A&A, 338, 612

Koester, D., Voss, B., Napiwotzki, R., Christlieb, N., Homeier, D., Lisker, T., Reimers, D., Heber, U., 2009, A&A, 505, 441

Kolb, U., 2010, Extreme Environment Astrophysics

Landolt, A. U., 1968, ApJ, 153, 151

Lasker, B. M., Hesser, J. E., 1971, ApJ Lett., 163, L89

Lattimer, J. M., Prakash, M., 2004, Sci, 304, 536

Lawrence, A., et al., 2007, MNRAS, 379, 1599

Lewin, W. H. G., van der Klis, M., 2006, Compact stellar X-ray sources

Liebert, J., Bergeron, P., Holberg, J. B., 2005, ApJS, 156, 47

Liu, Q. Z., van Paradijs, J., van den Heuvel, E. P. J., 2007, VizieR Online Data Catalog, 346, 90807

Llama, J., Jardine, M., Mackay, D. H., Fares, R., 2012, MNRAS, 422, L72

Lucas, P. W., et al., 2008, MNRAS, 391, 136

Lynden-Bell, D., Ostriker, J. P., 1967, MNRAS, 136, 293

Maccarone, T. J., et al., 2012, MNRAS, 426, 3057

Marsh, T. R., 1989, PASP, 101, 1032

Mauerhan, J. C., Muno, M. P., Morris, M. R., Bauer, F. E., Nishiyama, S., Nagata, T., 2009, ApJ, 703, 30

McGraw, J. T., 1979, ApJ, 229, 203

McMillan, P. J., 2011, MNRAS, 414, 2446

Meibom, S., et al., 2011, ApJ Lett., 733, L9

Mestel, L., 1952, MNRAS, 112, 583

Metcalfe, T. S., Salaris, M., Winget, D. E., 2002, ApJ, 573, 803

Minniti, D., et al., 2010, New Astronomy, 15, 433

Montgomery, M. H., 2005, ApJ, 633, 1142

Montgomery, M. H., Williams, K. A., Winget, D. E., Dufour, P., De Gennaro, S., Liebert, J., 2008, ApJ Lett., 678, L51

Morgan, W. W., Harris, D. L., Johnson, H. L., 1953, ApJ, 118, 92

Mukadam, A. S., Montgomery, M. H., Winget, D. E., Kepler, S. O., Clemens, J. C., 2006, ApJ, 640, 956

Mukadam, A. S., et al., 2004, ApJ, 607, 982

Mullally, F., Winget, D. E., Degennaro, S., Jeffery, E., Thompson, S. E., Chandler, D., Kepler, S. O., 2008, ApJ, 676, 573

Muno, M. P., et al., 2004, ApJ, 613, 1179

Muno, M. P., et al., 2009, ApJS, 181, 110

Mushotzky, R. F., Edelson, R., Baumgartner, W., Gandhi, P., 2011, ApJ Lett., 743, L12

Nather, R. E., Winget, D. E., Clemens, J. C., Hansen, C. J., Hine, B. P., 1990, ApJ, 361, 309

Nebot Gómez-Morán, A., et al., 2013, A&A, 553, A12

Nemec, J. M., et al., 2011, MNRAS, 417, 1022

Oke, J. B., Gunn, J. E., 1983, ApJ, 266, 713

Østensen, R. H., Bloemen, S., Vučković, M., Aerts, C., Oreiro, R., Kinemuchi, K., Still, M., Koester, D., 2011a, ApJ Lett., 736, L39

Østensen, R. H., et al., 2010, MNRAS, 409, 1470

Østensen, R. H., et al., 2011b, MNRAS, 414, 2860

Ozel, F., Psaltis, D., Narayan, R., McClintock, J. E., 2010, ArXiv e-print 1006.2834

Pickles, A. J., 1998, PASP, 110, 863

Pojmanski, G., 1997, Acta Astron., 47, 467

Prialnik, D., 2000, Stellar structure and evolution, Cambridge University Press, Cambridge

Primini, F. A., et al., 2011, ApJS, 194, 37

Prša, A., et al., 2011, AJ, 141, 83

Quirion, P.-O., Fontaine, G., Brassard, P., 2007, ApJS, 171, 219

Quirion, P.-O., Dupret, M.-A., Fontaine, G., Brassard, P., Grigahcène, A., 2008, in Werner, A., Rauch, T., eds., Hydrogen-Deficient Stars, vol. 391 of *Astronomical Society of the Pacific Conference Series*, p. 183

Ramsay, G., Doyle, J. G., Hakala, P., Garcia-Alvarez, D., Brooks, A., Barclay, T., Still, M., 2013, MNRAS, 434, 2451

Ratti, E. M., et al., 2013, MNRAS, 428, 3543

Remillard, R. A., McClintock, J. E., 2006, ARA&A, 44, 49

Ritter, H., Kolb, U., 1992, A&A, 259, 159

Ritter, H., Kolb, U., 2003, A&A, 404, 301

Robinson, E. L., et al., 1995, ApJ, 438, 908

Romero, A. D., Córsico, A. H., Althaus, L. G., Kepler, S. O., Castanheira, B. G., Miller Bertolami, M. M., 2012, MNRAS, 420, 1462

Ryan, S. G., Norton, A. J., 2010, Stellar Evolution and Nucleosynthesis

Saito, R. K., et al., 2012, A&A, 544, A147

Scaringi, S., Körding, E., Uttley, P., Groot, P. J., Knigge, C., Still, M., Jonker, P., 2012, MNRAS, 427, 3396

Schlegel, D. J., Finkbeiner, D. P., Davis, M., 1998, ApJ, 500, 525

Schwarzenberg-Czerny, A., 1993, in P. Grosbol & R. de Ruijsscher, ed., European Southern Observatory Astrophysics Symposia, vol. 47 of *European Southern Observatory Astrophysics Symposia*, p. 149

Sekiguchi, K., 1992, Nat, 358, 563

Servillat, M., Grindlay, J., van den Berg, M., Hong, J., Zhao, P., Allen, B., 2012, ApJ, 748, 32

Skrutskie, M. F., et al., 2006, AJ, 131, 1163

Soszyński, I., et al., 2011a, Acta Astron., 61, 1

Soszyński, I., et al., 2011b, Acta Astron., 61, 285

Steeghs, D., Casares, J., 2002, ApJ, 568, 273

Steeghs, D., McClintock, J. E., Parsons, S. G., Reid, M. J., Littlefair, S., Dhillon, V. S., 2013, ApJ, 768, 185

Still, M., Howell, S. B., Wood, M. A., Cannizzo, J. K., Smale, A. P., 2010, ApJ Lett., 717, L113

Stoughton, C., et al., 2002, AJ, 123, 485

Szymański, M. K., Udalski, A., Soszyński, I., Kubiak, M., Pietrzyński, G., Poleski, R., Wyrzykowski, Ł., Ulaczyk, K., 2011, Acta Astron., 61, 83

Tassoul, M., Fontaine, G., Winget, D. E., 1990, ApJS, 72, 335

Tauris, T. M., van den Heuvel, E. P. J., 2006, Formation and evolution of compact stellar X-ray sources, p. 623

Torres, M. A. P., et al., 2014, MNRAS, 440, 365

Tremblay, P.-E., Bergeron, P., 2009, ApJ, 696, 1755

Tremblay, P.-E., Bergeron, P., Gianninas, A., 2011a, ApJ, 730, 128

Tremblay, P.-E., Ludwig, H.-G., Steffen, M., Bergeron, P., Freytag, B., 2011b, A&A, 531, L19

Tremblay, P.-E., Ludwig, H.-G., Steffen, M., Freytag, B., 2013, A&A, 559, A104

Udalski, A., et al., 2012, Acta Astron., 62, 133

Valdivielso, L., et al., 2009, A&A, 497, 973

van den Berg, M., Penner, K., Hong, J., Grindlay, J. E., Zhao, P., Laycock, S., Servillat, M., 2012, ApJ, 748, 31

Van Grootel, V., Dupret, M.-A., Fontaine, G., Brassard, P., Grigahcène, A., Quirion, P.-O., 2012, A&A, 539, A87

Van Grootel, V., Charpinet, S., Brassard, P., Fontaine, G., Green, E. M., 2013, A&A, 553, A97

van Kerkwijk, M. H., Rappaport, S. A., Breton, R. P., Justham, S., Podsiadlowski, P., Han, Z., 2010, ApJ, 715, 51

Vauclair, C., 1997, in Provost, J., Schmider, F.-X., eds., Sounding Solar and Stellar Interiors, vol. 181 of *IAU Symposium*, p. 367

Verbeek, K., et al., 2012, MNRAS, 420, 1115

Viironen, K., et al., 2009, A&A, 504, 291

Vuille, F., 2000, MNRAS, 313, 170

Warner, B., 1995, Cataclysmic Variable Stars, Cambridge University Press, Cambridge

Williams, K. A., et al., 2010, AJ, 139, 2587

Winget, D. E., Kepler, S. O., 2008, ARA&A, 46, 157

Winget, D. E., Robinson, E. L., Nather, R. D., Fontaine, G., 1982, ApJ Lett., 262, L11

Winget, D. E., et al., 1991, ApJ, 378, 326

Witham, A. R., et al., 2006, MNRAS, 369, 581

Witham, A. R., et al., 2007, MNRAS, 382, 1158

Wood, M. A., Still, M. D., Howell, S. B., Cannizzo, J. K., Smale, A. P., 2011, ApJ, 741, 105

Wright, N. J., Barlow, M. J., Greimel, R., Drew, J. E., Matsuura, M., Unruh, Y. C., Zijlstra, A. A., 2009, MNRAS, 400, 1413

Wright, N. J., et al., 2008, MNRAS, 390, 929

Wu, Y., 2001, MNRAS, 323, 248

Wu, Y., Goldreich, P., 1999, ApJ, 519, 783

Yeates, C. M., Clemens, J. C., Thompson, S. E., Mullally, F., 2005, ApJ, 635, 1239